

https://dspace.org/

Characterisation of suitable fillers for a butt weld of creep aged X20 and virgin P91 pipes

Mphaphathi, Thendo

2021
https://hdl.handle.net/10539/32958

Downloaded from a DSpace repository. https://dspace.org/



Characterisation of Suitable Fillers for a Butt Weld of Creep Aged X20 and Virgin P91 Pipes.

MSc. RESEARCH DISSERTATION

Prepared by

Thendo Mphaphathi

Student No. 1055144

Submitted to

School of Chemical and Metallurgical Engineering, Faculty of Engineering and the Built Environment, University of the Witwatersrand, Johannesburg, South Africa

October, 2021

Declaration

I declare that this dissertation is my own unaided work. It is being submitted for the Degree of Master of Science in Engineering to the University of the Witwatersrand, Johannesburg. It has not been submitted before for any degree or examination to any other University.



_____

Signature

25 day of October year 2021

Abstract

The need to improve thermal efficiency in coal-fired power plants and to reduce emissions has led to the development of new creep resistant steels such as P91. These developments led to partial replacement of creep aged X20 pipes with the new P91 material in the power plants. In joining the transition welds, two different filler materials (X20 and P91) were used. Microstructural, mechanical and creep test of both pipe samples cross weld joints were evaluated to identify a suitable filler material. Microstructural studies on different weldment zones (weld metal (WM), heat affected zone (HAZ) and parent material (PM)) revealed comparable shape, orientation, and quantity of the characterised creep resistant metallurgical parameters such as precipitates, sub-grains and dislocation density for both different filler material weldments irrespective of the use of either X20 or P91 WM. Carbon migration was investigated using a scanning electron microscope (SEM) and nanoindentation hardness test across the fusion line. The results revealed a localised denuded zone, with a width of ~20μm located at the fusion line region of the welded joint. The presence of the denuded zone did not affect the mechanical (tensile and hardness tests) and creep (uniaxial and small punch creep test (SPCT)) results. Overall characterisation results in relation to the objectives of this study did not reveal any distinctive performance differences resulting from using either the X20 or P91 weld filler for a butt weld of creep aged X20 and virgin P91 pipes. Both weld fillers (X20 and P91) were deemed suitable since they gave comparable results based on short term uniaxial creept tests (i.e. max. 1302 hours of creep test) and from small punch creep tests (SPCT).

Acknowledgements

I thankfully acknowledge my academic supervisor Prof. Nthabiseng Maledi for the supervision provided throughout the entire research tenure. Her exceptional technical support, guidance and encouragement enabled me to successfully complete this research study.

I gratefully acknowledge my industrial mentors; Mr. Marthinus Bezuidenhout and Dr. Thobeka Pete for the exceptional technical input and fruitful discussions during research. Their brilliant input enabled this research work to be aligned with the power plants engineering maintenance roadmap.

My appreciation goes to Dr. Dreyer Bernard for the SPCT work that was successfully carried out at eNtsa in Nelson Mandela University. The SEM and TEM characterisation work that was successfully carried out at the Centre for HRTEM in Nelson Mandela University by Dr. Johan Westraadt is also highly appreciated.

I thankfully acknowledge Dr Mark Newby of the power plant Research Testing and Development (RT&D), for the laboratory X-ray diffraction residual stress measurements that were carried out in this research project.

My affectionate gratitude is directed to my family; to my caring wife Tshimangadzo Mphaphathi, for her sustained support while I'm at work and at school. It is gratifying to appreciate my handsome sons; Washu and Bebiwani, their smiles offer me the reason to progress on my studies. Finally, and more importantly, to my parents (Mr. AA. Mphaphathi and Mrs. MJ. Mphaphathi) and my siblings (Masindi Mphaphathi, Pembelani Mphaphathi and Adivhaho Mphaphathi) whom I'm fully appreciative for their continuous inspiration in my academic and career activities.

Publications

I (Thendo Mphaphathi) the author of this dissertation, have published the following 2 manuscripts (papers).

1. Mphaphathi, T., Maledi, N., Bezuidenhout, M., Pete, T., Westraadt, J. E., Bernard, D., (2019), *Characterisation of Suitable Fillers for Butt Weld of Creep Aged X20 and Virgin P91 Pipes*, In Joint EPRI-123HiMAT Conference on Advances in High Temperature Materials. Japan, Nagasaki, pp. 1109-1122.
2. Westraadt, J. E., Bernard, D., Mphaphathi, T., Bezuidenhout, M., (2019), *Microstructural Characterisation and Small Punch Creep Testing of 9-12Cr Steel Weldments*, In Joint EPRI-123HiMAT Conference on Advances in High Temperature Materials, Japan, Nagasaki, pp. 1270-1281.

Table of Content

DECLARATION ..... - 2 -

ABSTRACT ..... - 3 -

ACKNOWLEDGEMENTS ..... - 4 -

PUBLICATIONS ..... - 5 -

TABLE OF CONTENT 1

LIST OF FIGURES 3

LIST OF TABLES 8

LIST OF ABBREVIATIONS 9

1. INTRODUCTION 11

1.1. BACKGROUND 11
1.2. MOTIVATION FOR RESEARCH 13
1.3. RESEARCH QUESTIONS 14
1.4. HYPOTHESIS 15
1.5. RESEARCH AIM AND OBJECTIVES 15

2. LITERATURE REVIEW 17

2.1. INTRODUCTION 17
2.2. POWER PLANTS EFFICIENCY 17
2.3. MATERIALS DEFORMATION MECHANISMS 26
2.4. HIGH TEMPERATURE STRENGTH 27
2.5. CREEP MECHANISM 29
2.6. PRECIPITATION SEQUENCE 33
2.7. HISTORICAL IMPROVEMENT OF CREEP APPLICATION STEELS 36
2.8. THE DEVELOPMENT OF 9-12% CR STEELS FOR BOILER APPLICATION 38
2.9. TYPES AND EFFECTS OF WELDING PROCESS USED IN THIS STUDY 42
2.10. MICROSTRUCTURAL EVOLUTION OF WELDED JOINTS 43
2.10.1. Grain growth zone ($T_p >> A_{c3}$) *44*
2.10.2. Grain refined zone ($T_p > A_{c3}$) *44*
2.10.3. Partially transformed zone – intercritical HAZ ($Ac1 < T_p < A_{c3}$) *44*
2.10.4. Over-tempered region *45*
2.10.5. The unchanged base material zone *45*
2.11. STRESS ANALYSIS ON WELDED STRUCTURES 47
2.12. THE EVOLUTION OF 9-12%CR STEELS MICROSTRUCTURE DURING HEAT TREATMENT AND CREEP 48
2.13. DIFFUSION OF CARBON DUE TO DIFFERENCES IN CR CONCENTRATION ACROSS FERRITIC STEEL WELD INTERFACES 54
2.14. CHAPTER SUMMARY 57

3. EXPERIMENTAL METHODOLOGY 58

3.1. INTRODUCTION 58
3.2. MATERIALS 58
3.3. FABRICATION OF WELDS 63
3.3.1 Welding Processes *63*
3.3.2 Post Weld Heat Treatment *64*
3.3.3 Non-Destructive Testing (NDT) on Welds *65*
3.4. ANALYSIS OF WELD RESIDUAL STRESSES 66
3.5. HARDNESS TESTING 67
3.6. TENSILE TESTING 68

3.7. CHARPY IMPACT TESTING 69
3.8. SMALL PUNCH CREEP TESTS 70
3.9. UNIAXIAL CREEP TEST 77
3.10. MICROSTRUCTURAL CHARACTERISATION 78
3.10.1 Optical microscopy *78*
3.10.2 Scanning Electron Microscopy *78*
3.10.3 Transmission electron microscopy (TEM) *79*
3.10.4 X-ray diffraction *80*

4. RESULTS AND DISCUSSION 81

4.1. INTRODUCTION 81
4.2. NON-DESTRUCTIVE TESTING (NDT) ON FABRICATION OF WELDS 81
4.2.1 Magnetic Particle Inspection *82*
4.2.2 Phase Array Ultrasonic Testing (PA-UT) and Radiography Testing (RT) *82*
4.3 RESIDUAL STRESS ANALYSIS 82
4.4 MECHANICAL TESTING 86
4.4.1 Hardness Test *86*
4.4.2 Macro Hardness Test *86*
4.4.3 Micro Hardness Test *88*
4.4.4 Tensile Test *89*
4.4.5 Room Temperature (21°C) Tensile Test *90*
4.4.6 Hot Tensile (500°C) Test ..... *- 93 -*
4.4.7 Hot Tensile (550°C) Test ..... *- 95 -*
4.4.8 Charpy Impact Toughness ..... *- 99 -*
4.5 MICROSTRUCTURAL CHARACTERISATION ..... - 101 -
4.5.1 Microstructural Characterisation of Post-Weld Heat Treated Weldments ..... *- 101 -*
4.5.2 Characterization of Microstructural Parameters *107*
4.5.2.1 Microstructural Characterization of Parent Metals *109*
4.5.2.2 Microstructural Characterization of Weld Filler Metals *111*
4.5.2.3 Microstructural Characterization of ICHAZ Regions of the Different Dissimilar Welds *113*
4.5.2.4 Precipitates Analysis Summary *114*
4.5.2.5 Grain Size Analysis Summary *116*
4.5.2.6 Dislocation Density Analysis Summary *118*
4.5.3 Orowan Back Stress Calculations before Creep Test *120*
4.6 DIFFUSION CHEMICAL ANALYSIS 123
4.7 CREEP TESTING 127
4.7.1 Small Punch Creep Tests *127*
4.7.2 Uniaxial Creep Tests *132*
4.8 MICROSTRUCTURAL CHARACTERISATION AFTER UNIAXIAL CREEP TESTING 139
4.9 CHAPTER SUMMARY 144

5. DISCUSSION 147

6. CONCLUSIONS AND RECOMMENDATIONS 151

6.1 CONCLUSIONS 151
6.2 RECOMMENDATIONS FOR FURTHER WORK 152

7. REFERENCES 153

8. RESEARCH PAPERS 161

8.1 FIRST PAPER: CHARACTERISATION OF SUITABLE FILLERS FOR BUTT WELD OF CREEP AGED X20 AND VIRGIN P91 PIPES 161
8.2 SECOND PAPER: MICROSTRUCTURAL CHARACTERISATION AND SMALL PUNCH CREEP TESTING OF 9-12CR STEEL WELDMENTS 175

List of Figures

Figure 2.1: Schematic representation of a fossil fired power plant steam cycle (Thomson, 1992) 18
Figure 2.2: Graphical representation of the historical development of fossil-fired turbine-generators in terms of pressure, temperature, megawatts outputs and thermal efficiency (Masuyama, 2000). 19
Figure 2.3: Trends of steam conditions (pressure and temperature) for power generating plants in Japan (Masuyama, 2000). 20
Figure 2.4: Power plants heat rate vs. steam parameters (steam pressure and temperature) improvements over years in Europe (Germany) (Aghajani, 2009). 21
Figure 2.5: Global research and development ventures on advanced steam power stations materials (Blum and Hald, 2000) 22
Figure 2.6: Steam parameters (pressure and temperature) plots trends for ultra-supercritical power stations (Masuyama, 2000). 25
Figure 2.7: Stress/temperature map showing regions of temperature and stress with dominant areas of the deformation mechanisms (Bano, *et al*., 2014). 27
Figure 2.8: Relationship between permissible material temperature at 49 MPa of permissible stress and comparative cost of steels (Masuyama, 2000) 29
Figure 2.9: The schematic creep rupture curve under constant load conditions (Evans and Wilshire, 1985). 30
Figure 2.10: Effect of temperature change and stress on creep behaviour (Nabarro and de Villiers, 1995). 30
Figure 2.11: The process of climb and glide (Yardley, 2003). 31
Figure 2.12: Carbide stability diagram for 2 2.5Cr1Mo steel, using micro-analytical methods to identify precipitation phases and sequences (Nutting, 1999). 33
Figure 2.13: Characteristic microstructure of tempered martensitic 9-12% Cr steels with common precipitates (Masuyama, 2001). 35
Figure 2.14: Historical developments and improvements in cree- rupture strength of boiler application steels (Masuyama; 1998) 36
Figure 2.15: Advancement of ferritic alloy material for power-plant application (Musuyama, 200). 40
Figure 2.16: Strength properties of 9-12% Cr steels (Hagen and Bendick, 2002). 42
Figure 2.17: Graphic representation of microstructures developed in HAZ due to welding peak temperature, equivalent to calculated equilibrium phase diagram of X10CrMoVNb9-1 (P91) steel (Blondeau, 2008; Cerjak and Mayr, 2008). 43
Figure 2.18: Classification of cracks in a weld joint (Molokwane; 2014) 46
Figure 2.19: Schematic representation of 9-12% Cr steels tempered martensitic microstructure (Holzer, 2010). 49
Figure 2.20: Evolution of $M_{23}C_6$, VX and Laves phase precipitates under long-term thermal degradation (Aghajani, 2009) 52
Figure 2.21: Progression of $M_{23}C_6$, VX and Laves phase precipitates mean diameter in long-term thermal aging application (Aghajani, 2009). 53
Figure 3.1: Flow chart illustrating the experimental methodology that was followed to achieve the research objective. 58
Figure 3.2: Photograph showing the X20 and P91 base materials pipe samples with their respective dimensions. 59
Figure 3.3: Surface replication micrographs of the base materials used, (a) X20 had 60 creep voids / mm^2 and, (b) P91 had no creep damage (virgin material) at 500X magnification. 60
Figure 3.4: Schematic representation of a single-Vee joint type weld prepared-phase [distance is in mm and angle is in degrees] 63

Figure 3.5: Post weld heat treatment profile applied on the weld joints at 755°C for 4 hours using the ramp rates of 50°C per hour. 65
Figure 3.6: Photograph showing the set-up of a laboratory X-ray diffraction residual stress measurements technique. 66
Figure 3.7: Photograph of a close-up view showing a set-up of a laboratory X-ray diffraction residual stress measurement technique being applied on a mechanically polished (3μm surface finish) cross weld pipe sample. 67
Figure 3.8: Macrographs indicating the weld metal, HAZ and parent material of (a) the X20 weld filler metal, P91 parent material side and (b) X20 weld filler metal, X20 parent material side.... 71
Figure 3.9: Macrographs indicating the weld metal, HAZ and parent material of (a) the P91 weld filler metal, P91 parent material side and (b) P91 weld filler metal, X20 parent material side. ... 71
Figure 3.10: Stereo macrographs with scribe lines indicating where the HAZ samples were removed from the X20 weld filler material sample (a) P91 parent material side, (b) X20 parent material side. 72
Figure 3.11: Stereo macrographs with scribe lines indicating where the HAZ samples were removed from the P91 weld filler material sample (a) P91 parent material side, (b) X20 parent material side. 72
Figure 3.12: Photograph showing extraction of slithers where SPCT disc samples were removed... 72
Figure 3.13: Micrographs showing the appearance of the microstructure on each side of the SPCT disc of the X20 weld filler metal samples, at a thickness of approximately 560 μm. 73
Figure 3.14: Micrographs showing the appearance of the microstructure on each side of the SPCT disc of the P91 weld filler metal samples, at a thickness of approximately 560 μm. 74
Figure 3.15: Photograph showing eNtsa's SPCT equipment facility that has 11 testing platforms in total at NMU. 75
Figure 3.16: Photograph showing the close-up view of eNtsa's SPCT frames/equipment. 75
Figure 3.17: Photograph showing the close-up view of an opened eNtsa's SPCT equipment, indicating the sample loading and heating zone (furnace). 76
Figure 3.18: Schematic representation of a cross weld uniaxial creep test specimen showing the dimensional details in mm. 78
Figure 4.1: Residual axial and hoop stress measurement profile on as welded condition for X20 to P91pipes welded with (a) X20 weld filler and (b) P91 weld filler. 84
Figure 4.2: Residual axial and hoop stress measurement profile on as heat treated condition for X20 to P91pipes welded with (a) X20 weld filler and (b) P91 weld filler. 85
Figure 4.3: Photograph of the etched cross weldment showing hardness traverses tests indentations carried out from creep aged X20 PM side (LHS) to the virgin P91 PM side (RHS). 86
Figure 4.4: Macro hardness traverse for both X20 and P91 weld filler cross weld joints. 87
Figure 4.5: Micro hardness traverse for both X20 and P91 weld filler across weld joints. 89
Figure 4.6: Mechanical tensile stress vs tensile strain curves typical of high strength and high ductile materials after post weld heat treatment (Example from X20 weld filler cross weld sample tested at 21°C with its duplicate sample). 90
Figure 4.7: Room temperature (21°C) yield strength and UTS for both X20 weld filler cross weld specimen (on the left hand side) and P91 weld filler cross weld specimen (on the right hand side). 91
Figure 4.8: Fracture surface image of the room temperature tensile tested specimen with the appearance of partial ductile (low / limited ductility) morphology with a dull (greyish) colour appearance (a) Fractured half sample (towards X20 PM side, (b) Fractured half sample (towards P91 PM side). ..... - 92 -

Figure 4.9: Yield strength and ultimate tensile strength for X20 (on the left hand side) and P91 (on the right hand side) weld filler cross weld specimens at 500°C ..... - 93 -
Figure 4.10: Fracture surface stereo image of the 500°C hot tensile tested specimen showing cup and cone shape with dull (greyish) colour appearance (a) Fractured half sample (towards X20 PM side, (b) Fractured half sample (towards P91 PM side)..... - 94 -
Figure 4.11: Yield strength and UTS for X20 weld filler cross weld specimen (on the left hand side) and P91 weld filler cross weld specimen (on the right hand side) at 550°C. ..... - 96 -
Figure 4.12: Fracture surface stereo image of the 550°C hot tensile tested specimen showing cup and cone shape with dull (greyish) colour appearance (a) Fractured half sample (towards X20 PM side, (b) Fractured half sample (towards P91 PM side).....97
Figure 4.13: Mechanical tensile test results as a function of change in test temperature conditions (21°C, 500°C and 550°C) for cross weldment fused by X20 and P91 weld filler material..98
Figure 4.14: Stereo microscope images of impact fracture surfaces filler metals showing features of ductile fracture; dull grey colour with cup and cone morphology appearances. ..... - 100 -
Figure 4.15: Photograph of an etched cross sectional view of the cross weldment showing the specific locations that were carefully identified in order to quantify the microstructural parameters. [Etched in Villella's reagent]. ..... - 101 -
Figure 4.16: Optical micrograph of the PMs for (a) X20 showing tempered martensite microstructure with occasional creep voids, and for (b) P91 showing tempered martensite microstructure typical of virgin P91 material, [Etched in Villella's reagent, 500X Magnification]. .... - 103 -
Figure 4.17: Optical micrographs of the ICHAZ for (a) X20 and for (b) P91 showing small grained structure with a mixture of tempered martensite laths and ferrite. Occasional creep voids are also evident only on the X20 ICHAZ side, [Etched in Villella's reagent, 500X Magnification]. ..... - 105 -
Figure 4.18: Optical micrograph of weld filler for (a) X20 and (b) metals showing tempered martensite microstructure. It is apparent that X20 has more martensite laths and less ferritic phase fraction compare to P91microstructure, [Etched in Villella's reagent, 500X Magnification].- 106 -
Figure 4.19: Processed images showing outlines (red) of the various features identified: a) Cr-precipitates from the TKD-EDS, b) V-precipitates from the TKD-EDS, c) Micro-grains from the EBSD and d) Sub-structure from the ADF-STEM images.....108
Figure 4.20: Processed HAADF-STEM images annotating the dislocations and the sub-structure that were measured. 109
Figure 4.21: Microstructural constituents maps showing the distribution of: a) Cr-precipitates from the TKD-EDS (Top Left Image), b) V-precipitates from the TKD-EDS (Top Right Image), c) Micro-grains from the EBSD (Bottom Left Image) and d) Sub-structure from the ADF-STEM (Bottom Image) for the parent material. 110
Figure 4.22: Microstructural constituents maps showing the distribution of: a) Cr-precipitates from the TKD-EDS (Top Left Image), b) V-precipitates from the TKD-EDS (Top Right Image), c) Micro-grains from the EBSD (Bottom Left Image) and d) Sub-structure from the ADF-STEM (Bottom Image) for the weld filler material. 112
Figure 4.23: Microstructural constituents maps showing the distribution of: a) Cr-precipitates from the TKD-EDS (Top Left Image), b) V-precipitates from the TKD-EDS (Top Right Image), c) Micro-grains from the EBSD (Bottom Left Image) and d) Sub-structure from the ADF-STEM (Bottom Image) for the ICHAZ region. 113
Figure 4.24: Mean surface-surface distance for the precipitates measured with TDK-EDS. 115
Figure 4.25: Normalised mean surface-surface measurements of the precipitates ($M_{23}C_6$ and MX). 116

Figure 4.26: The mean values for the linear intercept of the sub-structure and the short-width of the elongated micro-grains. 117
Figure 4.27: Sub-grain size of the different microstructural areas imaged using ADF-STEM. 118
Figure 4.28: Typical ADF-STEM images of the different microstructural zones showing the relative sub-structure size and the regions of high dislocation density. 119
Figure 4.29: Free dislocation density determined from XRD peak measurements. 120
Figure 4.30: Total Orowan backs tress contributions for the different microstructural regions. 122
Figure 4.31: Normalised microstructural values for different weldment regions. A dotted line represents a visual aid to compare each material features state relative to the normalisation in which a new P91 material is assigned a value of 1. 122
Figure 4.32: EDS chemical analysis on the micrograph samples plotting the chromium concentration across dissimilar X20 Parent Metal - P91 Weld Filler Metal, and P91 Parent Metal - X20 Weld Filler Metal cross welds. Blue intermittent straight line indicates the position of the weld-fusion line. 124
Figure 4.33: *(a)* Secondary electron images of fusion-lines for dissimilar weldments, with the nanoindentation hardness measurement overlay. *(b)* Precipitate phase fraction colour plot (12 vol% max), with EDS-profile analysis (Cr wt.%) overlay for the fusion-line region, indicated with the red rectangle on the left. [dark blue: 0; yellow: 12 vol.%] 125
Figure 4.34: Tested SPCT specimen of P91 parent material and P91 WM and FGHAZ samples. .. 128
Figure 4.35: Tested SPCT specimen of P91 parent material and P91 filler metal samples. 129
Figure 4.36: Small Punch Creep Test curves for all 8 samples (PM, X20 PM, P91 WM, X20 WM, P91 FGHAZ adjacent to P91 WM, P91 FGHAZ adjacent to X20 WM, X20 FGHAZ adjacent to P91 WM, and X20 FGHAZ adjacent to X20 WM specimens) at 276 N and 625°C. 130
Figure 4.37: Photograph of the creep test specimens showing the creep rupture location (X20 HAZ location side) 132
Figure 4.38: Photograph showing longitudinal-section view of the creep tested and ruptured specimens with evidence of localised necking adjacent to ruptured location. 133
Figure 4.39: Creep curves (creep strain Vs time) for creep aged X20 PM – X20 weld filler – new P91 PM at 60 MPa and its duplicate, creep aged X20 PM – X20 weld filler – new P91 PM at 80 MPa and its duplicate, creep aged X20 PM – P91 weld filler – new P91 PM at 60 MPa and its duplicate, creep aged X20 PM – P91 weld filler – new P91 PM at 80 MPa and its duplicate cross weld samples 134
Figure 4.40: Creep curve (creep strain vs time) for creep aged X20 PM in comparison with creep aged X20 PM – X20 weld filler – new P91 PM at 63 MPa and its duplicate, creep aged X20 PM – X20 weld filler – new P91 PM at 80 MPa and its duplicate, creep aged X20 PM – P91 weld filler – new P91 PM at 60 MPa and its duplicate, creep aged X20 PM – P91 weld filler – new P91 PM at 80 MPa and its duplicate cross weld samples. 136
Figure 4.41: Creep sensitivity analysis curves for a virgin and for 15% creep aged X20 parent materials with the comparison of the creep aged X20 PM creep test results (illustrated by a red dot). 138
Figure 4.42: Photograph of the uniaxial creep test specimens showing the creep rupture location (X20 HAZ location side) 140
Figure 4.43: Photograph of a ruptured creep test specimen showing the polished and etched longitudinal sectional view at the failure location; on the X20 HAZ side. Necking of the creep test specimen is also observed adjacent to the failure / rupture location. 140
Figure 4.44: Micrograph of the longitudinal section view for the uniaxial creep tested specimen showing micro creep cracks and voids adjacent to the creep rupture location (ICHAZ on X20

material side), (a); X20 parent metal side, (b); P91 weld filler [Etched in Villella's reagent, 50X Magnification]..... 142
Figure 4.45: Micrograph of the longitudinal section view for the uniaxial creep tested specimen showing micro creep cracks and voids adjacent to the creep rupture location (ICGHAZ on X20 material side (a)) [Etched in Villella's reagent, 500X Magnification]. 143
Figure 4.46: Stereo macrograph of the creep fracture surface specimen showing the ductile failure mode features (i.e. ductile dimples, "cup and cone shape", dull grey colour appearance and necking adjacent to fracture surface). [10X Magnification]..... 144

List of Tables

Table 2.1: Ultra-supercritical power stations that are in operation (Blum and Hald, 2000)..... - 24 -
Table 2.2: Summary of common precipitates data. (Andrews et al., 1967; Yardley, 2003). 34
Table 2.3: Chemical composition (wt.%) and creep strength of commonly utilised ferritic steels for thermal power plant (Cerjak and Mayr, 2008). ..... - 37 -
Table 2.4: Diffusion coefficients (Dawson, 2012).....55
Table 3.1: Dimensions of the X20 and P91 test-pieces 60
Table 3.2: Chemical composition (in wt.%) of X10CrMoVNb9-1 and X20CrMoV11-1 pipe materials, according to the chemical analysis certificate in comparison with EN standards (BS EN 10216-2: 2002).....61
Table 3.3: Chemical composition (in wt.%) of X10CrMoVNb9-1 and X20CrMoV11-1 TIG rod welding consumables, according to Bohlër welding Technical handbook (Bohlër welding, 2009) 62
Table 3.4: Chemical composition (in wt.%) of X10CrMoVNb9-1 and X20CrMoV11-1 MMA covered electrode welding consumables, according to Analysis Certificate and Comparison with Bohlër welding Technical handbook (Bohlër welding, 2009).....62
Table 3.5: Essential welding parameters used for TIG and MMA Welding processes 64
Table 3.6: Tensile Test Matrix.....69
Table 3.7: Uniaxial Creep Test Matrix 77
Table 4.1: Room temperature (21°C) Charpy impact test results for X20 weld filler and P91 weld filler cross welds vs Böhler welding technical handbook (Böhler welding, 2009). ..... - 99 -
Table 4.2: Projected Area Microstructural Measurements of the Parent Material 111
Table 4.3: Microstructural Measurements for Filler Materials.....112
Table 4.4: Microstructural Measurements for HAZ Regions 114
Table 4.5: Orowan Back Stress Contributions from the Different Microstructural Features (Holzer and Kozeschnik, 2008) 121
Table 4.6: EDS Chromium Content Measurements 124
Table 4.7: Small punch creep test rupture times of all the samples.....131
Table 4.8: Uniaxial Creep Parameters for all ruptured samples 137

List of Abbreviations

ADF: Annular Dark Field

BC: Band Contrast

BF: Bright-Field

BSE: Backscattered Electrons

CGHAZ: Coarse-grained Heat Affected Zone

DF: Dark-Field

EBSD: Electron Backscattered Diffraction

EDS: Energy Dispersive Spectroscopy

ED: Electron Diffraction

EELS: Electron Energy Loss Spectroscopy

EFTEM: Energy Filtered Transmission Electron Microscopy

FFT: Fast Fourier Transform

FGHAZ: Fine-grain Heat Affected Zone

FIB: Focused Ion Beam (Ga+)

FM: Filler Metal

HAADF: High Angle Annular Dark Field

HAZ: Heat Affected Zone

HRTEM: High Resolution Transmission Electron Microscopy

HRSTEM: High Resolution Scanning Transmission Electron Microscopy

ID: Internal Diameter

IPF: Inverse Pole Figure

JEMS: Microscopy Simulation Package

MMA: Manual Metal Arc welding

OD: External Diameter

PM: Parent Material

PWHT: Post Weld Heat Treatment

SAD: Select Area Diffraction

SE: Secondary Electron

SEM: Scanning Electron Microscopy

SI: Spectrum Imaging

STEM: Scanning Transmission Electron Microscopy

TKD: Transmission Kikuchi Diffraction

TEM: Transmission Electron Microscopy

TIG: Tungsten Inert Gas welding

Tm: Absolute Melting temperature

WFM: Weld Filler Metal

WT: Wall Thickness

WM: Weld Material

XRD: X-rays Diffraction

CHAPTER 1

1. INTRODUCTION

1.1. Background

In power generating plants, components such as tubes, pipes and headers are operated in the creep regime (> 450°C), and these components have a finite life. The replacements of components that have exhausted their creep life can be executed as a partial or system replacement depending on the availability of the replacement material during outages, outage duration and/or costs that are to be incurred during the replacement.

Welding processes such as tungsten inert gas (TIG) and manual metal arc (MMA) welding are used to join the components during the replacements of the creep exhausted components. In some instances a partial change in the original design material to a more superior material is required in order to increase the life expectancy of the component or a system, and to increase performance efficiencies of the components.

The partial change of the initial design material may require the system to have a transition weld where the existing original design material is joined to the new superior material. A suitable weld filler metal for joining a creep aged X20CrMoV12-1 steel (original design material) to a virgin P91 (X10CrMoVNbV9-1) steel (superior material with improved creep resistance properties) has not yet been fully researched and there is a knowledge gap in this field.

Therefore the aim of this work is to study the effect of using the X20 and P91 welding consumables when making a weld joint between a creep aged X20 steel pipe and a virgin P91 steel pipe considering the fact that weldability and creep life extension on creep aged materials are dependent on factors such as, the microstructure (precipitates and damage / dislocations), the welding processes applied, the post-weld heat treatment, the intended operation time, and the operating conditions (Bezuidenhout *et al.,* 2008; David *et al.,* 2013).

Ferritic steel joints experience a decrease in their creep life due to Type-IV creep cracking i.e. enhanced creep voids formation resulting in the formation of creep micro cracking in the fine-grained heat affected zone (FGHAZ) (Sawada, 2008; Zhang, 2020). Therefore, an in-depth microstructural evaluation of the FGHAZ can provide a better understanding of the Type-IV creep cracking behaviour.

Creep ageing is a microstructural degradation process that leads to loss of strength and ductility in a material. The process exhibits quantifiable changes of precipitate composition, size, morphology and distribution as well as the formation of micro voids. Studies to quantify precipitate changes and micro void behaviour as a function of creep life have been the focus of many designers, researchers and lifing practitioners for over half a century (Auerkari *et al.* 2007; Maile, 2007; Masuyama, 2007). This vast amount of explicit and tacit knowledge has not only led to the development of designer steels with advanced creep properties but it is also used to continuously develop and improve component remaining life estimates (RLE) technologies (Bezuidenhout *et al.,* 2008).

The weldability of a material decreases with creep ageing, and a limit is reached where welding cannot be permitted on the aged material without adversely affecting material integrity. The behaviour of these types of dissimilar welds that consists of X20 / P91 weld filler and a service exposed EN 10216-2 X20CrMoV11-1 known as X20 steel as well as a virgin EN 10216-2 X10CrMoVNb9-1 commonly known as P91 steel is not available on the open literature. As a result, this research is being directed towards the characterisation of suitable weld filler that can be used to join these materials and subsequently extend component life.

The creep aged X20 and the virgin P91 materials were used to characterize suitable welding consumables for joining these materials during maintenance welding in this research study. The knowledge gathered from this research will be incorporated in the extensive life management and life extension knowledgebase that exists within the fossil power generation sector to define the appropriate weld filler for welding service exposed X20 material to new P91 material pipework.

1.2. Motivation for research

Increasingly utilities face the challenge of running ageing power plants whilst economic pressures demand that these plants continue to operate safely and reliably. The replacements of component(s) and / or system replacements on creep damaged (creep exhausted) components have to be conducted to avoid creep failure. Failure of high temperature pressure pipework (HTPP) can be catastrophic and therefore, must be avoided at all cost since the failure could result in life threatening incidents.

The X20 steel is the traditional material that is extensively used in most power plants. However, most of the X20 steel installed at the power plants are creep exhausted and are to be replaced as per the creep life management strategy. With recent developments in materials research, spurred by the drive to improve efficiencies, the power generation industry has to consider using the more advanced creep strength enhanced ferritic steels such as Grade 91 to replace old generation creep-aged X20 steel pipework. Both the X20 and P91 materials are fully martensitic steels with the latter steel having higher creep-rupture strength as a result of the precipitation of sub-microscopic niobium (Nb) and vanadium (V) carbonitrides and good fabrication (due to a lower carbon content) characteristics (BS EN 10216-2, 2013; Auerkari *et al.* 2007; Maile, 2007).

The replacement of existing materials with new material is due to the fact that the plant aging rate is not uniform throughout the system; therefore, the replacement will be conducted in parts in some of the sections of the components. Normally the boiler headers and turbine steam admission components have more creep life due to their conservative creep life design that has low stress level as a result of higher wall thickness to diameter ratio relative to the main steam and hot reheat pipework. Based on these circumstances, it is apparent that during a replacement, terminal weld connections will be made between new P91 alloy and creep exposed X20 alloy that has not reached its creep exhaustion yet.

Even though X20 and P91 are both martensitic stainless steels, a welded joint between these alloys constitutes a dissimilar metal joint. The choice of the best/suitable filler metal for a mismatched joint between these materials has to yield a weldment with the desired long-term creep life. The general guideline from filler metal manufacturers on the filler metal choice for a dissimilar welded joint between

steels with different chemistries is to select a filler metal that either, i) matches the lower alloy grade; or ii) matches the higher alloy grade or iii) mismatching both base metals. Prior to this study research data on the design and evaluation of dissimilar welds between creep aged X20 and new P91 material was lacking in open literature. Experimental data on the behaviour of such weldments will assist power stations to make more informed decisions in the selection of a suitable filler metal when requiring replace X20 pipe systems with P91 steel.

A study was undertaken to evaluate the microstructure and mechanical properties of two dissimilar pipe welded joints fabricated between service exposed X20 steel pipework from a fossil power generating plant and new P91 steel pipework. One weldment was fabricated with a P91 filler metal (Sample 1) and the other weldment was fabricated with a X20 filler metal (Sample 2).

1.3. Research questions

The key research questions addressed in this technical investigative study are as follows:

i. What is the suitable weld filler to join a creep aged X20 steel pipe to a virgin P91 steel pipe to obtain the optimal creep life for further operation?
ii. Are there any welding challenges that may lead to unwanted welding defects as a result of using either X20 or P91 weld filler, if yes, which weld filler proves to introduce lesser or no defects?
iii. Is there any difference in the welding residual stress levels and distribution when comparing the X20 and P91 weld filler cross welds?
iv. Is there any noticeable diffusion between the weld filler and the parent materials, and how will diffusion affect both the microstructure and the resultant creep life?
v. Are there any distinct differences in the precipitate morphology, dislocation density and sub-grain size between the X20 and P91 weld filler cross welds?
vi. Are there any distinct differences in the mechanical properties between the X20 and P91 weld filler cross welds?
vii. Are there any pronounced differences in the creep behaviour between the X20 and P91 weld filler cross welds?

1.4. Hypothesis

It is postulated that the X20 weld filler is more suitable for joining the creep aged X20 to virgin P91steel pipes, because of the combination of the expected lower creep-rupture strengths of the creep aged X20 base metal and the X20 filler metal, as a result of using the weld filler metal that matches the creep weaker parent metal that presents no metallurgical notch on the weld joint for the X20 base metal side.

1.5. Research Aim and Objectives

The aim of this research is to characterise dissimilar welds between creep aged X20 and virgin P91 steel pipes joined with different filler metals matching either one of the base metals.

The aim of this investigation will be achieved through the following objectives:

- To weld creep aged X20 pipe removed from service to a virgin P91 pipe using X20 and P91 welding consumables.
- To quantify and compare the welding residual stress levels and distribution.
- To determine and compare the mechanical properties of the welded joints.
- To characterise and compare the microstructure of the weldments before and after creep testing.

1.6. Structure of the Dissertation

The structure of this dissertation is outlined in the following manner;

Chapter One of this dissertation introduces the research study, background, motivation for research, research questions, hypothesis, research aim and objectives, justification and scope of the research as well as the structure of the dissertation.

Chapter Two details the literature review with respect to power plant efficiency in relation to materials development. The material deformation mechanisms and the fundamentals for high temperature strength are addressed. The review of creep mechanisms, precipitation sequence, historical development of creep resistant steels and the development of 9-12% Cr steels for boiler application are presented. The types and effects of welding processes used in this research study, microstructural evolution of the welded joints (including grain growth zone, grain refined zone,

partially transformed zone – intercritical HAZ, over-tempered region and the zone of unchanged base material), and the stress analysis on welded structures are given. A full literature review on the microstructural evolution of 9-12%Cr material steels during heat treatment and service exposure is presented. Finally, a brief review on the diffusion of carbon driven by differences in Cr concentrations between the joined ferritic base metals is also provided.

Chapter Three outlines the experimental procedure that was followed to achieve the objective of this research study. The materials sample selection and sample characterisation applied on various specimens extracted from the X20-P91 cross welds are presented. These methods include the welding process, post weld heat treatment, stress analysis, creep testing (both the small punch creep tests and uniaxial creep tests), microstructural evaluation (using optical microscope (OM), scanning electron microscope (SEM), transmission electron microscope (TEM) and X-Ray Diffraction (XRD), mechanical tensile testing at room temperature and hot tensile testing, hardness (nano, micro, and macro) and Charpy impact tests.

Chapter Four presents the results and discussion of all the tests, analysis and characterization that were carried out in this research study to characterize dissimilar welds between creep aged X20 and virgin P91 pipes. The findings and the discussion are focusing on the NDT on welds, residual stress analysis, chemical analysis, tensile testing (both room and hot tensile tests), hardness tests (macro, micro and nano-indentation hardness tests), Charpy impact tests, creep tests (both uniaxial and small punch creep tests) and microstructural characterization (for both pre-creep and post creep test conditions). Lastly, the conclusions and recommendations derived from the findings of this study are presented in **Chapters Five and Six**, respectively.

CHAPTER 2

2. LITERATURE REVIEW

2.1. Introduction

Energy preservation and environmental conservation are considered as very important matters globally since they have an effect on global climate change. There is a significant drive to design and commission power plants that require low fuel cost and emits low CO_2 emissions through further improvements in thermal efficiency since 1980s, hence the development and improvement of high temperature materials are essential (Fukuda, 2011; Masuyama, 2000; Viswanathan *et al*., 2006). The following sections outline the available literature on this subject focusing on the objective of this study; characterisation of suitable fillers for a butt weld of creep aged X20 and virgin P91 materials.

2.2. Power Plants Efficiency

In the coal/fossil-fired electricity generation power plants, efficiency is an essential performance parameter because it offers benefits such as reduced carbon dioxide (CO_2) emissions, where a 1% point improvement in overall efficiencies may result to as much as 3% reduction in CO_2 emissions, reduced emissions of pollutants, and resource conservation due to a decrease in the consumption of pulverised fuel coal used to fire the boiler (Anand, 2006; Viswanathan *et al*., 2006).

Thermal efficiencies in coal-fired energy plants (schematically illustrated in Figure 2.1) can be increased by reducing exhaust heat and heat transfer losses. The limit on reducing the exhaust heat losses has effectively been reached, and these exhaust heat losses are predominantly through the condensers for cooling boiler and turbine exhausts (Masuyama, 2000). However the heat transfer losses can still be further reduced by raising the pressure and temperature of the steam that is governed by the properties of the material being used to enable the power plant to operate in ultra-supercritical conditions (Paterson, 1997; Masuyama, 2000). Ultra-supercritical pressure is defined as a steam pressure that exceeds the conventional supercritical pressure steam conditions (24 MPa) with a superheater outlet temperature of 538°C, or can be defined by referring to the turbine inlet steam conditions of at least 24 MPa for main steam pressure and a temperature of at least 565°C for the main and reheat steam (Paterson, 1997). These raised steam conditions increase the plant efficiency and result in the improved resource and energy preservation. The

environmental protection is also simultaneously improved due to the preserved energy (Fukuda, 2011; Masuyama, 2000).

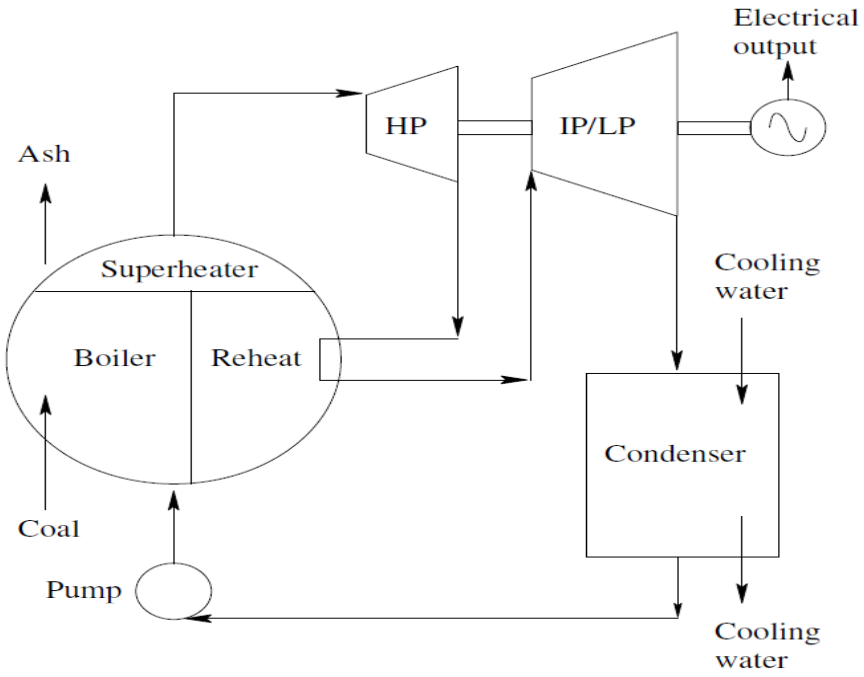


Figure 2.1: Schematic representation of a fossil fired power plant steam cycle (Thomson, 1992)

Figure 2.2 shows how the operating steam pressure and temperature have increased over the years in the United State (US). The used of carbon (C) steel materials created a limit on power stations operating steam temperature and pressure to not exceed 370°C and 4 MPa, respectively during the 1920s. Thereafter the use of Molybdenum (Mo) steel increased the operating pressure and temperature to 10 MPa and 480 °C, respectively. The development of CrMo steels further made it feasible for a power plant with operating pressure and temperature of 17 MPa and 566°C to be commissioned in the 1950s (Masuyama, 2000).

Since the late 1950s, bigger capacity power stations were built to meet an increased electricity demand, and both service pressure and temperature increased gradually. In year 1957 the Philo Unit 6 generating 125 MW began to operate with live-steam pressure and temperature of 31 MPa and 621°C, respectively. During year 1960, Eddystone Unit 1 generating 325 MW started its production at the maximum pressure of 34 MPa and temperature of 649°C conditions as a global best achieved limit by then (Masuyama, 2000).

In Europe, comparable large power stations that have the progressive steam cycles, Hüls Unit 1 (29 MPa, 600°C, 85 MW) in Germany and the Drakelow Unit 12 (24 MPa, 593°C, 375 MW) in the UK were commissioned in 1960. This led to increased erection costs due to upgrading of materials needed to increase operational efficiency. This caused a significant increase in power generating costs which resulted in the steam pressure and temperature conditions being decreased in most plants to 24 MPa and 538 °C in order to attain an economic balance (Fukuda, 2011; Masuyama, 2000).

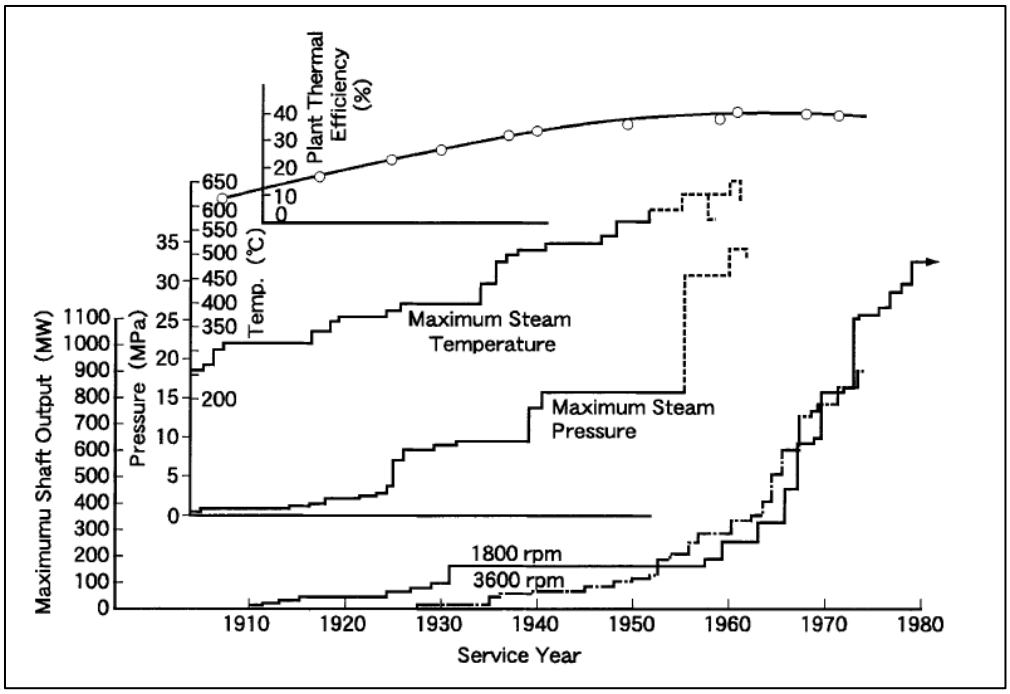


Figure 2.2: Graphical representation of the historical development of fossil-fired turbine-generators in terms of pressure, temperature, megawatts outputs and thermal efficiency (Masuyama, 2000).

The developments in Japan led to the steam pressure and temperature to increase sharply after 1950 as shown in Figure 2.3. The thermal efficiency was ranging between 30 - 40% that was delivered by supercritical steam conditions (24 MPa, 538°C) power plants (Masuyama, 2000; Yoshioka, 2017).

From approximately 1975, the two shifting (starts and stops) of coal-fired power stations have been progressively required for load adjustments purpose, complemented by the nuclear power generation and changes in electricity demand trends. Steam temperature and pressure conditions had been fixed at 538°C and 24 MPa or alternatively at 566°C and 19 MPa, respectively without allowing the additional ramp-up on the steam conditions. The increase in power demand from late 1960s was addressed by continuous

enlargement of power plant size over 20 years period. In 1989 the first ultra-supercritical sliding pressure plant was built as prompted by the oil crises in Japan. The operating conditions for succeeding recent power plants have been progressively increased above the conventional limits, and the current steam temperatures are ranging from 593°C to 600°C at constant pressure of 24 MPa. For future stage, there are intensive further research projects on the pipeline regarding high temperature advanced materials to be used at 630°C service application (Masuyama, 2000; Viswanathan *et al*., 2006).

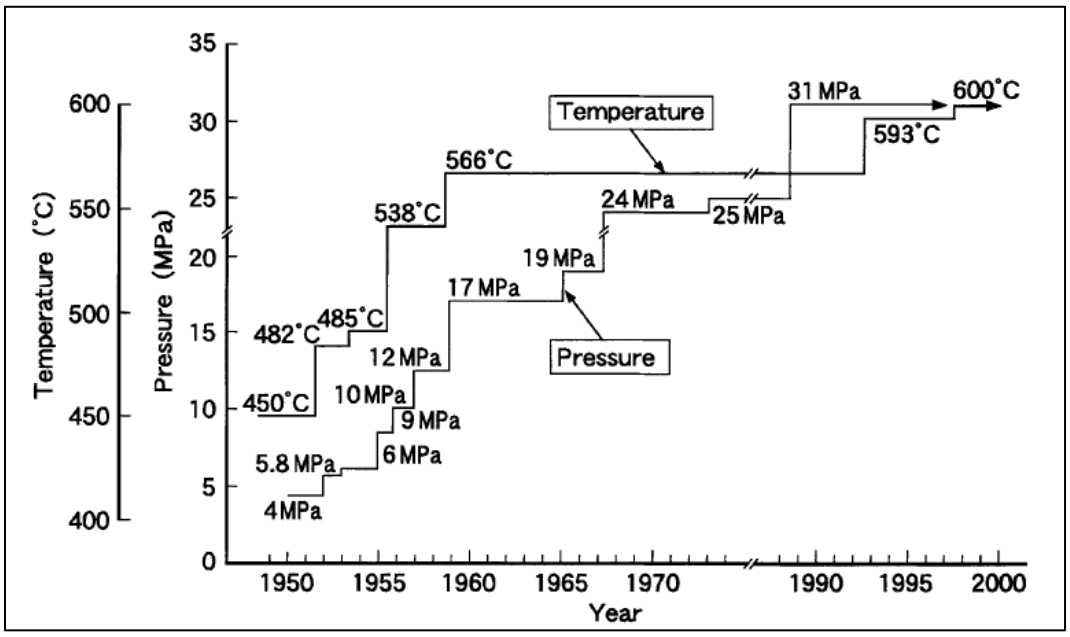


Figure 2.3: Trends of steam conditions (pressure and temperature) for power generating plants in Japan (Masuyama, 2000).

As part of improving the power plant thermal efficiency, there have been continuous and remarkable decrease in energy input (specific heat rate (kJ/kWh)) by increasing the steam parameters from 12 bar / 275°C since year 1900 to 300 bar / 620°C in year 2010 in Europe (Germany) as illustrated graphically in

Figure 2.4 (Aghajani, 2009). It is apparent from this figure that by increasing both steam conditions (i.e. pressure and temperature) there is an increase in power plant efficiency.

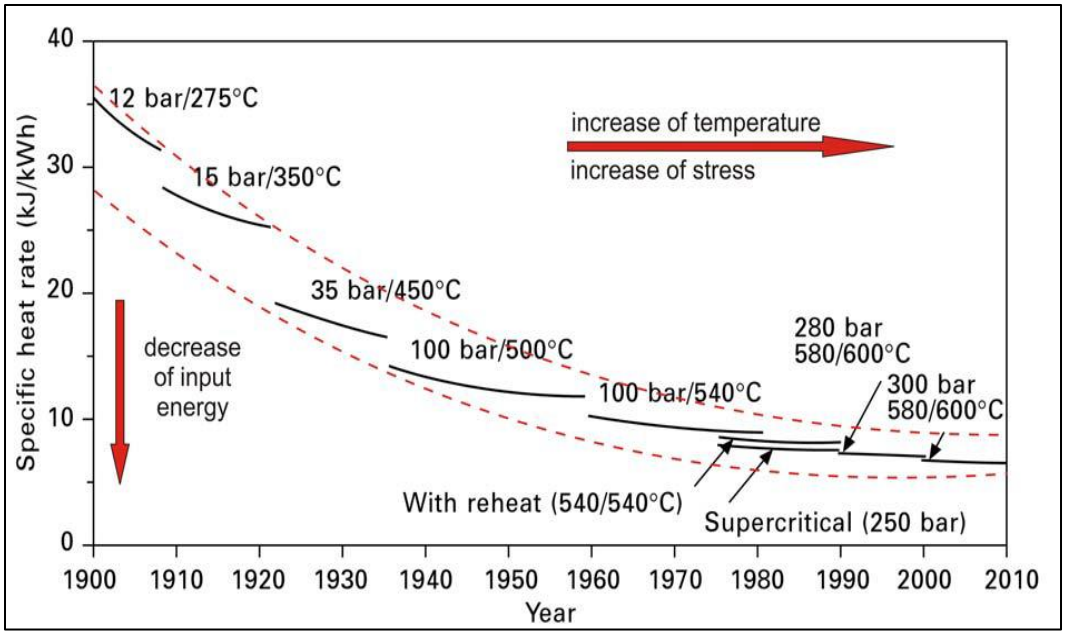


Figure 2.4: Power plants heat rate vs. steam parameters (steam pressure and temperature) improvements over years in Europe (Germany) (Aghajani, 2009).

Significant developments have been made to attain superior efficiency on fossil-fired power plant technologies in ultra-supercritical (USC) manner. Although the common subcritical plants can achieve 39% efficiencies, the USC power stations operating at the improved steam parameters, with temperatures of 620°C and pressures beyond 25 MPa yield in the design efficiencies of approximately 46% in some parts of the globe (Anand, 2006). The electricity generation capacity per unit for these kinds of power stations has extended to approximately 1100 MW. Based on the trends and future projection, the continuous advancement in high temperature materials technology will enable the best coal-fired station to operate at an improved efficiency level of 50% within year 2030 (Molokwane, 2013). Therefore, effective and tangible policies have to be effected to fast-track such research and technology progression focusing on the testing and application phases (Anand, 2006).

Significant progress in the research work to advanced steam cycle has mainly been carried out in Europe, United State and Japan. The overview of these universal research and development ventures on advanced steam cycles power stations is elaborated in Figure 2.5 (Blum and Hald, 2000). These research and development projects were commenced in the 1980s, and subsequently many types of creep resistant

material steels have been industrialised to reach ultra-supercritical steam parameters with optimal steam operating temperature of 630°C using 9–12%Cr steels (Blum and Hald, 2000; Masuyama, 2000).

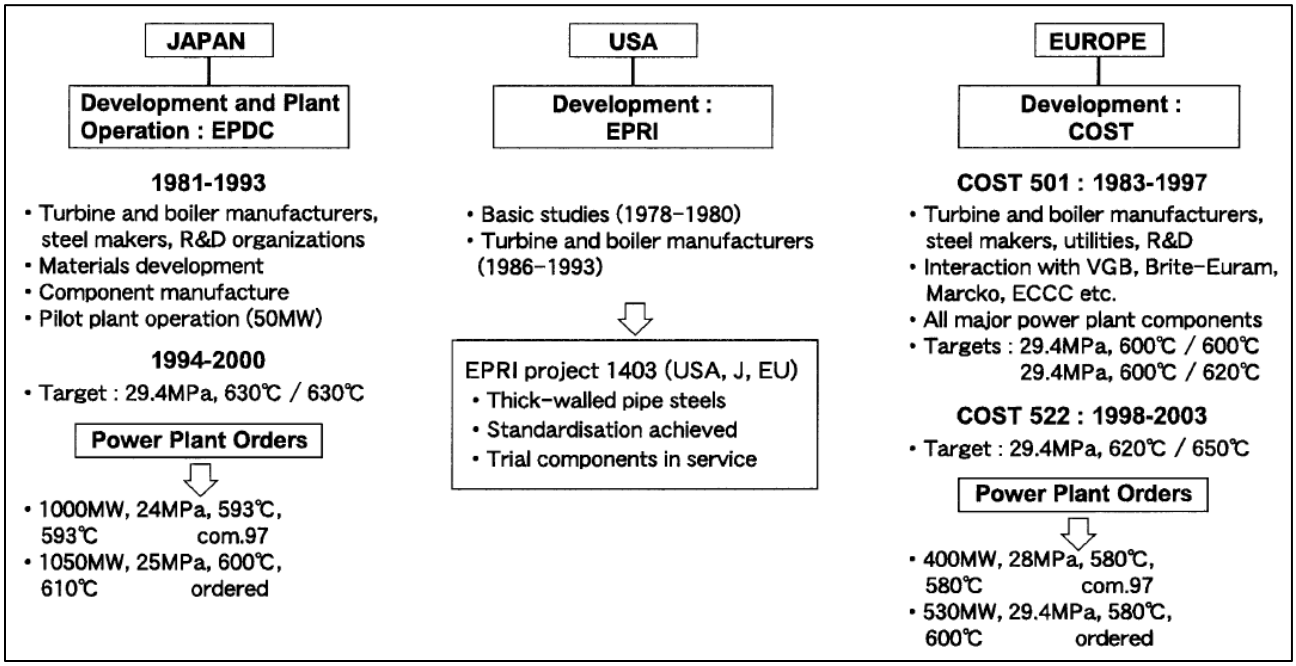


Figure 2.5: Global research and development ventures on advanced steam power stations materials (Blum and Hald, 2000)

Acknowledging that the enhancements in ultra-supercritical power plant conditions are not only achieved from the improved steam conditions, there is also a significant technology differences between recent power stations and those of the older generation (Masuyama, 2000). The ancient plants were constructed based on the design of constant load without load-adjustment and two shifting options which are vitally considered for the plants that are being preferably used nowadays. In the olden type of USC power stations that were built in the past, the elevated pressure and temperature were achieved by using large quantities of thick walls of austenitic steel that are susceptible to enormous thermal stresses on equipment parts such as boiler headers, steam pipes and turbine components (Fukuda, 2011; Masuyama, 2000).

In the current regime and in the foreseeable future, it is highly preferred to use ferritic steels having smaller coefficients of thermal expansion for thick-walled components in order to minimise undesired thermal stresses during the sliding and two-shifting operation in order to respond to the electricity demand fluctuation (Masuyama, 2000; Yoshioka, 2017).

Accordingly, the thermal stability of ferritic steels is the main determining factor of steam operating parameters (Masuyama, 2000). Table 2.1 shows ultra-supercritical power stations in operation that were employed in service between 1997 to 2002, illustrating the materials that were utilised for the boiler superheater, main steam pipework and turbine rotor, including the operating parameters (megawatt output, design steam pressure, design temperature, fuel used, commissioning year, efficiency percentage, boiler main steam material and turbine rotor material (Blum and Hald, 2000). It is apparent that in these recent USC power stations, the recently developed steels including P91 (X10CrMoVNb9-1) have been extensively utilised.

Table 2.1: Ultra-supercritical power stations that are in operation (Blum and Hald, 2000).

Power Station	Capacity (MW)	Steam Parameters		Energy Source	Commissioning Year	Efficiency (%)	Boiler/ Main Steam Pipe Materials	Turbine Materials
		Pressure (MPa)	SH/RH/RH Temperature (°C)					
Matsuura 2	1000	25.0	598/596	PC	1997		18Cr9NiCuNbN/P91	10.3Cr1.5MoVNbN
Skaerbaek 3	400	28.4	580/580/580	NG	1997	49	TP347HFG/P91	10Cr1MoVNbN (501F)
Haramachi 2	1000	25.4	604/602	PC	1998		18Cr9NiCuNbN/P91	10.3Cr1.2Mo0.3WVNbN
Nordjylland 3	400	28.4	580/580/580	PC	1998	47	TP347HFG/P91	10Cr1MoVNbN (501F)
Nanaoota 2	700	25.0	593/593	PC	1998		TP347H/P91	10Cr1Mo1WVNbN
Misumi 1	1000	25.4	604/602	PC	1998		18Cr9NiCuNbN/P91	10.2Cr0.5Mo1.8WVNbN
Lippendorf	934	26.4	554/583	Lignite	1999	42.3	18Cr12NiMo/P91	10Cr1Mo1WVNbN (501E)
Boxberg	915	26.4	555/578	Lignite	2000	41.7	18Cr12NiMo/P91	10Cr1Mo1WVNbN (501E)
Tsuruga 2	700	25.0	597/597	PC	2000		18Cr9NiCuNbN/P122	10Cr1Mo1WVNbN
Tachibanawan 2	1050	25.9	605/613	PC	2001		18Cr9NiCuNbN/P122/P92	10.2Cr0.5Mo1.8WVNbN
Avedore 2	400	29.4	580/600	NG	2001	49.7	TP347H/P92	10Cr1Mo1WVNbN (501E)
Niederauseen	975	26.0	565/600	Lignite	2002	>47	TP347HFG/P911	10Cr1Mo1WVNbN (501E)

PC : Pulverised Coal NG : Natural Gas SH/RH/RH : Superheater/Reheater/Reheater

Figure 2.6 shows steam conditions (pressure and temperature) trends for USC power stations. Time dependent service temperature ranges are also illustrated on this graph for ferritic and austenitic steels for thick-wall components such as boiler headers, main steam pipes and turbine rotors. It can be observed that the upper temperature limit for ferritic steels has increased from approximately 560°C to 630°C, and based on the trends in research and developments, it is predicted for further increment to 650°C in the near future (Masuyama, 2000).

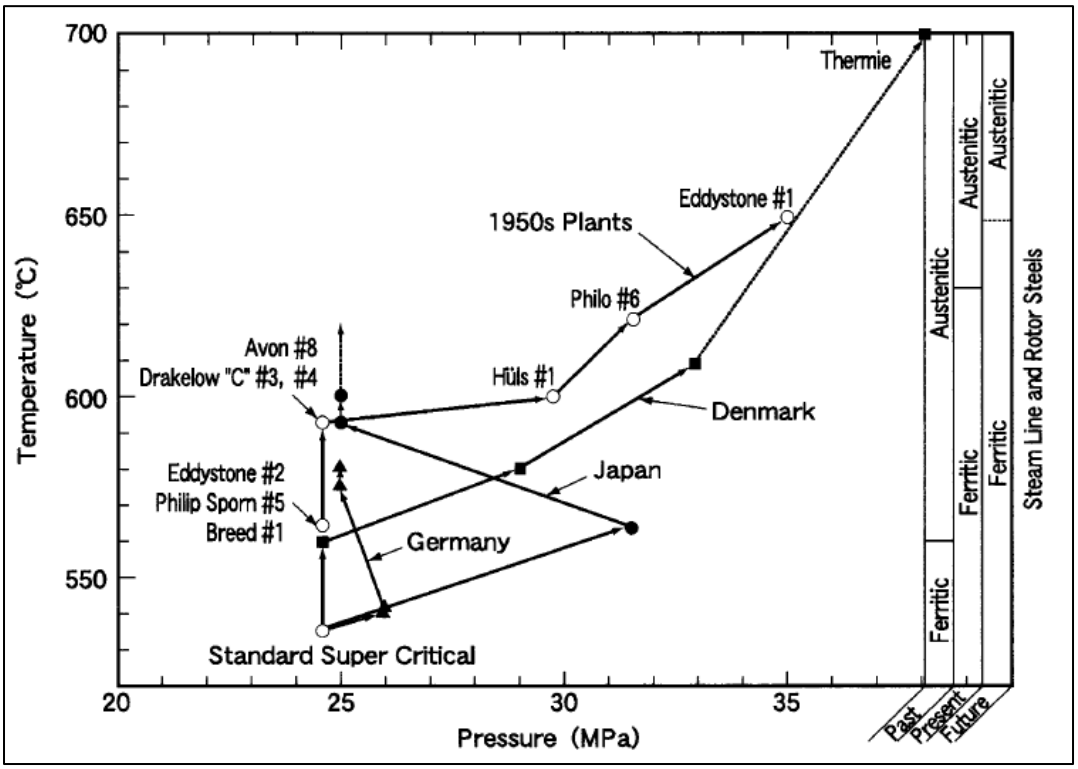


Figure 2.6: Steam parameters (pressure and temperature) plots trends for ultra-supercritical power stations (Masuyama, 2000).

Fossil power generating efficiency has been improved in South Africa by building and commissioning two super critical power plants.

The in-service conditions to which power plant materials are subjected cause material degradation and deformation mechanism over time, hence there is a need to understand the deformation mechanisms that degrade the material integrity. These deformation mechanisms need to be appreciated during the material

design and development stage (Bano, *et al*., 2014). The following section (Section 2.2) provides a brief overview on material deformation.

2.3. Materials Deformation Mechanisms

Deformation is known as a plastic flow of a material due to application of a load and is a kinetic process (Frost, 1982). Deformation mechanisms on materials are a function of temperature, stress, and strain rate (Bano, *et al*., 2014). These are considered as the fundamental drivers that cause flow on an atomic level. It is therefore vital to consider the following five groups of deformation mechanisms (Frost, 1982; Bano, *et al*., 2014)

1. Collapse at an ideal material strength; flow only occurs when the ideal shear strength is surpassed.
2. Lower temperature plasticity by dislocation glide; (a) confined by lattice resistance, (b) restricted by distinct hindrances, (c) confined by phonon or other drags, and (d) inclined by adiabatic heating.
3. Lower temperature plasticity by twinning.
4. Power-law creep by dislocation glide, or glide-plus-climb; (a) confined and controlled by glide progressions, (b) limited by lattice-diffusion controlled climb ("high-temperature creep"), (c) limited by core-diffusion controlled climb ("low-temperature creep"), (d) power-law breakdown (the transition from climb-plus-glide to glide alone), (e) Harper-Dorn creep, and (f) creep accompanied by recrystallization.
5. Diffusional movement, (a) effected by lattice diffusion ("Nabarro-Herring creep"), (b) confined by grain interface diffusion ("Coble creep"), and (c) transition-reaction moderated diffusional flow.

Most recent maps are mainly developed and applied through the use of experimental data or microstructure features evidence although very few are founded on the postulation and observations made from the materials related to complex engineering alloys (Bano, *et al*., 2014; Nabarro and de Villiers, 1995). Modern approaches and developments are needed to ensure that cross-checks on the validity and emerging maps expansion are carried out. For example, deformation/ distortion mechanism diagrams for high pressure (HP) turbine blade super-alloys have always been built through the postulation that interdiffusion creep is the predominant at low stress levels. However, over sometimes the experimental data revealed that creep rupture life that grain boundary sliding mechanism mainly controls creep deformation mechanism in long-term creep tests as potted on the deformation map considering the data about mechanism manifestation dominance range (Bano, *et al*., 2014). Figure 2.7 shows a deformation

mechanisms map which is divided into zones of stress and temperature in which each of the deformation/degradation mechanisms is prevailing (Bano, *et al*., 2014; Padmanabhan *et al*., 2001).

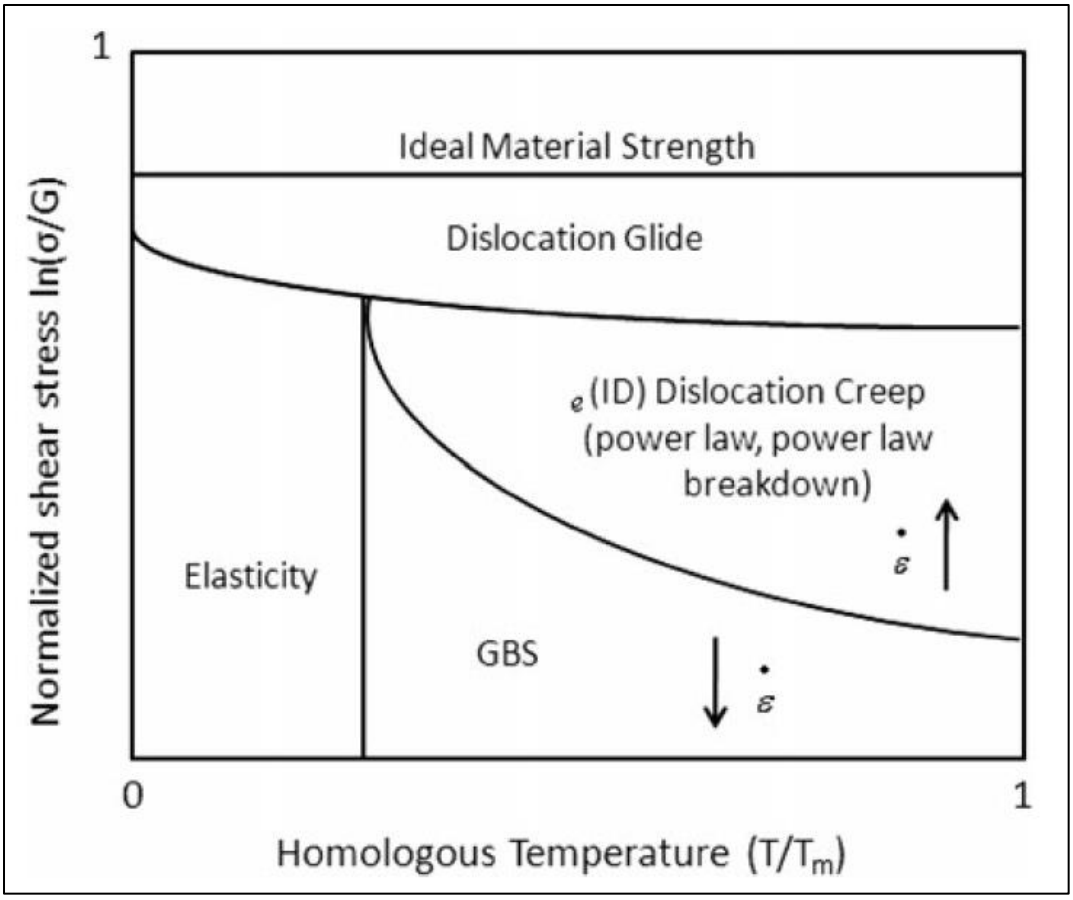


Figure 2.7: Stress/temperature map showing regions of temperature and stress with dominant areas of the deformation mechanisms (Bano, *et al*., 2014).

2.4. High Temperature Strength

There are several basis as a rule of thumb that have emerged for obtaining high-temperature strength materials, for instance, metals with a higher melting point incline to possess improved creep resistance, largely due to the degree of self-diffusion is predominantly associated with relative temperature (Nabarro and de Villiers, 1995). Metals with lower stacking-fault energy incline to have improved creep resistance, due to the extended halved dislocations that have retarded movement in both cross slipping and climbing mechanisms. Some of the creep-resistant alloys perform better at high temperature application because their dislocation cores dissociate by climb into configurations which cannot able to glide (Nabarro and de Villiers, 1995). In addition, the introduction of solid solution elements and finely dispersed precipitates hinders the dislocation motion, and these are well researched methods of improving high temperature strength and material thermal stability (Nabarro and de Villiers, 1995).

The materials choice for a given application is determined by the balance between several engineering requirements (e.g. required strength at design / operating conditions, resistance to high temperature oxidation, creep resistance and fatigue degradation tolerance) and by cost. The cost includes factors such as direct procurement cost, material availability, material lead time, simplicity of fabrication and maintenance / replacement costs (Nabarro and de Villiers, 1995).

In power plant applications, the cheaper low-alloy materials that contain Cr, Mo and/or V are generally used for moderate stress and/or temperature components and systems (Masuyama, 2000). In instances where corrosion or oxidation resistance is imperative, economic considerations may justify the use of ferritic or austenitic stainless steels that contain higher content of Cr and Ni. These are more expensive and may cause more challenges during the manufacturing and fabrication processes (Nabarro and de Villiers, 1995).

The stresses imposed on metal components at elevated temperatures produce a continuously increasing strain even below the yield point, and thus result in material degradation mechanism known as creep or long term overheating (Nabarro and de Villiers, 1995). Creep is defined as material time-dependent inelastic strain taking place under stress which is lower than yield point and at elevated temperature (Nabarro and de Villiers, 1995).

High temperature strength and economic factors are always considered in the selection of materials. As a general rule, high temperature strength materials are also high in cost (Masuyama, Haneda, and Roberts, 1988). Figure 2.8 illustrate the relationship between the permissible temperature at the permissible stress of 49 MPa and the comparative material cost for various power plant boiler pipe steels (Masuyama, Haneda, and Roberts, 1988). The comparative cost of these boiler materials was determined by only considering a steel pipe with normal dimensions (Diameter / Wall Thickness $\geq$ 2.5), and an allowable stress of 49 MPa. Based on the observed trends, it is apparent that the permissible temperature improves as the material cost increases at constant stress (Masuyama, 2000).

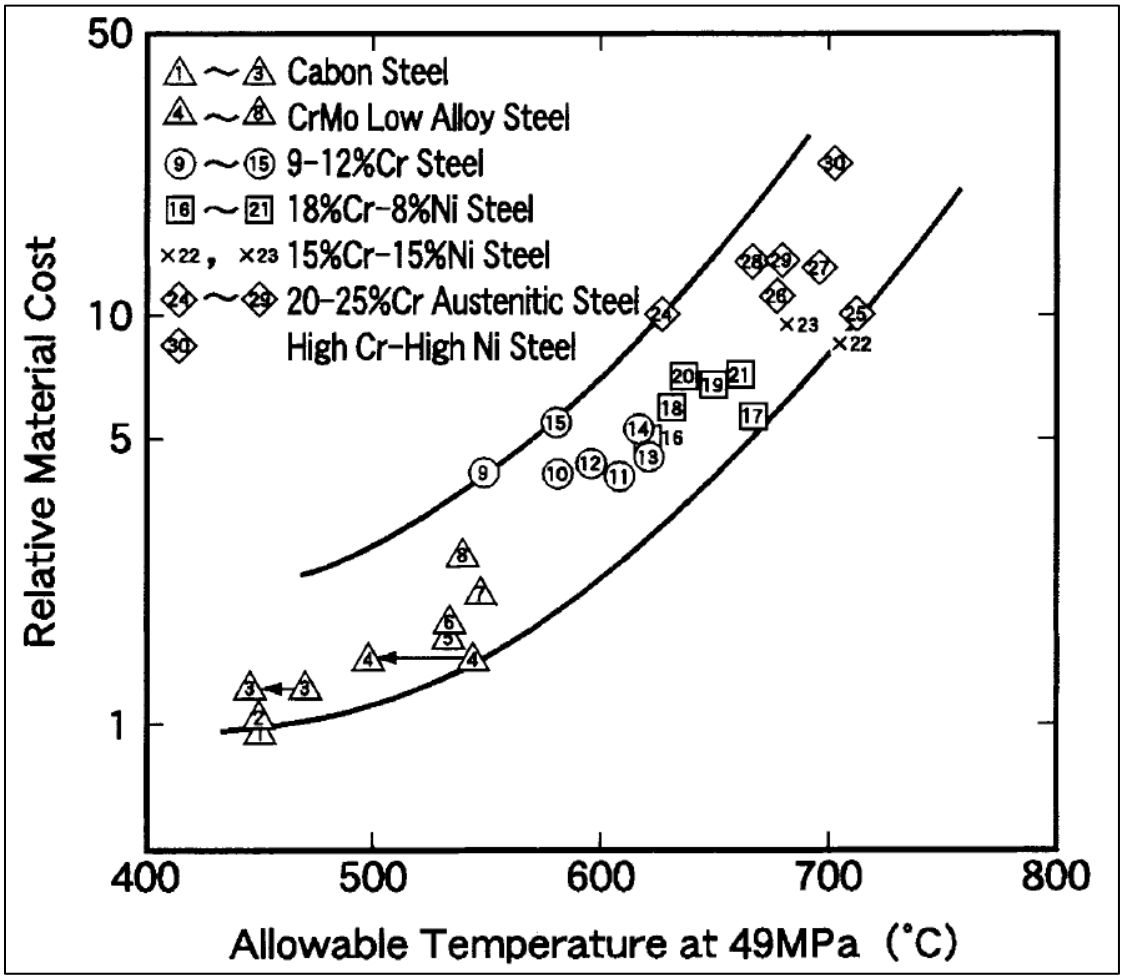


Figure 2.8: Relationship between permissible material temperature at 49 MPa of permissible stress and comparative cost of steels (Masuyama, 2000)

2.5. Creep mechanism

Creep is a material aging mechanism which causes a continuous permanent deformation and weakening of a material under constant stress below yield point, over time, at elevated temperatures (Nabarro and de Villiers, 1995). Elevated temperature in this content is well-defined as temperature in excess of 40% of melting temperature of the affected material, i.e. > $0.4T_m$ for metals (Bhadeshia *et al.*, 1998; Nabarro and de Villiers, 1995; Reed-Hill and Abbaschian, 1992). Typically, an acceptable creep-strain rate for power plant is approximately $3x10^{-11}s^{-1}$ (Bhadeshia *et al.*, 1998). Creep mechanism is categorised into three stages which are; primary, secondary and tertiary creep stages.

The primary stage is an initial stage where there is a decrease in strain-rate, and the extent of this initial strain is purely dependent on the applied stress. Secondary stage is a stage where there is constant strain rate and is a stage with the longest time. The last stage called the tertiary stage, is where there is a strain rate increase until creep rupture/failure occurs (Evans and Wilshine, 1985; Nabarro and de Villiers, 1995). The creep rupture curve under constant load conditions is schematically illustrated in Figure 2.9.

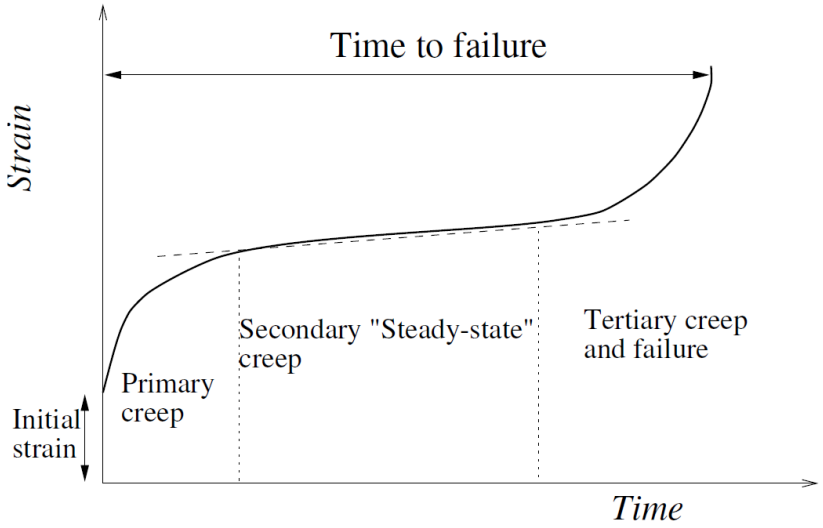


Figure 2.9: The schematic creep rupture curve under constant load conditions (Evans and Wilshire, 1985).

Temperature and strain/stress play a significant role in on the manifestation of creep rate. Figure 2.10 shows the effect of temperature and stress on the creep curve.

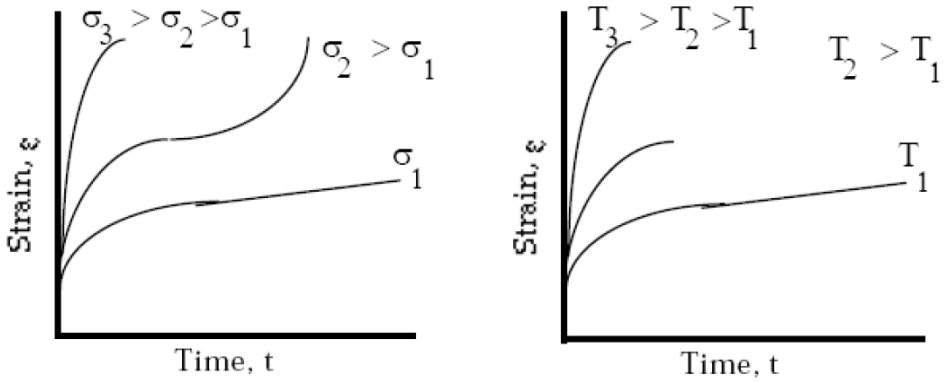


Figure 2.10: Effect of temperature change and stress on creep behaviour (Nabarro and de Villiers, 1995).

The dominant mechanism in which deformation manifests is governed by the temperature and stress magnitude (Frost and Ashby, 1982; Ashby and Jones, 1989). It is reportedly found that under typical

power plant operating conditions, creep occurs by dislocation glide and climb, rather than by bulk diffusion (Abbaschian, 1992; Yardley, 2003).

Figure 2.11 shows how dislocation glides and climb manifest. The act of stress results into free the dislocations movement laterally on slip planes up-until they meet an obstacle like precipitate(s) (Yardley, 2003). When the service temperature is lower (i.e. towards ambient temperature), dislocations move through the obstacles by cutting through the affected obstacle(s). Though, at elevated temperatures the dislocations can also pass the obstacles by means of climbing to the adjacent plane(s) that does not have an obstacle due to the thermal diffusional energy in the atoms at an increased temperature (Yardley, 2003).

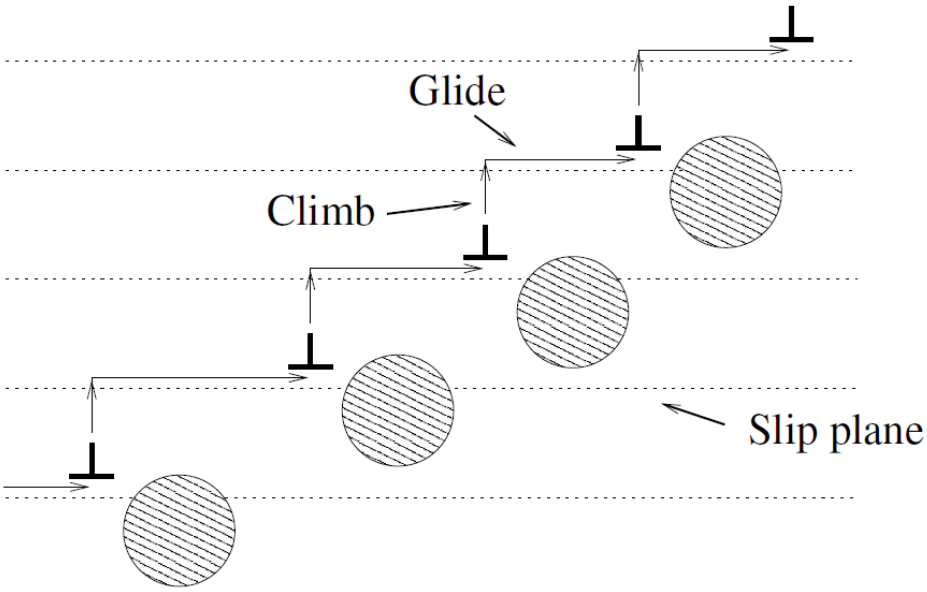


Figure 2.11: The process of climb and glide (Yardley, 2003).

Creep strength is fundamentally acquired from the resistance to creep deformation on the steel. The creep deformation is retarded by the opposing force for movement of dislocation in a microstructure level of the steel. There are numerous metallurgical parameters that play a role on the creep strengthening of an alloy (twi-global.com); and are outlined as follows (Reed-Hill and Abbaschian, 1992 and Masuyama, 2000).

Dislocation substructure that is defined as a steady network of dislocations that provides an intrinsic pull-back-force to dislocation displacement/movement within the steel (Reed-Hill and Abbaschian, 1992). This substructure can develop and coarsen due to creep strain. Coarsening of the substructure consequently results to the creep strength decrease. The fine dispersedly precipitates have an important role to stabilise

the dislocation structures, therefore the precipitates spacing distance and their stability are fundamentally vital in resisting the creep progression (Reed-Hill and Abbaschian, 1992).

The material grain size contributes to the creep strength of the steel without considering some other microstructural features. For the purpose of obstructing the long-range dislocation movement, finer grain size is beneficial. Conversely, this effect is mostly compensated by the influence of precipitate dispersion and/or sub-structural enhancement to creep strength (Reed-Hill and Abbaschian, 1992).

The transformation structure of the alloy contributes to the creep strength as well. This advantageous contribution is attained from the first applied heat treatment cycle, for instance in the ferritic alloy steels the transformation microstructure products such as martensitic and bainitic structures have lath that contributes to the creep strength (Reed-Hill and Abbaschian, 1992).

Solid solution strengthening impedes the free dislocations movement by means of the distortion of lattice structure. For instance, the presence of molybdenum in ferrite enables substantial solution strengthening in the 9-12%CrMo and 2.25%CrMo steels. This promotes the creep-inherent strength in these ferritic creep resistant steels after the prolonged operation in the creep regime, once precipitation strengthening is no longer effective as a consequence of coarsened particles/precipitates (Watanabe, 1983; Reed-Hill and Abbaschian, 1992).

Creep resistant precipitates such as carbides or intermetallics (VC, MO_2C) that are finely dispersed in microstructure matrix hinder the free dislocation movement by climbing and gliding (Beech *et al.,* 1984; Masuyama, 2000). Precipitate particles spacing has a significant role. It has been reported that there is an antithetical relationship between the spacing and the creep rapture strength; i.e. fine and close-spaced particles/precipitates provide the superior creep strength compared to widely-spaced and coarsened dispersions (Reed-Hill and Abbaschian, 1992; Masuyama, 2000). The resistance of precipitates coarsening due to their thermal stability at creep temperature is paramount on providing and sustaining the long-term creep strength. In most instances, the creep strength is significantly lost after over-aging or prolonged application at elevation temperature because of the coarsening of precipitate particles. The precipitates morphology, shape, size, mechanical properties and boundary features, are also deemed essential in defining the level of creep strength (Martin, 1980; Reed-Hill and Abbaschian, 1992; Masuyama, 2000).

2.6. Precipitation Sequence

Both the tempering temperature and the steel composition determine the order and the phase of precipitation in an alloy steel (Thomson, 1992). Precipitation of carbides in alloy is designated with a universal formula MxCy or MxXy, where M denotes an elemental component and C or X denotes the combination of nitrogen (N) and carbon (C) elements (Thomson, 1992). Figure 2.12 illustrates the map for precipitates phase stability conditions and sequence for 2.25Cr1Mo steel and for 9-12% Cr steels, the sequence of precipitates formation is identical, however the rate of precipitation is different (Thomson, 1992).

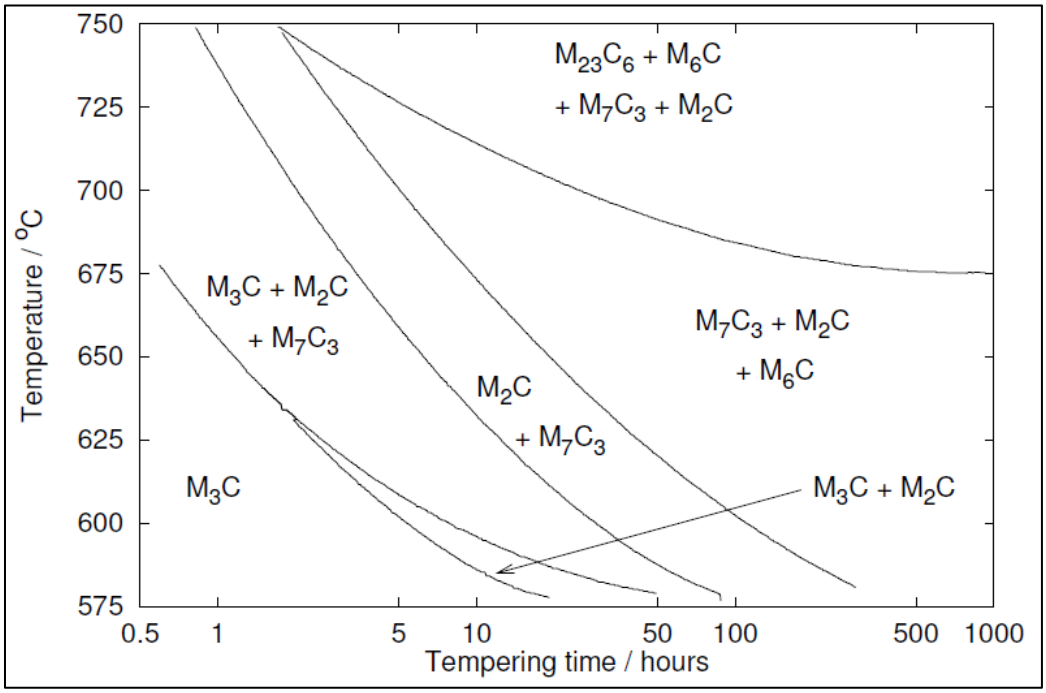


Figure 2.12: Carbide stability diagram for 2 2.5Cr1Mo steel, using micro-analytical methods to identify precipitation phases and sequences (Nutting, 1999).

The characteristics of precipitation phases that are normally experienced in the thermal power plant materials are summarily tabulated in Table 2.2. Nucleation could take place in-situ on the interface between an existing precipitate and the ferrite matrix (Dawson, 2012; Yardley, 2003), as an alternative it may also take place on the prior austenite grain boundaries, on sub-grains boundaries, on intralath dislocations, or on the lath boundaries depending on the free energy of the preferred nucleation sites (Dawson, 2012; Yardley, 2003).

Table 2.2: Summary of common precipitates data. (Andrews et al., 1967; Yardley, 2003).

Precipitation phase name	Crystal structure	Nucleation site	Common size	Shape	Benefits to creep strength
M_3C	Orthorhombic	In-situ, MLB, PAGB,	Coarse	Plates, then spheroidises	
M_2X	Hexagonal	D, MLB	Fine	Needle	Yes
M_7C_3	Trigonal	In-situ	Coarse	Spheroidal	No
$M_{23}C_6$	Cubic F	PAGB, MLB	Fine	Spheroidal	Yes
			Coarse	Spheroidal	No
M_6C	Cubic F	In-situ, PAGB, MLB	Coarse	Spheroidal	No
MX		Undissolved/on MX	Fine	Spheroidal/platelike	Yes
Laves		PAGB, MLB, lath interior	Coarse	Spheroidal	Short term

Note; D: dislocations, MLB: martensitic lath boundaries, PAGB: prior austenite grain boundaries.

Figure 2.13 illustrates a characteristic tempered martensitic microstructure in 9-12 wt. % steel. All common precipitates/phases that are found in the martensitic creep resistant steels are schematically presented. It has been demonstrated that lath boundaries in 9-12%Cr steels (particularly, P91 and X20 steels) alloy are inhabited by $M_{23}C_6$ and MX precipitates; and the intralath precipitates are consists mainly of the MX phase. The relationship between sub-gain boundary $M_{23}C_6$ precipitation inter-particle spacing and sub-grain size has been established by Dawson (2012). The relationship was experiential to be valid when merely considering $M_{23}C_6$ distributions, however the dispersion of other precipitation did not hold the same observation. It was then conclusive that $M_{23}C_6$ precipitation contributes significantly more to stabilise the sub-grain boundary as compared to MX precipitates (Dawson, 2012).

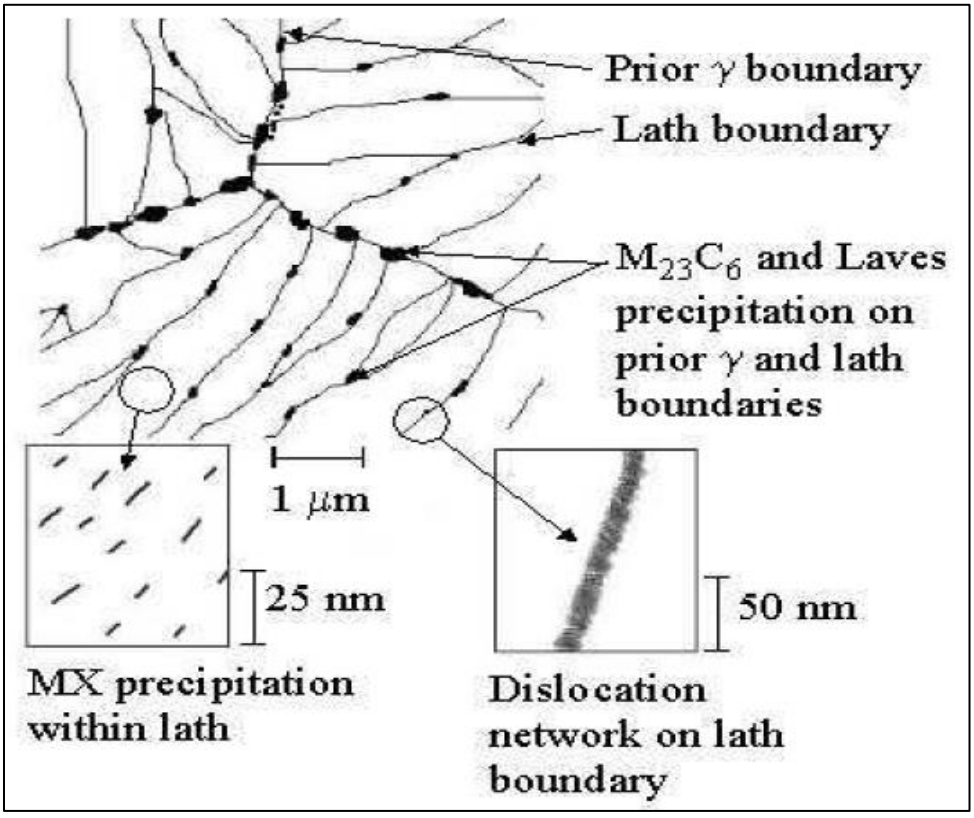


Figure 2.13: Characteristic microstructure of tempered martensitic 9-12% Cr steels with common precipitates (Masuyama, 2001).

It has also been reported that the during creep service the loss of precipitation hardening during consequently lead to in the loss of creep strength in the material. This is fundamentally due to the microstructural thermal degradation and evolution that exhibits as coarsening of the sub-grain and lath is enhanced, leading to a weakening of the sub-structure hardening effect (Abe, 2008; Dawson, 2012).

2.7. Historical Improvement of Creep Application Steels

Progressive research and development in power plant materials has gradually introduced the higher creep resistant materials over time. Figure 2.14 (Masuyama, 1998) shows an increase in creep strength of creep resistant steels for boilers application, in terms of change in the 10^5 hours creep rupture strength at 600 °C, for the steels that were developed in the 20th century period. The chemistry of these commonly used materials and their 100k hours creep rupture strengths are presented in Table 2.3 **(**Cerjak and Mayr, 2008).

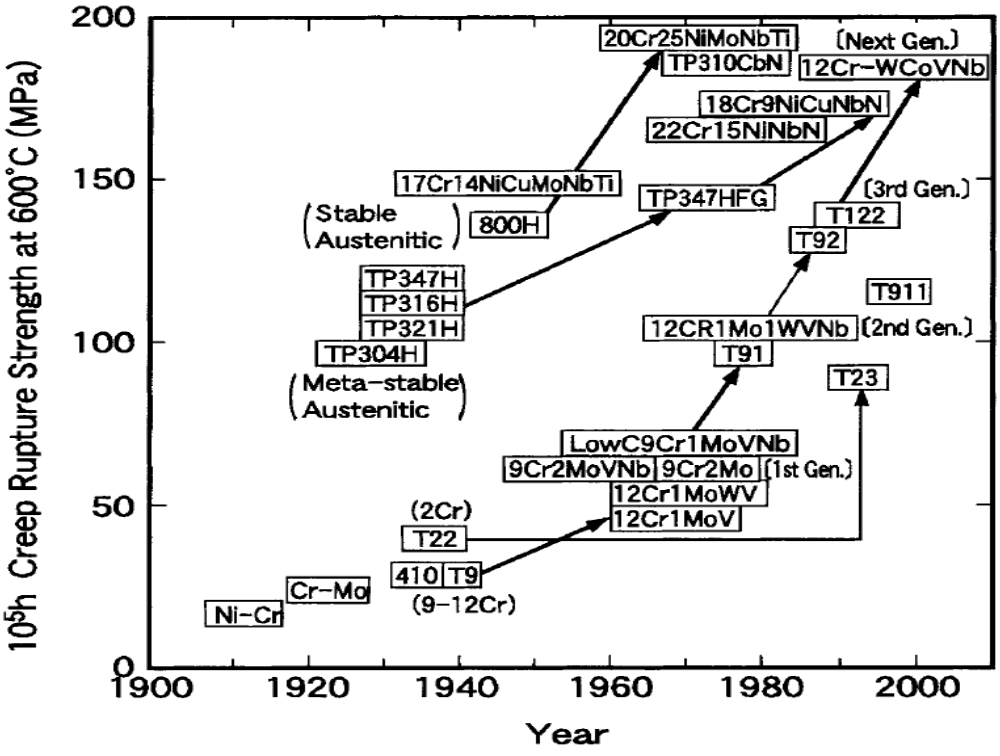


Figure 2.14: Historical developments and improvements in cree- rupture strength of boiler application steels (Masuyama; 1998)

Table 2.3: Chemical composition (wt.%) and creep strength of commonly utilised ferritic steels for thermal power plant (Cerjak and Mayr, 2008).

Low Cr steels		C	Si	Mn	Cr	Mo	Cu	W	Ni	V	Nb	B	N	Ti	T_W^1 (°C)	$R^2_{m\times10^5/T_W}$ (MP_a^3)
13CrMo4-4	min	0.08		0.40	0.70	0.40									550	49
(T/P12)	max	0.18	0.35	1.00	1.15	0.60	0.30						0.012			
10CrMo9-10	min	0.08		0.40	2.00	0.90									550	68
(T/P22)	max	0.14	0.50	0.80	2.50	1.10	0.30						0.012			
7CrWVMoNb9-6	min	0.04		0.10	1.90	0.05		1.45		0.20	0.02	0.0005			550	130
T/P23	max	0.10	0.50	0.60	2.60	0.30		1.75		0.30	0.08	0.0060	0.030			
7CrMoVTiB10-	min	0.05	0.15	0.30	2.20	0.90				0.20		0.0015		0.05	550°C	147
10 (T/P24)	max	0.10	0.45	0.70	2.60	1.10				0.30		0.0070	0.010	0.10		
9% Cr steels																
X11CrMo9-1	min	0.08	0.25	0.30	8.00	0.90									550	92
(T9)	max	0.15	1.00	0.60	10.00	1.10	0.30									
X10CrMoVNb9-1	min	0.08		0.30	8.00	0.85				0.18	0.06		0.030		600	94
(T/P91)	max	0.12	0.50	0.60	9.50	1.05	0.30		0.30	0.25	0.10		0.070			
X11CrMoWV Nb9-1-1	min	0.09	0.10	0.30	8.50	0.90		0.90	0.10	0.18	0.06	0.0005	0.050		600	98
(E911)	max	0.13	0.50	0.60	9.50	1.10		1.10	0.40	0.25	0.10	0.0050	0.090			
X10CrWMoVNb9-2	min	0.07		0.30	8.50	0.30		1.50		0.15	0.04	0.0010	0.030		600	113
(T/P92)	max	0.13	0.50	0.60	9.50	0.60		2.00	0.40	0.25	0.09	0.0060	0.070			
12% Cr steels																
X20CrMoV12-1	min	0.17			10.00	0.80			0.30	0.25					600	49
	max	0.23	0.50	1.00	12.50	1.20			0.80	0.35						
T/P122	min	0.07			10.00	0.25	0.30	1.50		0.15	0.04	0.0005	0.040		600	103
HCM12A	max	0.14	0.50	0.70	12.50	0.60	1.70	2.50	0.50	0.30	0.10	0.0050	0.100			

1service temperature;
2 100 000 h creep rupture strength at service temperature;
3 Software Stahlschlüssel 2004, Verlag Stahlschlüssel Wegst GmbH. Version 4.00.0005; www.stahlschluessel.de;
4 The T23/T24 Book – *New Grades for Waterwalls and Superheaters*, Vallourec & Mannesmann Tubes, 2000;
5 ECCC Data Sheets, 2005, compiled and published by D G Robertson and S R Holdsworth, ETD Ltd;
6 METI (Ministry of Economy, Trade and Industry) Thermal Power Standard Code, Japan (single phase with no delta ferrite).

2.8. The development of 9-12% Cr steels for boiler application.

Chromium (Cr) content control and increase to above 9 wt.% in CrMo-steels had led to a development of steels group that have a martensitic microstructure which induces structural hardening. This martensitic microstructure is typically characterized large amount of dislocation density and a finely distributed martensitic lath structure that is stabilized mainly by $M_{23}C_6$ phase precipitates. Therefore, an increase in the microstructural strength is by means of structural hardening in these martensitic steels. Additional enhancements particularly of the creep strength have been attained by alloying martensitic steels with vanadium, niobium, tungsten and boron (Hagen and Bendick, 2002; Maruyama *et al.*, 2001)

The 9-12wt.% Cr steels are ferritic boiler steels that were designed and developed based on the global strong motivation by two major demands, namely;

(i) Realisation of thermal power plants for public electricity generation (supply), operating at steam temperatures ranging from 538 – 566 ^{o}C during the 1950s.

(ii) The target to develop high efficient and low-pollution power plants operating at turbine steam admission temperatures of 600 – 650 ^{o}C with ultra-supercritical pressure up to 35MPa during the 1980s (Vaillant, *et al.*, 2008), (Albert *et al.*, 2005), (Eggeler *et al.*, 1994), (Spigarelli and Quadrini, 2002) and (Tu ma and Kosec, 2007).

Figure 2.15 illustrates the development on ferritic creep steels from 2, 9 to 12%Cr steels with creep rupture strength of 10^5 hours at 600^{o}C. These 9-12%Cr high strength ferritic creep resistant steels exhibit relatively good corrosion, high temperature oxidation and creep resistance and can be alternatively be utilised since is much less expensive than 18%Cr-8%Ni based materials. The alloys also possess added benefits of allowing the usage of reduced pipe wall thicknesses as the strength is high (Masuyama, 2000).

The 9Cr2Mo steel which is a low carbon 9%Cr–2%Mo steel has been developed and employed to service for more than 28 years in the power utility plants and has more than 2 000 tons of tube and pipe materials operating on the superheater and reheater systems (Yukitoshi *et al.*, 1980). The creep rupture strength for this steel (9Cr2Mo) lies between TP304H and 2.25Cr1Mo steels and is mainly utilised in the reheater circuit tubing as a replacement for 18%Cr–8%Ni stainless materials. Low carbon steels such as 9Cr1MoVNb, 9Cr2MoVNb and 9Cr1MoVNb (ASME T91) (Sikka *et al.*, 1981) are altered 9%Cr materials with elevated temperature properties improvement by the introduction of carbonitride-forming elements like V and Nb (Musuyama, 2000). From these modified and improved 9%Cr steels, T/P91 that

was developed in the US possesses a higher strength for boiler equipment application (Musuyama, 2000; Kalwa *et al.,* 1983). The reduction of Mo content well as the substitution of Mo by the introduction of W alloying element resulted in the development of T/P92 alloy steel material grade. The content of Mo was reduced to 0.5% and 1.8% of W alloying element was introduced to T/P91 grade to attain a recent T/P92 alloy steel, while ±1% W has been introduced to T/P91 grade to obtain T911 alloy steel (Musuyama, 2000).

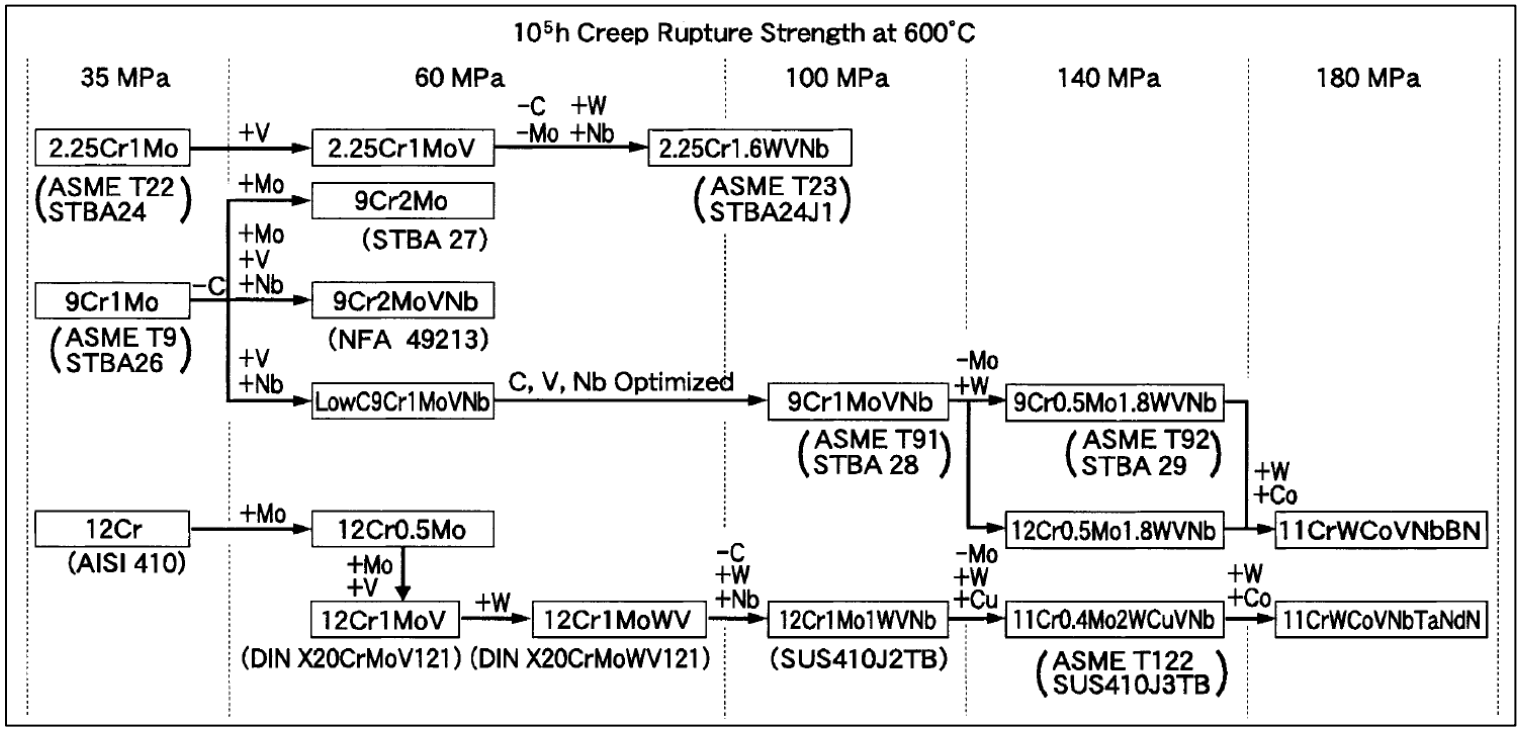


Figure 2.15: Advancement of ferritic alloy material for power-plant application (Musuyama, 200).

In the family of 12%Cr steels, EN 10216-2 X20CrMoV11-1 (Kalwa *et al.*, 1983) is widely utilised in the tubing and piping applications and has enormous operating experience in Europe and South Africa. However, due to its high carbon content (±0.2%), its weldability and fabrication are observed to be slightly challenging, it is scarcely utilised in other Asian countries (Masuyama, 2000). The advancements on 12%Cr steels for boiler components were made by developing the; 12Cr1Mo1WVNb (Iseda *et al.*, 1988) and 12Cr0.4Mo2WCuVNb (ASME T122) (Iseda *et al.*, 1992) to reduce the disadvantages of typical 12%Cr alloy steels. Consequently, 12Cr1Mo1WV-Nb alloy steel was also developed from 12%Cr steel to attain a slight improvement of creep properties and weldability by having the microstructure that has both tempered martensite and ferritic matrix. Elevated temperature properties of this material grade were achieved mainly by introducing finely dispersion of VN precipitates and by tempering at temperature as high as above 800°C (Abe *et al*., 2008; Masuyama, 2000). This alloy steel has consequently attained the allowable stress which is superior to T/P91 material. For more than 20 years of service, this steel had a remarkable experience in boiler applications, with its added usability in resisting corrosion activity. The T122 steel grades are the improved 12Cr1Mo1WVNb, and they have demonstrated that they can be safely utilised to fabricate the thick walled components without compromising the toughness because it retards the formation of delta-ferrite (Abe *et al*., 2008; Masuyama, 2000).

During the progression of ferritic power-plant steels several methodologies for advancing high temperature properties have been explored, and the progress is illustrated in Figure 2.15. The steels with 10^5 hours creep-rupture strengths of 180 MPa at 600°C and 130 MPa at 650°C were previously made available on small research quantity in the workshop (Ohgami *et al.*, 1997). All of these steels have the chemical compositions which include an increased addition of Co (Cobalt) and W (Tungsten) content. The 11Cr2.6W2.5CoVNbBN alloy steel has 2.5% Co, 2.6% W and with <1% B (Boron) alloying elements as compared to the conventional steels (Ohgami *et al.*, 1997). Meanwhile, the 11Cr3W3CoVNbTaNdN alloy steel (Igarashi and Sawaragi, 1997) has 3% of Co and W all together, as well as the addition of Ta (Tantalum) and Nd (Neodymium). Research has confirmed that both Ta and Nd provide finely stabilized nitride precipitates that are important in enhancing creep performance at the service range between 600°C and 650°C (Igarashi and Sawaragi, 1997).

The developments of 9-12%Cr steels have successfully achieved the improved material strength, namely proof yield strength ($R_{p0.2}$) and creep-rupture strength at 10 000 hours ($R_{m10000h}$) are shown in Figure 2.16 (Hagen and Bendick, 2002).

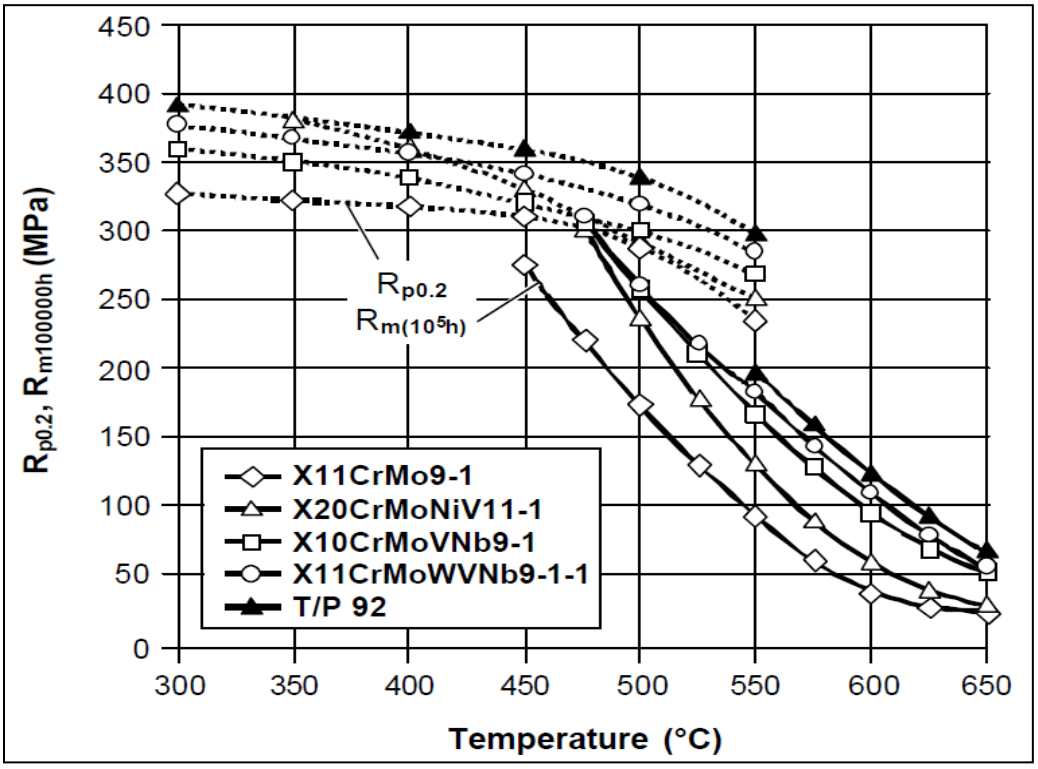


Figure 2.16: Strength properties of 9-12% Cr steels (Hagen and Bendick, 2002).

2.9. Types and effects of welding process used in this study

Welding is a major joining technology for power plant components. The joints can either be between similar material; similar metal welding (SMW) or between dissimilar materials (DMW). The most commonly used welding processes for joining the power plant steel components are TIG (Tungsten Inert Gas) and MMA (Manual Metal Arc) welding (Juffes, 2012).

In the TIG process the heat energy that produced by the arc being sustained in the middle of the work piece and tungsten electrode, is utilised to melt and fuse the metal. A welding arc is consistently established and preserved in the passive gas that enables the protection of a molten weld metal aid it adjacent surrounding out of environmental impurity (Juffes, 2012). This welding technique possesses high arc heat concentration, tremendous weldment quality, versatile control mechanism and multi-pass welding procedure that enhance the tempering of welds after each pass however, it has low productivity due to low weld deposition rate (Arivazhagan and Vasudevan, 2014).

Manual Metal Arc welding process is also known as Shielded Metal Arc Welding (SMAW) process and is still referred to as stick welding in the fabrication industry (Juffes, 2012). It is customarily operated as a manual process hence it is labour demanding. When it is operated by a skilled and experienced operator, good quality welds without defects/indications are achieved in all types of components irrespective of the wall thickness and geometry. The drawback in this manual process is mainly the low productivity (Juffes, 2012).

2.10. Microstructural Evolution of Welded Joints

The weld joint consists of six distinct regions namely; Weld Metal (WM), Coarse-grained Heat Affected Zone (CGHAZ), Fine-grained Heat Affected Zone (FGHAZ), Inter-critical Heat Affected Zone (ICHAZ), Over-tempered region and unchanged Base Material (BM). These gradients of microstructures are formed near the fusion zone are due to different thermal cycles experienced during welding (El-Azim *et al.,* 2012). The microstructural regions of a ferritic weldment are shown in Figure 2.17.

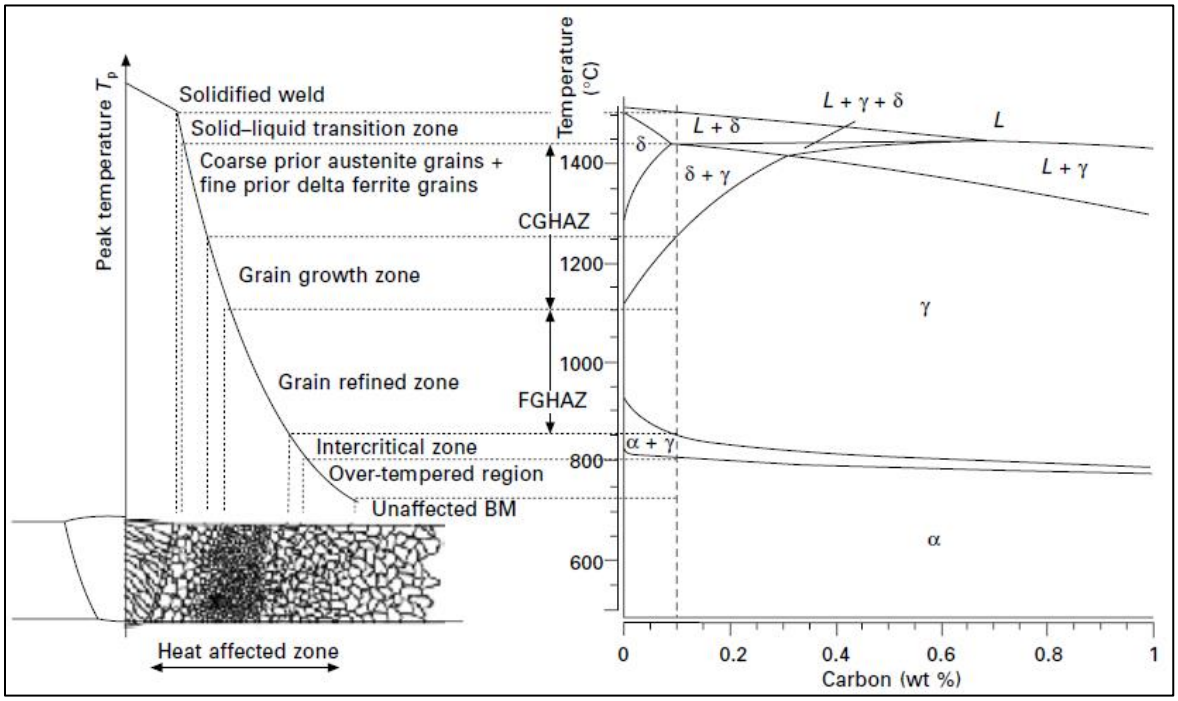


Figure 2.17: Graphic representation of microstructures developed in HAZ due to welding peak temperature, equivalent to calculated equilibrium phase diagram of X10CrMoVNb9-1 (P91) steel (Blondeau, 2008; Cerjak and Mayr, 2008).

The creep behaviour of all these weld joint regions has been intensively studied and it was found and reported that the zone with the poor creep strength is the IGHAZ (El-Azim *et al.,* 2012). The HAZ sub-zones for a typical Cr power-plant material are defined below.

2.10.1. Grain growth zone ($T_p >> A_{c3}$)

The grain growth zone is a zone adjacent to the weld fusion line and it experience temperatures that are fairly exceeding the Ac_3 transformation temperature (Abe *et al.,* 2008). All precipitates that hinder the growth of austenite grains tend to melt/dissolve at this temperature, resulting into austenite grains coarsening. At the maximum peak temperatures (T_p); $T_P > 1250°C$, delta ferrite grain could nucleate (Abe *et al.*, 2008). When cooling the low Cr steels; bainite or martensite microstructure is formed however for 9-12wt.%Cr steels; martensite microstructure is instantaneously formed upon cooling. The coarse-grained heat affected zone (CGHAZ) has the maximum hardness and the lowest toughness in the entire weldment zones. This coarse-grained zone is susceptible to reheat / stress relief cracking during creep application (Abe *et al.*, 2008).

2.10.2. Grain refined zone ($T_p > A_{c3}$)

At the minimum peak temperature of ±1100°C, which is just above the A_{c3} transformation temperature line, there is a development of an undesired austenite phase, subsequent to the α/ϒ transformation during heating (Abe *et al.*, 2008; Zhang *et al.,* 2020). This thermal cycle produces small austenitic grains resulting to a zone called fine-grained heat affected zone (FGHAZ). Furthermore, a peak temperature might not be sufficiently high enough to fully dissolve the precipitate(s), subsequently this limit the grain coarsening by restraining the austenite grain boundaries. During cooling, there is then the formation of either a fine-grained bainite microstructure for lower Cr alloy steels or a martensitic microstructure for higher Cr alloy materials. This fine-grained zone of the weldment is known to be the most creep strength inferior zone on the entire weldment. During longer term creep applications, majority of creep steels weldments are prone to fail at this region due to Type-IV mechanism, also known as Type-IV creep cracking (Abe *et al.,* 2008; Zhang *et al.,* 2020).

2.10.3. Partially transformed zone – intercritical HAZ ($Ac1 < T_p < A_{c3}$)

When the welding peak temperature is between A_{c1} and A_{c3} transformation temperatures lines, there is partial (incomplete) transformation of α into ϒ during heating stage (Abe *et al.,* 2008; Zhang *et al.,* 2020). While newly transformed austenite grains nucleate at their preferable sites (i.e. area of high free energy)

such as prior austenite grain boundaries or the martensite lath boundaries, the untransformed bainitic or tempered martensitic microstructure is tempered again for the second due to this weld thermal cycle. During a subsequent PWHT, there is fractional dissolution of precipitates as well as the coarsening of the precipitates that did not dissolved in this part of the HAZ. During cooling, a dual microstructure containing of recently transformed phases (i.e bainite, for low Cr steels, and un-tempered martensite for higher Cr alloy steels), as well as the tempered microstructure of the original phase are present. This intercritical HAZ possesses the smallest grain size among the entire weldment and has the lowest hardness compared to all regions. This is the sub-region of the HAZ which is also susceptible to Type-IV cracking, similarly to the grain refined zone (Abe *et al*., 2008; Zhang *et al.*, 2020).

2.10.4. Over-tempered region

The weldment HAZ sub-zone microstructure that experiences the peak temperatures below A_{c1} tends to not transform to any phase however it does experience tempering (Abe *et al.*, 2008; Zhang *et al.*, 2020). Consequently, the coarsening of precipitates is highly experienced due to greater diffusion coefficient at this temperature. Therefore, other alloys may exhibit the hardness values that are at the lower range, in this over aged sub-region (Abe et al., 2008).

2.10.5. The unchanged base material zone

This weldment-zone of unaffected parent material microstructure is observed below the temperatures of approximately 700°C. At this low temperature, there are no changes in the microstructure morphology and constituents. Therefore the microstructure appears to be the same as that of the original base material. (Abe et al., 2008; Buchmayr *et al.*, 1989).

The low creep rupture strength on the FGHAZ of the welded joint is due to the microstructural evolution as follows:

1. Sub-grains coarsening and dislocations recovery contribute to softening of the FGHAZ during creep exposure. The martensite lath recovery by means of dislocations annihilation and the elimination of low-angle lath boundaries during PWHT lead to the development of these sub-grains. In 9-12 %Cr steels, the sub-grain size of the FGHAZ tends to coarsen from approximately 0.718 mm after PWHT to roughly 1.23 mm subsequent of creep at 650°C and 40 MPa stress. Consequently, the density of dislocation decreases from $6.3x10^{9}$ cm^{-2} after PWHT to $2.4x10^{9}$ cm^{-}

^{2} post the creep exposure at the same operating conditions, i.e. 650°C and 40 MPa (El-Azim *et al.*, 2012).

2. Dissolution of the finely dispersed $M_{23}C_6$ carbides that obstruct the coarsening of sub-grains by grain boundary pinning mechanism. This result in an acceleration of the sub-grain growth rate, which equate to an increase softening rate. It was observed that the $M_{23}C_6$ particles become coarser (±158nm in average size) after PWHT and 173 nm post creep exposure (El-Azim *et al.*, 2012).
3. Formation of fine V-rich carbonitride (V(C,N)) precipitates with the approximately 70nm in average size after creep exposure, however these precipitate they form adjacent to the coarse $M_{23}C_6$ particles. Consequently, this inhibits their role in the precipitates strengthening.
4. Loss of fine niobium-carbonitride precipitates throughout the creep service which were observed after PWHT and the development of coarse precipitates of Z phase (i.e. Cr(V,Nb)N) with approximately 279 nm in size. The Z phase formation after prolonged creep service has been confirmed by its composition chemical examination using EDX. The gain of unwanted of Z phase at the disbursement of the finely dispersed vanadium nitride and niobium-carbonitride precipitates has been noted in the 9–12 %Cr alloy steels. (El-Azim *et al.*, 2012; Masuyama, 2000).

The cracking morphology that is experienced in weldments is typically categorized in terms of the location of the crack as shown in Figure 2.18. Type-I and Type-II modes take place in the weld body, Type-I is limited to the WM while Type-II could extend out of the WM towards HAZ region. Type-III crack develops in the coarser grain zone of the HAZ. Type-IV is an enhanced rate of creep voids formation an intercritical/fine-grained HAZ of the weldment, resulting to premature rupture as compared to an unwelded (parent) material (Masuyama, 2000).

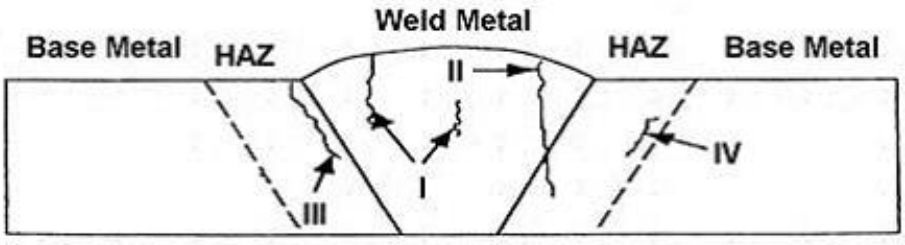


Figure 2.18: Classification of cracks in a weld joint (Molokwane; 2014)

2.11. Stress Analysis on Welded Structures

Stress analysis on weld joints of P91 material pre and post the PWHT have been intensively examined (Dong *et al.,* 2014; Paddea *et al.,* 2012) and the findings are as follows:

1. The maximum tensile residual stresses of ±600 MPa are evident at the interface of the HAZ and the immediate base metal, as well as within the root of the weld towards the inner diameter surface of a pipe in the as-welded form. An area with the maximum tensile stress after applying the PWHT is consistently found at the HAZ locality, having approximately 120 MPa which is about 24% yield strength of the base metal (Paddea *et al.,* 2012).
2. Significant residual tensile stresses of approximately 400 MPa are produced in the HAZ area, and after the effected PWHT, these stress levels are considerably relieved to the levels of ±50 MPa (Paddea *et al.,* 2012).
3. The measured compressive stresses of about -220 MPa in the WM body after welding corresponded to the last weld bead. These residual compressive stresses found in the last capping weld-run could be attributed to the fact that a constrained material surface that have experienced temperatures beyond the Ac_3 temperature line during the heating/welding process will possess a minimum residual stress at ambient temperature than the material surface that has experienced temperatures less than the Ac_1 temperature line, because during cooling (temperature ramp down period) the material in austenite phase tends to form the transformation strain which compensate for thermal contraction strains.
4. The maximum tensile residual stresses were found to coincide with the HAZ interface region, which has a known microstructural that is prone to Type-IV creep degradation mechanism. Further regarding the effect of residual stress on the creep rupture strength for long term creep service still need to be researched to determine the effect of these undesired tensile residual stresses on the Type-IV creep cracking premature failure in weldments (Paddea *et al.,* 2012; Zhang *et al.,* 2020).

The stress analysis profiles of a single pass butt weld, and that of multi-pass butt welds are reportedly different. For a single weld pass, there is a trend of tensile residual stresses at the middle of the weld. In contrary, for multi-pass weld, the middle of the weld is under compressive residual stresses as confirmed and supported by the FEA (finite element analysis) study (Brikstad *et al.,* 1998). FEA showed that as the number of weld runs/passes increased the residual stress on outside surface of the weld goes into compression (Brikstad *et al.,* 1998)

2.12. The Evolution of 9-12%Cr Steels Microstructure During Heat Treatment and Creep

The 9-12wt.%Cr martensitic materials are optimally heat treated by a normalisation heat treatment in the austenite phase region, typically at the between 1040°C to 1100°C. This normalising heat treatment is usually followed by tempering cycle(s) at temperatures between ±650°C and ±780°C subject to the type or dimensions of the of an equipment/component, example; turbine rotor(s), boiler tubing or steam piping (El-Azim *et al.*, 2012 and Maruyama *et al.*, 2001). Subsequent to austenitising, while the material is being air cooled, the material transforms fully into martensite as a result of its hardenability which is controlled by the chemical composition that includes Cr content (Krauss, 1999). The prior austenite grains for these alloy steels are partitioned into grain packets and as well as into blocks, as illustrated in Figure 2.19(a). Thus the resultant microstructure at this current form is consisted of martensitic lath as well as high dislocation density structure (Sonderegger 2005).

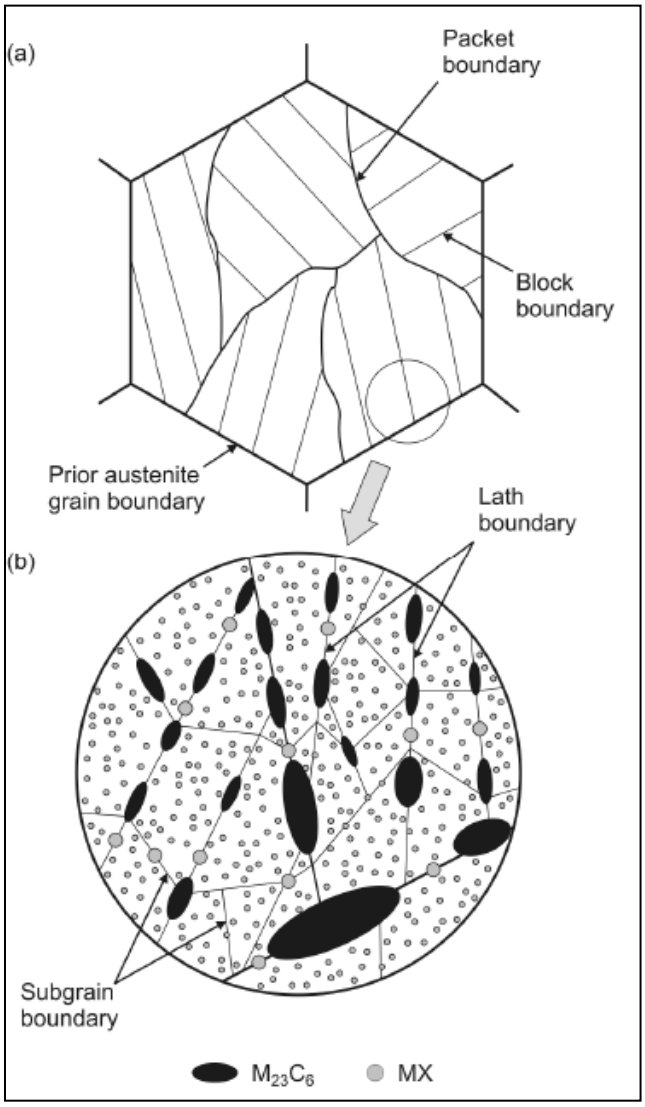


Figure 2.19: Schematic representation of 9-12% Cr steels tempered martensitic microstructure (Holzer, 2010).

When the tempering heat treatment is applied, the dislocation density decreases while the dislocation substructures/sub-grains are introduced. These sub-grain structures are consisted by small angle grain boundaries due to the rearrangement of dislocations through annealing process. These formed small angle boundaries that appear to be smaller than the martensite lath and are different from the martensitic lath boundaries that are also part of microstructure constituents. The measurements from EBSD clearly revealed the significant variance between sub-grain and martensitic lath interfaces based on their misorientations (Abe, 2008; Sonderegger *et al.*, 2008). It has been reported that the disorientations of smaller-angle grain boundaries are fully unsystematic while that of martensitic lath boundaries are predominantly of axes-angle mixture (Maruyama *et al.*, 2001; Abe, 2008).

The precipitation of secondary phase particles occurs during tempering heat treatment, however $M_{23}C_6$ and MX carbonitrides precipitates are the key strengthening precipitation phases in these alloy steels (Foldyna, 1996; Hald, 1996; Maruyama *et al.*, 2001). The types and morphology of these particles are mainly influenced by the actual chemistry of the material. The Cr carbides $M_{23}C_6$ precipitates are commonly precipitated at the grain and sub-grain boundaries (Hald, 1996). Subsequent to tempering, the $M_{23}C_6$ precipitates sizes can be in a range between 50 – 100 nm prior to creep application (Abe, 2008; Sonderegger, 2005).

The MX carbonitrides that are relatively smaller are generally classified into VN and NbC precipitate phases (Lee, 2006), but some of the N in VN and C in NbC are usually replaced by C and N, correspondingly (Ennis, 1997; Sonderegger, 2005). These MX precipitates have size of approximately 20 – 50 nm before creep service (Abe, 2008; Sonderegger, 2005).

These MX precipitates are considered superior in creep resistance in 9-12% Cr material grades as compared to the $M_{23}C_6$ precipitates. It has been found that these precipitates are nucleated on the sub-grains and on the sub-boundaries (Abe, 2008; Hald, 1996; Holzer, 2010). Therefore, the microstructure of 9-12% Cr alloy steel that was normalised and tempered typically consists of prior austenite grains, sub-grain boundaries, martensite lath and small finely dispersed precipitates, as schematically shown in Figure 2.19 (Holzer, 2010).

A 9-12%Cr ferritic creep resistant steel is constituted by numerous microstructural parameters that are designed to be impediments on the movement of dislocations. These desired obstacles are sub-boundaries, sub-grains with free dislocations, $M_{23}C_6$, Fe_2M laves phase that form during creep service, and MX precipitates. Solid solution strengthening using solute atoms like Mo and W, always plays an added role on the improvement of high temperature strength. The creep strengthening mechanisms achieved from these microstructure parameters are summarily categorised as follows (Maruyama *et al.*, 2001):

- Solid solution strengthening due to W and Mo in solution.
- Dislocation hardening because of sub-boundaries and free dislocations within sub-grains.
- Particle hardening due to $M_{23}C_6$ and Fe_2M precipitation.

Even though the structural network of dislocation on the normalised and tempered martensitic steel is considerably stable at elevated temperature, the recovery of dislocation substructure is initiated and

promoted by the plastic deformation. The research study by Maruyama *et al.,* (2001) found that the density of free dislocation in the sub-grains tend to decrease while the sub-grains coarsen when creep deformation is progressive. These microstructural alterations are a result of the dislocation substructure recovery. Consequently, the recovery of the dislocation substructure controls creep deformation mechanism as well as the creep rupture strength until failure stage (Abe, 2008; Maruyama *et al.*, 2001).

For the recovery of sub-grains network to take place, the following two processes must be full filled (Maruyama *et al.*, 2001);

1. Reduction of sub-grain boundaries through eradication of free dislocations that are in the sub-boundary, and
2. The common sub-boundaries annihilation on the two adjacent interfaces that have different attractive polarity.

The initial systematic process is primarily taking place during the first phase of recovery however, the last method could come in to play at an advanced phase. The dislocations that are constructing sub-boundaries are mostly steady subsequent to tempering; they cannot climb their adjacent sub-grain boundaries. Nevertheless, if the dislocations glide from the sub-grain interior to the sub-grain boundaries there will be a balance disturbance in the sub-grain boundaries that forces the annihilation of dislocations in the sub-grain boundaries. Consequently, the density of dislocations tends to significantly decrease both in sub-boundary and in the sub-grain interior simultaneously (Abe, 2008; *et al.*, 2001).

The important precipitates for the 9-12% Cr alloy materials are the finely dispersed MX carbo-nitride within sub-grains and $M_{23}C_6$ carbide and fine Fe_2M Laves phase on the sub-grain boundaries. The precipitates located at the sub-grain boundaries are responsible to pin the dislocation climbing movement in order to retard the sub-grain structure recovery rate. The precipitation density of $M_{23}C_6$ particles is significantly more than that of Fe_2M, signifying that $M_{23}C_6$ particles are the major barrier of dislocation climbing at sub-grain interfaces (Maruyama *et al.*, 2001).

The undesirable coarsening for $M_{23}C_6$ precipitates in 9-12%Cr steels is evident after elevated temperature application as shown in Figures 2.20 – 2.21 (Panait, 2010). The coarsening of precipitates size and a reduction in precipitates density is observed (Aghajani, 2009; Panait, 2009). The $M_{23}C_6$ precipitates that are at the vicinity of the sub-grain boundaries were reportedly found to coarsen earlier and faster than those that have lost the interface contact, this was attributed to short-circuit diffusion along sub-grain boundaries (Hald, 2008; Kostka *et al.*, 2007). The recent research studies have reported that the stability

of $M_{23}C_6$ precipitates against coarsening is significantly improved by introducing boron (B) as the alloying element (Abe, 2008; Aghajani, 2009).

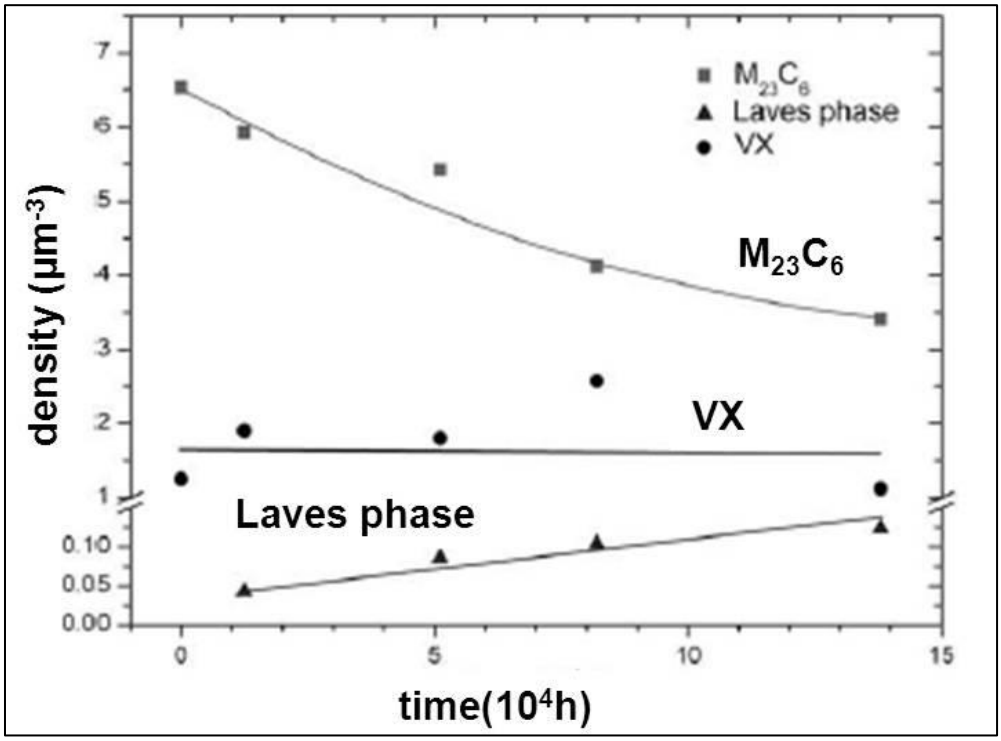


Figure 2.20: Evolution of $M_{23}C_6$, VX and Laves phase precipitates under long-term thermal degradation (Aghajani, 2009)

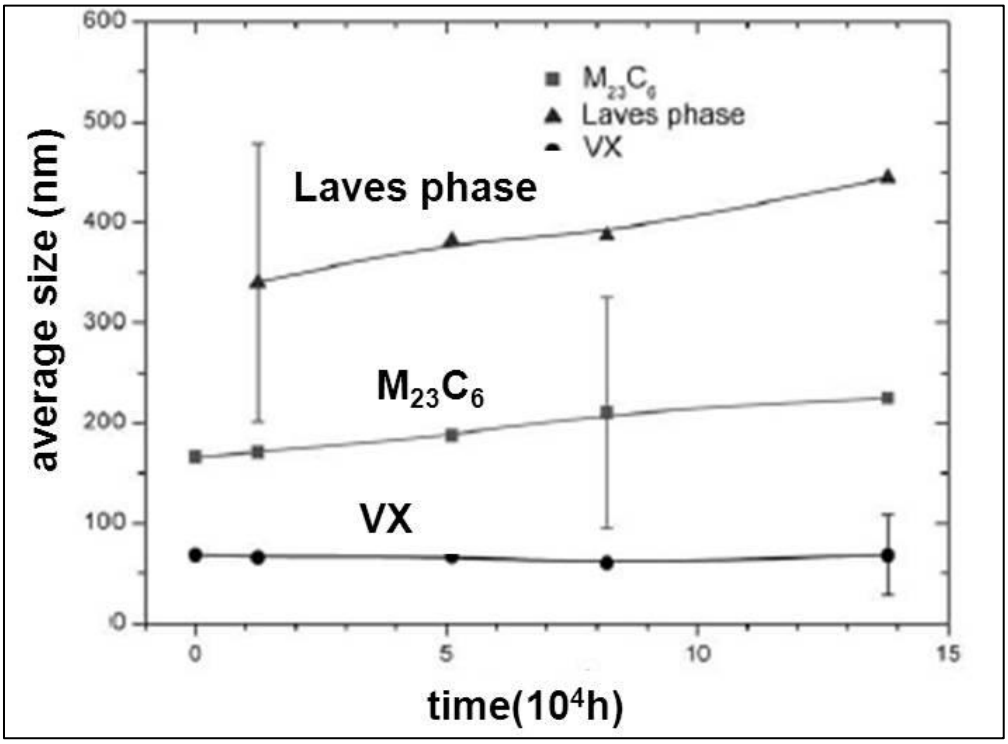


Figure 2.21: Progression of $M_{23}C_6$, VX and Laves phase precipitates mean diameter in long-term thermal aging application (Aghajani, 2009).

The behaviour of MX precipitates were experiential to be more stable during creep degradation, since their changes in particle size and distribution were insignificant as shown Figures 2.20 – 2.21 (Aghajani, 2009; Cerri *et al.,* 1998). The MX carbonitrides precipitates rich in Nb and V are very resistant to coarsening, however they tend to dissolve and disappear when the precipitation of nitride Z-phase (Cr(V,Nb)N) occur. Thus possess a significant challenge on the alloy steels that contain Nb and Cr contents in excess of 10 wt.% (Aghajani, 2009).

After creep exposure, the Laves phase precipitates were observed. This has a negative impact towards creep life and are reportedly undesired for extended period in creep application (Aghajani, 2009). The addition of silicon promotes the nucleation and coarsening of Laves phase (Armaki *et al.,* 2010; Panait, 2010).

In 9-12%Cr alloy steels, the deterioration in creep rupture strength has been confirmed to be as a result of $M_{23}C_6$ carbide precipitates coarsening, formation of coarse Laves phases, development of coarse Z-phases precipitates at the expense of the finely distributed MX particles and significant dislocations recovery in the matrix. The observed significant coarsening of creep strengthening precipitates that occurs during

creep service promotes the microstructure degradation and significantly contributes on the unwanted reduction in creep properties (Aghajani, 2009; Panait, 2010).

2.13. Diffusion of Carbon due to Differences in Cr Concentration Across Ferritic Steel Weld Interfaces

The phenomenon of elemental re-distribution through atomic diffusion is essential considering that most of the phase changes that take place in metallurgy depend on it. The atoms only migrate if the Gibbs free energy product results in a net reduction (Dawson, 2012; Elder, 2011; Kirkaldy and Young, 1987).

Atoms diffusivity through a crystalline material is dependent on the change in temperature, conforming to Arrhenius type relationship set by Equation 2.1:

$$D = D_0 exp(-Q/RT)$$

(Equation 2.1)

Where, D_0 is a coefficient of diffusion, that is a constant value which depend on an atomic vibration frequency, Q is defined as an activation energy ($J.mol^{-1}$), R is a gas constant (8.31446 ($Jmol^{-1}K^{-1}$)), T is the absolute temperature (°K) and Q is define as the required activation energy ($J.mol^{-1}$) to move an atom to the adjacent site. This movement is only possible when the following two conditions are met;

1. Vacancy creation
2. Sufficient energy to overcome the opposing force for an atom to diffuse.

Therefore, the required activation energy can be expressed by Equation 2.2:

$$Q = \Delta H_v + \Delta H_m$$

(Equation 2.2)

Where, ΔH_v is the vacancy creation force and ΔH_m is the force/energy required for atom to move (Dawson, 2012).

The diffusion of carbon across dissimilar metal weld interfaces between X20 and P91 (9-12%Cr alloy materials) has not yet been conveyed in published literature however that of 2.25%Cr and 9%Cr has been extensively studied and published. The up-hill diffusion of C in 2.25%Cr and 9%Cr dissimilar welds has been publicised to manifest under PWHT period and during the elevated temperatures applications (Dawson, 2012).

In the P291/P22 steels weld transition joints, the carbon's re-distribution driving force is caused by the variation in the chemical potential of elemental carbon in alloys that have dissimilar concentrations of chromium. This elemental re-distribution by means of diffusion result into the formation of chromium carbides. However for the steel alloys that contain other carbides strong formers such as V and Nb, the formation enthalpy of VC and NbC carbides is larger than that of Cr_7C_3 and $Cr_{23}C_6$ carbides, (Abe, 2008; Dawson, 2012), therefore the strong carbides formers (Nb and V) have higher preference to react with carbon than chromium to react with carbon.

For estimation purposes the width or distance (x) that could be subjected to the solute species through diffusion in an alloy steel is provided by Equation 2.3;

$$x = \sqrt{Dt}$$

(Equation 2.3)

Where, t is defined as time in seconds and D is representing a diffusion coefficient as given in Table 2.4 (Dawson, 2012).

Table 2.4: Diffusion coefficients (Dawson, 2012)

Diffusion species	**Host species**	**$D_0(m^2s^{-1})$**	**Activation energy Q_d(KJ/mol)**	**Calculated/drived values**	
				T(^{o}c)	**$D(m^2s^{-1})$**
Carbon	ɤFe	$2.3x10^{-5}$	148	1100	$5.38x10^{-11}$
Carbon	αFe	$6.2x10^{-7}$	80	730	$4.23x10^{-11}$
Nitrogen	αFe	$3.0x10^{-7}$	76	730	$3.3x10^{-11}$
Chromium	αFe	$2.53x10^{-4}$	240.6	730	$7.47x10^{-17}$
Iron	αFe	$0.5x10^{-4}$	240	730	$1.59x10^{-17}$
Vanadium	αFe	$0.61x10^{-4}$	259	730	$1.98x10^{-18}$
Noibium	αFe	$1.27x10^{-6}$	224	730	$2.74x10^{-18}$
Molybdenum	αFe	0.78	305	730	$1.02x10^{-16}$
Tungsten	αFe	$3.8x10^{-2}$	293	730	$2.09x10^{-17}$

For example, when the αFe is being tempered at 730°C, the carbon could diffuse through the steel over a distance of;

$$x\ of\ carbon = \sqrt{D\ of\ carbon \text{ x } t}$$

$$x\ of\ carbon = \sqrt{4.23\text{x}10^{-11} \text{ x } 7200}$$

$$x\ of\ carbon = 550\mu m$$

and the chromium could diffuse through the steel over a distance of;

$$x\ of\ chromium = \sqrt{D\ of\ chromium \text{ x } t}$$

$$x\ of\ chromiun = \sqrt{7.47\text{x}10^{-17} \text{ x } 7200}$$

$$x\ of\ chromium = 0.7\mu m$$

Based on this example calculation it is apparent that the carbon atoms migrate more than chromium atoms, i.e. carbon atoms diffuses towards chromium atoms to form chromium carbides while chromium atoms are relatively immobile as compared to carbon atoms (Dawson, 2012; Kirkaldy and Young, 1987).

These estimated calculations are over-simplified for the actually complex state in the alloys, however as a rule of thumb, they only provide an expected diffusion widths on the affected area as an indication. For accurate diffusion width determination, many important factors such as the overall chemical composition of both the alloys being welded together, microstructure at the applicable temperature, and paramagnetic features of the alloys must be accounted for (Dawson, 2012; You *et al*., 2001).

In chromium containing steels, it has been reportedly found that C migrates from the lower/less Cr content containing steel to the higher Cr content bearing steel, and consequently forms chromium carbides on the high Cr containing steel interface side (You *et al.*, 2001). This leads to the development of a C depleted area band in the lower Cr steel side along the weld fusion line. It has been reportedly found that the carbon-depleted area is soft and it has poor mechanical properties when operated in the creep temperature range (Dawson, 2012; Elder, 2011; Oates and Saitta, 1998).

2.14. Chapter Summary

In summary, based on the available literature survey, there is a research knowledge gap on characterisation of a suitable weld filler to fuse a butt weld of creep aged X20 pipe material to a virgin P91 pipe material in consideration of attaining the optimal creep life from the affected weld joint. However there is vast published research pertaining to the development and characterisation of creep behaviour of parent material of both virgin X20 and P91 alloys without considering the effect of welding on the creep aged material. Literature reveals that these 9-12%Cr ferritic creep resistant alloys have proven to be the most economic high temperature power plant materials. The development of these alloy materials over the past decades have enabled a significant improvement on the power plant thermal efficiency and reduction in carbon dioxide (CO_2) emissions. The main creep strength contributing parameters (i.e precipitates morphology, dislocation density and sub-grain size) have been explicitly characterised for these 9-12%Cr steels and it have been reportedly found that the latter P91 alloy has a better long term creep life as compared to the X20 alloy steel.

The projections informed by the literature are showing that 9%Cr grade materials (in which P91 alloy belongs) are the future material in fossil power plant, due to their superior creep life while compared to the traditionally used 12%Cr grade materials (in which X20 alloy belongs) and will also be used in partial or fully system replacements. Therefore the characterisation of a dissimilar weld joint between a creep aged 12%Cr alloy steel and a virgin 9%Cr alloy steel to determine a suitable weld filler metal that will give optimal creep life is still needed to close this research knowledge gap.

CHAPTER 3

3. EXPERIMENTAL METHODOLOGY

3.1. Introduction

The experimental approach that was adopted to achieve the objective of this research study entails the following; materials sample selection and preparation, welding process, post weld heat treatment, stress analysis, hardness testing, tensile testing, Charpy impact testing, uniaxial creep test, small punch creep test and microstructural evaluation, as per the flow chart in Figure 3.1. The details of this experimental methodology are elaborated in sections 3.2 - 3.10.

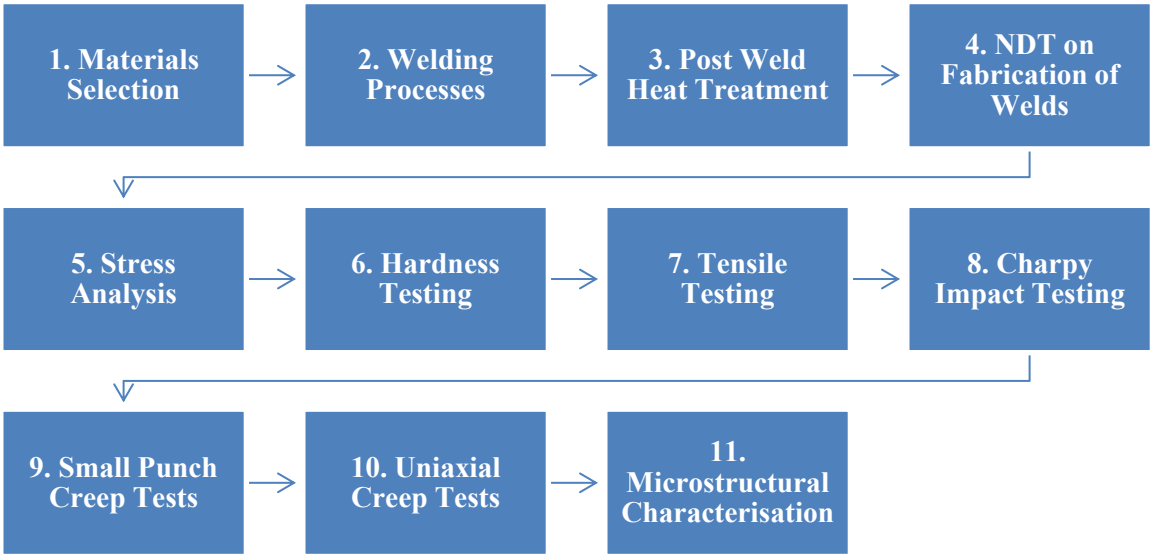


Figure 3.1: Flow chart illustrating the experimental methodology that was followed to achieve the research objective.

3.2. Materials

The base materials used in this research work were seamless pipes of normalised and tempered new (virgin) P91 steel and service exposed X20 steel pipework used in power generation plants. The two pipes are shown in Figure 3.2. The creep cavitation damage level of the service exposed X20 material as expressed in terms of creep void density was 60 voids / mm^2 as confirmed by the creep voids counting on the lifted surface replica micrographs shown in Figure 3.3.

The design temperature and pressure of the main-steam pipework materials are 544°C and 18.9 MPa, respectively, with a design operating life of 200 000 hours. However, the actual operating conditions were slightly lower (539°C and 17.1 MPa respectively), relative to the design conditions.



Figure 3.2: Photograph showing the X20 and P91 base materials pipe samples with their respective dimensions.

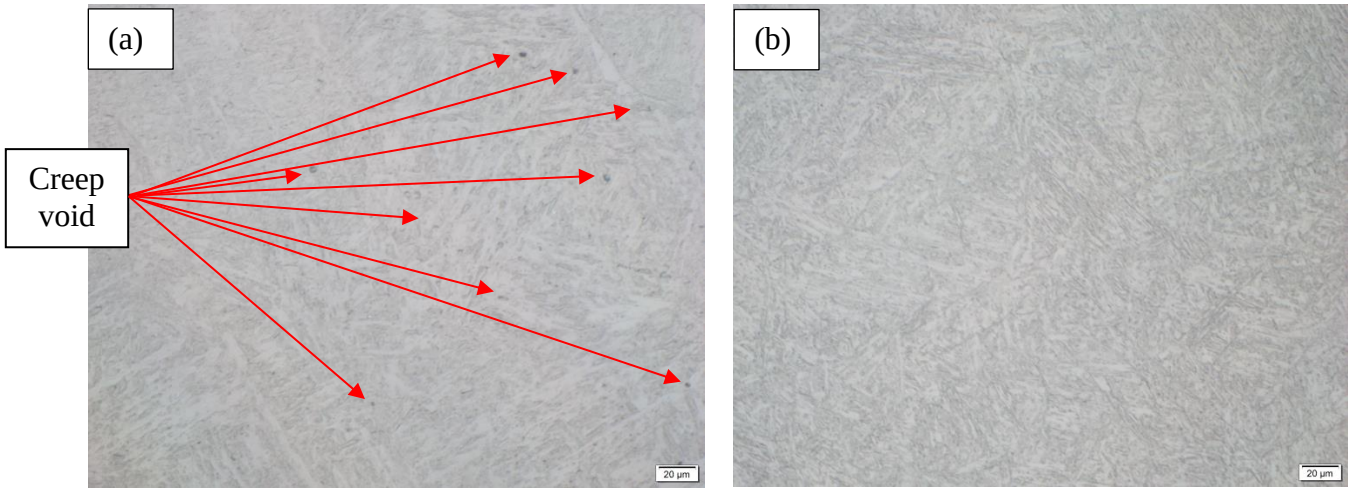


Figure 3.3: Surface replication micrographs of the base materials used, (a) X20 had 60 creep voids / mm^2 and, (b) P91 had no creep damage (virgin material) at 500X magnification.

The test pieces had a length of 200 mm, internal diameter (ID) of 366 mm, and the wall thickness (WT) of 44 mm for alloy X20 and the WT of P91 alloy was 42 mm, as summarised in Table 3.1. The outer diameter of X20 material pipe was machined to match that of P91 pipe by removing 2 mm on the outer wall radius (total of 4 mm on outer diameter).

Table 3.1: Dimensions of the X20 and P91 test-pieces

	X20 Pipe Material	**P91 Pipe Material**
ID (mm)	336	336
OD (mm)	424 before machining	420
WT (mm)	44 before machining	42

The actual analysed chemical composition for the P91 (X10CrMoVNb9-1) and X20 (X20CrMoV11-1) pipe materials that were used in this study as well as the EN standards (BS EN 10216-2: 2002) specification are as shown in Table 3.2. The chemical composition of the TIG and the MMA consumables were compared to the manufacturer's datasheet (Bohlër Welding, 2009) as tabulated in Tables 3.3 and 3.4 respectively.

Table 3.2: Chemical composition (in wt.%) of X10CrMoVNb9-1 and X20CrMoV11-1 pipe materials, according to the chemical analysis certificate in comparison with EN standards (BS EN 10216-2: 2002).

Steel Grade	C	Si	Mn	P max	S max	Cr	Mo	Ni	Al tot	Cu	Nb	V	N
X10CrMoVNb9-1 Pipe Sample Results	0.09	0.33	0.46	0.007	0.007	8.61	0.97	0.18	0.013	0.13	0.094	0.20	-
X10CrMoVNb9-1 Pipe Material (BS EN 10216-2: 2002)	0,08 to 0,12	0,20 to 0,50	0,30 to 0,60	0,020	0,010	8,00 to 9,50	0,85 to 1,05	≤ 0,40	≤ 0,040	≤ 0,30	0,06 to 0,10	0,18 to 0,25	0,030 to 0,070
X20CrMoV11-1Pipe Sample Results	0.16	0.22	0.56	0.009	0.007	11.7	0.96	0.69	0.029	0.08	0.021	0.29	-
X20CrMoV11-1 Pipe Material (BS EN 10216-2: 2002)	0,17 to 0,23	0,15 to 0,50	≤ 1,00	0,025	0,020	10,00 to 12,50	0,80 to 1,20	0,30 to 0,80	≤ 0,040	≤ 0,30	-	0,25 to 0.35	-

Table 3.3: Chemical composition (in wt.%) of X10CrMoVNb9-1 and X20CrMoV11-1 TIG rod welding consumables, according to Bohlër welding Technical handbook (Bohlër welding, 2009)

Welding Consumable	C	Si	Mn	P max	S max	Cr	Mo	Ni	W	Cu	Nb	V	N
X10CrMoVNb9-1 – TIG wire (C9 MV-IG)	0,11	0,35	0,45	-	-	9,0	1,0	0,75	1,05	-	0,06	0,2	0,04
X20CrMoV11-1 –TIG wire (20MVW-IG)	0,19	0,37	0,55	0.010	0,003	11,1	0,85	0,1	0,42	< 0,1	<0,01	0,25	-

Table 3.4: Chemical composition (in wt.%) of X10CrMoVNb9-1 and X20CrMoV11-1 MMA covered electrode welding consumables, according to Analysis Certificate and Comparison with Bohlër welding Technical handbook (Bohlër welding, 2009)

Weld Sample / Welding Consumable	C	Si	Mn	P max	S max	Cr	Mo	Ni	W	Cu	Nb	V	N
X10CrMoVNb9-1 Weld Sample (MMA electrode sample results)	0.079	0.26	0.59	0.01	0.013	8.59	1.03	0.49	-	0.05	0.061	0.22	-
X10CrMoVNb9-1 (Böhler Fox C9 MV)	0.11	0.2	0.7	-	-	9.0	1.0	0.75	-	-	0.06	0.22	-
X20CrMoV11-1 welding rod sample) Results	0.12	0.28	0.67	0.009	0.012	10.8	0.92	0.49	-	0.04	0.022	0.22	-
X20CrMoV11-1 (Böhler Fox 20MVW)	0,18	0,24	0,67	0.010	0,007	10,8	0,90	0,5	0,50	< 0,1	< 0,01	0,21	-

3.3. Fabrication of Welds

The welds fabrication process involved welding process, post weld heat treatment (PWHT) and non-destructive testing (NDT).

3.3.1 Welding Processes

The welded joints of creep aged X20 steel and new P91 steel were prepared using the welding parameters given in Table 3.5. The weld preparation was a single-Vee joint type as shown on Figure 3.4.

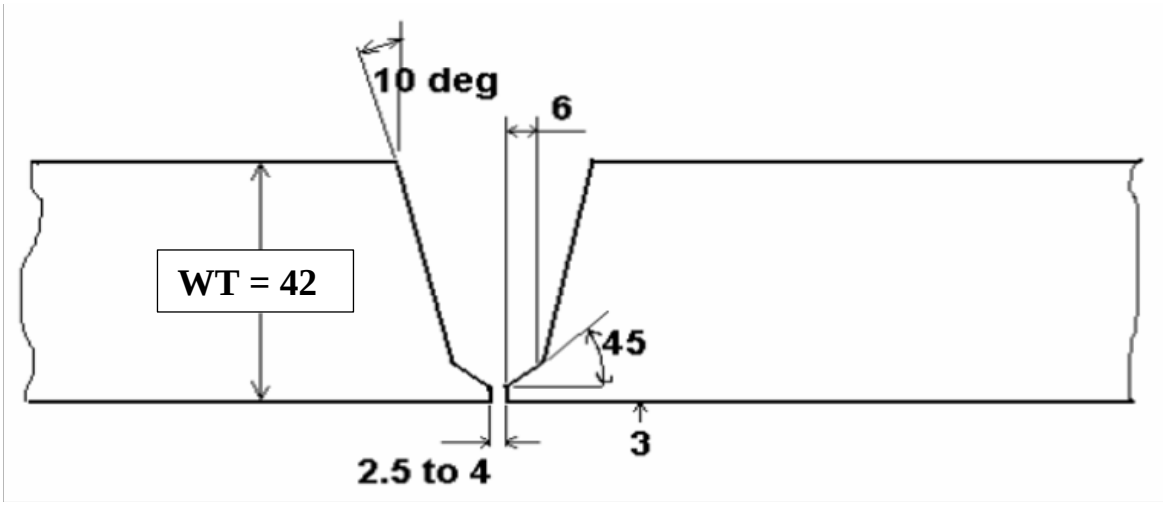


Figure 3.4: Schematic representation of a single-Vee joint type weld prepared-phase [distance is in mm and angle is in degrees]

The weld pre-heat of 250°C was applied to the area to be welded before the commencement of the welding process. The pipes were welded using the Tungsten Inert Gas (TIG) welding process for the root pass, and Manual Metal Arc (MMA) welding for the filling of the passes. The TIG weld deposit thickness of 4 mm at the root was achieved by welding only two weld passes. The weld interpass temperature was 200°C-300°C. The essential welding parameters that were used as determined from the recorded welding parameter sheets are presented in Table 3.5

Table 3.5: Essential welding parameters used for TIG and MMA Welding processes

	Process variables	
Welding parameters	**TIG**	**MMA**
Welding current (A)	90 – 121	104 – 127
Welding voltage (V)	8.7 – 12.8	19.7 – 22.8
Time per run (s)	50	59
Weld length (mm)	110	120
Weld travel speed (mm/s)	2.2	2
Heat Input (KJ/mm)	0.8 – 1.2 using the arc efficiency of 0.35	0.12 – 0.25 using the arc efficiency of 0.8

3.3.2 Post Weld Heat Treatment

The weld joints were allowed to cool to a temperature below 100°C before the samples were post weld heat treated (PWHT). The importance of cooling below 100°C was to ensure a fully transformed martensitic microstructure by reaching martensite finish (M_f) transformation temperature before PHWT as the residual untransformed austenite does not respond to the PWHT and can lead to fresh un-tempered martensite (Zhang *et al.,* 2000). The PWHT for both weld joints was carried out in the furnace at 755°C for 4 hours (soaking time) using the ramp rates of 50°C per hour as shown in Figure 3.5. The choice of PWHT parameters was informed by the previous research publication on grade 9-12%Cr steels (Böhler welding, 2009) and with consideration of the condition of the creep aged X20 material, so that optimal tempering of the weld joint is achieved without compromising (over tempering) the creep aged material.

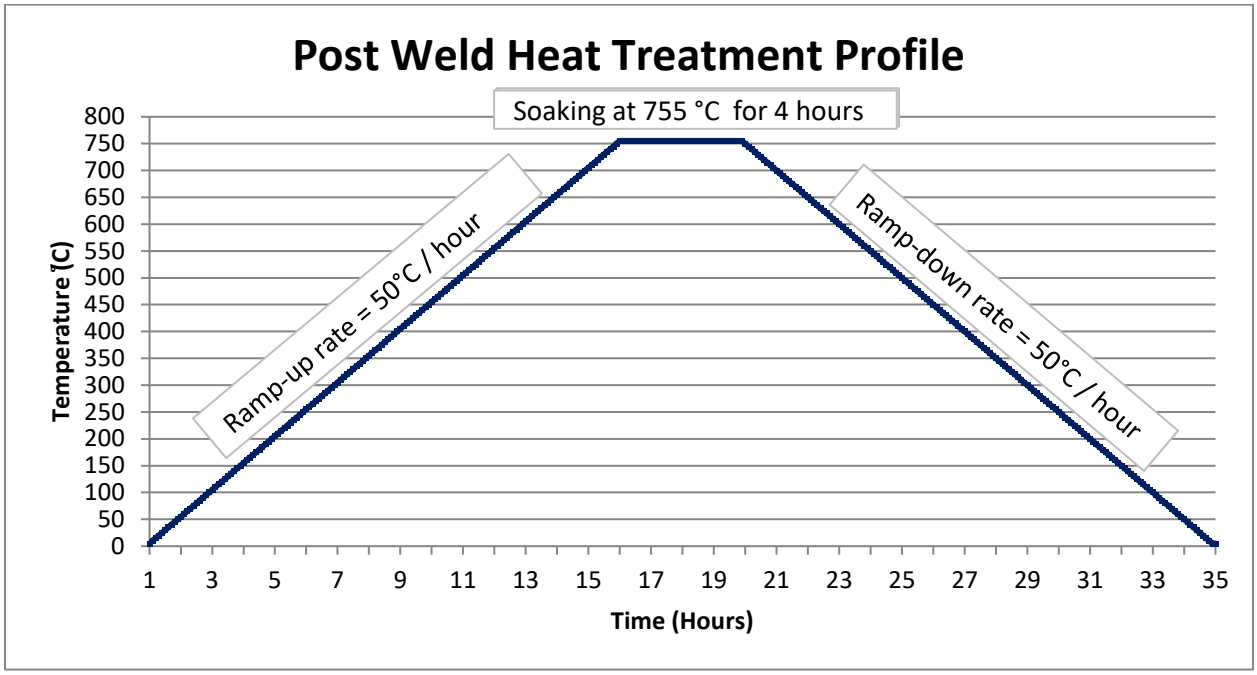


Figure 3.5: Post weld heat treatment profile applied on the weld joints at 755°C for 4 hours using the ramp rates of 50°C per hour.

3.3.3 Non-Destructive Testing (NDT) on Welds

Non-Destructive Testing (NDT) namely; MPI (Magnetic Particles Inspection), Phased-Array UT (PA Ultrasonic Testing) and Radiographic Testing (RT) were conducted after welding, to determine the soundness of the welded joints before further tests were carried out.

The MPI testing was carried out using a Gammatec Yoke (with Serial Number ZY006) equipment in accordance to the DIN EN ISO 17638 - 2010 standard for quality schedule and DIN EN ISO 23278 – 2010 standard for acceptance criteria.

Phased array UT was carried out using an OMNI-M2-16128 (with Serial Number OMNI2-104877) instrument with probe type 5L64-A12 (probe serial Number H1414). The tests were carried out according to BS EN 1712 – 1997 standard for flaws acceptance criteria.

Radiographic testing was carried out using IR-192 and film type AGFA D5 10X25 cm equipment, according to EN 1435 - 1997 specification standard and BS EN ISO 5817 – 2014 standard for acceptance criteria.

3.4. Analysis of Weld Residual Stresses

Stress analysis was carried out to determine the residual stress levels acting on the pipe weld joints without the internal pressure stress and operating system loading using a laboratory X-ray diffraction equipment manufactured and supplied by Proto Manufacturing Ltd, with serial number 10202040111. The analysis was carried out on the as welded and post weld heat treated samples. Surface preparation was carried out to remove metal oxides and to obtain a smooth flat surface by means of mechanical grinding and polishing up to 3 μm surface finish, while taking care not to remove more than 1 mm metal wall thickness. The set-up of the laboratory X-ray diffraction residual stress measurements technique that was used to measure the stresses on the weld joints is shown in Figures 3.6 – 3.7. Measurements of lattice parameters were made in the hoop and axial orientations. The parameters that were used for X-ray diffraction measurements on the sample using a tube with a Cr target are; 20 kV tube voltage, 4 mA tube current, Cr-Kα X-Ray with two detectors, 156.0° on the 211 plane Bragg angle (2θ), 1 mm collimator aperture diameter, and 3° psi oscillation 1s exposure. The instrument was calibrated using Fe powder sample for zero stress and a high stress reference sample of -496 MPa prior to recording measurements.

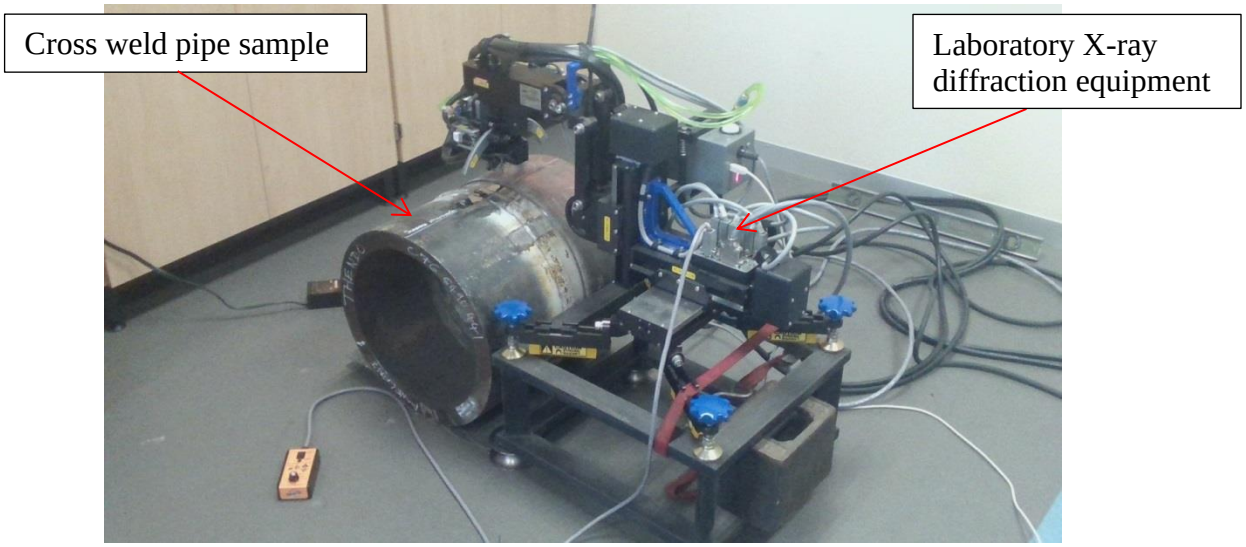


Figure 3.6: Photograph showing the set-up of a laboratory X-ray diffraction residual stress measurements technique.

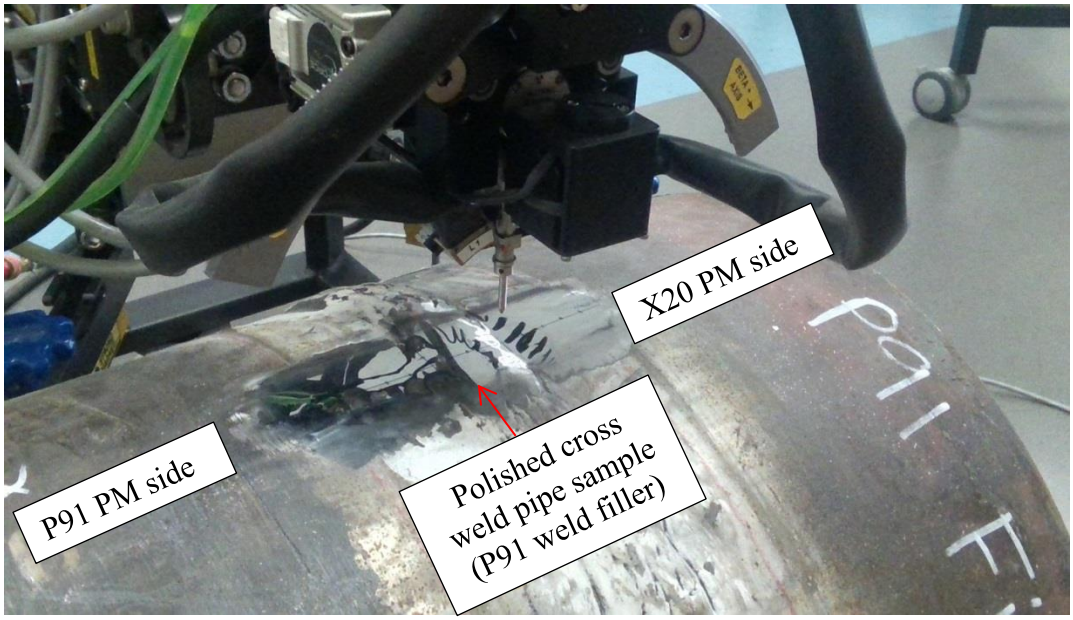


Figure 3.7: Photograph of a close-up view showing a set-up of a laboratory X-ray diffraction residual stress measurement technique being applied on a mechanically polished (3µm surface finish) cross weld pipe sample.

3.5. Hardness Testing

Samples sectioned from the two post weld heat treated pipes namely; (1) creep aged X20 PM - X20 weld filler - new P91 PM and (2) creep aged X20 PM – P91 weld filler - new P91 PM cross weld specimens, were prepared following standard procedures for ferrous alloys. The samples were ground using a silicon carbide paper (80, 120, 240,500, 800 and 1200 grit size) and polished using 3 µm and 1 µm diamond paste. The samples were then etched using Villela's Reagent (1gram picric acid, 5 ml hydrochloric acid and 100 ml ethanol). Macro, micro and nano-indentation hardness measurements were carried out on the prepared samples.

Macro and micro Vickers hardness tests were carried out on the prepared samples using EMCO TEST DURASCAN Vickers hardness testing equipment. Hardness profiles were obtained across the weldments using a load of 10 kgF for macro hardness measurements and a load of 300 gF for micro Vickers hardness measurements. The indentation for macro and micro hardness measurements were in 1 mm and 0.5 intervals, respectively. The dwell time for hardness indentations was 5 seconds. The micro hardness test trends were also used as markers for SEM and TEM analysis.

The Vickers hardness test method was as per the ISO 6507-1 standard of metallic materials (ISO 6507-1, 2005). Hardness measurements were carried out on the BM, HAZ and the WM areas of the weldment samples.

Nano-indentation hardness measurements were taken across the fusion line for the dissimilar weld metal/parent material samples to investigate a possible "carbon denuded" zone. A Berkovich (triangular) tip was used to perform the measurements at a load of 500 mN using the nanoindentation tester platform from CSM Instruments. The converted Vickers hardness measurement was calculated automatically from the load-displacement curve generated during indentation.

3.6. Tensile Testing

Tensile tests at room temperature (21°C), 500°C and 550°C were performed to study and compare the effect of maintenance welding on both weld joints (P91 weld filled joint and X20 weld filled joint). All 3 test conditions for both samples (X20 and P91 filler weldment cross weld pipe sample) were duplicated, with the tests amounting to a total of 12 test specimens as summarised by the test matrix in Table 3.6. The test strain rate of 0.00025 s^{-1} was used. These tests were carried out on PWHT materials.

Uniaxial tensile tests were carried out on the standard round gauge length tensile specimens using the Universal Tensile Testing Machine. The test load was applied as per the BS EN ISO 6892-1 standard of tensile testing method on metallic materials at ambient temperature (BS EN ISO 6892-1, 2009) and BS EN ISO 6892-2 standard of tensile testing method on metallic materials at elevated temperatures (BS EN ISO 2892-2, 2011). The weldment joint sample regions that were subjected to tensile testing included a BM, HAZ and WM as a cross weld joint sample. All tensile test specimens were sampled in the longitudinal direction of the pipe butt weld at the centre of the pipe wall thickness, only in MMA welded region without intersecting the TIG welded region. The test specimen had the 6mm diameter and the gauge length of 30mm.

Table 3.6: Tensile Test Matrix

	Specimen No.	Temperature (°C)
X20 (X20CrMoV11-1) Filler weldment cross weld pipe	1	21
	2 (Duplicate)	21
	3	500
	4 (Duplicate)	500
	5	550
	6 (Duplicate)	550
P91 (X10CrMoVNb9-1) Filler weldment cross weld pipe	7	21
	8 (Duplicate)	21
	9	500
	10 (Duplicate)	500
	11	550
	12 (Duplicate)	550

3.7. Charpy Impact Testing

The Charpy impact test, also known as the Charpy V-notch test, is a material toughness test by high strain-rate testing that involves striking and breaking a standard notched specimen with a controlled weight pendulum swung from a set height (ASTM: A370 – 97a, 1997). The Charpy impact test assists in measuring the amount of energy absorbed by the material specimen during fracture. The amount of energy absorbed during fracture is recorded and this provides toughness level of the tested material. The test reveals whether the material can be classified as brittle or ductile. Brittle materials absorb a small amount of energy during impact testing, whereas ductile materials absorb substantial amount of energy (ASTM: A370 – 97a, 1997).

Samples sectioned from post weld heat treated (i) creep aged X20 PM welded with X20 weld filler to new P91 PM and (ii) creep aged X20 PM welded with P91 weld filler to new P91 PM, as cross weld specimens were prepared following standard procedure for notched Charpy impact testing, with the specimen size of 10 × 10 × 55 mm. All specimens were sampled in the longitudinal direction of the pipe butt weld, in the

MMA welded region without intersecting the TIG welded region. These samples were then notched at the centre of the weld metal from the weld cap side.

Impact test were carried out in accordance with ASTM standard test methods for notched bar impact testing of metallic materials (ASTM: E23 − 12c, 2016). The impact test temperature for all samples was kept at 21°C. Two different samples (i.e. (i) with X20 weld filler and (ii) that of P91 weld filler) with their duplicates were tested.

3.8. Small Punch Creep Tests

Small punch creep test (SPCT) samples were removed from the parent material (P91 and X20), weld metal, and the fine-grained heat affected zone (FGHAZ) from both sides of each weldment. In order to ensure that the FGHAZ samples were extracted from the correct location, the weld cross section had to be polished and etched to identify the different weld regions. The FGHAZ samples were the most critical sections that were to be removed from the correct position, since FGHAZ is a narrow zone of ~1.0 – 1.5 mm. Once discs were removed from these regions, they were polished on both sides to a final thickness of 500 μm and etched with Villela's Reagent (1 g picric acid, 5 ml hydrochloric acid and 100 ml ethanol) to ensure that the microstructure was mostly similar on both sides.

Sections were cut from the butt welded samples which were polished to a final finish using 0.05μm colloidal silica and etched with Villela's reagent. The samples welded with X20 filler metal are shown in Figure 3.8, while the samples welded with P91 filler metal are shown in Figure 3.9.

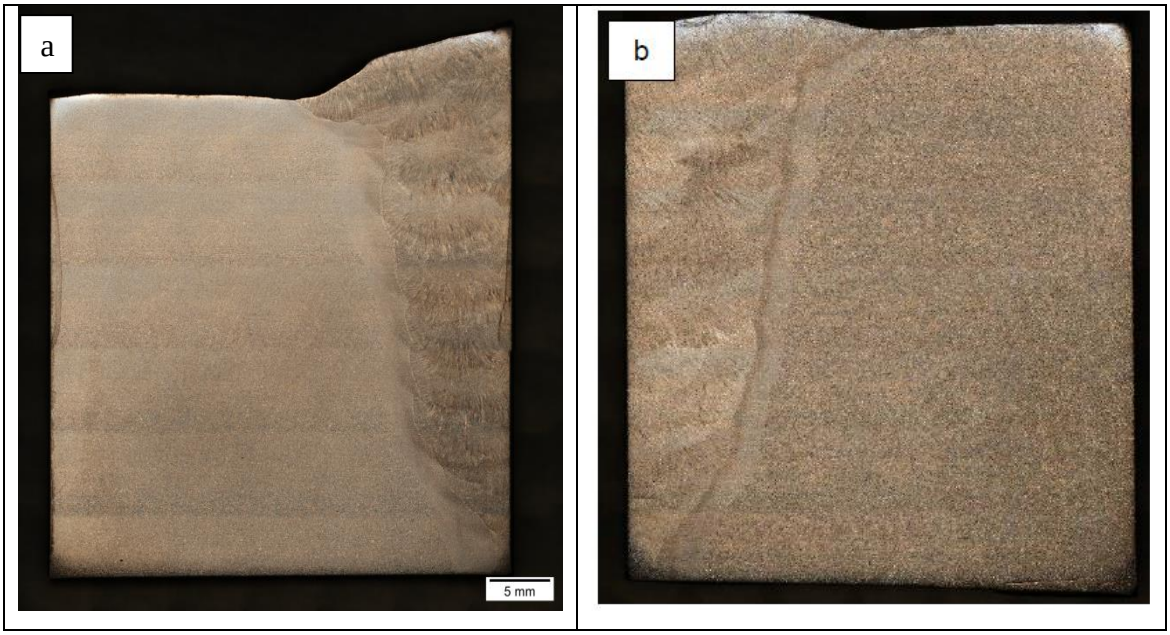


Figure 3.8: Macrographs indicating the weld metal, HAZ and parent material of (a) the X20 weld filler metal, P91 parent material side and (b) X20 weld filler metal, X20 parent material side.

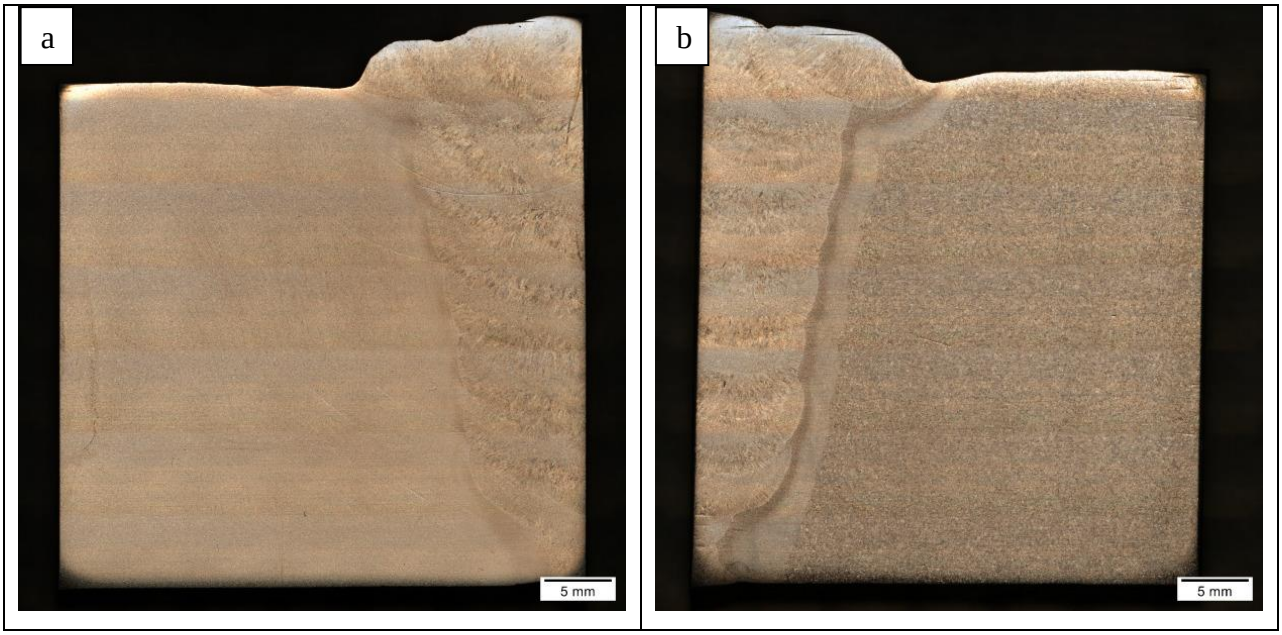


Figure 3.9: Macrographs indicating the weld metal, HAZ and parent material of (a) the P91 weld filler metal, P91 parent material side and (b) P91 weld filler metal, X20 parent material side.

To ensure that the fine-grained HAZ area was properly sampled, the samples were scribed along the edges of the HAZ (X20 filler metal samples are shown in Figure 3.10, while P91 filler metal samples are shown in Figure 3.11). Slithers were wire-cut from the samples, and SPCT discs were removed from these slithers

at a position which coincided with the centre of the pipe wall thickness. The slithers were extracted from the samples as shown in Figure 3.12.



Figure 3.10: Stereo macrographs with scribe lines indicating where the HAZ samples were removed from the X20 weld filler material sample (a) P91 parent material side, (b) X20 parent material side.



Figure 3.11: Stereo macrographs with scribe lines indicating where the HAZ samples were removed from the P91 weld filler material sample (a) P91 parent material side, (b) X20 parent material side.

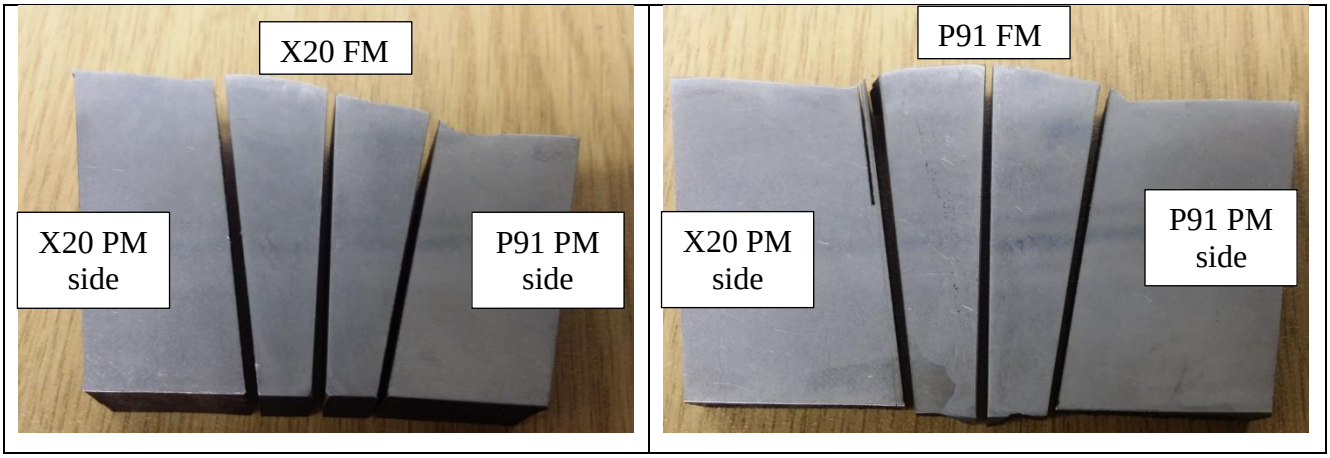


Figure 3.12: Photograph showing extraction of slithers where SPCT disc samples were removed.

To ensure that the samples from the HAZ were of the correct microstructure, the sectioned discs were ground incrementally. Both faces were polished and etched, and the surfaces were examined using light microscopy to ensure that the microstructure was similar on both sides (i.e. both front disc faces and rear disc face), and consistent with a fine-grained HAZ appearance. When the microstructure was not acceptable, the sample was ground further, and this process was repeated until acceptable microstructure was attained. The resultant microstructures (at a thickness of approximately 500 μm) are shown in Figure 3.13 and Figure 3.14 for X20 filler metal and P91 filler metal samples respectively.

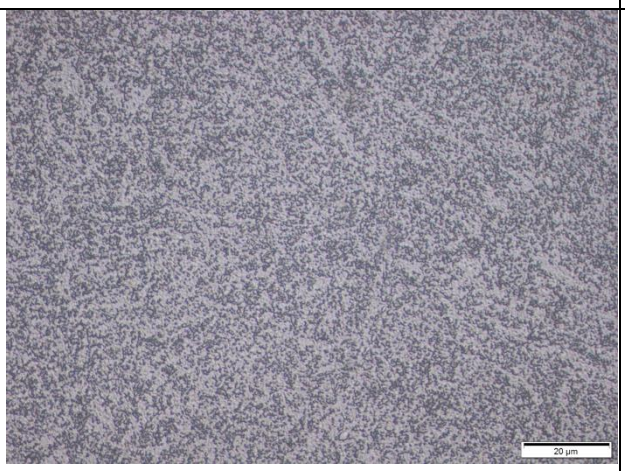
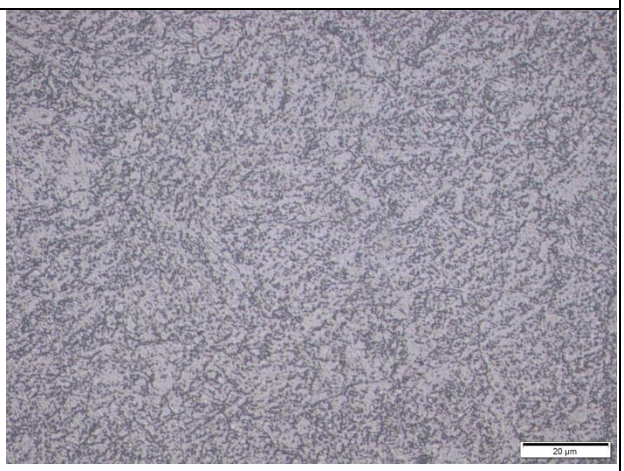
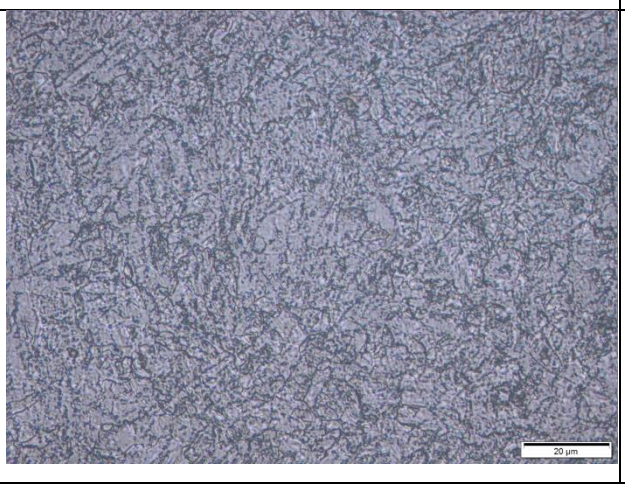
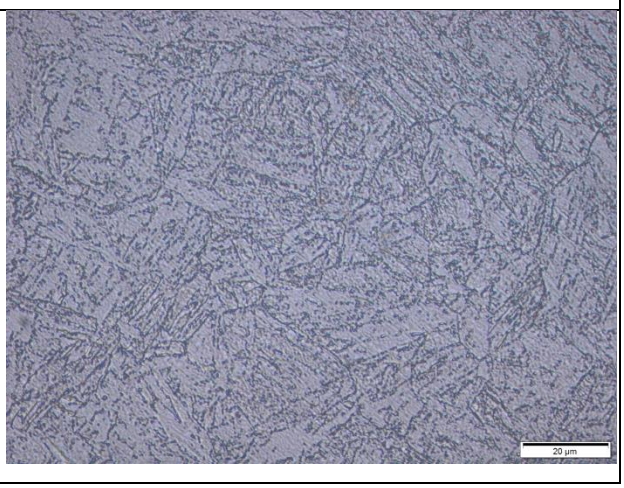
	Front Face (Side)	Rear Face (Side)
X20 FM / X20 HAZ		
X20 FM / P91 HAZ		

Figure 3.13: Micrographs showing the appearance of the microstructure on each side of the SPCT disc of the X20 weld filler metal samples, at a thickness of approximately 560 μm.

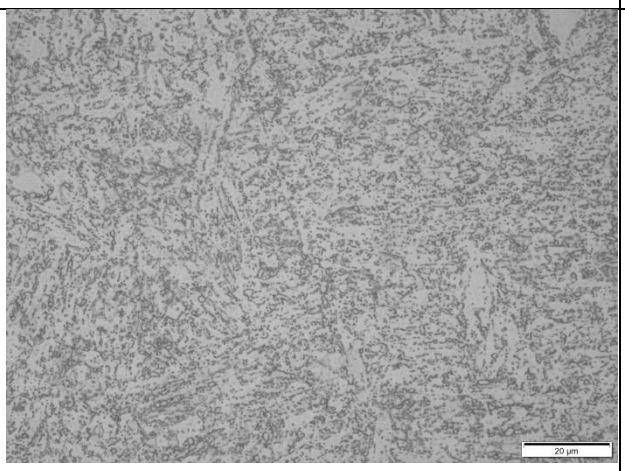
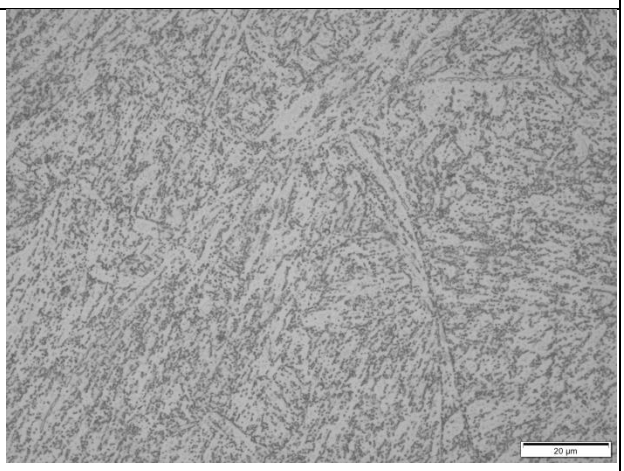
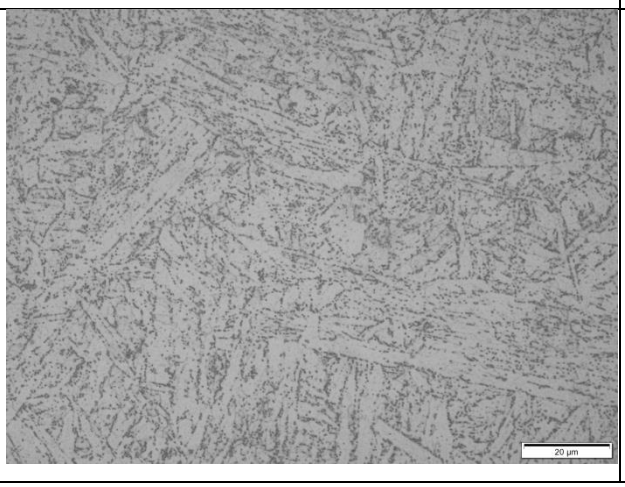
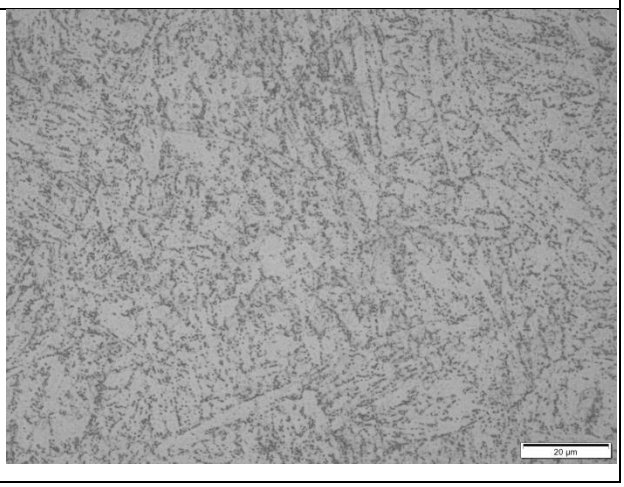
	Front Face (Side)	Rear Face (Side)
P91 FM / X20 HA Z		
P91 FM / P91 HA Z		

Figure 3.14: Micrographs showing the appearance of the microstructure on each side of the SPCT disc of the P91 weld filler metal samples, at a thickness of approximately 560 μm.

The samples were tested using the small punch creep testing (SPCT) machine at eNtsa at the Nelson Mandela University. Figures 3.15 - 3.17 show the SPCT machines that were used. These machines were developed by eNtsa at the Nelson Mandela University and hence the name; eNtsa NMU SPCT machine. The test parameters were chosen such that the P91 parent material would reach a rupture time of approximately 500 hrs. The test parameters were based on previous studies from previous research on P91 samples. The tests were carried out at a load of 276 N, and a temperature of 625°C.

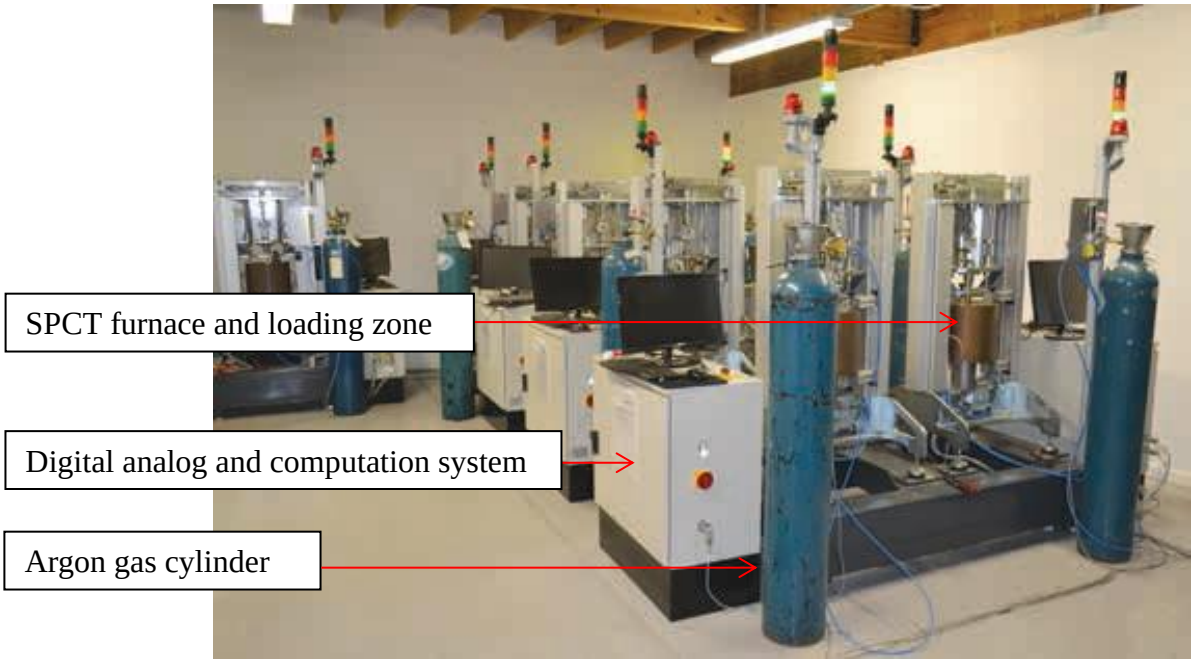


Figure 3.15: Photograph showing eNtsa's SPCT equipment facility that has 11 testing platforms in total at NMU.

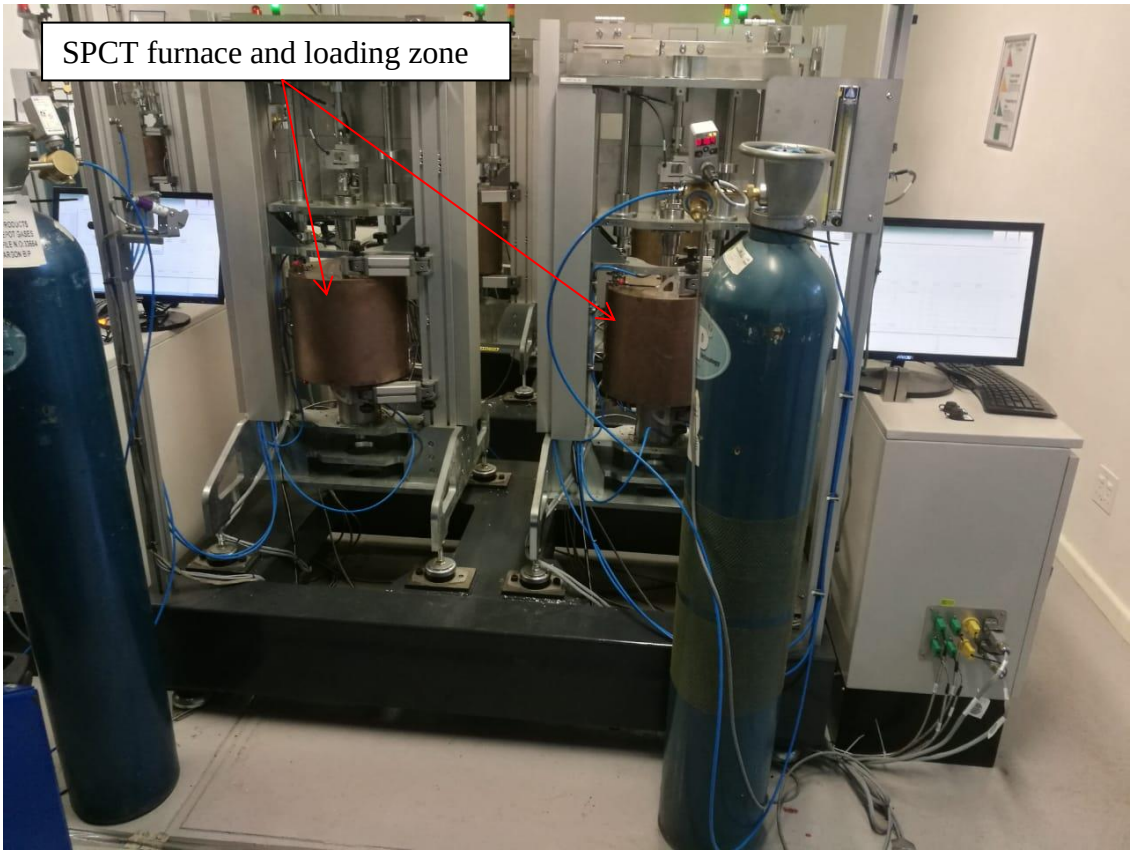


Figure 3.16: Photograph showing the close-up view of eNtsa's SPCT frames/equipment.

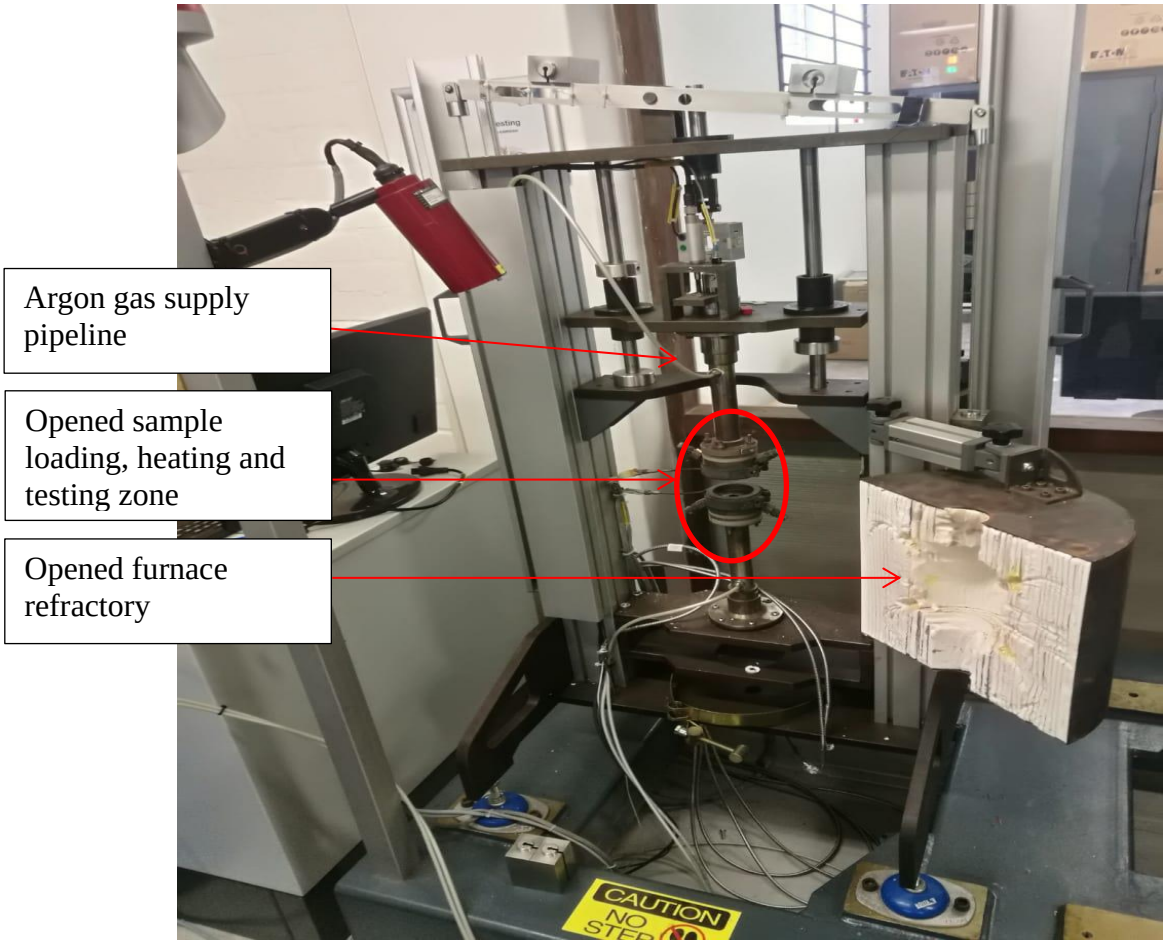


Figure 3.17: Photograph showing the close-up view of an opened eNtsa's SPCT equipment, indicating the sample loading and heating zone (furnace).

The SPCT was performed on the 8 different regions of the cross-weld samples at constant test temperature and load as shown in the test matrix in Table 3.7.

Table 3.7: Small Punch Creep Test Matrix

	Specimen No.	Temperature (°C)	Load (N)
P91 Parent Material	1	625	276
X20 Parent Material	2	625	276
P91 Weld Material	3	625	276
X20 Weld Material	4	625	276
P91 FGHAZ adjacent to P91 WFM	5	625	276
X20 FGHAZ adjacent to P91 WFM	6	625	276
P91 FGHAZ adjacent to X20 WFM	7	625	276
X20 FGHAZ adjacent to X20 WFM	8	625	276

3.9. Uniaxial Creep Test

Cross-weld and parent metal uniaxial creep tests were conducted using Applied Test Systems (ATS) 2330-CCM-230 Series 2330-CCM Lever Arm creep machines to assess the creep behaviour of the two dissimilar joints. The creep tests were conducted at 610°C, under the applied stress of 63 MPa and 80 MPa in an inert (argon gas) environment to avoid excessive high temperature oxidation. All these test conditions had duplicate tests except the X20 parent material as summarised by the test matrix in Table 3.9.

Table 3.7: Uniaxial Creep Test Matrix

	Specimen No.	Temperature (°C)	Stress (MPa)
X20 (X20CrMoV11-1) Filler weldment cross weld pipe	1	610	63
	2 (Duplicate)	610	63
	3	610	80
	4 (Duplicate)	610	80
P91 (X10CrMoVNb9-1) filler weldment cross weld pipe	5	610	63
	6 (Duplicate)	610	63
	7	610	80
	8 (Duplicate)	610	80
X20CrMoV11-1 Parent material pipe	9	610	80

The round tensile test specimens with 77 mm (length) × 10 mm (diameter) uniform gauge cross section was machined from the welded joints. Figure 3.18 shows the schematic representation of a creep test specimen.

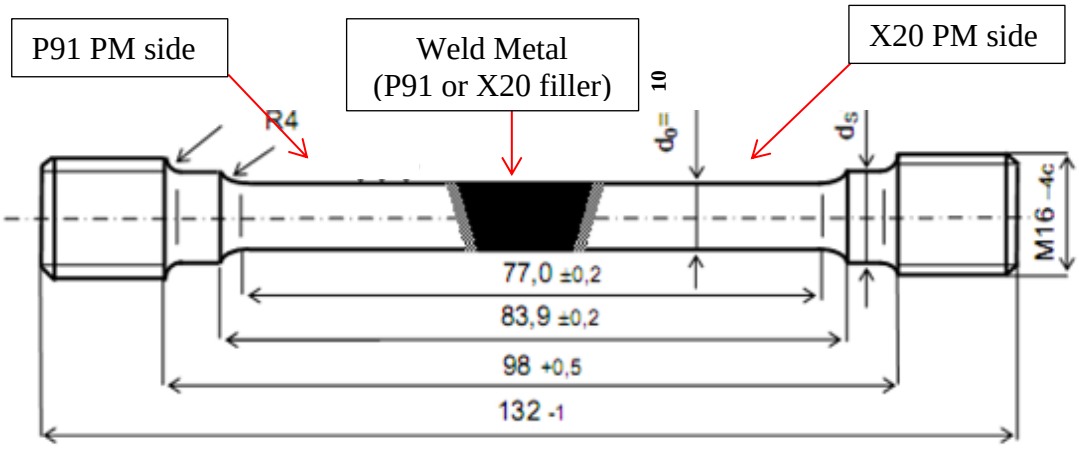


Figure 3.18: Schematic representation of a cross weld uniaxial creep test specimen showing the dimensional details in mm.

3.10. Microstructural Characterisation

The microstructural characterisation of dissimilar butt welds of creep aged X20 and virgin P91 steels pipes were studied in the laboratory using optical microscopy (OM), scanning electron microscopy (SEM), transmission electron microscopy (TEM) and X-Ray diffraction (XRD) techniques.

3.10.1 Optical microscopy

The objective of utilising the optical microscopy was to identify and evaluate the phase constituents and to count the creep voids (creep density) at 500X magnification. The evolution of creep voids during welding and creep testing was studied by evaluating creep voids on the BM, HAZ and WM.

3.10.2 Scanning Electron Microscopy

The scanning electron microscope with EDX (Energy Dispersive X-rays) was used to determine the composition of the phases and carbides present in the matrix. Scanning electron microscope (SEM) imaging was performed using secondary electrons (SE) and backscattered electrons (BSE) in a JEOL JSM 7001F instrument fitted with an X-Max 20mm^2 energy dispersive spectrometer (EDS) from Oxford Instruments.

The electron backscattered diffraction (EBSD) and transmission Kikuchi diffraction (TKD) data were collected using a Nordlys HKL high-sensitivity detector. Simultaneous EDS measurements were taken from the samples during the EBSD/TKD acquisition using the AZTec software from Oxford Instruments. The results were then processed using the Channel5 HKL software for the visualisation and exporting of the data.

3.10.3 Transmission electron microscopy (TEM)

Transmission electron microscopy was used to analyse the morphology of the carbide precipitates and sub-grains. This fulfilled the objective of analysing the dislocation networks.

Site-specific samples in the heat affect zones (HAZ), parent material (PM) and weld metal (WM) of each of the weldments were identified using optical microscopy on the etched surfaces. The 2 mm thick sections were removed from the HAZ using electro-discharge machining. These sections were then further sized down to 500 μm thickness followed by mechanical punching to remove 3 mm disks that were subjected to jet-poling using a 5% Perchloric acid – methanol solution to electron transparency. The samples were investigated using TKD-EDS, ADF-STEM, XRD, EBSD and BSE to measure the different microstructural features (i.e. precipitates, sub-grains/micro-grains and dislocations). For each sample, a TKD-EDS map of a single 10 × 10 μm area was collected, and 10× images (5×5 μm area) were taken using ADF-STEM for the sub-structure and dislocation analysis. EBSD bulk scans were performed on the surface (250 ×180 μm) using a step size of 0.2 μm on the jet-polished samples. The micro-grain size was measured from the EBSD data, using the minor axis (short-width) of elongated (aspect ratio > 2) micro-grains ($\Theta_c = 2°$) in the sample. Polished samples were sent for XRD analysis over the angular range of 20 – 100° 2Θ, this range included the three peaks for ferrite (α) iron. Whole pattern Rietveld refinement using TOPAS^{TM} was used to determine the crystallite size (L) and micro-strain broadening (ε_0) for each sample. These values were then used to calculate the free-dislocation density of the sample. The surface of the jet-polished samples was imaged using 5 kV backscattered images to investigate the presence of Laves phase, show the sub-structure of the micrograins and the location of the $M_{23}C_6$ and MX precipitates relative to the sub-structure.

Scanning electron microscope (SEM) imaging was performed using secondary electrons (SE) and backscattered electrons (BSE) in a JEOL JSM 7001F instrument fitted with an X-Max 20mm^2 energy dispersive spectrometer (EDS) from Oxford Instruments.

The electron backscattered diffraction (EBSD) and transmission Kikuchi diffraction (TKD) data were collected using a Nordlys HKL high-sensitivity detector. Simultaneous EDS measurements were taken from the samples during the EBSD/TKD acquisition using the AZTec software from Oxford Instruments. The results were then processed using the Channel5 HKL software for the visualisation and exporting of the data.

Low angle annular dark-field (ADF) images were collected from the jet-polished samples using a JEOL JEM 2100 LaB6 transmission electron microscope (TEM) in scanning mode (ADF-STEM) using a camera length of 40 cm.

3.10.4 X-ray diffraction

Dislocation densities in all samples were quantified by using a powder X-ray diffraction peak profile analysis. The samples were scanned from 20º to 120º degrees 2θ, to include the three peaks for ferrite (α) iron. A silicon powder reference sample was used to calibrate the instrument line broadening. TOPAS^{TM} software was used to apply whole pattern Rietveld refinement to determine the crystallite size (Crys-L) and micro-strain (ε_0) in the sample, from which the dislocation density was determined.

MIPAR^{TM} was used for the automatic thresholding and quantification of the different microstructural features from the various images collected on the electron microscopes.

CHAPTER 4

4. RESULTS AND DISCUSSION

4.1. Introduction

Chapter 4 presents the results and discussion of all tests, analyses and characterisation that were carried out in this study to determine the suitable weld filler for a butt weld of a creep aged X20 to virgin P91 pipe material. The results and discussion are presented in sections 4.2 – 4.8. Section 4.2 consists of NDT on fabrication of welds, 4.3 residual stress analysis, 4.4 mechanical testing ((both room temperature and hot tensile tests), hardness testing (i.e. macro, micro and nano-indentation hardness tests), Charpy impact tests), 4.5 microstructural characterisation (for both pre creep and post creep test conditions), 4.6 diffusion chemical analysis, 4.7 creep test (both uniaxial and small punch creep tests) and 4.8 microstructural characterisation after uniaxial creep testing.

4.2. Non-Destructive Testing (NDT) on fabrication of welds

Weldability of dissimilar creep strength enhanced ferritic (CSEF) such as the alloys used in this research study (X20 and P91), is influenced by both the metallurgical and non-metallurgical factors. These factors include composition of the parent and weld filler metals, mechanical properties, process parameters and restraint. These factors are qualified by performing weldability test during fabrication and during service (Abstoss *et al.,* 2019; David *et al.,* 2013).

Qualification of dissimilar welds forms an integral part of the welding procedures, choice of filler material and post weld heat treatment. The dissimilar welds between X20 and P91 were subjected to the standard

qualification process which included the performance of non-destructive and mechanical tests evaluation. The purpose of these tests was to make sure that the welded joints are sound with no defects and have the required strength and toughness. Ordinarily, welded joints are not defect free, hence acceptance criteria are used to determine if the defects are acceptable or not.

The three NDT methods that were used to evaluate the soundness of the fabricated welds are magnetic particle inspection (MPI), phase array ultrasonic testing (PA-UT) and radiography testing (RT). The different techniques were used because of their respective capabilities and limitations.

4.2.1 Magnetic Particle Inspection

Magnetic particle inspection was used to evaluate surface cracks with acceptance criteria according to DIN EN ISO23278 2010. The MPI results showed that there were no defect indications on both the X20 weld and the P91 weld joints at the time of inspection.

4.2.2 Phase Array Ultrasonic Testing (PA-UT) and Radiography Testing (RT)

Volumetric inspection of inner defects such as pore, internal cracks, and fusion were assessed using PA-UT and RT. The acceptance criteria guidelines were set out according to BS EN 1712 1997 for PA-UT, and BS EN ISO 5817 2014 for RT. Both PA-UT and RT also confirmed that the welded sample were acceptable in accordance with the NDT acceptance criterion specification. From the results obtained, it was concluded that both weldments were defect free.

The use of either X20 or P91 weld filler had no relevant recordable weld defects indications as revealed by the applied NDT (i.e. surface crack test and volumetric inspections) that was carried out on both butt welds pipe samples. The absence of relevant recordable indications on both butt welds pipe samples provided the assurance of the weld integrity of the joints and eliminated the uncertainty on the possibility of weld defects that could have a detrimental effect on weld performance test to be carried out. Both welds were acceptable in accordance with the NDT acceptance criteria specification.

4.3 Residual Stress Analysis

The thermal cycles induced during welding introduce residual stresses and distortion in welded joints (Ahmed *et al.,* 2018; David *et al.,* 2013). The challenge with residual stresses is that it affects the weld performance by increasing stress corrosion cracking, heat cracking and hydrogen induced cracking (David *et al.,* 2013). However, the detrimental effects presented by residual and triaxial stresses can be mitigated by performing post weld heat treatment (PWHT). Therefore, stress analysis was performed to analyse weldment residual stresses on the pipe weld joints of as welded and post weld heat treated samples. The residual stress measurement results were generated by using a laboratory X-ray diffraction technique with a Proto iXRD combo instrument by means of the $\sin^2\psi$ technique. The overall accuracy of the measurements, taking into account curve fitting and material properties was estimated at ± 50 MPa. The

limitation of X-ray diffraction for measuring residual stresses close to the surface is approximately < 0.025mm depth (Prevéy, 1986).

Figures 4.1 (a) and (b) depicts the plot of axial and hoop residual stresses of X20 weld and the P91 weld before heat treatment. From the plots it was observed that the parent material was under tension whilst the weld was under compressive stresses. This observation is similar to that of a finite element analysis study of the residual-stress level analysis on the circumferential weld constructed by multi-pass welding on a stainless sample (Brikstad *et al.*, 1998), which showed that as the number of weld passes increased the residual stress on the outside surface can go into compression. The average compressive stresses in the X20 and P91 welds were -185 MPa and -148 MPa, respectively.

The as-welded samples were subjected to PWHT, with the intention of improving mechanical properties such as hardness, creep strength and toughness, and prevent premature Type-IV cracking (Pandey *et al.*, 2019; Wang *et al.*, 2018).

Results presented in Figures 4.2 (a) and (b) show the response of the welded joints after PWHT. From the figures, it was evident that PWHT led to a substantial reduction in both the compressive and tension stresses in the welded joints. The compressive stresses in the X20 and P91 weld joints were reduced to -52 MPa and -43 MPa, respectively after heat treatment.

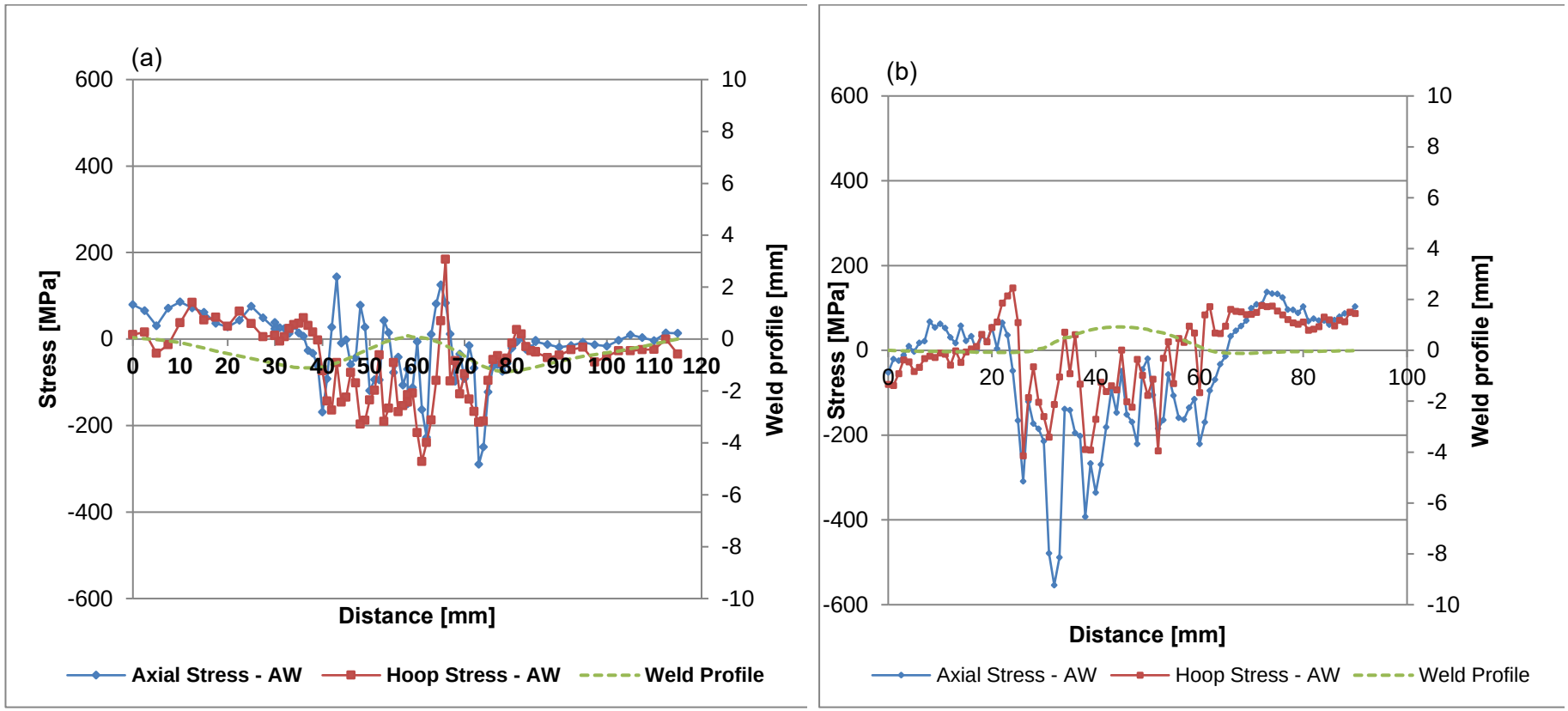


Figure 4.1: Residual axial and hoop stress measurement profile on as welded condition for X20 to P91pipes welded with (a) X20 weld filler and (b) P91 weld filler.

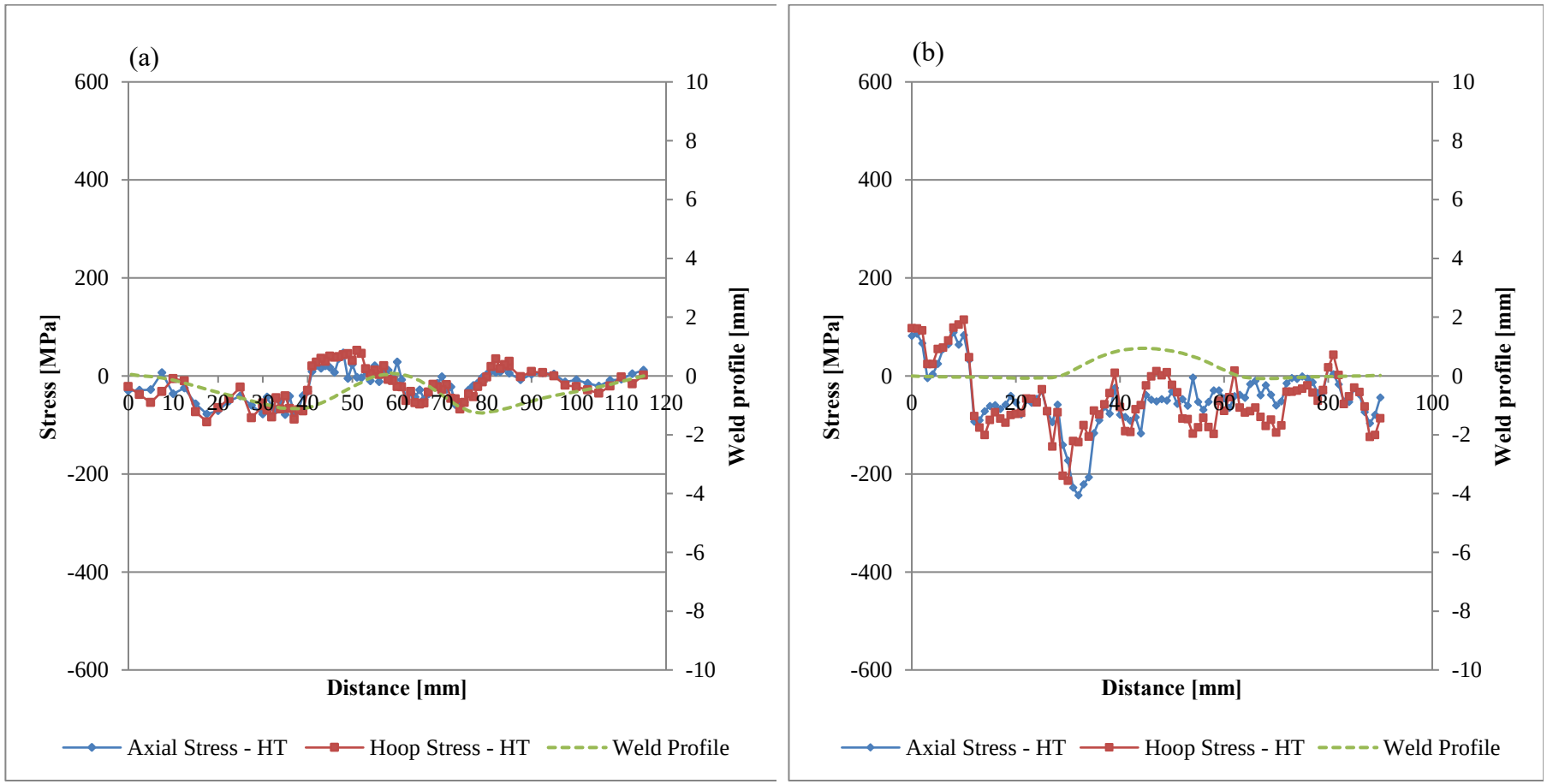


Figure 4.2: Residual axial and hoop stress measurement profile on as heat treated condition for X20 to P91pipes welded with (a) X20 weld filler and (b) P91 weld filler.

Based on the results of this residual stress analysis, there is no significant differences in the stresses found in the two cross welds. Both weld fillers had the same residual stress distribution effects across the welded joints. This could have been due to the fact that X20 and P91 have similar properties and are therefore comparable.

4.4 Mechanical Testing

Mechanical tests were conducted to assess the soundness of the weld joint, and to evaluate the effect of PWHT. Mechanical tests results presented in this section include hardness, room temperature tensile, hot tensile and impact tests.

4.4.1 Hardness Test

Macro and micro hardness tests were carried out across the weldments on the 1 μm polished surface finish. The hardness traverses were carried out across the weldment joint from X20 parent material side to P91 parent material side as illustrated in Figure 4.3.

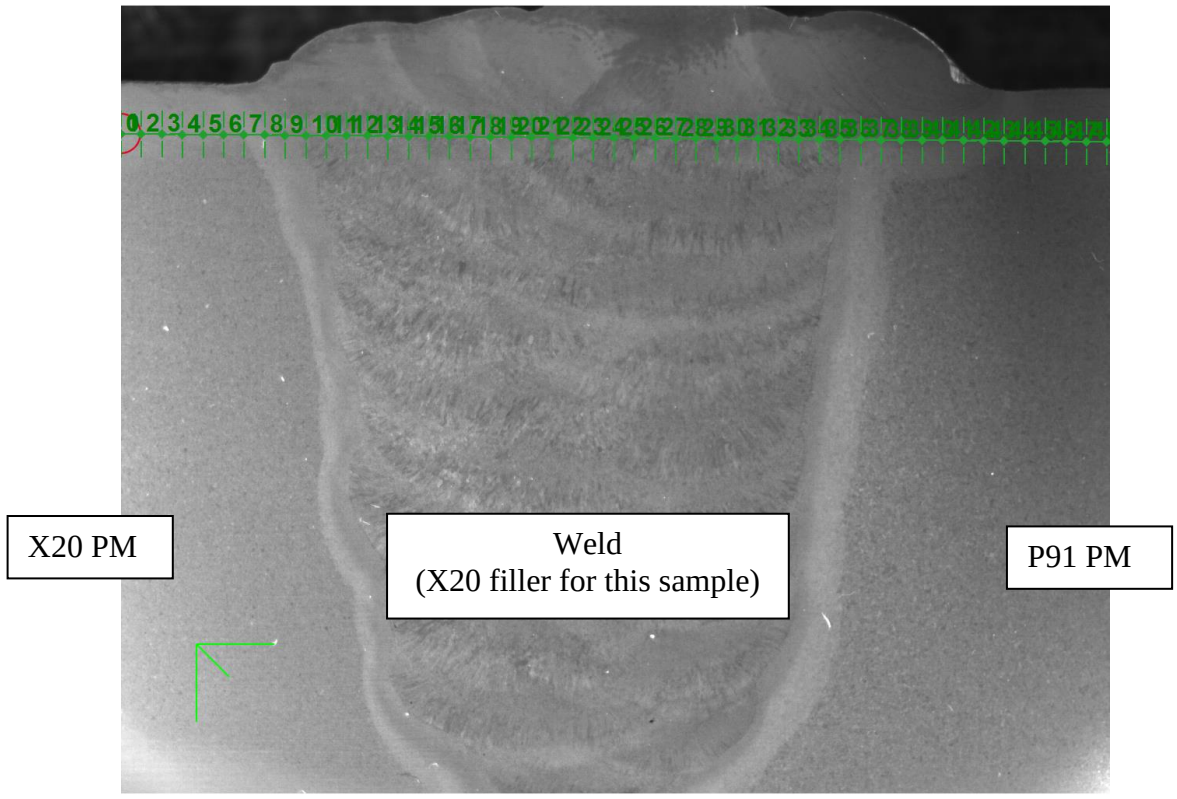


Figure 4.3: Photograph of the etched cross weldment showing hardness traverses tests indentations carried out from creep aged X20 PM side (LHS) to the virgin P91 PM side (RHS).

4.4.2 Macro Hardness Test

The hardness traverse results are shown in Figure 4.4. Macro hardness variations were observed in the different regions across the welded joint. For X20 weld filler sample the maximum hardness recorded in the HAZ region was 255 HV_{10} whilst the hardness in the weld metal was 262 HV_{10}. The reported hardness

values are within the required specification limit of less than 300 HV for EN 10216-2:2002+A2:2007 (E) code.

The maximum hardness for P91 weld filler sample was 264 HV_{10} in the HAZ, and 240 HV_{10} in the weld metal. The hardness values in the HAZ and the weld metal are within the required specification limit of 280 HV_{10} for P91 material according to the EN 10216-2:2002+A2:2007 (E) code. The hardness values obtained on the X20 PM averaging at 238 HV_{10} was within the required specification (216 – 257 HV_{10}) for EN 10216-2:2002+A2:2007 (E) code. The hardness value of P91 PM was recorded as 206 HV_{10} and was within the required specification of 194.84 - 254.84HV_{10} for EN 10216-2:2002+A2:2007 (E) code.

It is worth noting that the hardness of X20 PM is higher than the hardness of P91 PM. The difference in hardness values between X20 and P91 parent materials can be attributed to high carbon content in X20 (C = 0.16 wt.%) while P91 has lower carbon content of 0.09 wt.% (Bròzda and Zeman, 2003). From the macro hardness results it was deduced that the PHWT was effective in tempering the microstructure of the weldments.

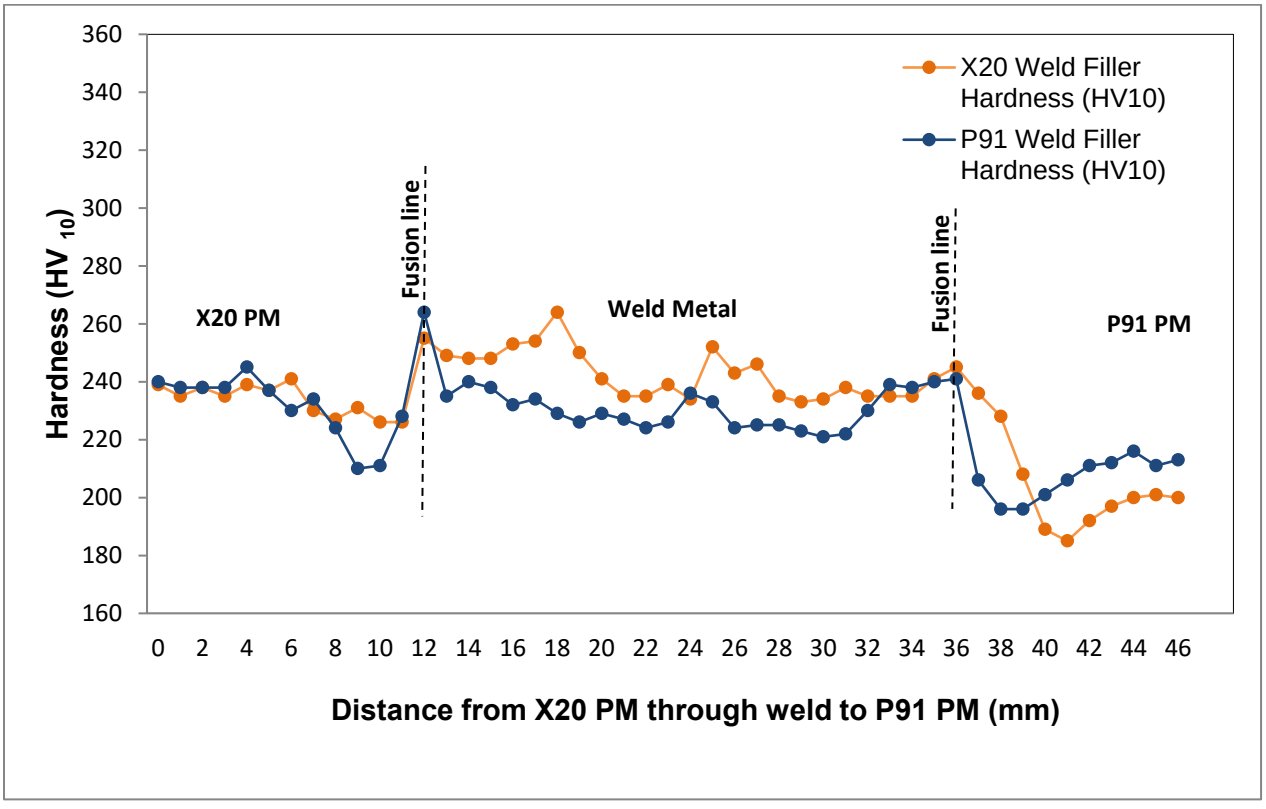


Figure 4.4: Macro hardness traverse for both X20 and P91 weld filler cross weld joints**.**

Based on the results of these macro hardness tests, there are no observed significant differences between X20 and P91 weld filler cross weld joint samples. Both weld fillers had the comparable hardness profile across the welded joints.

4.4.3 Micro Hardness Test

Microhardness was carried out using a 300 gf Vickers load and the hardness results are shown in Figure 4.5. The hardness indentation spacing intervals was set at 0.5 mm on the PM (Parent Material) and the WM (Weld Metal). However, on the HAZ region, the indentation intervals were minimised to 0.25 mm so that the hardness of all the different HAZ zones (i.e. coarse-grained (CGHAZ), inter-critical (ICHAZ) and fine-grained (FGHAZ) heat affected zone) were measured.

The lowest hardness value of 224 HV was obtained in the X20's ICHAZ that was welded using the X20 weld filler, whilst the hardness of 226 HV was recorded on the X20's ICHAZ that was welded using P91 weld filler. On the P91 ICHAZ side, for both weldment samples (i.e. (i) with X20 filler weldment and (ii) with P91 filler weldment), similar hardness value of 188 HV was obtained. The soft zone in the ICHAZ was due to partial austenitisation during welding whereas the remaining tempered martensitic structure was over-aged as a result of the welding thermal cycle experienced by the joint and subsequent PWHT (Paddea *et al*., 2011). The thermal cycles and PWHT induced a relatively soft microstructure which lost its strengthening mechanism due to the dissolution of carbo-nitrides which are essential for creep resistance (Paddea *et al*., 2011; Zhang *et al*., 2000).

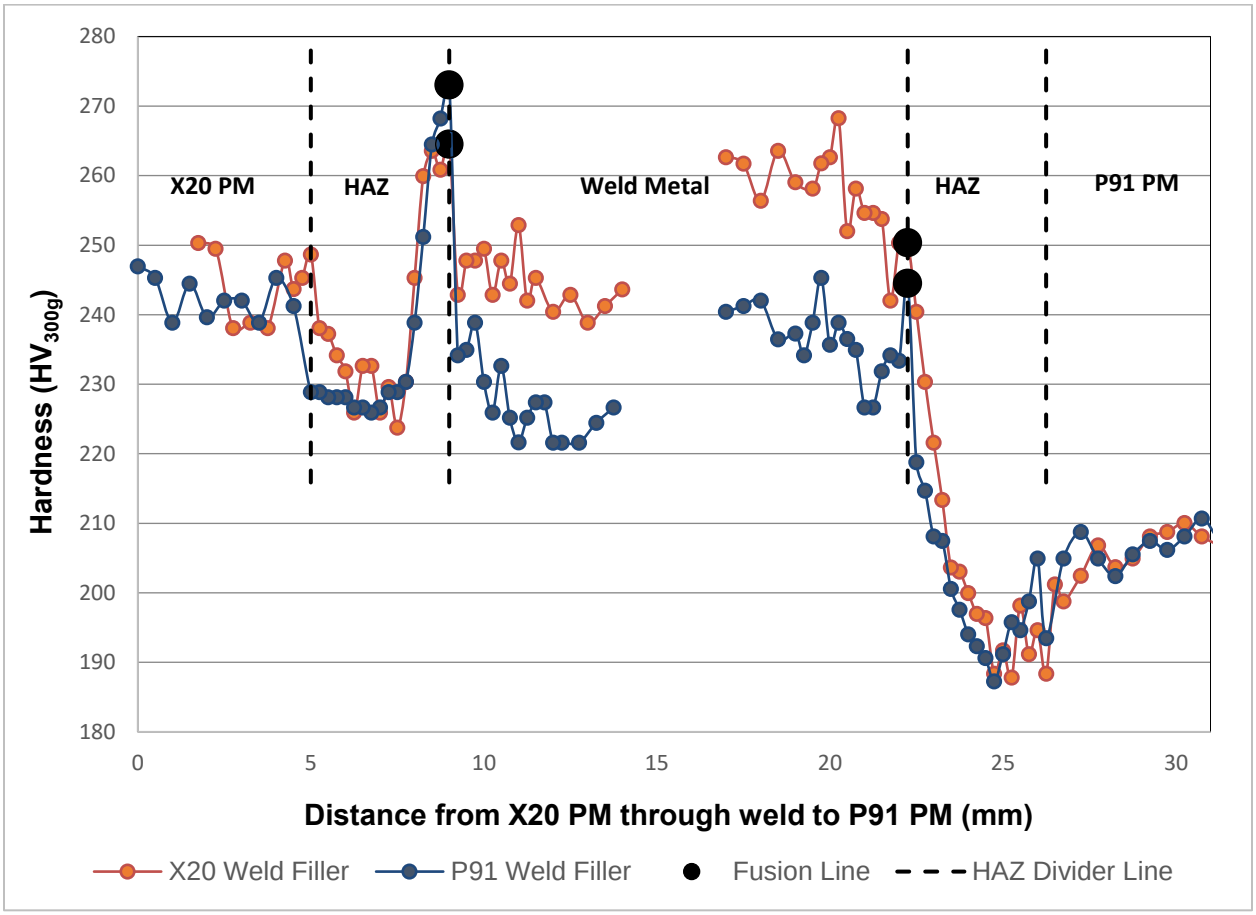


Figure 4.5: Micro hardness traverse for both X20 and P91 weld filler across weld joints.

Based on the results of the micro hardness tests, both X20 and P91 weld filler cross weld joints have comparable hardness profile. It is therefore conclusive that both weld fillers have similar effect on the hardness trends for the HAZ and PM.

4.4.4 Tensile Test

Tensile tests were carried out on two cross weld test pieces (creep aged X20 and virgin P91) using either X20 or P91 weld filler. The test was carried out to evaluate the strength performance of the X20 and P91 weld metals. The typical tensile stress vs strain curves of high strength and ductility materials obtained during tensile testing is shown in Figure 4.6.

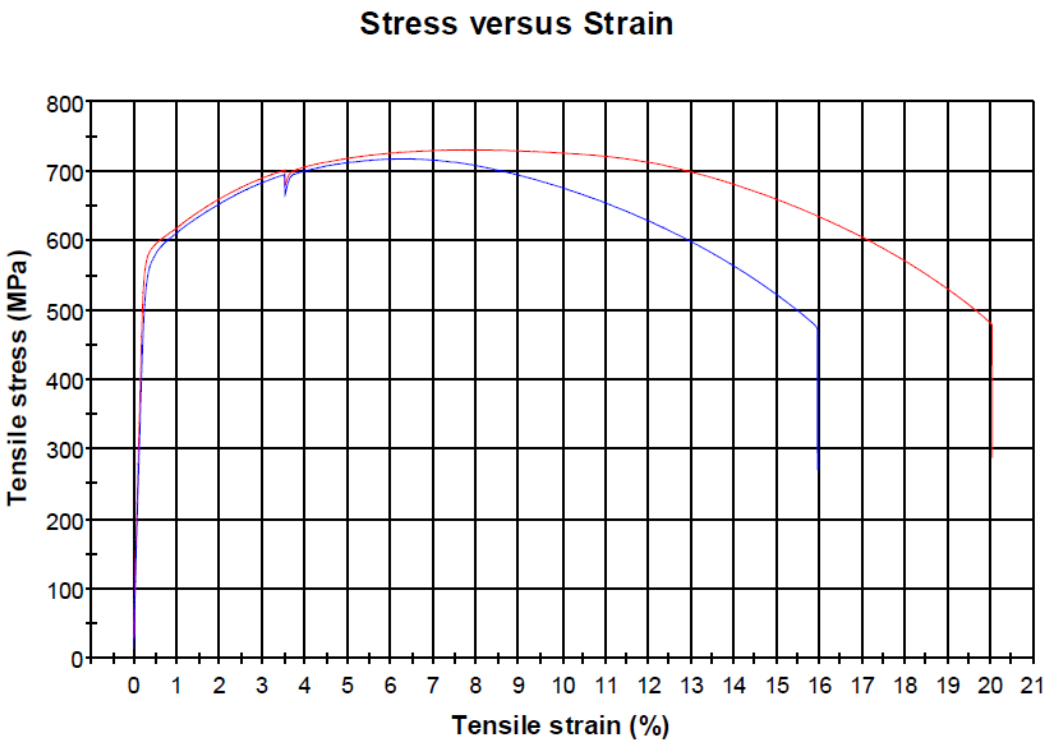


Figure 4.6: Mechanical tensile stress vs tensile strain curves typical of high strength and high ductile materials after post weld heat treatment (Example from X20 weld filler cross weld sample tested at 21°C with its duplicate sample).

The tensile test results of all 3 test conditions (21°C, 500°C and 550°C) are presented and discussed under the following subsections.

4.4.5 Room Temperature (21°C) Tensile Test

The results of room temperature tensile test are shown in Figure 4.7. The resultant ultimate tensile strength (UTS) measured was 738 MPa and 724 MPa for the X20 and P91 filler welded samples, respectively. The UTS results conform to the requirements of EN 10216 code (BS EN 10216-2, 2013) in which X20 has UTS ranging between 690 – 840 MPa, and P91 has UTS of 630 – 830 MPa. The measured yield strength of X20 filler welded sample and P91 filler welded sample was 576 MPa and 584 MPa, respectively. The yield strength of both samples conforms to the requirements of EN 10216-2:2013 (E) code (BS EN 10216-2, 2013) which specify yield strength ≥ 490 MPa for X20 PM and ≥ 450 MPa for P91 PM. The slight difference in tensile strength results between X20 and P91 filler welded sample is considered to be within the same scatter band.

Tensile rupture occurred at the P91 PM side of the weldment on both samples and these findings agree with EN 10216 code (BS EN 10216-2, 2013) considering that P91 PM has lower tensile properties compared to X20 PM. The difference in tensile properties can be attributed to lower carbon content of the P91 PM. The tensile properties are consistent with the results obtained from hardness traverses.

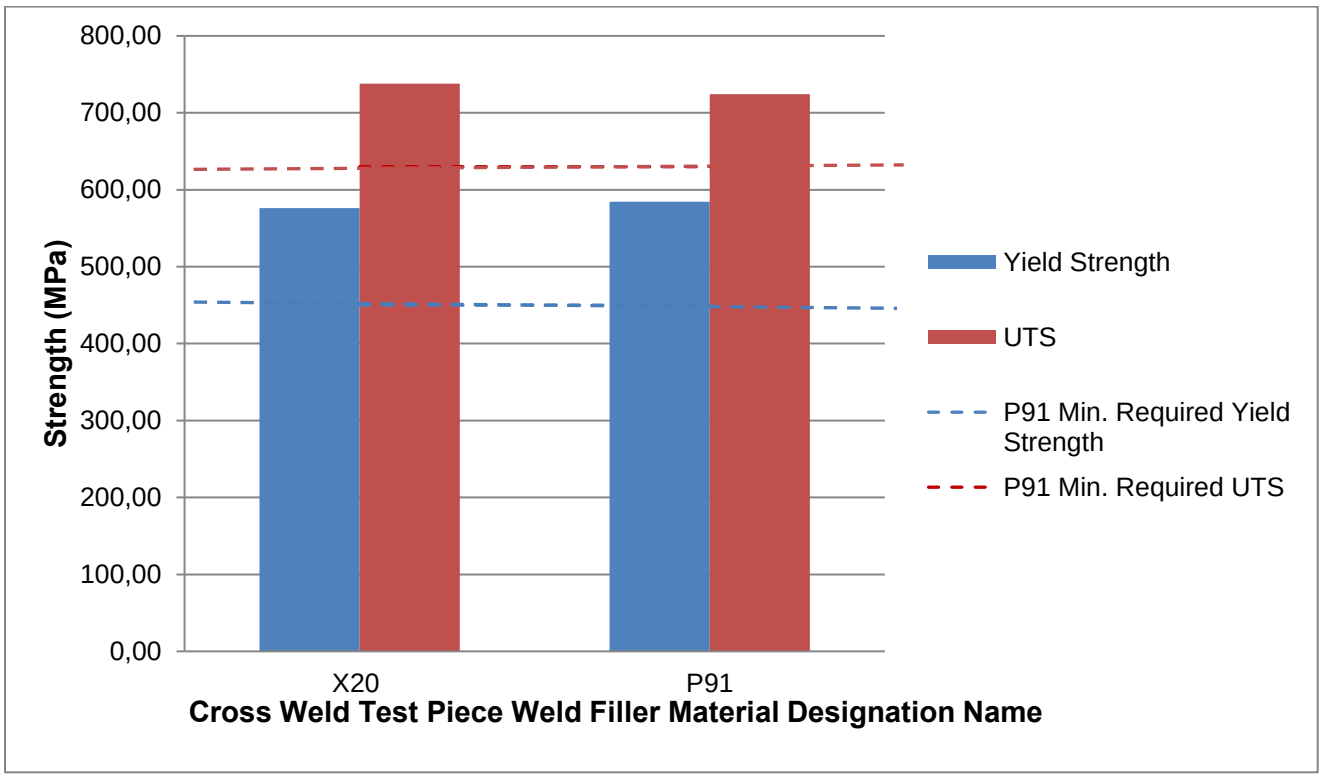


Figure 4.7: Room temperature (21°C) yield strength and UTS for both X20 weld filler cross weld specimen (on the left hand side) and P91 weld filler cross weld specimen (on the right hand side).

The fracture surface of the test specimens was typical of a ductile fracture mode with an appearance of partial ductility (low /limited ductility) morphology with a dull greyish colour appearance as shown in Figure 4.8. This limited ductility appearance is consistent with the obtained tensile test area reduction of 5% and the elongation of 11%. The limited ductility can be attributed to room temperature test.

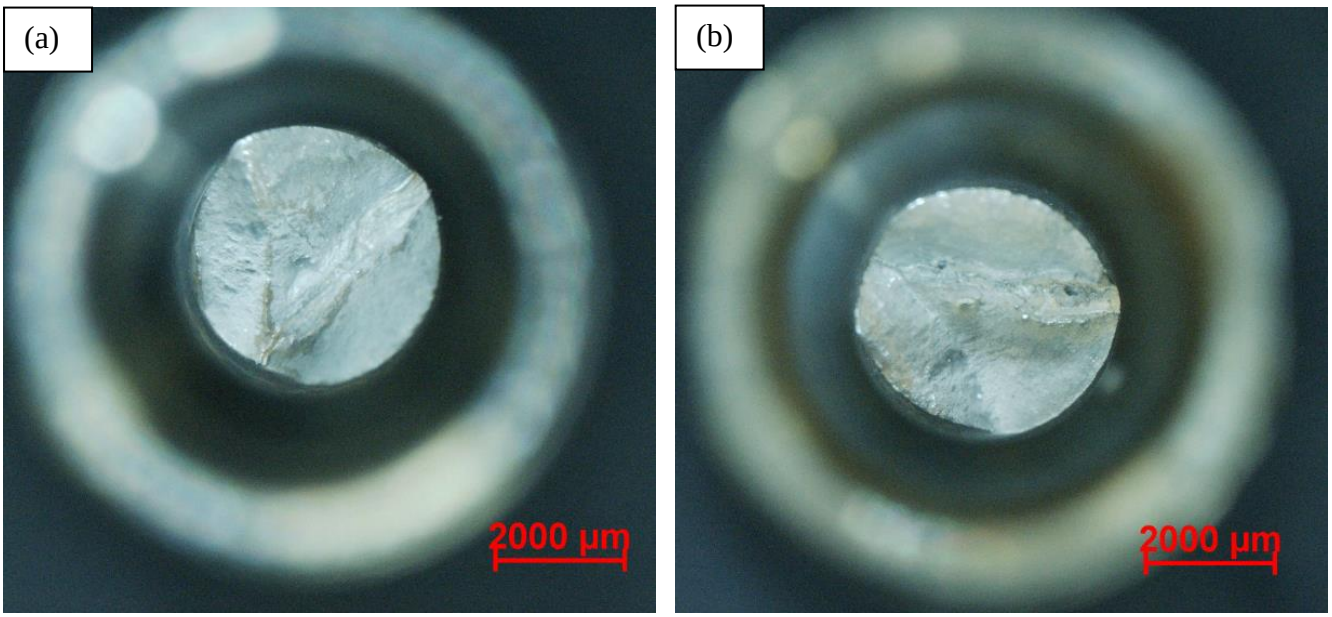


Figure 4.8: Fracture surface image of the room temperature tensile tested specimen with the appearance of partial ductile (low / limited ductility) morphology with a dull (greyish) colour appearance (a) Fractured half sample (towards X20 PM side, (b) Fractured half sample (towards P91 PM side).

The tensile test results at room temperature (21°C) revealed that both X20 filler and P91 filler are quite comparable to fuse with creep aged X20 PM and P91 PM. Consequently, there is no apparent evidence that can be used to choose one filler over the other. Moreover, the tensile rupture did not occur on either the weld material, HAZ regions or the service exposed X20 parent material, it consistently occurred on the P91 parent material as a result of its design of lower mechanical strength at lower temperature as compared to X20 parent material. Therefore, there is no observed distinct effect on using either X20 or P91 weld filler with respect to mechanical properties performance.

4.4.6 Hot Tensile (500°C) Test

Figure 4.9 show the results of hot tensile tests that were carried out at 500°C. The measured resultant yield strength (YS) for X20 filler welded sample and P91 filler welded sample were 409 MPa and 412 MPa, respectively. The UTS results reported for X20 and P91 filler welded samples were recorded at 452 MPa and 457 MPa, respectively. The hot tensile properties of both samples conformed to the specification requirements of EN 10216-2:2013 (E) code (BS EN 10216-2, 2013) which specify the yield strength ≥ 290 MPa for X20 parent material and ≥ 319 MPa for P91 parent material.

Tensile rupture occurred on the X20 parent material location on both samples and these findings agree with EN 10216-2:2013 (E) code considering that at elevated temperatures (500°C) X20 parent material has lower tensile strength than P91 parent material (BS EN 10216-2, 2013). This can be attributed to higher thermal stability of P91 material as compared to X20 due to the optimised chemical composition of P91 material for high temperature application (Iseda *et al.*, 1988; Masuyama, 2000). The minor difference of tensile strength results between X20 and P91 filler welded sample is considered to be within the same scatter band. These results revealed that there is no effect on using either X20 or P91 weld filler material on the tensile strength of these dissimilar cross weld samples.

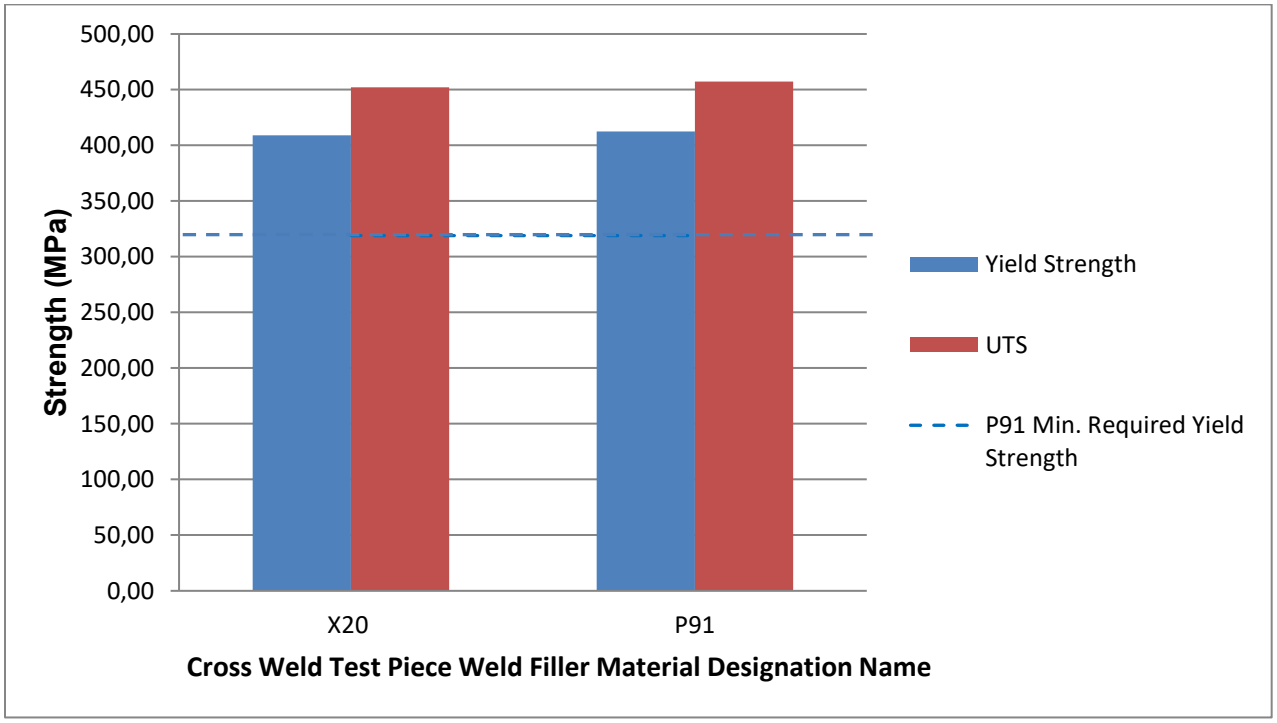


Figure 4.9: Yield strength and ultimate tensile strength for X20 (on the left hand side) and P91 (on the right hand side) weld filler cross weld specimens at 500°C

The fracture surface of the investigated samples was typical of a ductile fracture mode and has a cup and cone shape with dull (greyish) colour appearance as shown in Figure 4.10. This apearence of high ductility is in agreement with the obtained tensile test reduction in area (70%) as well as the elogation (14%).

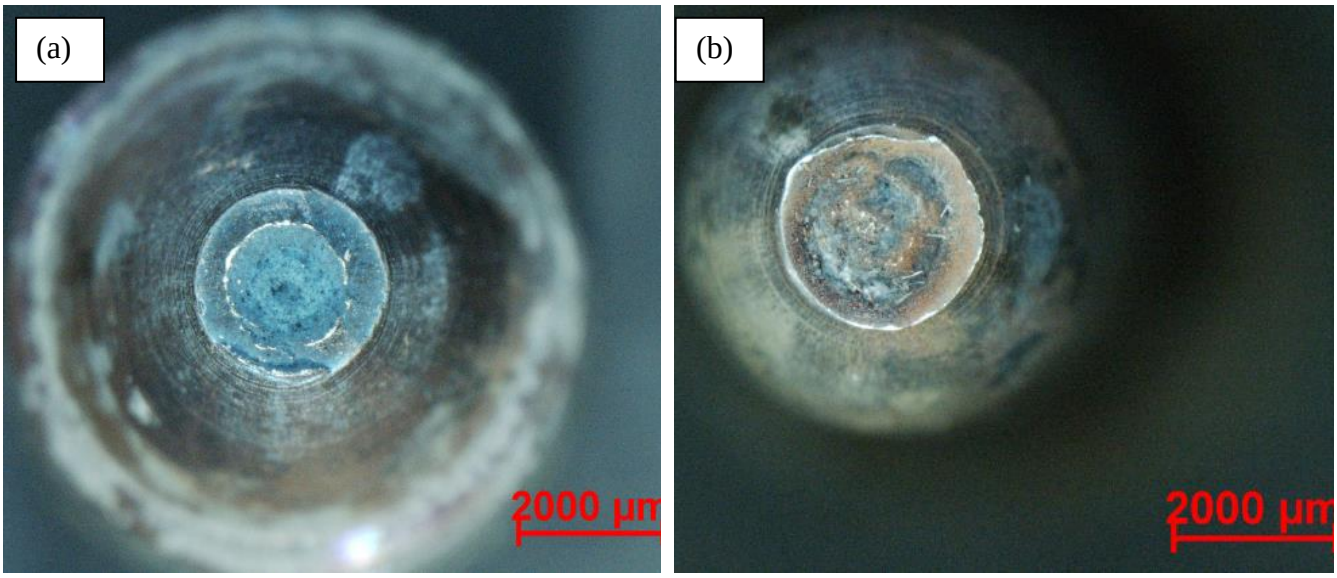


Figure 4.10: Fracture surface stereo image of the 500°C hot tensile tested specimen showing cup and cone shape with dull (greyish) colour appearance (a) Fractured half sample (towards X20 PM side, (b) Fractured half sample (towards P91 PM side).

Based on these high temperature (500°C) tensile test results, it is conclusive that both X20 filler and P91 filler are quite comparable to fuse with creep aged X20 PM and P91 PM. There is no effect on using either X20 or P91 weld filler material on the tensile strength of these dissimilar cross weld samples.

4.4.7 Hot Tensile (550°C) Test

Figure 4.11 show the results of hot tensile tests that were carried out at 550°C. The measured yield strength is 352 MPa and 353 MPa for X20 filler welded sample and P91 filler welded sample, respectively. The measured resultant ultimate tensile strength (UTS) is 413 MPa and 404 MPa for X20 filler welded sample and P91 filler welded sample, respectively. Both samples conform to the requirements of EN 10216-2:2013 (E) code (BS EN 10216-2, 2013) which specify the yield strength ≥ 250 MPa for X20 parent material and ≥ 270 MPa for P91 parent material.

Tensile rupture occurred on the X20 parent metal location on both samples and these findings are supported by the EN 10216-2:2013 (E) code considering that at elevated temperatures (500°C) the X20 parent metal has lower tensile strength than P91 parent metal (BS EN 10216-2, 2013). This can be attributed to higher thermal stability of P91 material as compared to X20 due to the optimised chemical composition of P91 material for high temperature application. The small difference of tensile strength results between X20 and P91 filler welded sample is considered to be within the same scatter band. These results revealed that there is no effect on using either X20 or P91 weld filler material on the tensile strength of these dissimilar cross weld samples since none of the tensile rupture occurred on neither the weld material nor HAZ regions.

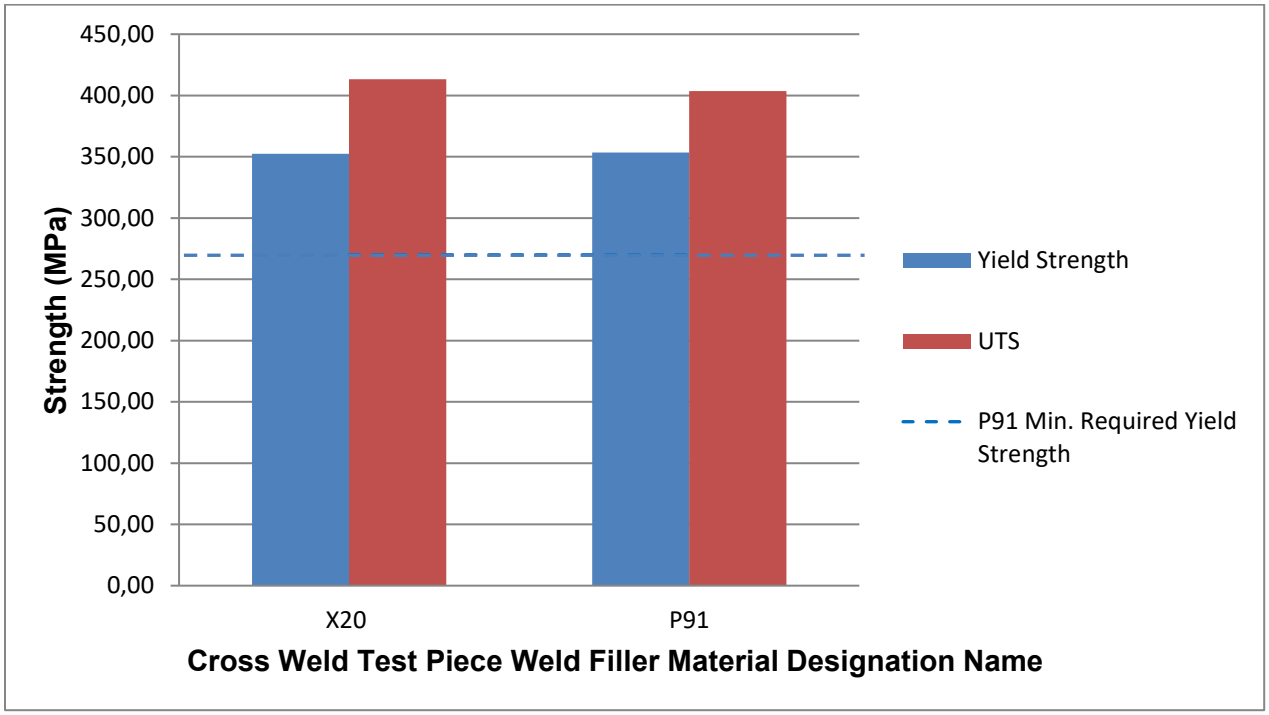


Figure 4.11: Yield strength and UTS for X20 weld filler cross weld specimen (on the left hand side) and P91 weld filler cross weld specimen (on the right hand side) at 550°C.

The fracture surface is typical of a ductile fracture mode and has a cup and cone shape with dull (greyish) colour appearance as shown in Figure 4.12. The obtained tensile test reduction in area of 79% as well as the elongation of 15% are consistent with this ductile fracture surface appearance.

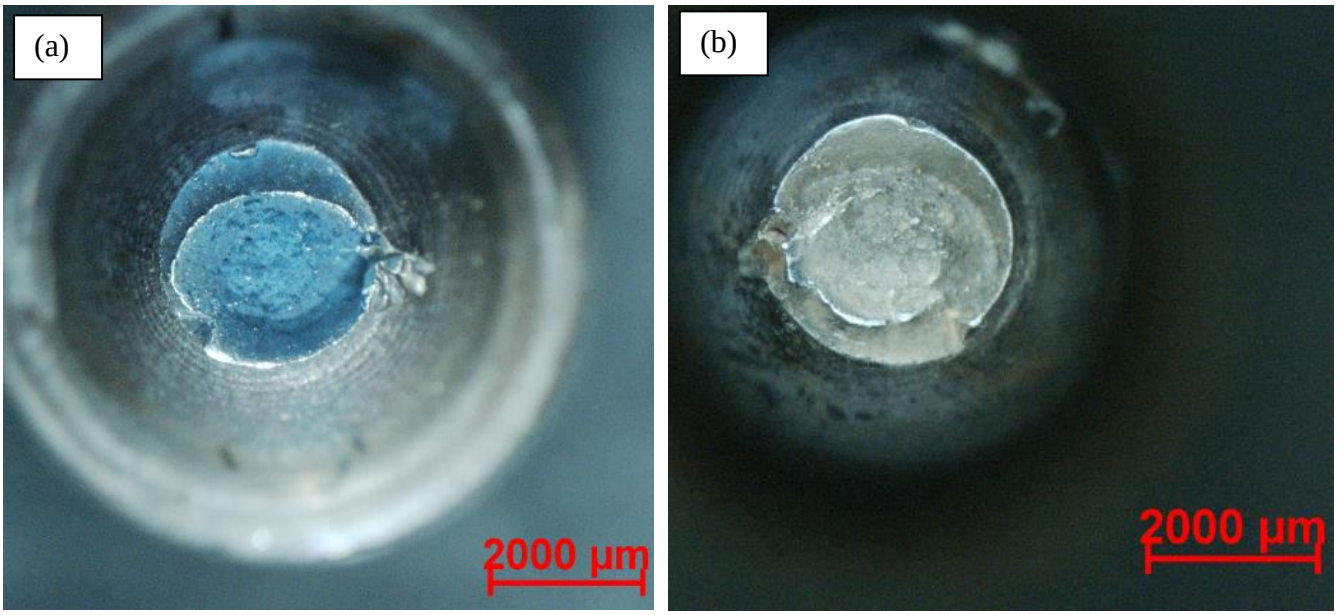


Figure 4.12: Fracture surface stereo image of the 550°C hot tensile tested specimen showing cup and cone shape with dull (greyish) colour appearance (a) Fractured half sample (towards X20 PM side, (b) Fractured half sample (towards P91 PM side).

In summary based on the results from 3 tensile test conditions (21°C room temperature, 500°C and 550°C) that were carried out, the strength performance of both cross welds samples fused by either X20 or P91 weld metals is satisfactorily meeting the code requirements (BS EN 10216-2, 2013). As expected and in line with literature (Xiong and Liew, 2020), the tensile strength decreased with an increase in test temperature (i.e. UTS at room temperature was ranging from 724 – 738 MPa, at 500°C UTS ranged between 452 – 457 MPa, and at 550°C UTS was 404 – 413 MPa. Similar trend was also observed on the yield strength as illustrated in Figure 4.13.

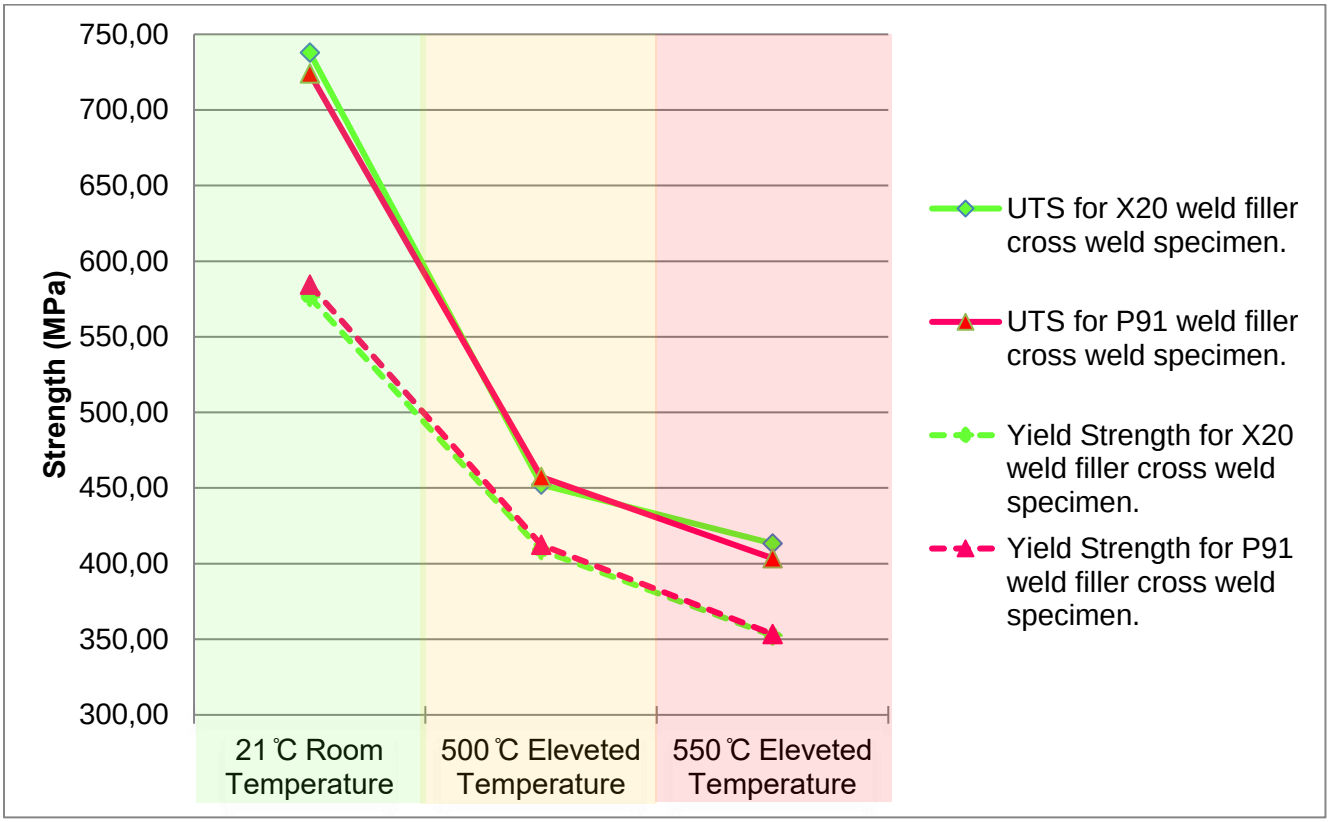


Figure 4.13: Mechanical tensile test results as a function of change in test temperature conditions (21℃, 500℃ and 550℃) for cross weldment fused by X20 and P91 weld filler material.

There was no noticeable difference on strength performance when comparing the results for both dissimilar cross weldment fused by either X20 or P91 weld filler material. None of the tensile rupture occurred on the weld material or on HAZ regions. All tensile rupture occurred on the parent material that has the lower mechanical strength at the specific test temperature (BS EN 10216-2, 2013). Therefore, it is conclusive that based on the mechanical tensile test results, both weld fillers (X20 and P91) are compatible to fuse the virgin P91 to creep aged X20 materials.

4.4.8 Charpy Impact Toughness

Charpy impact tests were carried out to study and compare impact toughness for both welded joints. The specimens tested were notched in the weld metal. The results revealed that impact toughness (energy absorbed) of P91 weld material (50 J) is higher than the energy absorbed by X20 (44 J) weld material by 12% as shown in Table 4.1. This is attrubuted to the higher carbon content of the X20 weld metal (0.12 wt % C) compared to P91 weld metal (0.09 wt % C) (Bròzda and Zeman, 2003). Both X20 and P91 weld filler metals did meet the specified minimum absorbed energy of 35 J and 47 J respectively as per the Böhler welding technical handbook (Böhler welding, 2009).

Table 4.1: Room temperature (21°C) Charpy impact test results for X20 weld filler and P91 weld filler cross welds vs Böhler welding technical handbook (Böhler welding, 2009).

Weld Sample	**Test Results, Total Energy Absorbed (J)**	**Bohlër Welding Specification Required Energy Absorbed (J)**
X20 Weld Filler (Böhler Fox 20MVW)	44	≥ 35
P91 Weld Filler (Böhler Fox C9 MV)	50	≥ 47

The fracture surfaces for both tested specimens are typical of a ductile fracture mode and have a cup and cone morphology, with dull (greyish) colour appearance as shown in Figure 4.14.

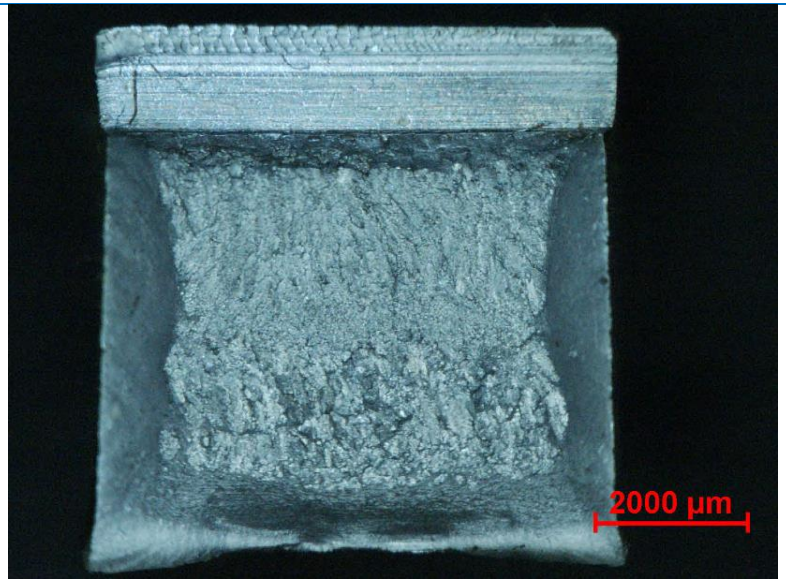
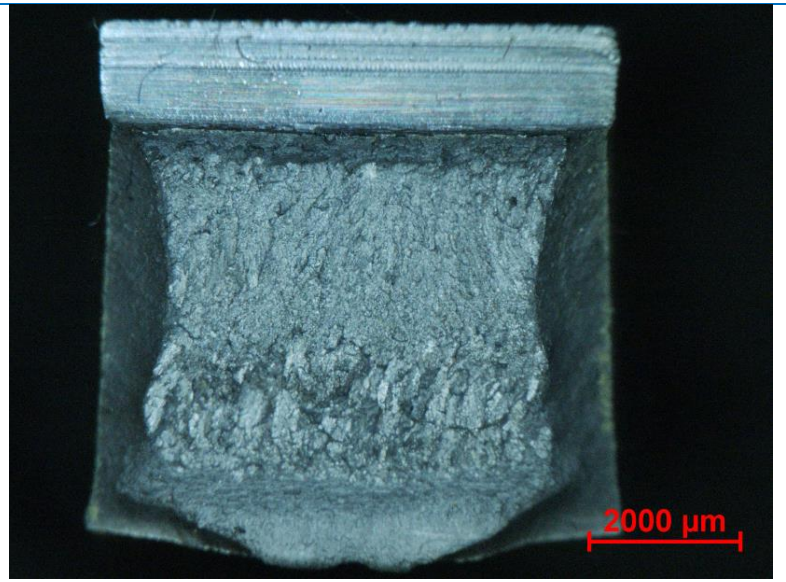
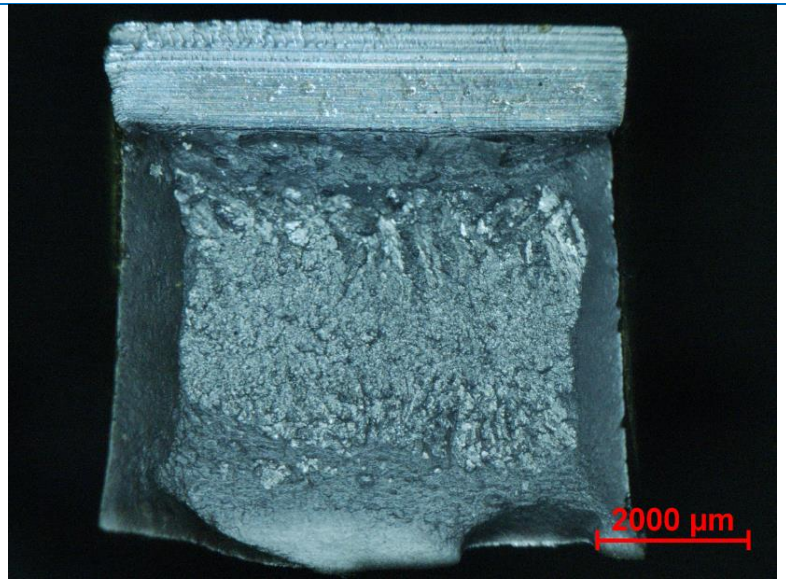
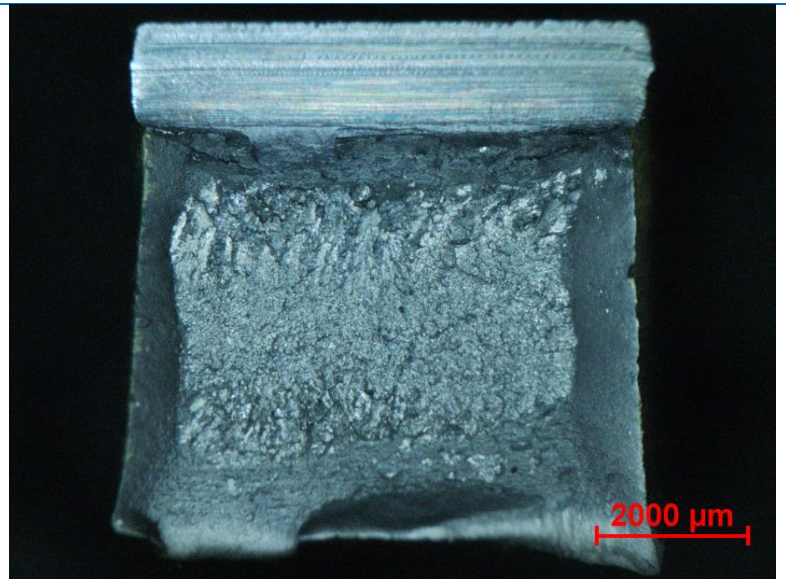
	LHS Fractured Half Sample (Towards X20 PM Side)	RHS Fractured Half Sample (Towards P91 PM Side)
X20 Weld Filler Metal Sample		
P91 Weld Filler Metal Sample		

Figure 4.14: Stereo microscope images of impact fracture surfaces filler metals showing features of ductile fracture; dull grey colour with cup and cone morphology appearances.

4.5 Microstructural Characterisation

This section presents microstructural characterization of the X20 filler and P91 filler welded materials after PWHT, but before creep testing. Areas of interest that were analysed are the base metal, weld metal and the heat affected zone.

4.5.1 Microstructural Characterisation of Post-Weld Heat Treated Weldments

Microstructural characterization was carried out on weldment samples after PWHT to quantify the microstructural parameters contributing to creep strength. Specific locations (of the cross weldments) were carefully selected for the analysis. Site-specific samples in the heat affect zones, parent metals and weld metal of each weldment were identified using optimal microscopy, on etched surfaces as show in Figures 4.15 – 4.18.

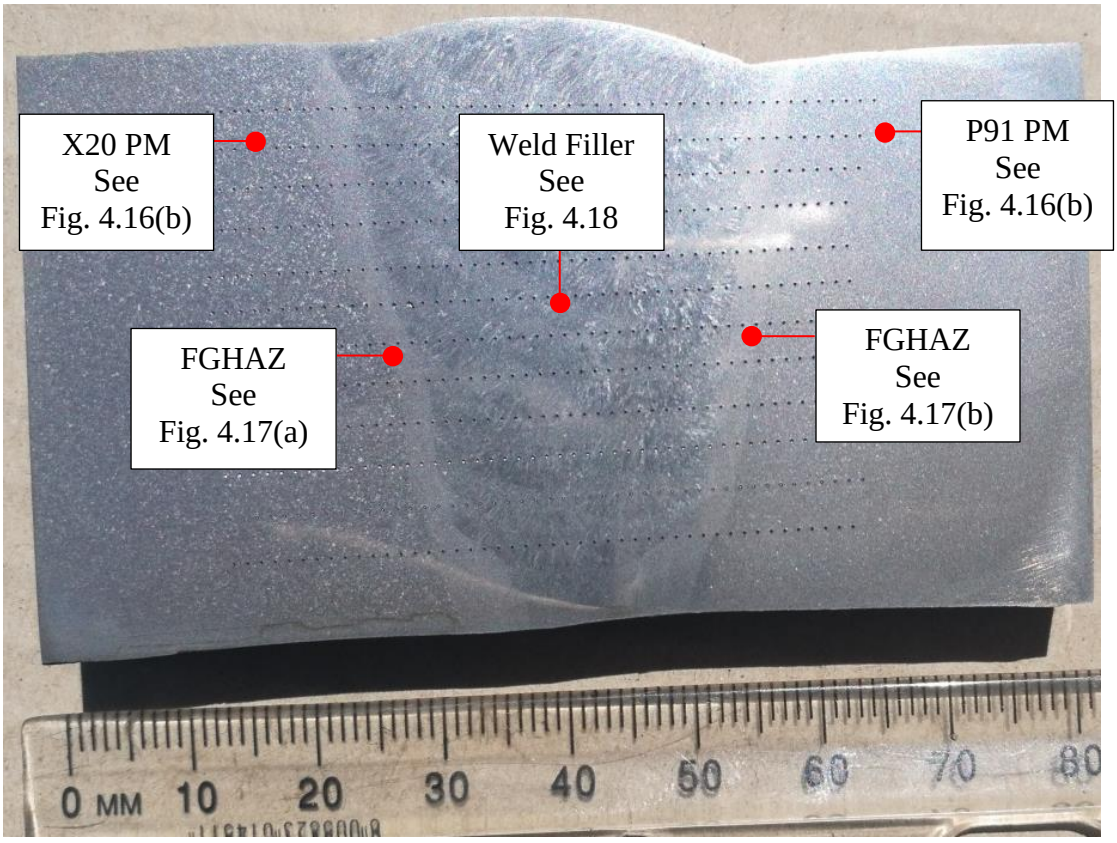


Figure 4.15: Photograph of an etched cross sectional view of the cross weldment showing the specific locations that were carefully identified in order to quantify the microstructural parameters. [Etched in Villella's reagent].

4.5.1.1 Parent Materials Microstructures

Figure 4.16 shows the tempered martensite microstructure of the parent materials, a) X20 and b) P91. Occasional creep voids are visible on the X20 PM, and none on the virgin P91 material. The X20 microstrucrure is typical of the austenitised, normalised and tempered heat treated X20 parent material, and it shows no microstructural anomalies other than creep voids. This microstructure is characteristic of X20 material that was subjected to a heat treatment cycle consisting of austenitizing between 1020 - 1080 ºC, normalisation and tempering between 730 - 780 ºC as required by the technical delivery conditions for seamless steel tubes for pressure purposes EN 10216-2:2013 (E) code (BS EN 10216-2, 2013). The P91 microstructure is typical of the austenitised, normalised and tempered P91 PM without microstructural anomalies. This microstructure is characteristic of P91 material that was subjected to a thermal cycle for austenisation between 1040 - 1090°C, normalisation and tempering between 730 - 780°C as required by the technical delivery conditions for seamless steel tubes for pressure purposes EN 10216-2:2013 (E) code (BS EN 10216-2, 2013).

Prior-austenite grain size ranged from approximately 40 μm to 70 μm in both parent materials. The microstrustural constituents of tempered martensitic laths and finely dispersed carbides ($M_{23}C_6$ and MX) on the ferittic matrix can also be seen (these will be more clearly visible on the electron microscope micrographs, section 4.5.2). The presence of these precipitates is considered to improve creep rupture strength through precipitation hardening (Abe, 2008 and Dawson, 2012). In addition, the $M_{23}C_6$ precipitates primarily stabilises the martensitic lath structure during creep application (Milovic´ *et al*., 2013). Similar findings regarding precipitation hardening in these 9-12%Cr creep resistance steels have been made by other researchers (Buchmayr *al.*, 1989; Matsuyama, 2000; Milovic´ *et al*., 2013).

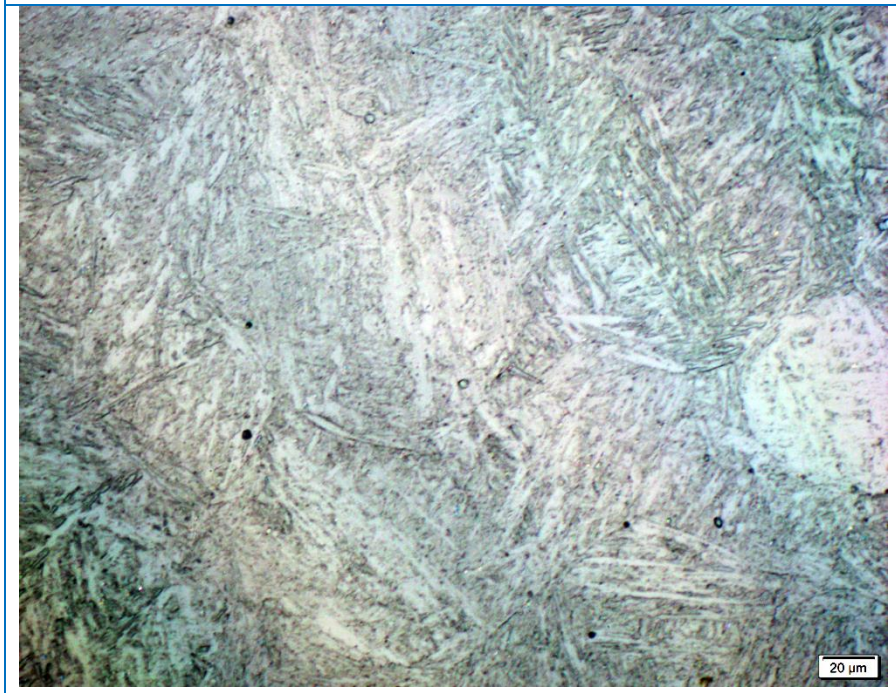
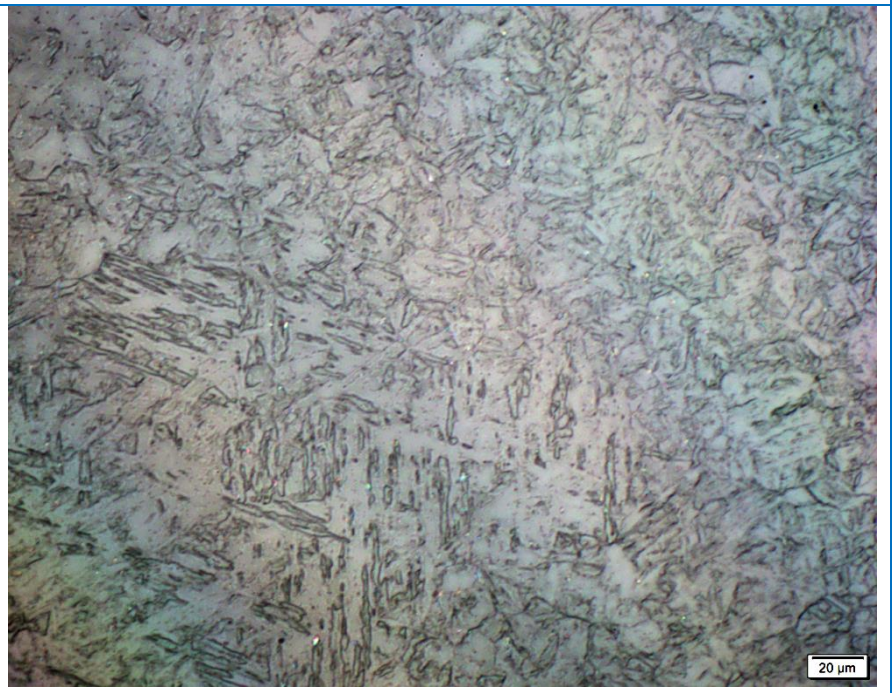
(a) X20 PM	(b) P91 PM
	

Figure 4.16: Optical micrograph of the PMs for (a) X20 showing tempered martensite microstructure with occasional creep voids, and for (b) P91 showing tempered martensite microstructure typical of virgin P91 material, [Etched in Villella's reagent, 500X Magnification].

4.5.1.2 Heat Affected Zone Microstructures

Figure 4.17 shows the microstructure of the intercritical heat affected zone (ICHAZ), a) X20 and b) P91 materials. These microstructures are typical of a product of the parent material structure that was originaly tempered martensite which then later partialy transformed into austenite. The latter phase subsquently transformed into martensite during cooling following the welding thermal cycle with a peak temperature (T_p) between A_{c1} and A_{c3}; $850^{\circ}C < T_p < 925^{\circ}C$. These findings were also reported by Abe *et al*. (2008) and Milovic´ *et al*. (2013). This microstructure within the ICHAZ is known to exhibit the lowest hardness values in weldments and is susceptible to Type-IV creep cracking (Abe *et al*., 2008; Masuyama, 2000). Occasional creep voids were evident on the creep aged X20 HAZ side. These creep voids are as a result of the pre existing voids on creep aged X20 PM.

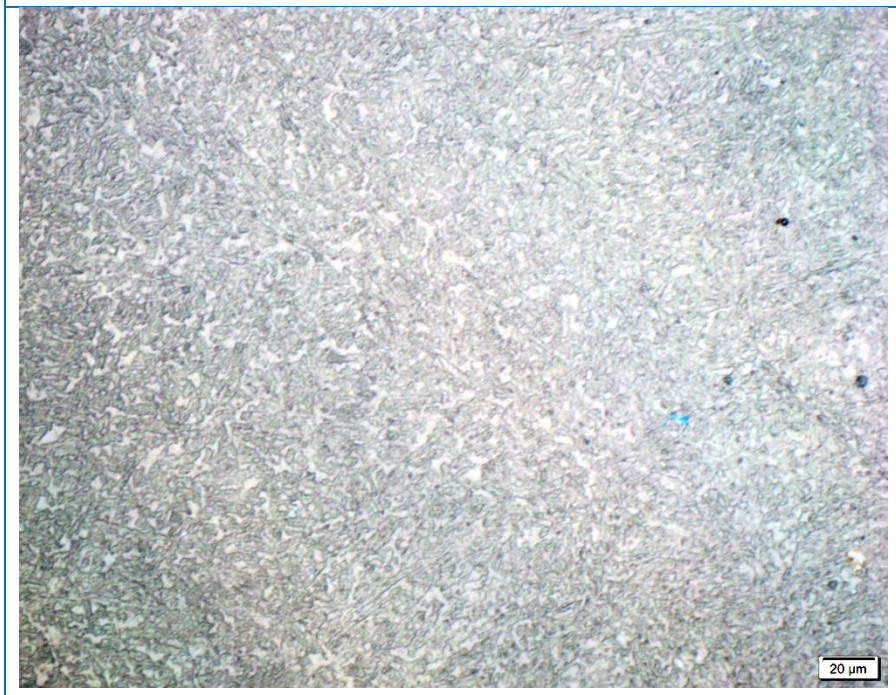
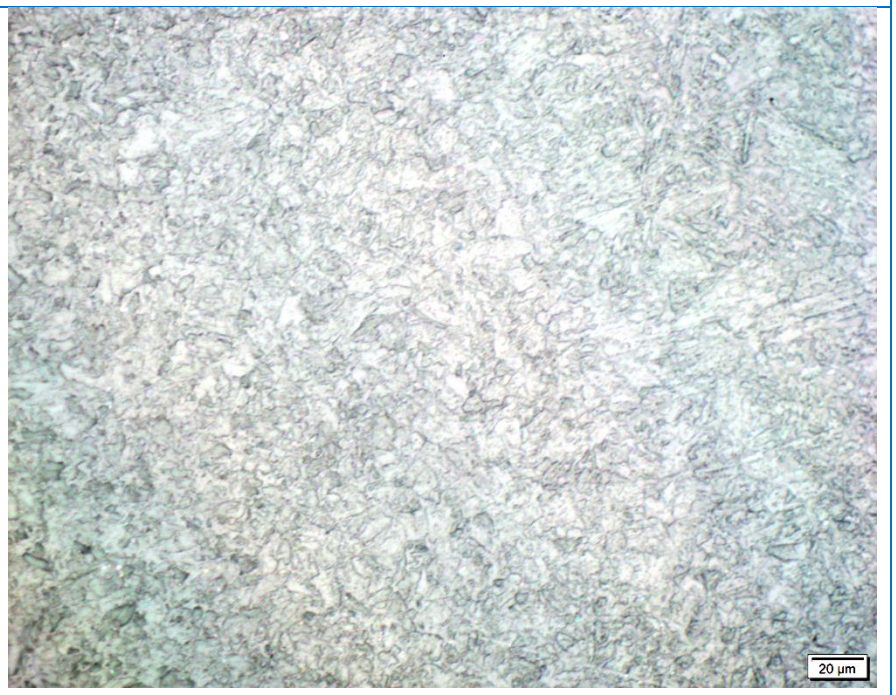
(a) X20 ICHAZ	(b) P91 ICHAZ
	

Figure 4.17: Optical micrographs of the ICHAZ for (a) X20 and for (b) P91 showing small grained structure with a mixture of tempered martensite laths and ferrite. Occasional creep voids are also evident only on the X20 ICHAZ side, [Etched in Villella's reagent, 500X Magnification].

4.5.1.3 Weld Filler Metal Microstructures

Figures 4.18 illustrates the microstructures of weld filler metals, a) X20 and b) P91 respectively. These microstructures show a tempered martensite structure without anomalies.

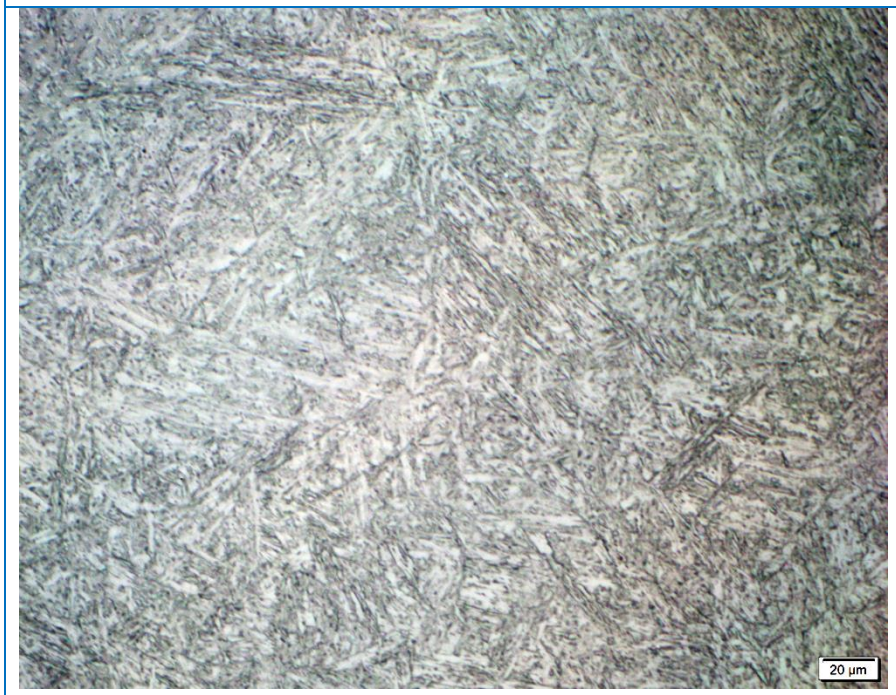
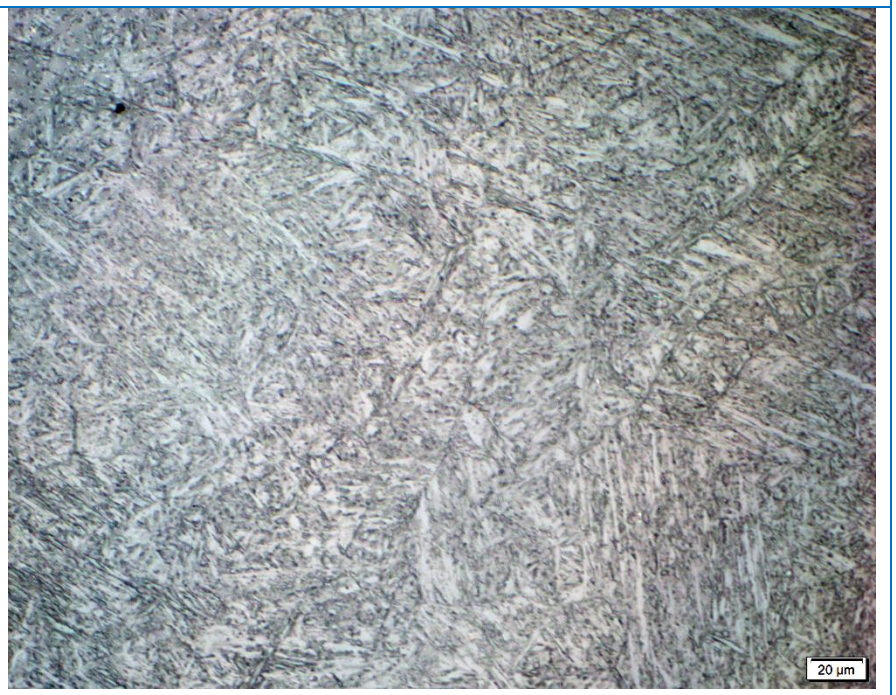
(a) X20 Weld Filler Metal	(b) P91 Weld Filler Metal
	

Figure 4.18: Optical micrograph of weld filler for (a) X20 and (b) metals showing tempered martensite microstructure. It is apparent that X20 has more martensite laths and less ferritic phase fraction compare to P91microstructure, [Etched in Villella's reagent, 500X Magnification].

4.5.2 Characterization of Microstructural Parameters

The contribution to creep strength is determined by the several metallurgical parameters such as precipitate density, sub-grain / micro-grains and dislocation density (Masuyama, 2000). The samples were investigated using TKD-EDS, ADF-STEM, XRD, EBSD and BSE to measure these different microstructural features that contribute to creep-strength. The collected images were processed using custom recipes in MIPAR to identify the features of interest.

Figure 4.19 shows the feature outlines of the different microstructural contributions of precipitates, micro-grains and substructure. The MIPAR^{TM} software was then used to quantify the phase fractions, equivalent circle diameter (ECD) for each of the Cr-rich and V-rich precipitates from the TKD-EDS maps. In addition, the mean linear intercepts for the sub-structure were measured from the ADF-STEM images. Figure 4.20 shows and annotates the dislocations and the sub-structure that were analysed using HAADF-STEM.

Dislocation measurements on the ADF-STEM were not successful due to the low magnification (20 000 X) and low image resolution (1024×1024). The EBSD data were processed using the M-Tex plugged in to Matlab in order to first identify the elongated micro-grains and then determine the minor axis (short-width) of each micro-grain.

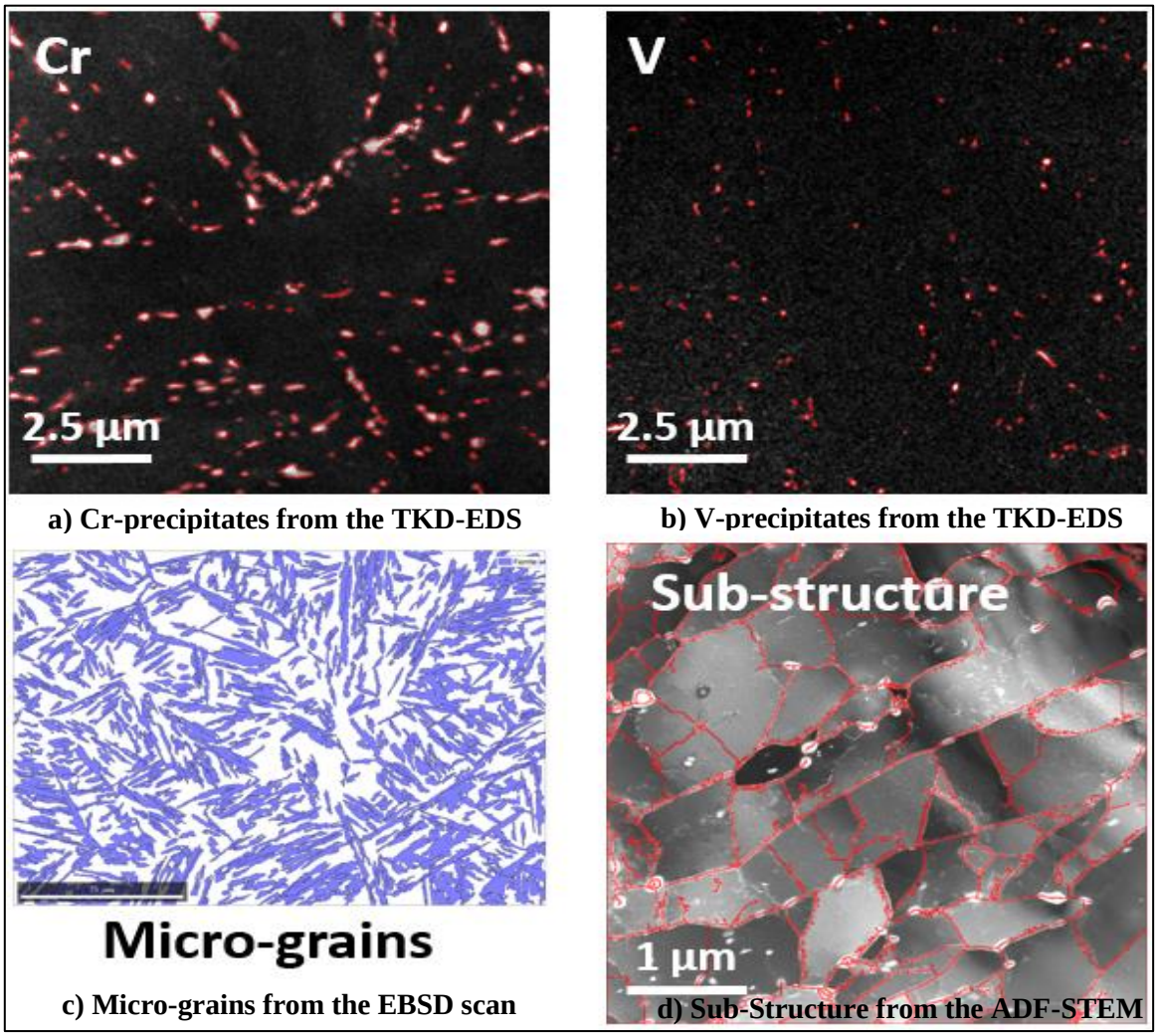


Figure 4.19: Processed images showing outlines (red) of the various features identified: a) Cr-precipitates from the TKD-EDS, b) V-precipitates from the TKD-EDS, c) Micro-grains from the EBSD and d) Sub-structure from the ADF-STEM images.

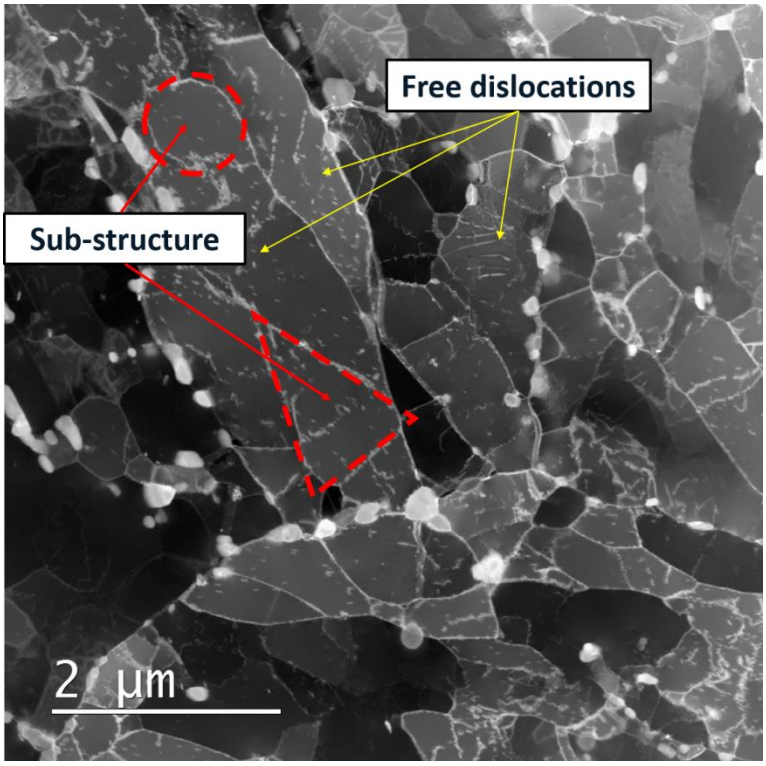


Figure 4.20: Processed HAADF-STEM images annotating the dislocations and the sub-structure that were measured.

The processed images show a projection of a slice through the 3D (three dimensional) microstructure of the material. As an approximation, it was assumed that the precipitates were spherical in shape and that the size was in the order of 50-150 nm in diameter. The TEM specimen thickness was assumed to be 100 nm throughout the sampled areas. The location of the precipitate in relation to the sectioned slice will determine the measured size, which would generally be smaller than the actual 3D size distribution. In addition, the sectioned precipitate might not extend through the foil thickness, thus the measured phase fraction will be an overestimation of the true volume phase fraction of the precipitate.

4.5.2.1 Microstructural Characterization of Parent Metals

Figure 4.21 shows the distribution of the $M_{23}C_6$ (Cr-map), MX (V-map) from TKD-EDS, micro-grains from the EBSD and sub-structure from ADF-STEM images of the parent materials.

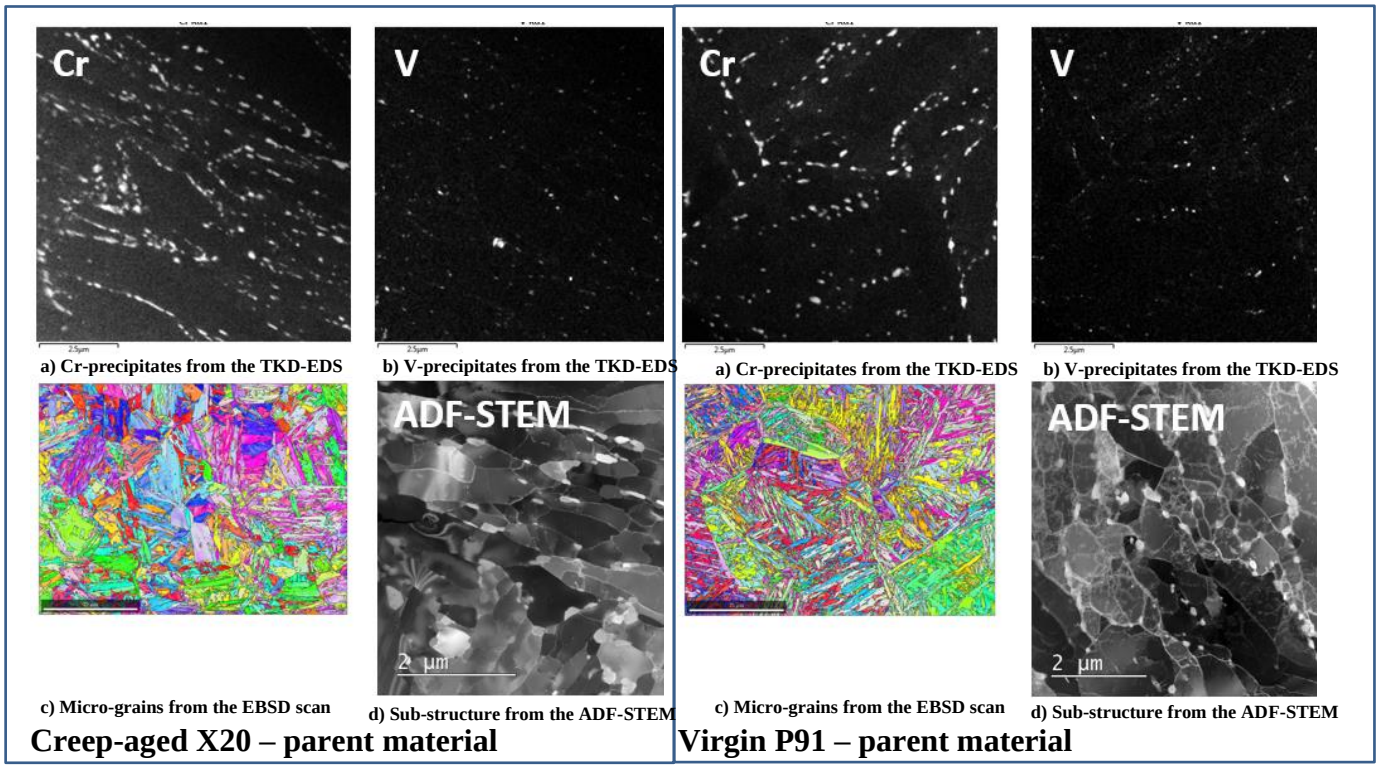


Figure 4.21: Microstructural constituents maps showing the distribution of: a) Cr-precipitates from the TKD-EDS (Top Left Image), b) V-precipitates from the TKD-EDS (Top Right Image), c) Micro-grains from the EBSD (Bottom Left Image) and d) Sub-structure from the ADF-STEM (Bottom Image) for the parent material.

From the images in Figure 4.22, the $M_{23}C_6$ (Cr-carbides) precipitates are located on the prior austenite grain boundaries. The MX (V-carbides) precipitates are located within the sub-grains as well as on the sub-boundaries. The MX precipitates are considered to confer superior creep strength to 9-12% Cr steels compared to the $M_{23}C_6$ precipitates (Abe, 2008; Hald, 1996; Holzer, 2010).

Table 4.2 shows the projected microstructural parameter measurements for the parent materials. The mean equivalent circle diameters (ECD) and phase fractions of precipitates ($M_{23}C_6$ and MX) for X20 and P91 parent materials were comparable. The calculated ECD values for X20 and P91 are 117 ± 6 nm and 115 ± 6 nm respectively, while the $M_{23}C_6$ precipitates phase fractions were 4.60 vol.% and 4.52 vol.% respectively. This implies that creep aged X20 parent material microstructural precipitates have coarsened compared to that of virgin P91 parent material. The coarsening of these precipitates has a negative effect on the remaining creep (Maile, 2007, Auerkari et al. 2007).

Although it was possible to identify the V-rich precipitates via EDS, their small size combined with the interaction volume of the technique made reliable size measurements on these small precipitates difficult. The sub-structure size measurements taken from the ADF-STEM images showed that the

creep-aged X20 parent material had a larger sub-structure (0.32 ± 0.03 µm) than the virgin P91 material (0.25 ± 0.03 µm). This could be attributed to the fact that X20 material had already operated for 167303 hours at temperatures of 539°C and pressures of 17.1 MPa, yielding to a calculated operating hoop stress of 71 MPa. This resulted in a 15% creep life exhaustion on the creep aged X20 parent material based on the theoretical creep life calculations using operating conditions and ISO-20% material properties. This level of creep exhaustion is considered acceptable for maintenance welding purposes in fossil power plants (Bezuidenhourt *et al.*, 2008; Molokwane, 2013). In support of this theoretical creep life exhaustion, the creep cavitation damage level of the service exposed X20 material as expressed in terms of creep void density was only 60 voids / mm^2 when counted from the lifted surface replica micrographs; as previously illustrated in Figure 3.3.

Table 4.2: Projected Area Microstructural Measurements of the Parent Material

Microstructural Parameters			**Creep-aged X20**	**Virgin P91**
Precipitates	$M_{23}C_6$	*Mean ECD (nm)*	117 ± 6	115 ± 6
		Fraction (vol.%)	4.60	4.52
	MX	*ECD (nm)*	93 ± 5	66 ± 4
		Fraction (vol.%)	1.44	0.75
Elongated micro-grains (µm)			1.137	0.845
Sub-structure (µm)			0.32 ± 0.03	0.25 ± 0.03
Free-dislocations (10^{-14} m^{-2})			0.54	4.67

Therefore, it is apparent from the parent material microstructural characterisation results that the creep aged X20 parent material microstructural parameters (i.e. precipitates, micro-grains and sub-structure) have coarsened compared to that of virgin P91 parent material. The coarsening of these parameter has a damaging effect on remaining creep life since the creep strength is determined by finely distributed state of these parameters (Maile, 2007, Auerkari *et al.*, 2007).

4.5.2.2 Microstructural Characterization of Weld Filler Metals

Figure 4.22 illustrates the distribution of the $M_{23}C_6$ (Cr-map), MX (V-map), sub-grains (band contrast) and dislocation network (ADF-STEM) for the weld filler materials. Based on the uncorrected mean measured parameters presented in Table 4.3, there is no significant difference between the microstructures, other than the phase fraction of $M_{23}C_6$, that is 4.20 vol.% for X20 weld filler metal and 3.31 vol.% for P91 weld filler metal. The reason for higher phase fraction of $M_{23}C_6$ precipitates on X20 weld filler material is attributed to high Cr (11.1 wt.%) and high C content (0.19 wt.%) in X20

welding rod filler compared to the Cr and C content in P91 welding rod filler with 9 wt.% Cr and 0.11 wt.% C (Böhler welding, 2009).

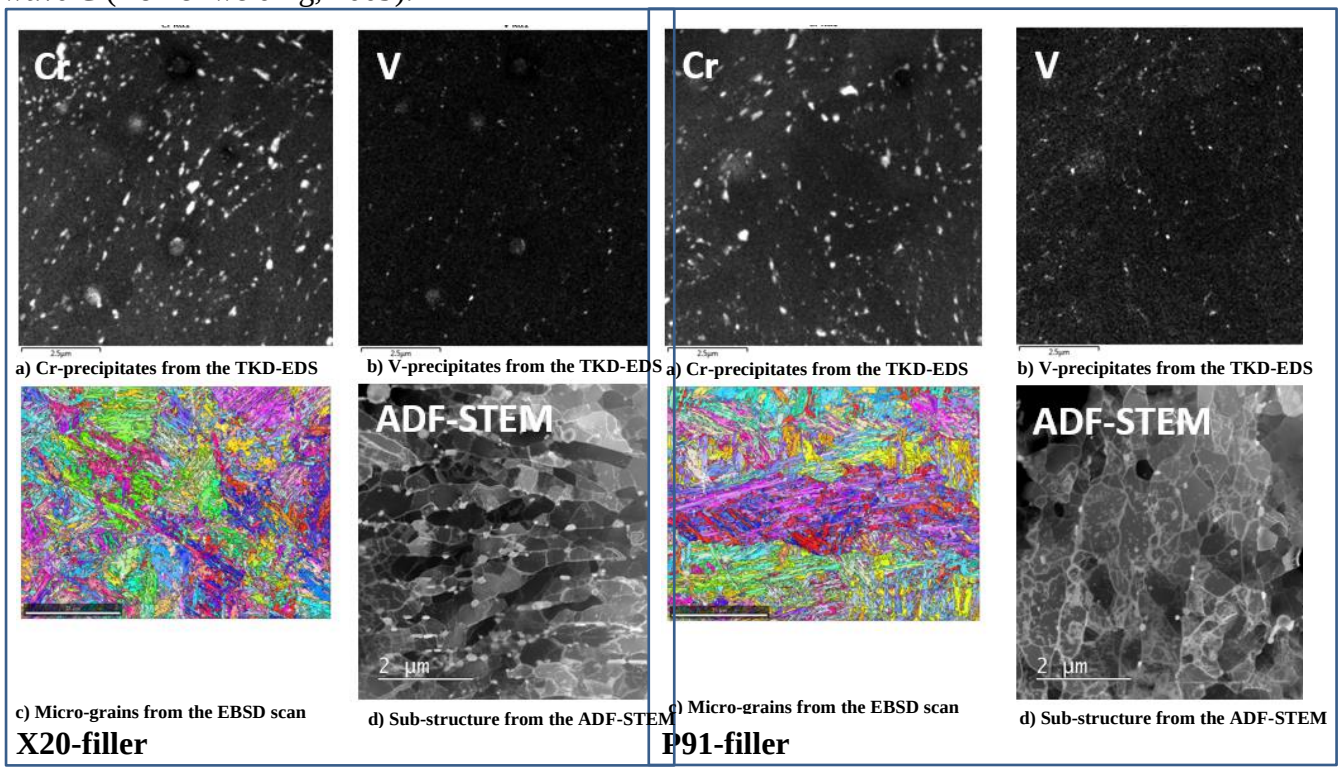


Figure 4.22: Microstructural constituents maps showing the distribution of: a) Cr-precipitates from the TKD-EDS (Top Left Image), b) V-precipitates from the TKD-EDS (Top Right Image), c) Micro-grains from the EBSD (Bottom Left Image) and d) Sub-structure from the ADF-STEM (Bottom Image) for the weld filler material.

Table 4.3: Microstructural Measurements for Filler Materials.

Microstructural Parameters			**X20 filler**	**P91 filler**
Precipitates	$M_{23}C_6$	*Mean ECD (nm)*	120 ± 6	130 ± 7
		Fraction (vol.%)	4.20	3.31
	MX	*ECD (nm)*	89 ± 4	96 ± 4
		Fraction (vol.%)	0.93	1.50
Elongated micro-grains (µm)			0.999	0.958
Sub-structure (µm)			0.23 ± 0.02	0.18 ± 0.01
Free-dislocations (10^{-14} m^{-2})			3.07	2.35

4.5.2.3 Microstructural Characterization of ICHAZ Regions of the Different Dissimilar Welds

Figure 4.23 illustrates the distribution of the $M_{23}C_6$ (Cr-map), MX (V-map), sub-grains (band contrast) and dislocation network (ADF-STEM) for ICHAZ regions in the different parent materials welded with dissimilar filler materials. All four ICHAZ regions, namely; (1) X20 ICHAZ adjacent to X20 WM, (2) X20 ICHAZ adjacent to P91 WM, (3) P91 ICHAZ adjacent to X20 WM, and (4) P91 ICHAZ adjacent to P91 WM were analysed. Based on the uncorrected mean measured parameters reported on Table 4.4, there was no significant difference between the microstructures, other than the phase fraction of $M_{23}C_6$ precipitates. The X20 ICHAZ adjacent to X20 WM had 5.23 vol.% $M_{23}C_6$ phase fraction and 5.65 vol.% $M_{23}C_6$ phase fraction on the X20 ICHAZ adjacent to P91 WM. The P91 ICHAZ adjacent to X20 WM had 3.37 vol.% $M_{23}C_6$ phase fraction and 2.87 vol.% $M_{23}C_6$ phase fraction on the P91 ICHAZ adjacent to P91 WM. The reason for higher phase fraction of $M_{23}C_6$ precipitates on X20 ICHAZ is attributed to high chromium content in X20 parent material (10 – 12.5%) compared to that in the P91 parent material (8 – 9.5%), (BS EN 10216-2: 2002; Maile, 2007).

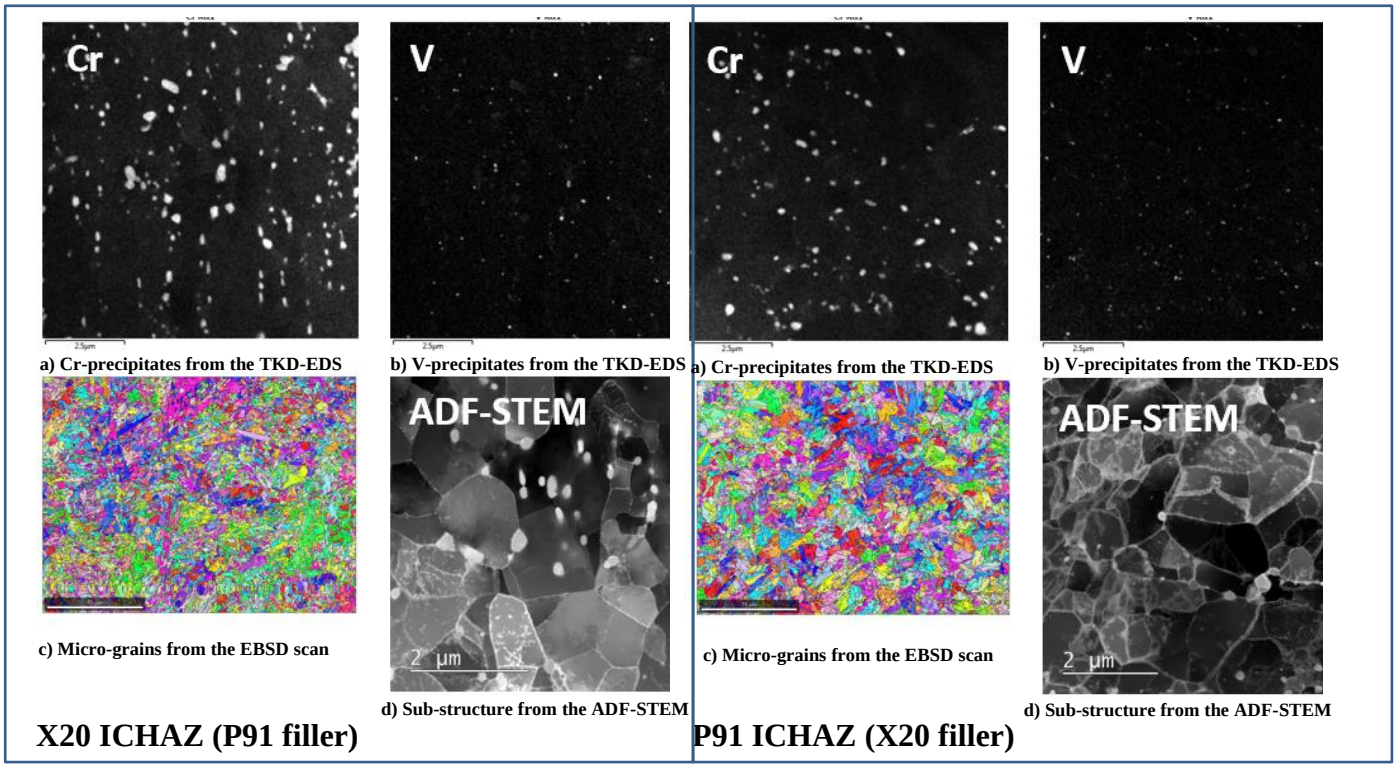


Figure 4.23: Microstructural constituents maps showing the distribution of: a) Cr-precipitates from the TKD-EDS (Top Left Image), b) V-precipitates from the TKD-EDS (Top Right Image), c) Micro-grains from the EBSD (Bottom Left Image) and d) Sub-structure from the ADF-STEM (Bottom Image) for the ICHAZ region.

It is also apparent that the $M_{23}C_6$ precipitates are coarser on the X20 FGHAZ than on the P91 FGHAZ. As stated earlier, the coarser precipitates found in the X20 FGHAZ was as a result of previous service

history of the X20 material. The phenomenon of precipitates coarsening at creep operating conditions has also been reported by Abbaschian (1992), Masuyama (2000), and Yardley (2003).

Table 4.4: Microstructural Measurements for HAZ Regions

Microstructural Parameters			**X20 ICHAZ**		**P91 ICHAZ**	
			X20 HAZ nearer to the X20 weld filler metal	**X20 HAZ nearer to the P91 weld filler metal**	**P91 HAZ nearer to the X20 weld filler metal**	**P91 HAZ nearer to the P91 weld filler metal**
Precipitates	$M_{23}C_6$	*Mean ECD (nm)*	155 ± 10	156 ± 10	150 ± 10	158 ± 10
		Fraction (vol.%)	5.23	5.65	3.37	2.87
	MX	*ECD (nm)*	88 ± 4	94 ± 4	89 ± 4	98
		Fraction (vol.%)	0.99	1.46	1.32	1.23
Elongated micro-grains (µm)			1.113	1.099	1.256	1.239
Sub-structure (µm)			0.39	0.30	0.34	0.25
Free-dislocations (10^{-14} m^{-2})			1.29	2.31	0.78	1.14

4.5.2.4 Precipitates Analysis Summary

The role of precipitates in the dislocation movement obstruction is directly interrelated to the mean inter-particle spacing (λ_{ss}). This parameter is a function of not only the size of the particle (precipitate), but also the phase fraction of the precipitate. In calculating λ_{ss}, the effect of sectioning the precipitates for TEM examination, as well as the foil projections are accounted for in order to calculate the true 3D inter-particle spacing. The correction factor calculation for a given precipitate distribution and a TEM foil thickness were carried out according to the study in the MSc dissertation by Marx (Marx, 2016). Details of this correction factor calculations for a given precipitate distribution and a TEM foil thickness can be found in Sonderegger (2006).

Figures 4.24 and 4.25 show the comparison of the mean surface-to-surface particle spacing calculated from the different precipitates (i.e. $M_{23}C_6$ and MX) distributions of the different microstructural zones. Higher mean particle spacing values would indicate lower resistance to dislocation movement which would indicate lower creep strength and indentation hardness. The highest normalised inter-particle ($M_{23}C_6$) spacing were measured in the P91 ICHAZ regions. This was due to lower number of

precipitates in quantity. The smallest inter-particle ($M_{23}C_6$) spacing values were measured in the filler materials, due to the rapid cooling from a molten metal and subsequent growth of the precipitates during the post-weld heat treatment. These two regions (P91 HAZ and weld metals) correlated to the lowest (187 HV) and highest (268 HV) hardness values, respectively as reported in the previous Section 3.4.3 (Micro Hardness Test) as well as in Figure 4.5 (Micro hardness traverse for both X20 and P91 weld filler cross weld joint). The MX precipitates in the different microstructural regions had similar inter-particle spacing. This could partly be due to the limitations of the measuring technique.

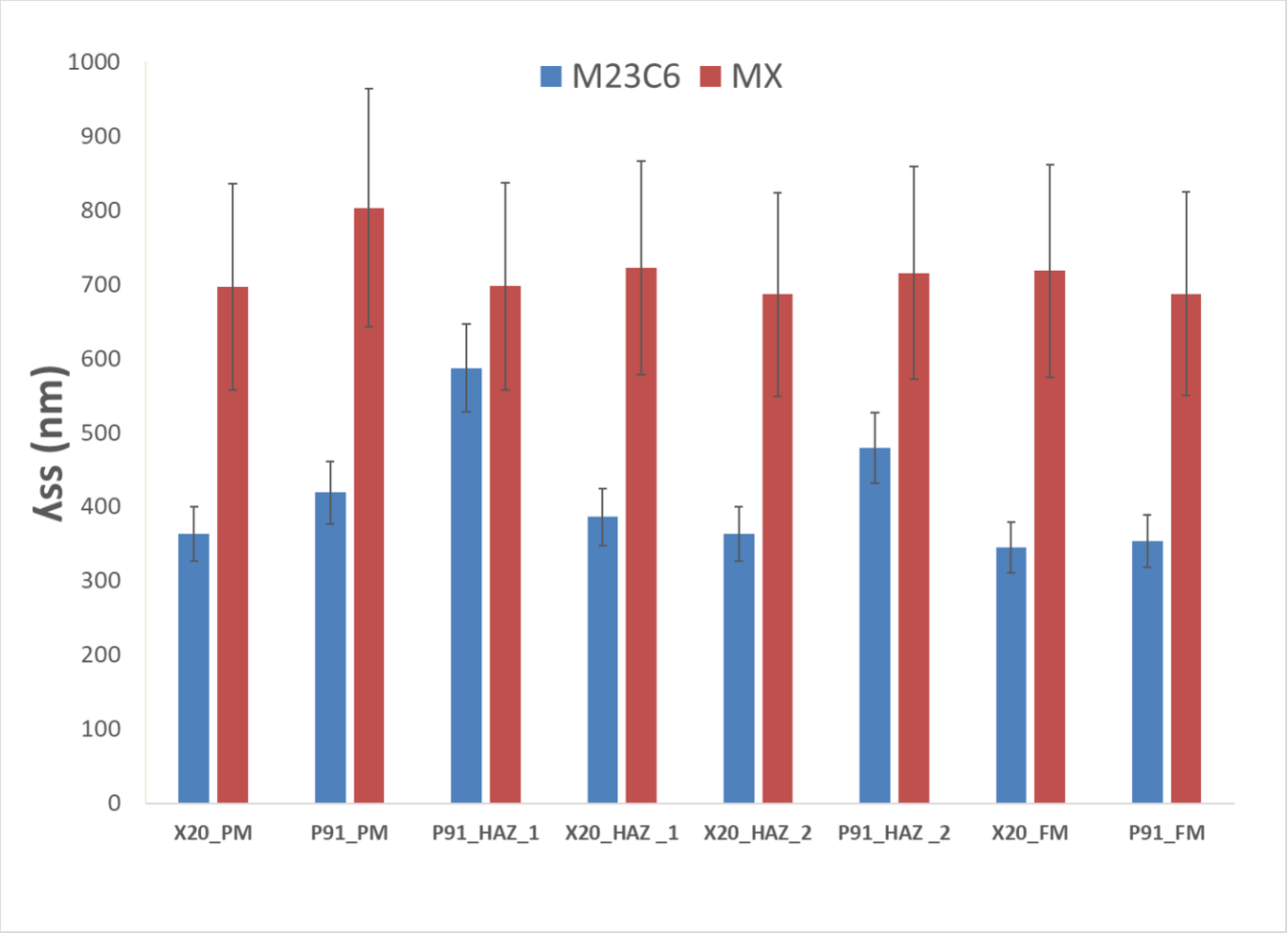


Figure 4.24: Mean surface-surface distance for the precipitates measured with TDK-EDS.

The significance of the dotted line in figures 4.25, 4.27 and 4.31 is that for all the feature values (precipitate spacing, sub-grains and dislocation density) in the bar graphs were normalised relative to the new P91 material, which had a value of 1. The dotted line is added as visual aid to see and compare each material state relative to this normalisation.

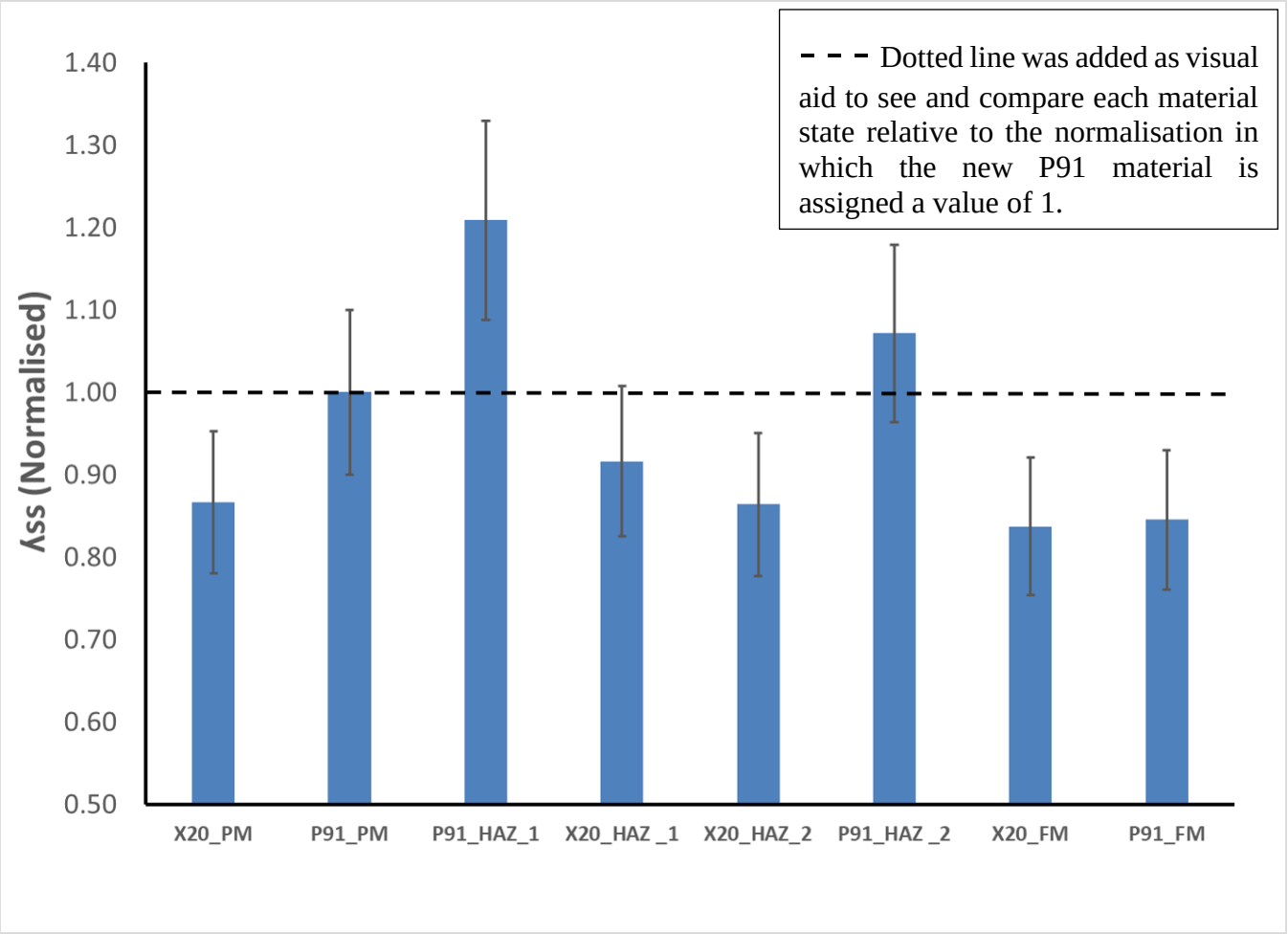


Figure 4.25: Normalised mean surface-surface measurements of the precipitates ($M_{23}C_6$ and MX).

4.5.2.5 Grain Size Analysis Summary

Figure 4.26 presents the comparison of the mean linear intercept size of the sub-structure measured in the different microstructural zones using the ADF-STEM images. The formation of the sub grain boundaries can be attributed to the decrease in dislocation densities during tempering (Pešička *et al.*, 2003). The HAZ regions had the largest sub-grain structures, while the filler materials had the smallest sub-grain structures. This correlates with the measured hardness values in these zones. The creep aged X20 parent material had a larger sub-grain structure than the one found in virgin P91 parent material. The sub-structure and micro-grain sizes of the different microstructural areas imaged using ADF-STEM are presented graphically herein Figure 4.27.

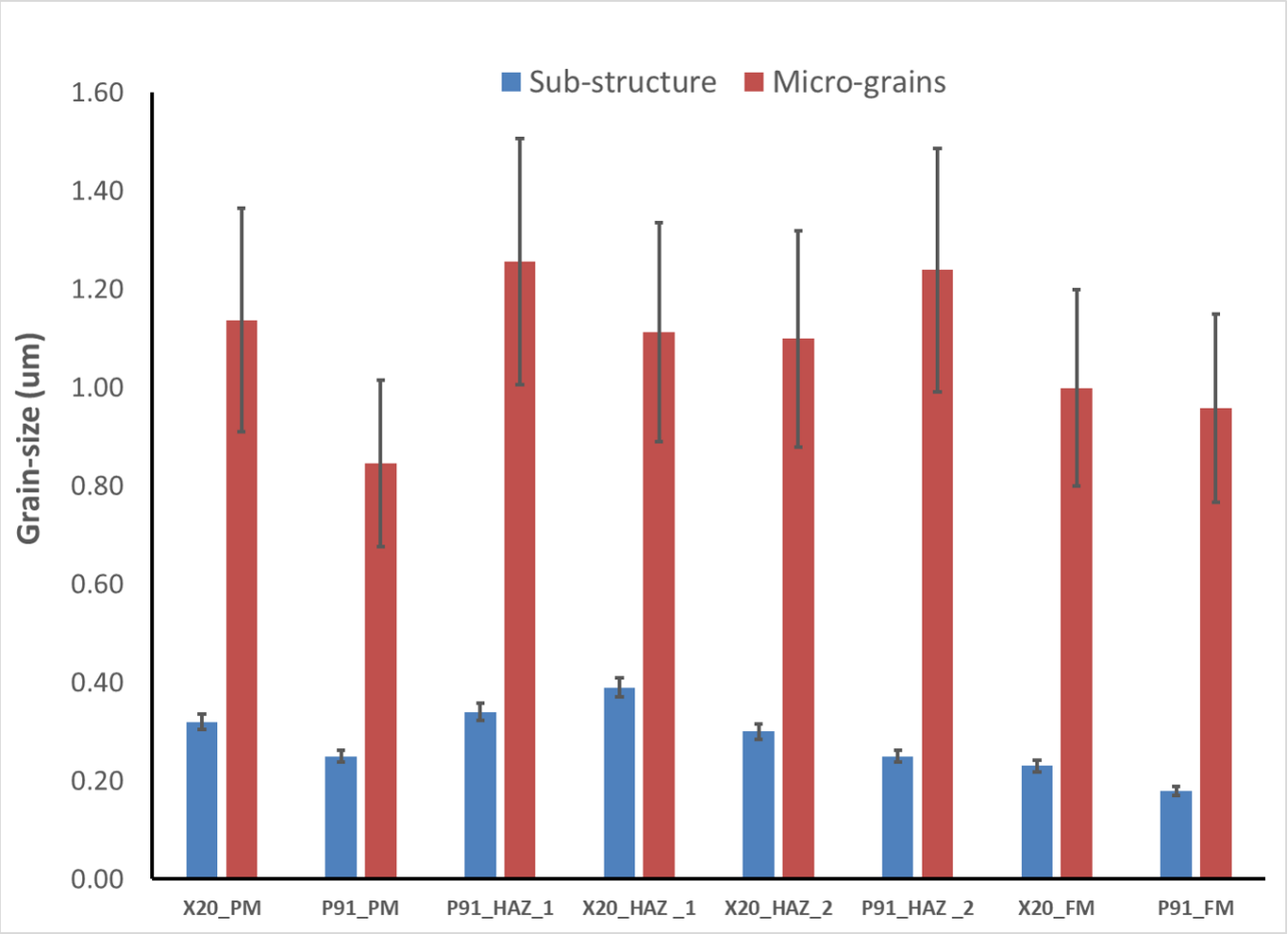


Figure 4.26: The mean values for the linear intercept of the sub-structure and the short-width of the elongated micro-grains.

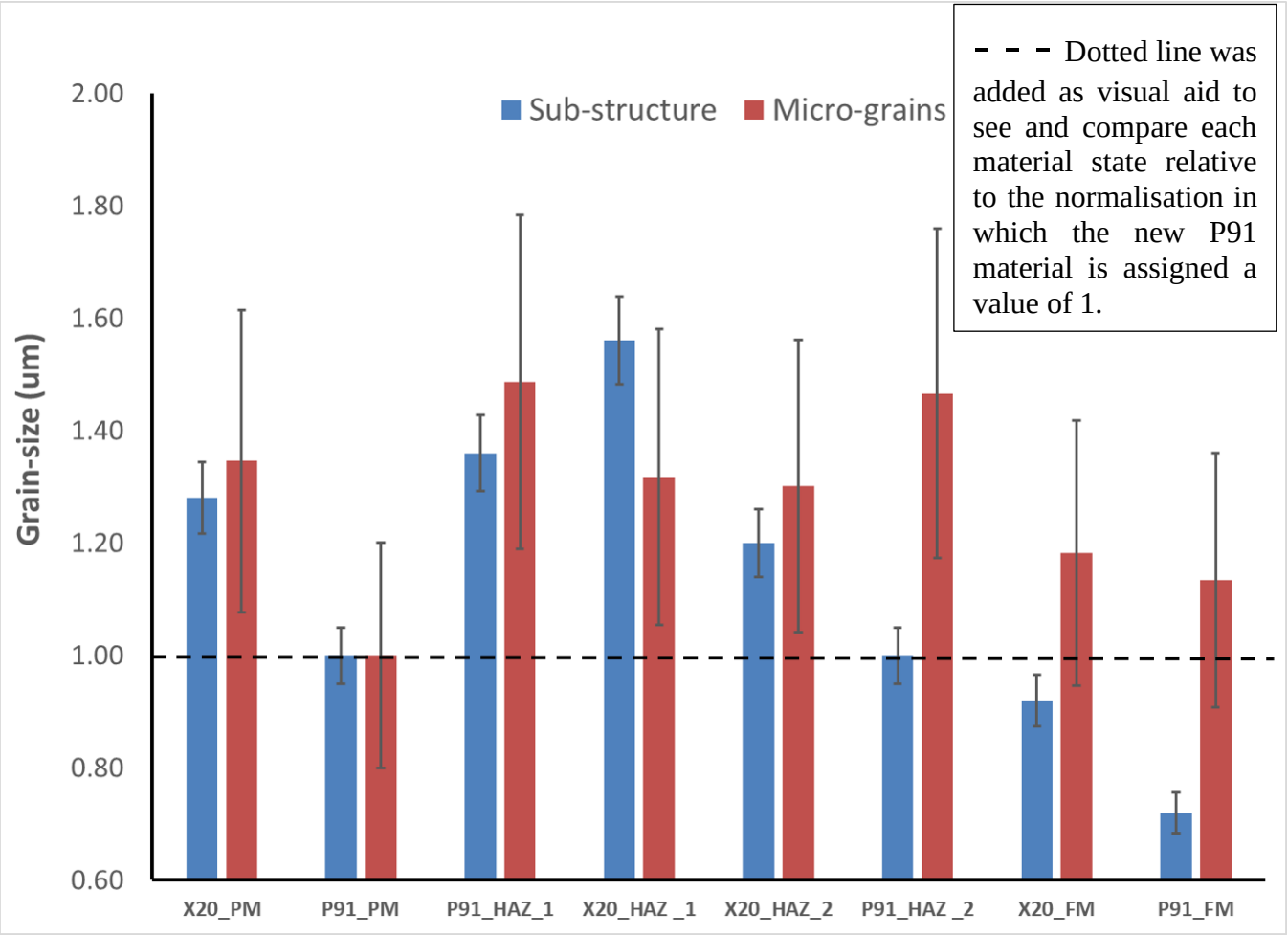


Figure 4.27: Sub-grain size of the different microstructural areas imaged using ADF-STEM.

After normalising the measured grain-size values for all analysed regions to that of the virgin P91 parent material region value, it is apparent that the micro-grain size is predominantly high on both X20 and P91 HAZ regions. This could be attributed to the welding thermal cycle that results in the coarsening of the microstructure's sub-grain structure in the ICHAZ. Abe *et al.* (2008) reported similar finding, whereby applied heat input contributed to the coarsening of grains and sub-grains. This microstructural notch contributes to the creep weak zone on the weldment and promotes the formation of Type-IV creep cracking on the ICHAZ during creep loading (Abe *et al.*, 2008; Zhang *et al.*, 2020).

4.5.2.6 Dislocation Density Analysis Summary

Figure 4.28 shows the typical ADF-STEM images taken from the different microstructural zones in the weldment. The virgin P91 parent metal had numerous dislocations within smaller sub-grains compared to the creep aged X20 parent metal. The sample removed from the FGHAZ in the P91 material (bottom left) showed significant growth of the sub-grains and very low dislocation density. The filler metal had very small sub-grains and contained a significant number of free dislocations

within the sub-grains. The dislocation density in the material had a very strong influence on the dislocation creep strength of the material, based on the Orowan back-stress concept (Abe, 2008; Holzer, 2010; Marx, 2016). ADF-STEM was used to quantify the bulk dislocation density on the sections that were removed from the different regions of the weldment.

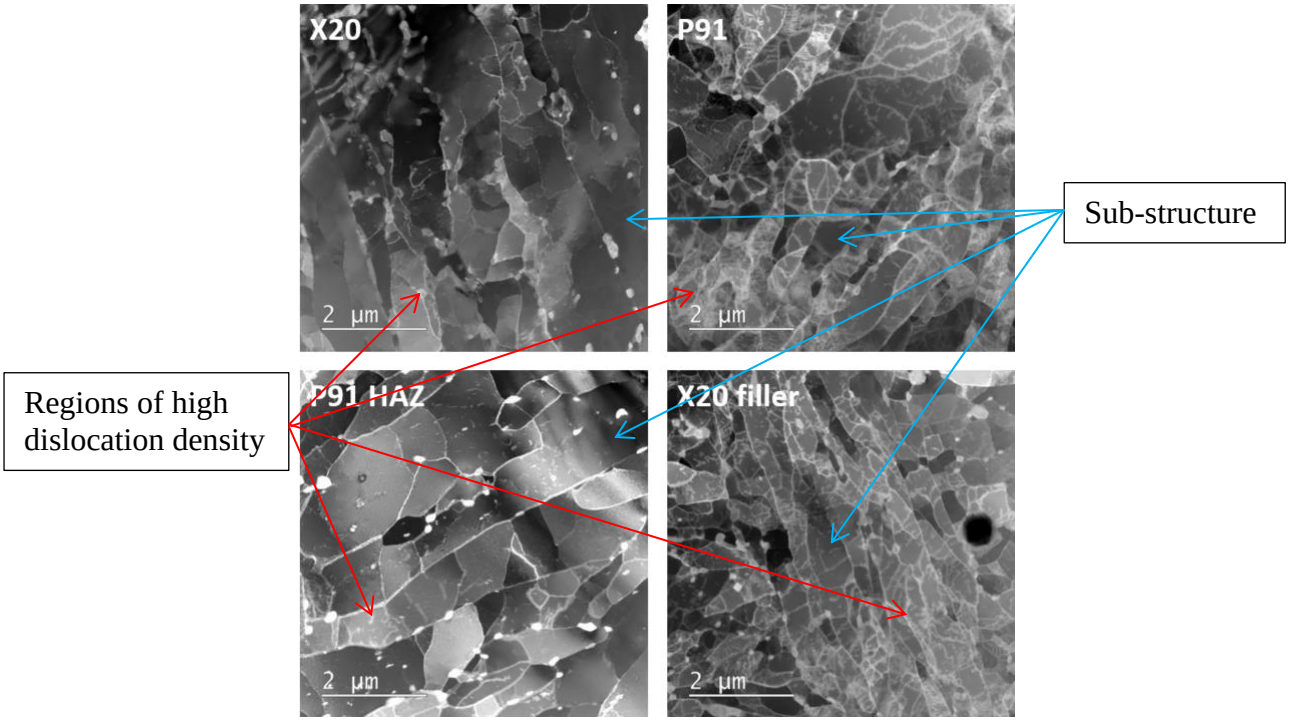


Figure 4.28: Typical ADF-STEM images of the different microstructural zones showing the relative sub-structure size and the regions of high dislocation density.

X-ray diffraction performed on the different sections was used to quantitatively measure the bulk dislocation density, and the results are graphical shown in Figure 4.29. This was carried out using peak profile analysis on the XRD patterns for each microstructural region. Based on these results, it is apparent that the virgin P91 parent material has the highest dislocation density (approximately 4.6×10^{14} m^{-2}) compared to the creep aged X20 parent material (approximately 0.5×10^{14} m^{-2}), this could be attributed to the fact that X20 material has already operated in creep service hence the coarsening of sub-grains that was observed and previously illustrated in ADF-STEM images (Figure 4.31). The P91 FGHAZ had lower dislocation density (ranging between 0.8×10^{14} m^{-2} and 1.2×10^{14} m^{-2}) compared to X20 FGHAZ density (ranging between 1.4×10^{14} m^{-2} and 2.3×10^{14} m^{-2}). These quantitative XRD results agree with the qualitative observation from the ADF-STEM images results.

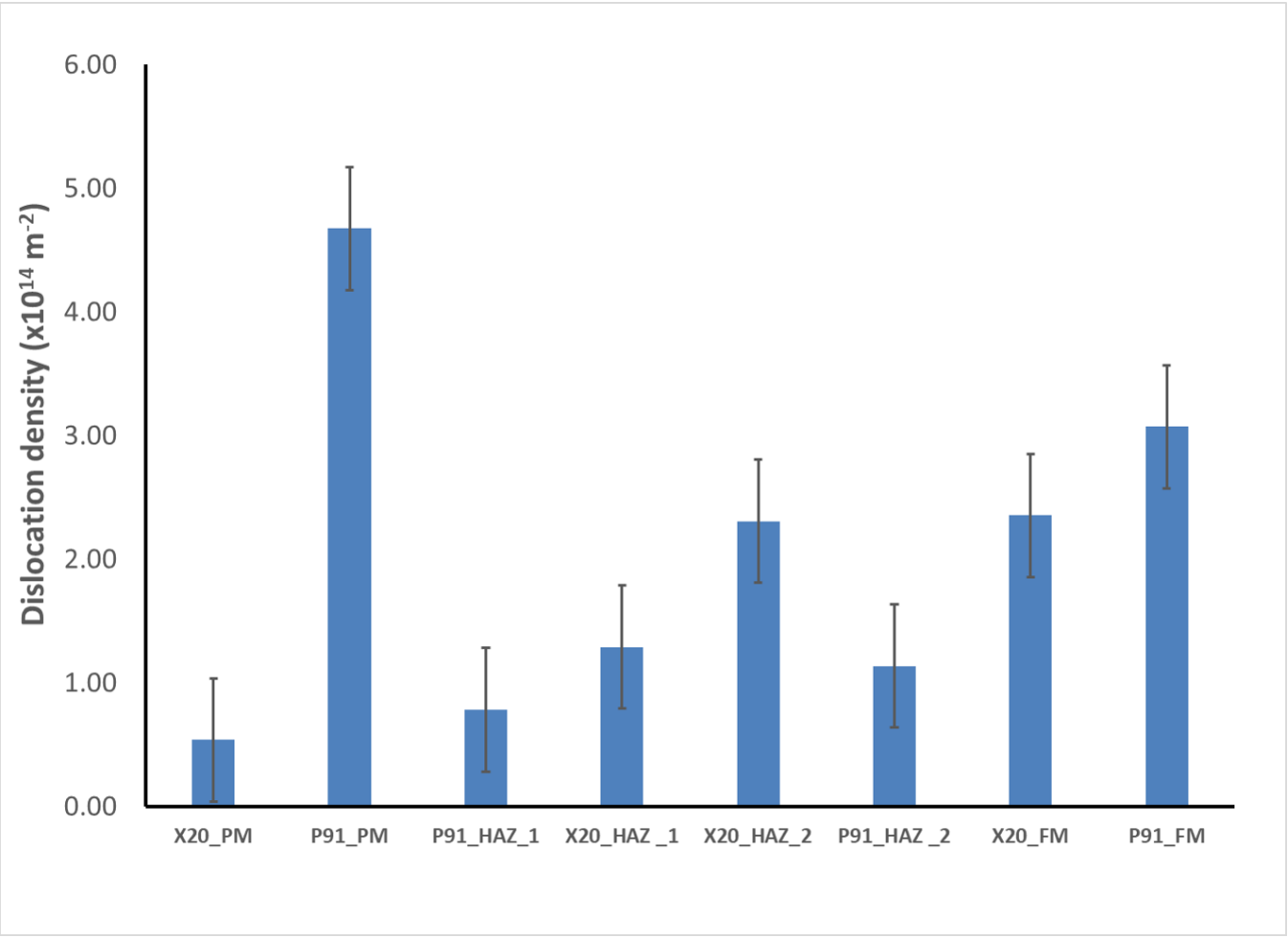


Figure 4.29: Free dislocation density determined from XRD peak measurements.

4.5.3 Orowan Back Stress Calculations before Creep Test

Material's resistance to creep can be quantified using the Orowan back-stress concept model. This concept states that if there is an applied load or stress on the metallic material, a considerable amount of this applied stress is counteracted by the microstructural strengthening features such the interfaces and/or precipitates. Consequently, the applied stress may cause the microstructural deterioration/ deformation, however, not all of the applied stress is deemed to contribute in the creep microstructural degradation (Holzer, 2010). Therefore, only that fraction of the applied stress which surpasses the total internal stress resistant force provided from desired microstructural parameters does effectually plays a role to the microstructural deterioration. This material internal deformation resistant stress which plays a role to retard the microstructural degradation is called material back stress; and has enabled the development and the application of Orowan back stress concept (Holzer and Kozeschnik 2008). However, this model has several limitations and makes a number of assumptions regarding the interactions between dislocations, precipitates and the grain boundaries.

Therefore, more work is needed on the development of physical models to link microstructural information to the measured mechanical properties. Table 4.5 shows the Orowan back stress values manifesting from the microstructural features that act as obstacles (precipitates, grain boundaries and dislocations) for dislocation movement in the material.

Table 4.5: Orowan Back Stress Contributions from the Different Microstructural Features (Holzer and Kozeschnik, 2008)

Precipitate Hardening (PH)	$\sigma_{Or} = \frac{0.8MGb}{\lambda}$ $\lambda = \sqrt{\frac{\ln 3}{2\pi N_V \bar{r}} + 4\bar{r}^2} - 1.63\bar{r}$	(1)	Where: σ_{Or} ≡ Orowan stress λ ≡ Mean 2D surface-to-surface interparticle spacing M ≡ Taylor factor (3) G ≡ Shear modulus (65 GPa) b ≡ Burgers vector (2.5 x 10^{-10} m) $\bar{r} = \frac{\bar{d}}{2}$ ≡ Mean particle radius of precipitates
Sub-Boundary Hardening (SBH)	$\sigma_{sg} = \frac{10Gb}{\lambda_{sg}}$	(2)	Where: σ_{sg} ≡ SBH stress λ_{sg} ≡ Elongated subgrain short width
Dislocation Hardening (DH)	$\sigma_\rho = 0.5\ MGb\sqrt{\rho_f}$	(3)	Where: σ_{sg} ≡ DH stress ρ_f ≡ Free dislocation density

Figure 4.30 shows the calculated Orowan back stress for each microstructural region. The total back stress values were calculated using equations from Table 4.8. Each microstructural contribution (precipitates, dislocations and micro-grains) were summed up linearly to produce the stacked bar chart shown in Figure 4.34. Using this very simplistic model, it was noted that the virgin P91 parent material had the highest calculated back-stress of 800 MPa, while the creep-aged X20 parent material had the lowest calculated back-stress of 420 MPa. The dislocations had the largest contribution to the calculated back stress.

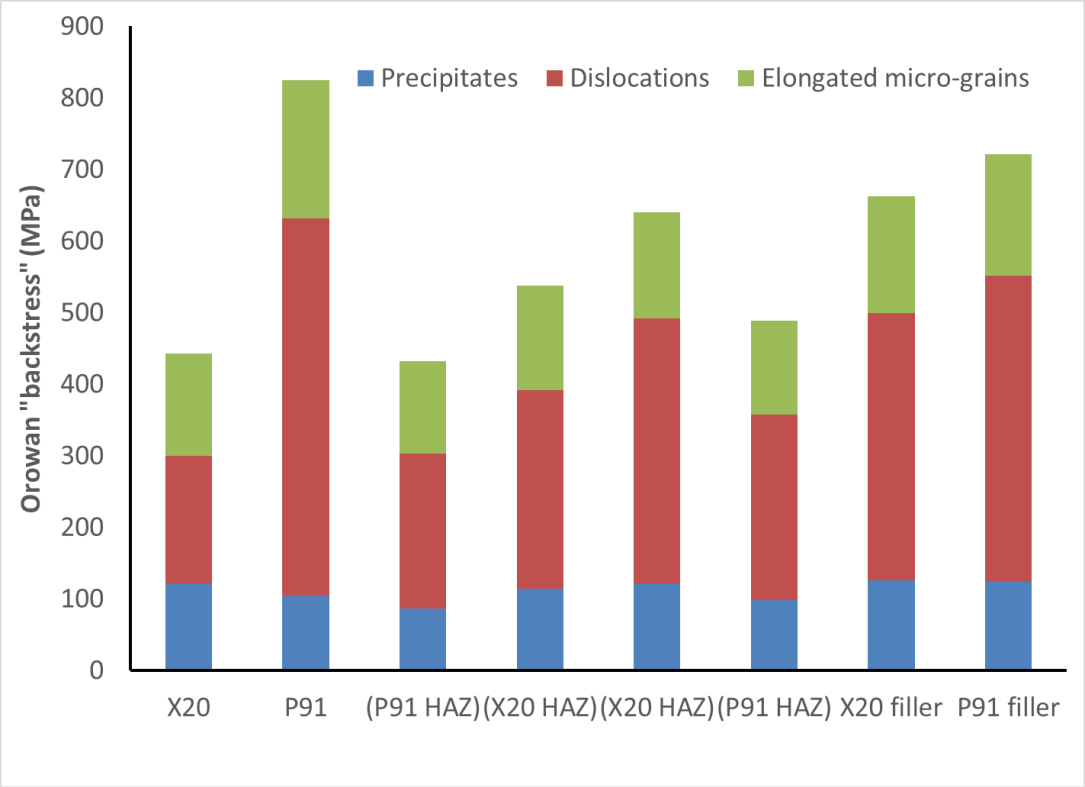


Figure 4.30: Total Orowan backs tress contributions for the different microstructural regions.

The assumption of a linear summation of the back-stress contributions necessitates a consideration for each microstructural feature separately. In addition, the measurements relative to a reference standard could be compared. Figure 4.31 shows the Orowan back stress contribution (σ_i) for each microstructural feature separately, relative to the virgin P91 parent material for comparison purposes.

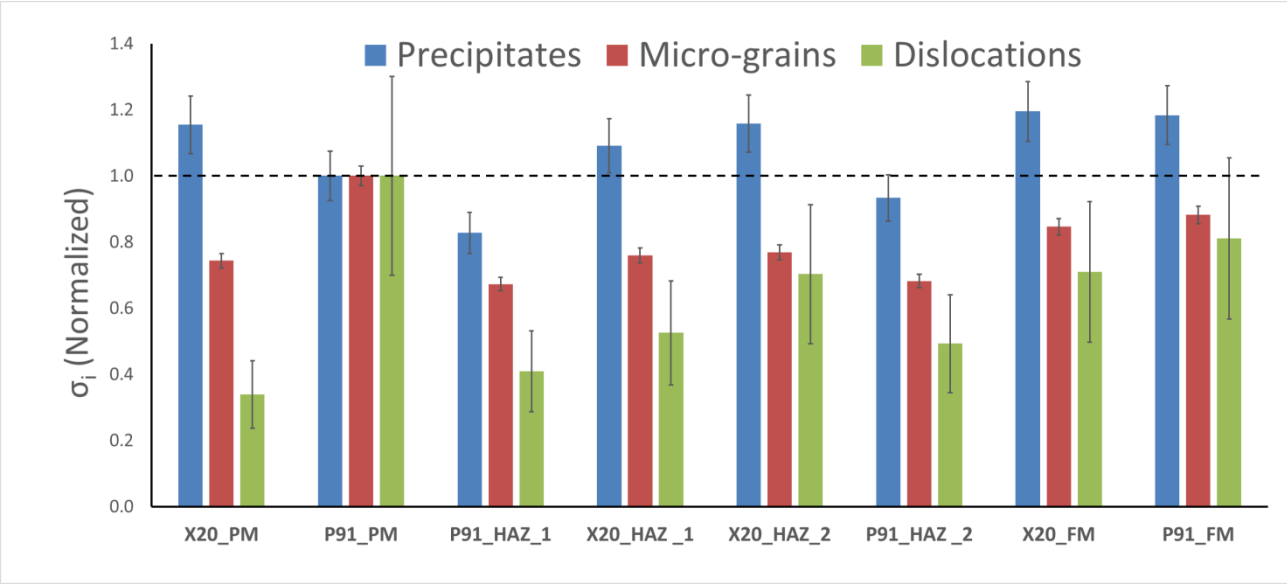


Figure 4.31: Normalised microstructural values for different weldment regions. A dotted line represents a visual aid to compare each material features state relative to the normalisation in which a new P91 material is assigned a value of 1.

The dislocation density for the virgin P91 material is the highest while the dislocations contribution to the Orowan strength in the creep-aged X20 material is only 35% of that value. The precipitate contribution to the Orowan strength is higher for the X20 material, due to the higher phase fraction of carbides, thus the inter-particle spacing is lower. The Orowan strength for the WM is higher than the virgin P91 PM, due to the smaller size of the precipitates in this region. The micro-grain contribution to the Orowan strength is lower in all the weldment regions as compared to the virgin P91 material.

Based on the Orowan back stress contribution model, it is apparent that the virgin P91 parent material had the highest calculated back-stress (800 MPa). The creep-aged X20 parent material had the lowest calculated back-stress (420 MPa). Dislocation density had the largest contribution to the calculated back-stress value. These findings are consistent with the results presented by Abe, (2008), Holzer, (2010) and Marx, (2016).

4.6 Diffusion Chemical Analysis

Welding of dissimilar materials can result in chemical elements diffusing across the weld fusion line due to concentration gradients. Elements such as C can diffuse from lower Cr base metal to higher Cr weld metal to form Cr-rich precipitates such as chromium carbides (You *et al.*, 2001). Carbon migration can result in negative undesired properties on mechanical and creep strength of the weldment at high temperatures, leading to premature failure. Therefore, it is vital to determine and quantify any diffusion that may have occurred in the dissimilar joints analysed in this research study. EDS chemical analysis with the objective of evaluating the diffusion patterns of C and Cr elements was performed. The results confirmed that the Cr analysis of both the X20 and P91 parent materials comprised the required concentration of Cr as per EN standards (BS EN 10216-2, 2002) specification. The results did not reveal any noticeable Cr diffusion across the dissimilar fusion lines (X20 Parent Metal - P91 Weld Filler Metal) and (P91 Parent Metal – X20 Weld Filler Metal) as illustrated in Figure 4.32.

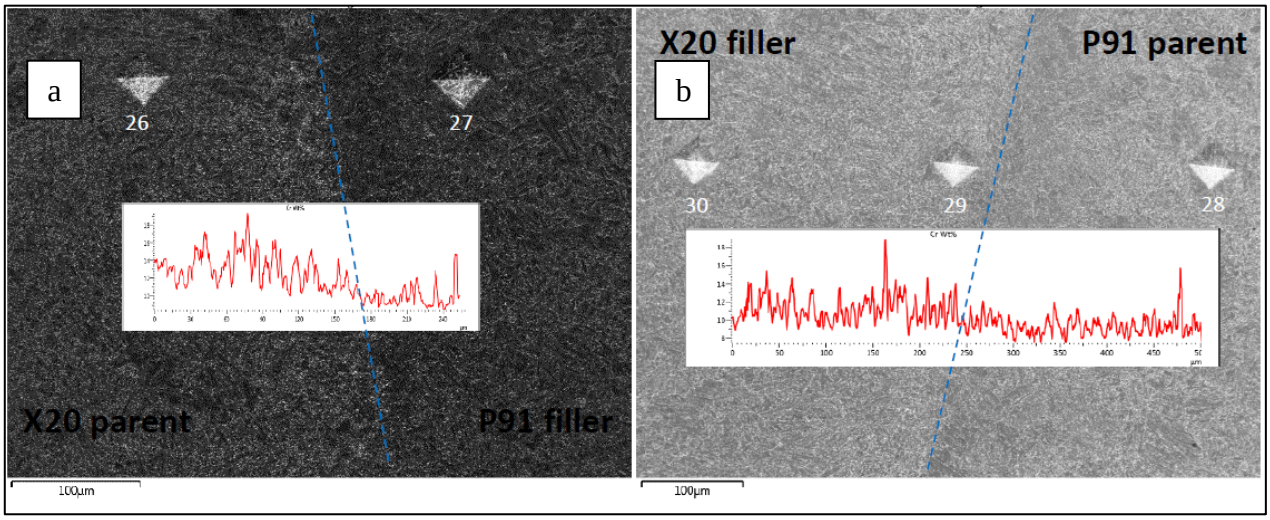


Figure 4.32: EDS chemical analysis on the micrograph samples plotting the chromium concentration across dissimilar X20 Parent Metal - P91 Weld Filler Metal, and P91 Parent Metal - X20 Weld Filler Metal cross welds. Blue intermittent straight line indicates the position of the weld-fusion line.

There is a noticeable contrast difference across the fusion line as detected by secondary electron imaging, and the measured Cr-content is presented in Table 4.6.

Table 4.6: EDS Chromium Content Measurements

	Weldment Region	**Cr (wt.%)**
(a) X20 Parent Material Weld Joint Side Sample	X20 parent material	12.2
	P91 weld filler material	9.3
(b) P91 Parent Material Weld Joint Side Sample	P91 parent material	9.2
	X20 weld filler material	11.1

The EDS line profiles for Fe showed an inverted profile compared to that of Cr which is expected based on the specification from EN standards (BS EN 10216-2: 2002).

Carbon (C) migration was analysed and quantified by using SEM secondary electron imaging and nano-indentation hardness measurements across the fusion line. Figure 4.33(a) shows the secondary electron images for fusion line regions where dissimilar materials are in contact (left). Local measurements of the precipitate phase fractions using image analysis and elemental analysis using EDS were also carried out to investigate the "carbon denuded zone" at the fusion line. The position of weld-fusion-line is seen through the change in contrast of a secondary electron image. This position corresponds with the micro Vickers hardness measurements that were presented and discussed in detail in Section 4.3.2. The nano-indentation measurements (60 µm spacing) followed the same profile as

the Vickers hardness measurements. From these measurements, there was no clear indication of a "soft-zone" on either side of the dissimilar fusion lines.

High-resolution SEM images were taken and processed to measure the precipitate phase fraction as a function of position over a sliding area 7 × 7 μm, as shown on the coloured image in Figure 4.33(b). The phase fraction increased from the P91 to X20 material as evidenced by the change in colour [dark blue = 0; yellow: 12 vol.%]. The EDS elemental line profile showed an increase in the Cr content from the P91 side (~9 wt.%) to the X20 side (~12 wt.%).

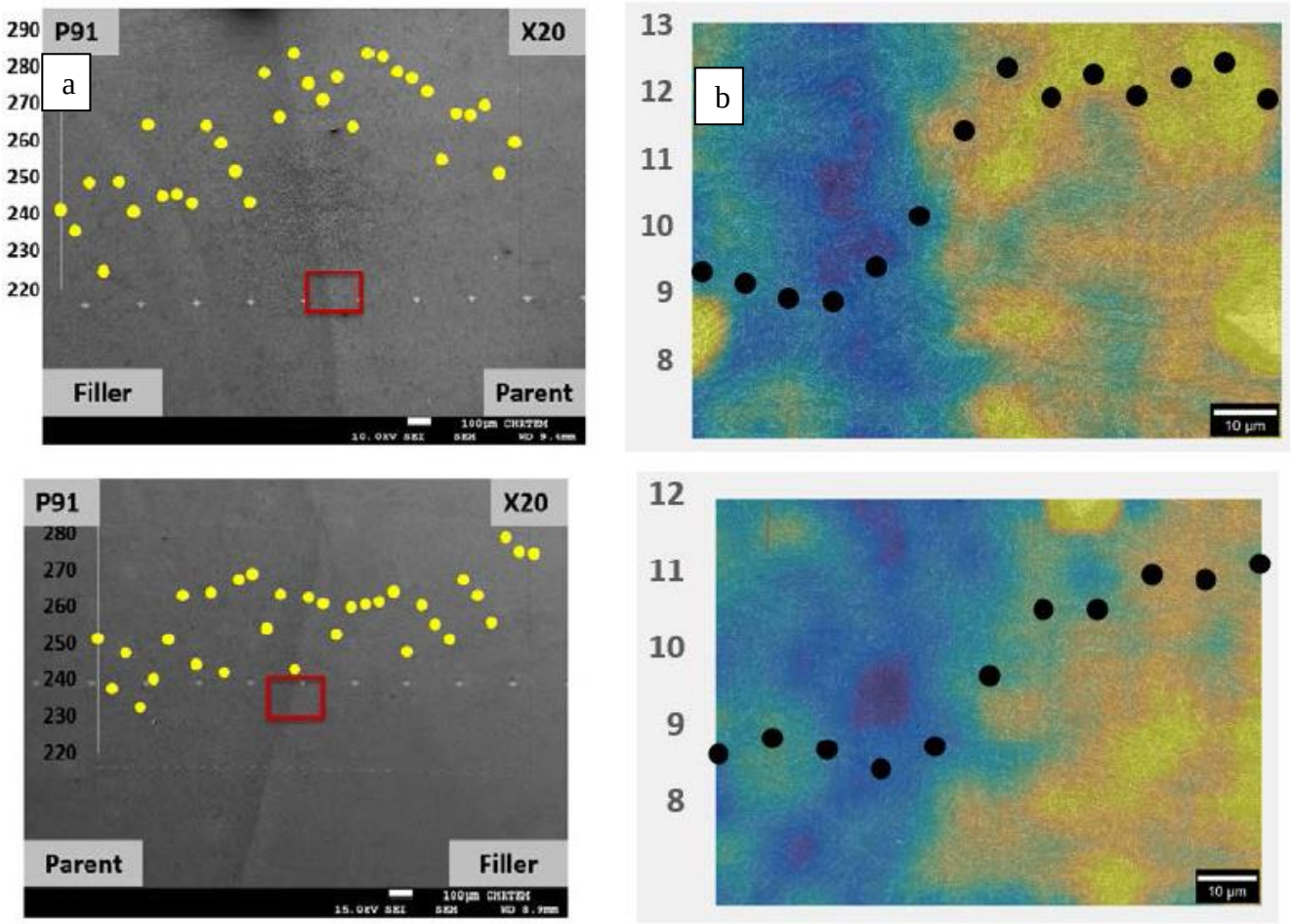


Figure 4.33: *(a)* Secondary electron images of fusion-lines for dissimilar weldments, with the nanoindentation hardness measurement overlay. *(b)* Precipitate phase fraction colour plot (12 vol% max), with EDS-profile analysis (Cr wt.%) overlay for the fusion-line region, indicated with the red rectangle on the left. [dark blue: 0; yellow: 12 vol.%]

Both the precipitate phase fraction and the EDS measurement indicated the presence of a localised "denuded zone" that was ~20 μm in width. The effect of this tiny denuded zone was also not evident in measured mechanical (tensile and Charpy impacts) tests. This negligible localised carbon denuded zone found in this investigation is in agreement with theoretical studies of determining the chemical

potential gradient of carbon in dissimilar cross weld joints using the Kirkady model (Elder, 2011; Kirkaldy and Young, 1987).

The model assumes there is equilibrium that locally occurs at the joint fusion-interface, and that the chemical potential of carbon is derived from instantaneous chemical composition-index. The elements (i.e. chromium, molybdenum, and vanadium) that promote the formation of carbides decrease the chemical-potential of carbon, and the precipitation of carbides in high-alloy steel alters the solubility limit of carbon in the ferrite phase, and may slow down its diffusivity in steels. Carbon activity for diffusion is determined by all elements present in the steel and is driven by thermodynamics (Elder, 2011; Kirkaldy and Young, 1987).

Interstitial carbon atom diffuses down the chemical potential gradient across a dissimilar steel joint from low Cr concentration to high Cr concentration as reportedly found by Dawson (2012), and Kirkaldy and Young (1987). Findings by Dawson (2012), Kirkaldy and Young (1987) are in support of what was observed in this research study; whereby a localised "denuded zone" of approximately 20 μm in width was noticeable. The denuded zone was considered negligible because of its size. This was attributed to a small chemical composition variation between P91 and X20 materials, particularly the Cr and C contents that ranged from 9-12 wt.% for Cr and 0.1 – 0.2 wt.% for C.

In summary, based on the microstructural characterisation observations, there is no noticeable difference on the ICHAZ microstructure as a result of using either X20 or P91 weld filler. Therefore, it is conclusive that both weld fillers (X20 and P91) are compatible to fuse the virgin P91 to creep aged X20 materials.

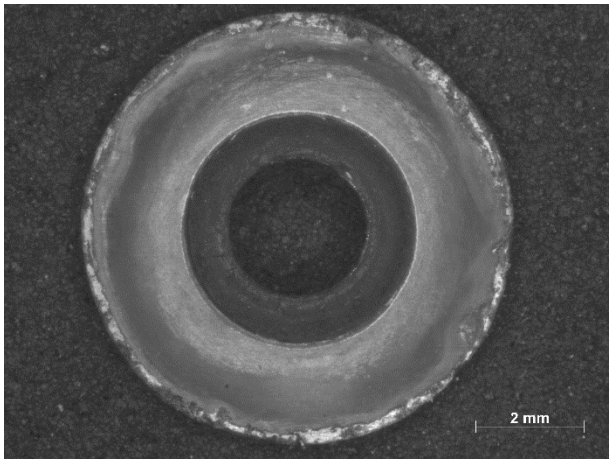
4.7 Creep Testing

Creep testing is often conducted to determine life performance of the materials at high temperatures. The two types of creep tests that were carried out in this study are the small punch creep test (SPCT) and the uniaxial creep test.

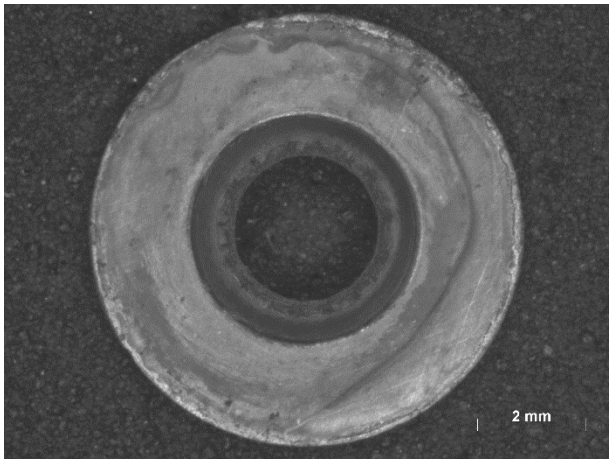
4.7.1 Small Punch Creep Tests

SPCT test is a small-scale testing method that is gaining momentum because of the size of the sample required to conduct the test. Images of the tested samples are shown in Figures 4.34 - 4.35. The difference in the diameter of the punched hole is not a function of the sample, but rather a characteristic of the test and equipment. Once the sample fails, the punch rod is pushed through the sample, forcing the punched hole to be larger after the completion of the test. The position where the punch rod finally comes to rest differs slightly between platforms, resulting in different hole diameters. However, this does not influence the test results.

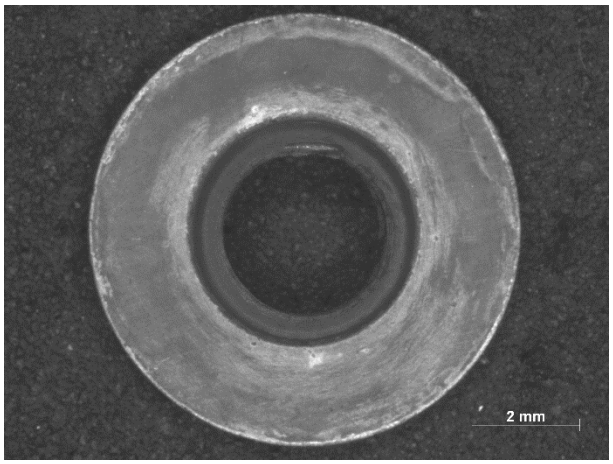
P91 PM



P91 WM



FM P91_FGHAZ P91



FM P91_FGHAZ X20

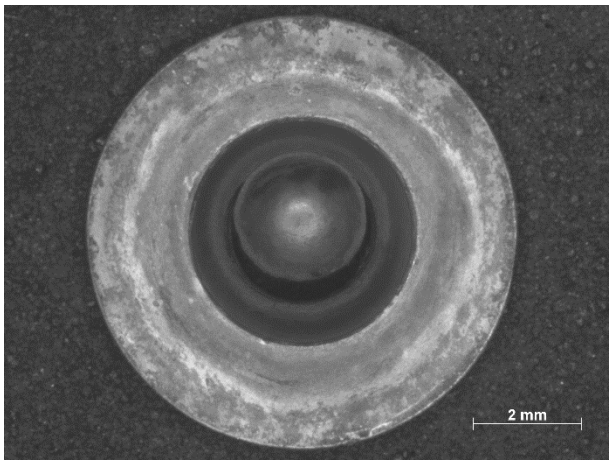


Figure 4.34: Tested SPCT specimen of P91 parent material and P91 WM and FGHAZ samples.

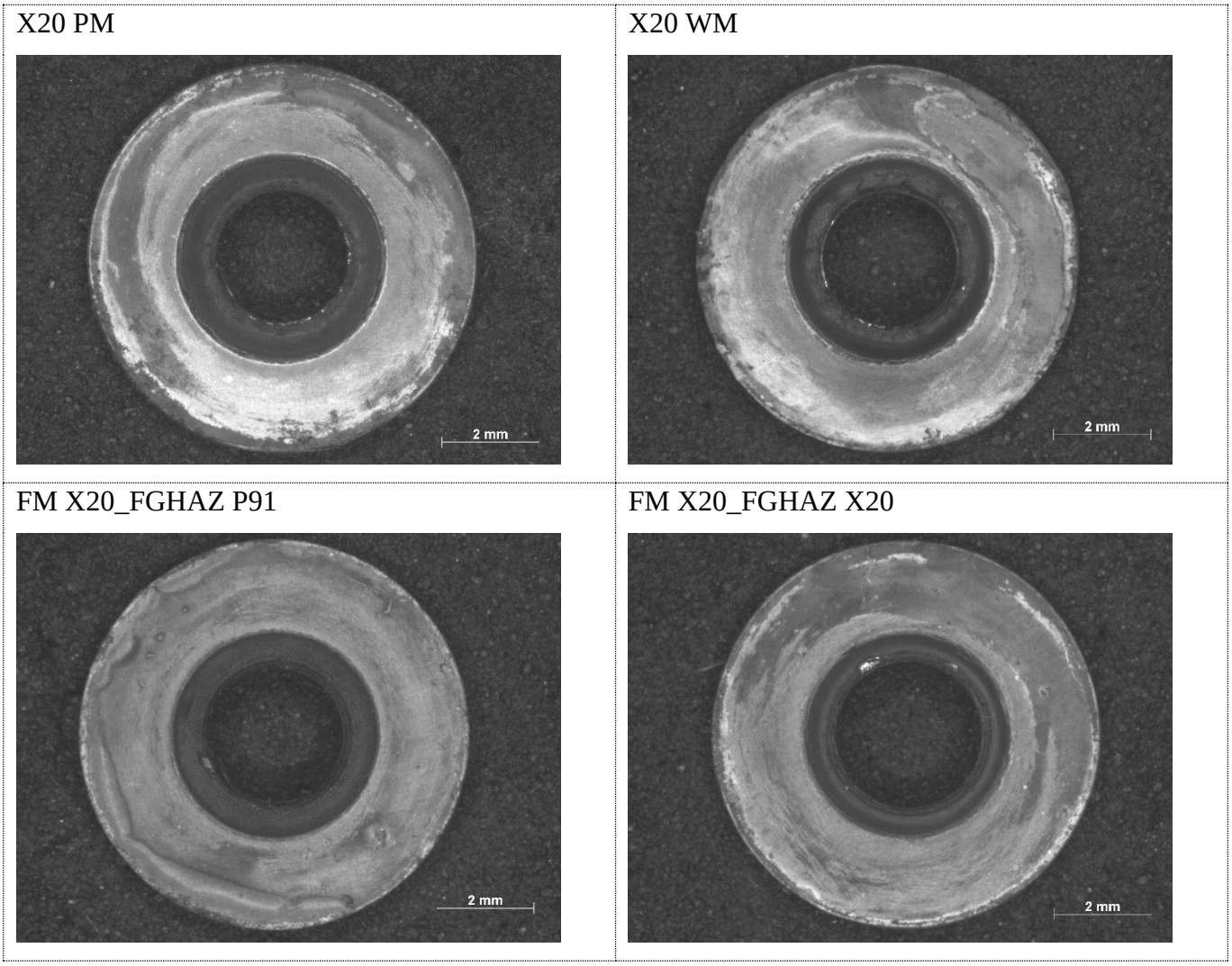


Figure 4.35: Tested SPCT specimen of P91 parent material and P91 filler metal samples.

A single test per specific location of the welded joint was carried out in this study considering that the repeatability of small punch tests carried out within an individual test laboratory or using the same testing equipment is very good, and reportedly found to be perfectly comparable with the repeatability of results from the conventional uniaxial creep tests (Eskner and Sandström, 2004; Ule *et al.*, 1999).

The creep deflection versus time curves for all the tests are illustrated in Figure 4.36. Rupture times of all tested samples are summarily presented in Table 4.7. From the obtained creep curve graphs, it is noted that the initial steep deformation was as a result elastic-plastic deformation mechanism.

.

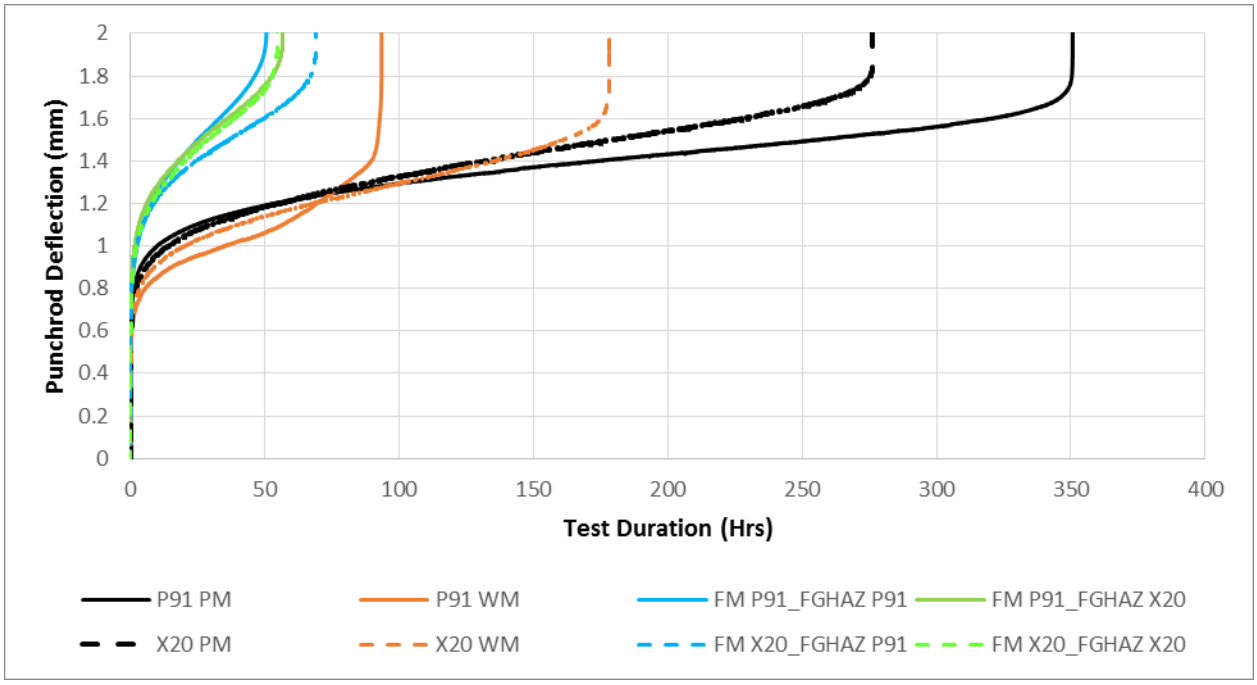


Figure 4.36: Small Punch Creep Test curves for all 8 samples (PM, X20 PM, P91 WM, X20 WM, P91 FGHAZ adjacent to P91 WM, P91 FGHAZ adjacent to X20 WM, X20 FGHAZ adjacent to P91 WM, and X20 FGHAZ adjacent to X20 WM specimens) at 276 N and 625°C.

The P91 parent material achieved the highest rupture time, followed by the creep aged X20 parent material. These findings were anticipated since P91 parent material has high creep strength compared to X20 material. According to EN 10216-2:213 (E) specification, the rupture creep strength for 10 000 hours at 625°C for P91 is 92 MPa while that for X20 is 67 MPa. The other reason for this parent material SPCT results is that X20 material has already operated for 167303 hours at 539°C and 17.1 MPa pressure resulting in a calculated operating hoop stress of 71 MPa where 15% creep life had already been exhausted (consumed), based on the theoretical creep life calculations using operating conditions and ISO-20% material properties.

A close examination of the weld metal revealed that the X20 filler metal outperformed the P91 filler metal by a difference of 84.6 hours since X20 weld ruptured at 176 hours and P91 weld ruptured within 91.4 hours. This difference in rupture time is attributed to the short testing duration and high stress levels that did not allow diffusional creep mechanism from taking place.

All the FGHAZ samples reached similar rupture times, ranging from 49 to 68 hours. The low rupture times of the HAZ samples does not make it possible to draw conclusions regarding the performance of materials because of the small differences between their rupture times**.** This finding of similar rupture times irrespective of the weld filler chemical composition can be attributed to no significant chemical diffusion

found between the different weld fillers cross both weldment samples, only a tiny denuded zone of approximately 20 μm in width was observed, and could not even be detected by the nanoindentation measurements. This means that there was no substantial alteration in the chemical composition of the HAZ that can alter the mechanical properties of the HAZ. It is therefore evident that the mechanical properties of the HAZ for these weldments will only be altered by the welding heat input. For both welded joints, the measured welding heat input was the same, in a range between 0.12 – 0.25 kJ/mm for MMA welding technique region using the same welding procedure.

From all cross weldments' regions (PM (i.e. X20 and P91), HAZ and both weld filler materials (i.e. X20 and P91) that were subjected to SPCT, it was evident that the lowest creep life was obtained on the HAZ (i.e. FGHAZ). This finding is in covenant with the findings by Abel *et al.* (2008) and Masuyama (2000) who reported that the fine-grained area of the HAZ is considered as the most weakest link in the weld-joint under creep application (Abe *et al.*, 2008; Masuyama, 2000). This FGHAZ is commonly known to experience a premature failure due to the mechanism called Type-IV creep cracking (Abe *et al*., 2008; Masuyama, 2000; Zhang *et al.*, 2020).

Table 4.7: Small punch creep test rupture times of all the samples

Sample Location	SPCT Rupture Time (Hrs)
P91 PM	349
X20 PM	276
X20 WM	176
P91 WM	91.4
FM P91_FGHAZ P91	49
FM P91_FGHAZ X20	57
FM X20_FGHAZ P91	68
FM X20_FGHAZ X20	54

In summary, based on the SPCT results focusing on the FGHAZ regions specimen results, there is no distinctive difference on the creep life performance when using either P91 or X20 weld filler metal. All the FGHAZ samples reached similar rupture times, ranging from 49 to 68 hours irrespective of the weld filler material grade used. This makes it impossible to draw conclusions regarding the performance of materials because of the small differences between their rupture times.

4.7.2 Uniaxial Creep Tests

Uniaxial creep testing method has been developed to determine the creep rupture strength for materials that are designed to operate at elevated temperature. Uniaxial creep test was conducted in this research study to obtain and analyse the creep performance of the cross-weld samples.

Figures 4.37 - 4.38 show the locations where all 8 cross weld creep tested samples ruptured, on the X20 HAZ side of the weldment. The consistency of failure location on the X20 creep side can be attributed to the lower creep strength of X20 compared to that of the P91 material. According to EN 10216-2:2013 (E) specification, the creep-rupture strength for 10 000 hours at 625°C for P91 is 92 MPa while that for X20 is 67 MPa. The other attributing factor for the failure to be on the X20 side is that X20 material has already been in creep application service for 167303 hours in which 15% of its creep life was consumed as informed by the theoretical creep life calculations using operating conditions and ISO-20% material properties. It is worth noting that all failures occurred in the FGHAZ, referred to as the Type-IV cracking, as expected, since the fine-grained region of the HAZ possesses the lowest creep life in weldments during creep application as a result of its creep inferior microstructure (Abe *et al.*, 2008; Masuyama, 2000).

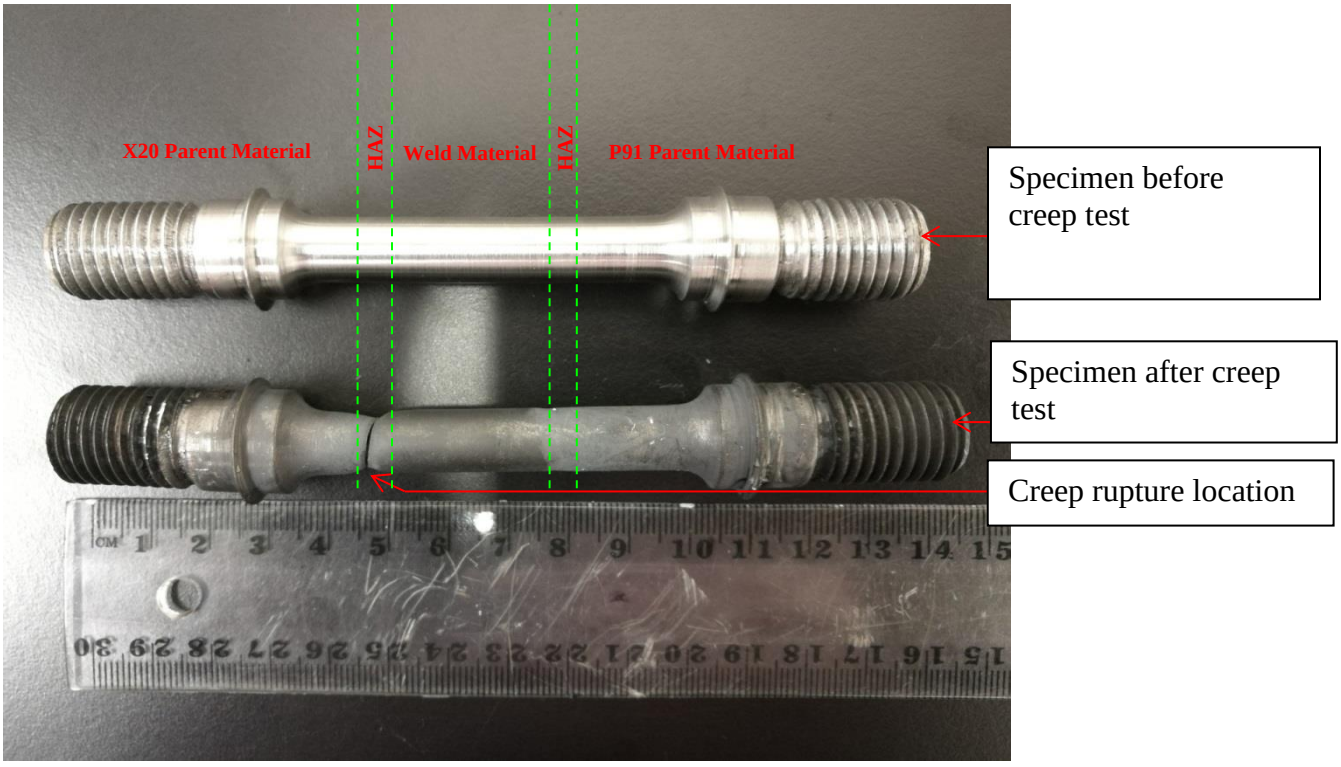


Figure 4.37: Photograph of the creep test specimens showing the creep rupture location (X20 HAZ location side)

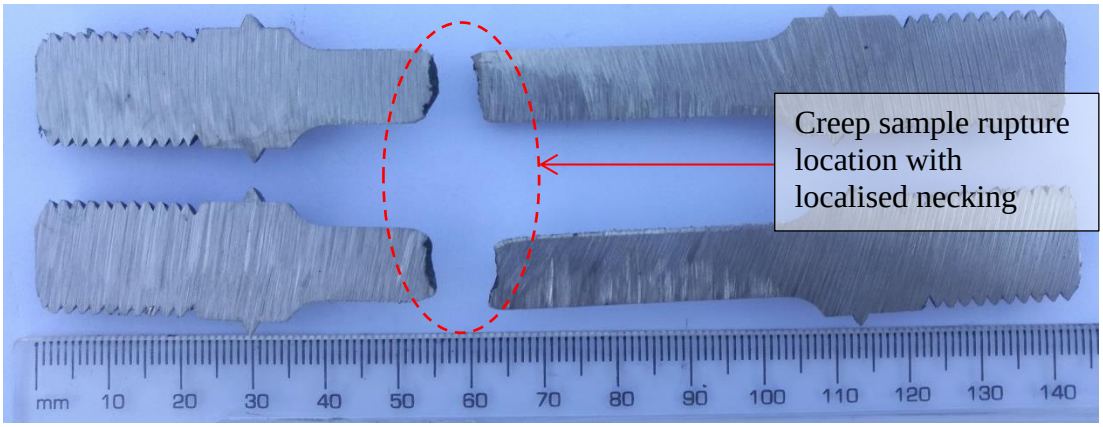


Figure 4.38: Photograph showing longitudinal-section view of the creep tested and ruptured specimens with evidence of localised necking adjacent to ruptured location.

Figure 4.39 shows creep curves (creep strain vs time) obtained for cross weld samples of dissimilar welds of creep aged X20 parent material welded to the new P91 parent material using X20 and P91 weld fillers at and their duplicates at 63 and 80 MPa. All these creep tests were conducted at a constant test-temperature of 610°C. The plotted creep curves indicate how the creep-strain increases with time in hours.

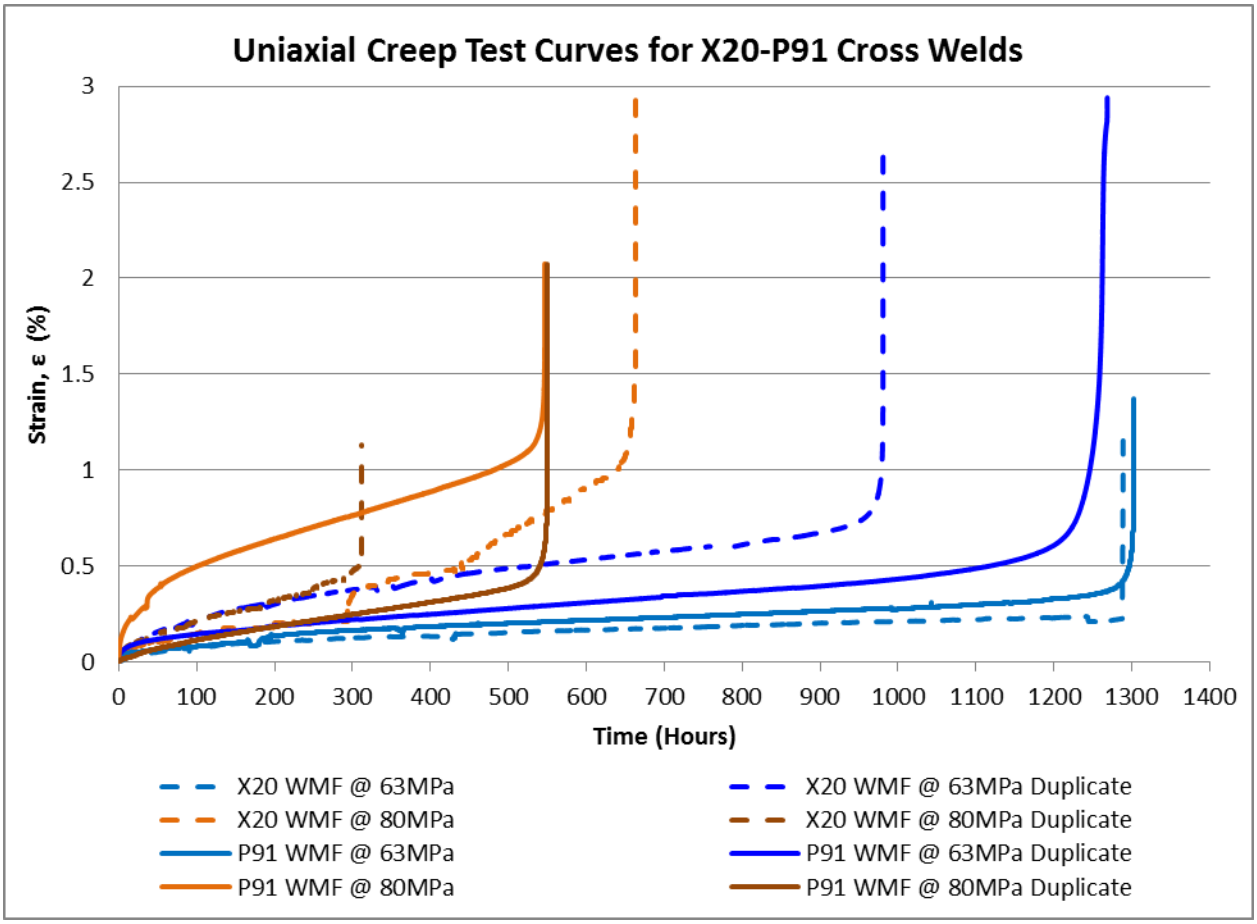


Figure 4.39: Creep curves (creep strain Vs time) for creep aged X20 PM – X20 weld filler – new P91 PM at 60 MPa and its duplicate, creep aged X20 PM – X20 weld filler – new P91 PM at 80 MPa and its duplicate, creep aged X20 PM – P91 weld filler – new P91 PM at 60 MPa and its duplicate, creep aged X20 PM – P91 weld filler – new P91 PM at 80 MPa and its duplicate cross weld samples.

Based on the observations on Figure 4.39, it can be deduced from the creep curves that the total strain accumulation at rupture ranged from 1.15 % - 3.02 %, and the creep rupture time ranged from 312.07 hours – 1302.39 hours. A considerable increase of creep-strain at the last stages of the creep curves can be attributed to nucleation of voids and local deformation known as necking as previously shown in Figure 4.38.

For comparison purposes, additional uniaxial creep test was carried out on the creep aged X20 parent metal from the same material batch that was used for the cross weld samples, to determine and compare the effect of welding on creep aged material which is technically known as the weld reduction factor on creep aged material. The parent material that was creep tested was only of the X20 and not of P91 because all 8 creep tests that were conducted on the dissimilar cross weld samples failed on X20 PM side consistently on its FGHZA region and no failure was experienced on the P91 parent material side. Figure

4.40 gives creep strain vs time for creep aged X20 parent metal plotted together with the creep curves for the cross-weld samples. From the results presented in the figure, it is apparent that the aged X20 parent material had longer creep rupture time (2774.80 hours) compared to that of the cross weld samples (ranges from 312.07 hours – 663.19 hours) tested at the same stress condition (80 MPa). The percentage weld reduction factor (%WRF) was calculated, and it ranged between 11 – 24%.

%WRF = (Welded Base Metal Creep Life $_{\text{lower range limit}}$ / Base Metal Creep Life) x 100 %

= (312.07 hours / 2774.80 hours) x100%

= (0.11) x 100 %

= 11 %

and,

%WRF = (Welded Base Metal Creep Life $_{\text{high range limit}}$ / Base Metal Creep Life) x 100 %

= (663.19 hours / 2774.80 hours) x100%

= (0.24) x 100 %

= 24 %

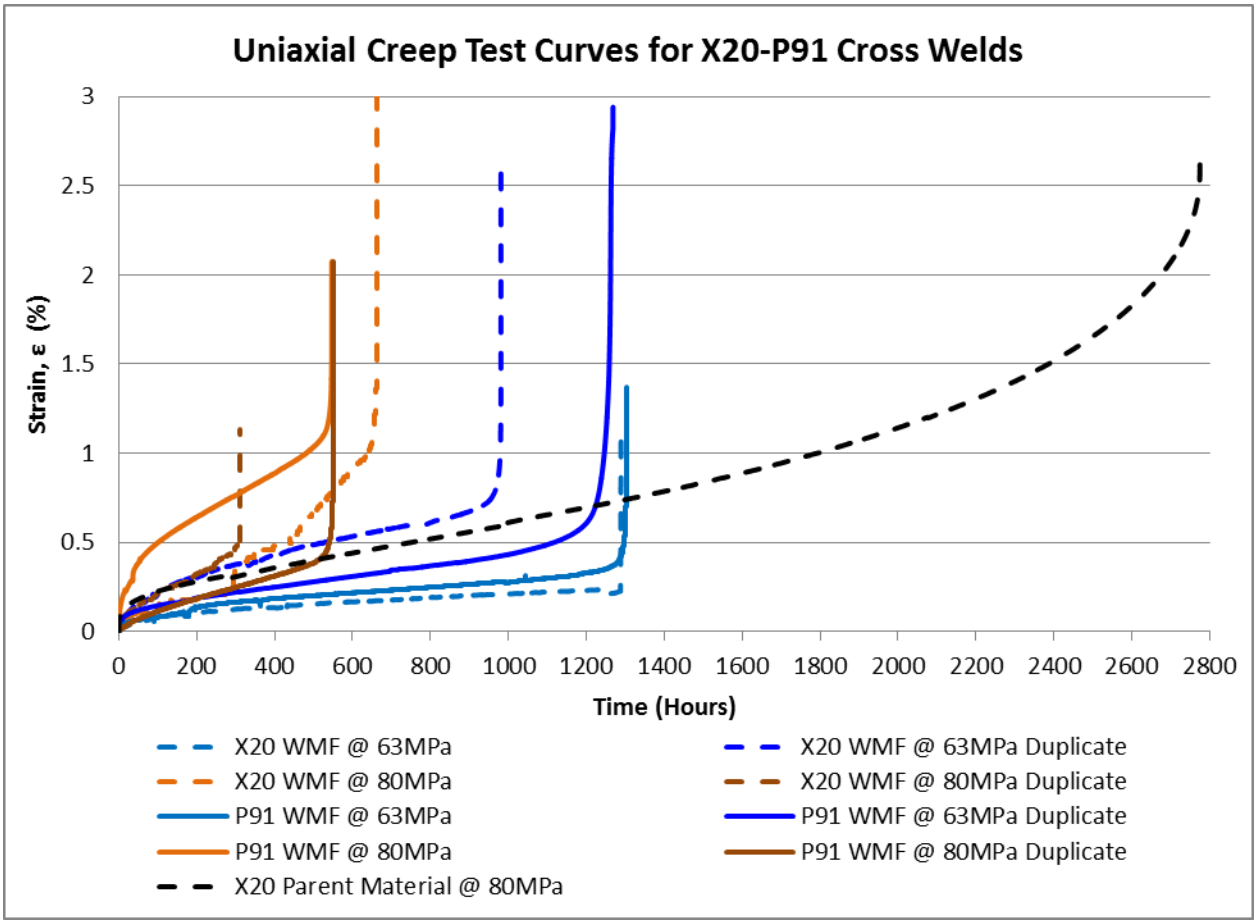


Figure 4.40: Creep curve (creep strain vs time) for creep aged X20 PM in comparison with creep aged X20 PM – X20 weld filler – new P91 PM at 63 MPa and its duplicate, creep aged X20 PM – X20 weld filler – new P91 PM at 80 MPa and its duplicate, creep aged X20 PM – P91 weld filler – new P91 PM at 60 MPa and its duplicate, creep aged X20 PM – P91 weld filler – new P91 PM at 80 MPa and its duplicate cross weld samples.

The creep parameters (minimum creep rate; $\acute{\varepsilon}_{min}$ (s^{-1}), strain at minimum creep rate; $\varepsilon_{\acute{\varepsilon}min}$ (%), time at minimum creep rate; $t_{\acute{\varepsilon}min}$ (hours), time of rupture; t_R (hours) and strain at rupture; ε_R (%)) for all tested specimens are summarily tabulated in Table 4.8;

Table 4.8: Uniaxial Creep Parameters for all ruptured samples

Creep Test Sample Name	Minimum creep rate; $\acute{\varepsilon}_{min}$ (s^{-1})	Strain at minimum creep-rate; $\varepsilon_{\acute{\varepsilon}min}$ (%)	Time at minimum creep-rate; $t_{\acute{\varepsilon}min}$ (hours)	Time of rupture; t_R (hours)	Strain at rupture; ε_R (%)
X20 WMF @ 63MPa	4.61×10^{-08}	0.21	1261	1289	1.15
X20 WMF @ 63MPa Duplicate	2.09×10^{-07}	0.67	901	981	2.64
X20 WMF @ 80MPa	1.65×10^{-07}	0.21	293	663	3.02
X20 WMF @ 80MPa Duplicate	4.00×10^{-07}	0.36	244	312	1.13
P91 WMF @ 63MPa	4.49×10^{-08}	0.27	994	1302	1.37
P91 WMF @ 63MPa Duplicate	1.20×10^{-07}	0.43	1006	1268	2.94
P91 WMF @ 80MPa	1.37×10^{-07}	0.64	201	547	2.08
P91 WMF @ 80MPa Duplicate	2.09×10^{-07}	0.34	451	550	2.08
X20 Parent Material @ 80MPa	1.51×10^{-07}	0.89	1603	2775	2.63

Based on these uniaxial creep test results, it is evident that the samples tested at lower stress of 63 MPa had longer creep rupture time (averaging at 1210 hours) while the higher test stress (80 MPa) samples had shorter creep rupture time (averaging at 518 hours). It is beneficial to note that when comparing the creep rupture time of X20 weld filler cross weld samples against P91 filler cross weld samples at constant test parameters (temperature and pressure), there was no obvious difference between the two samples. Therefore, the use of either X20 weld filler or P91 weld filler did not affect the creep rupture life of dissimilar welds between creep exposed X20 and new P91 as informed by the short-term creep assessments undertaken herein study.

Figure 4.41 illustrates the comparison of creep aged X20 PM creep test results (illustrated by a red dot) and the X20, PD 6525 creep life vs stress at 610°C. The comparison was done at a test stress of 80 MPa. In order to obtain the relevant theoretical creep sensitivity curves that considers that the creep tested X20 pipe has already been exposed to service conditions, creep life sensitivity calculations were carried out according to the ISO master creep curves equation constants specified in the British Standard PD 6525 for

Elevated Temperature Properties for Pressure Purposes Steels (BS PD 6525, 1990) using the steam operating conditions (610°C temperature and 17.1MPa pressure).

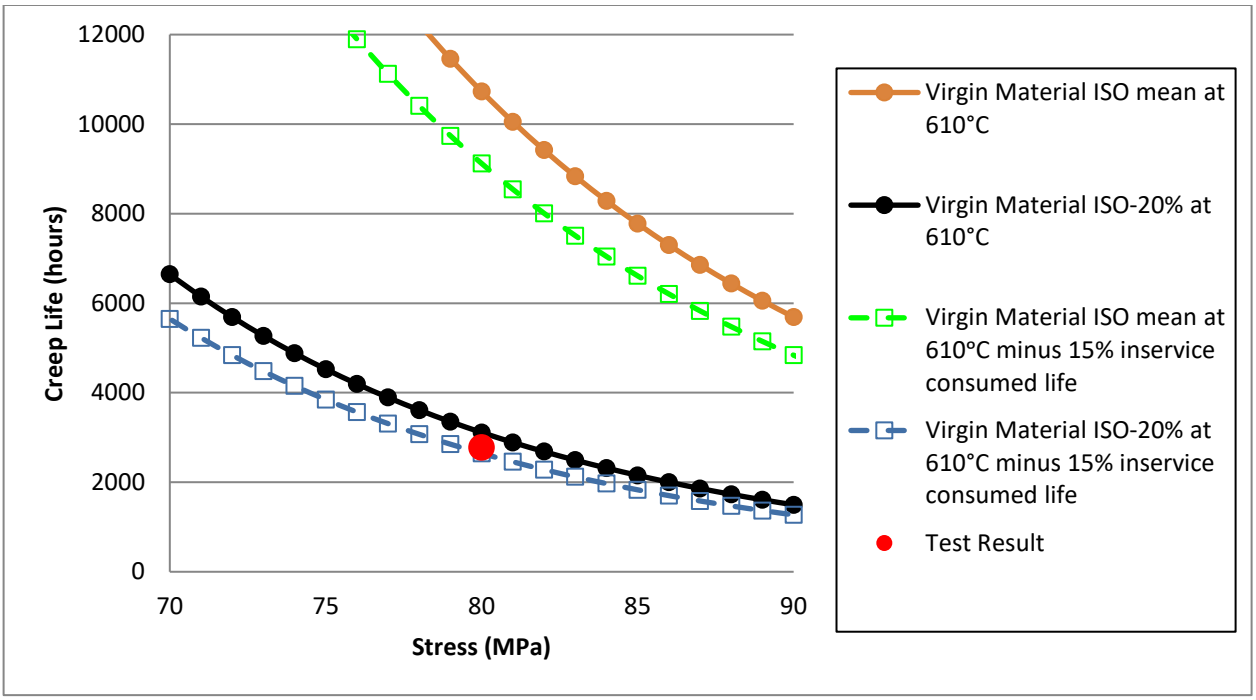


Figure 4.41: Creep sensitivity analysis curves for a virgin and for 15% creep aged X20 parent materials with the comparison of the creep aged X20 PM creep test results (illustrated by a red dot).

These calculations revealed that the X20 creep aged material was at 15% creep life exhaustion before it was subjected to laboratory uniaxial creep test. Based on these creep curves, it can be deduced that the tested creep aged X20 PM result (red dot on the graph) has ISO-18% creep properties. Further comparison shows that if this tested creep aged X20 material was a virgin material, the resultant creep test life would be approximately 3112 hours based on ISO-20% creep properties at 610°C and 80 MPa stress.

In summary, it is observed that the use of either X20 or P91 weld filler did not affect the creep rupture life of dissimilar welds between creep exposed X20 and new P91 based on the short-term creep tests and theoretical creep life sensitivity curves undertaken in this study.

4.8 Microstructural Characterisation After Uniaxial Creep Testing

Microstructural characterisation was carried out on the creep ruptured (failure) location of crept specimens to characterize the failure surface and changes in the microstructures.

Optical microscopy was utilised to characterise the failure area of the cross weldment and to analyse the failure morphology. For all creep tested samples, irrespective of the weld filler metal (X20 and P91 weld fillers) used, creep rupture of the cross weldment occurred on the X20 HAZ location side as shown in Figures 4.42 - 4.45. The reason of the failure location to be on the on the X20 creep aged side can be attributed to the occasional creep cavities (60 voids/mm^2) that were observed in the baseline replicas micrographs that were lifted on the pipe base metal samples before the commencements of this study's characterisation, as well as the lower creep strength on X20 compared to P91 material. According to EN 10216-2:2013 (E) code specification, the creep rupture strength for 10 000 hours at 625°C for P91 is 92 MPa while that for X20 is 67 MPa. In addition, the other reason for creep-rupture on the X20 material side is that X20 material has already operated in creep application in the plant and that resulted to the coarsening of the creep resistant precipitates (i.e. MX and $M_{23}C_6$), micro-grains and sub-structure as observed during the microstructure characterization compared to that of virgin P91 microstructure as previously presented on Table 4.5. This negative effect of coarsened precipitates on creep life has also been reportedly found by other researchers; Masuyama, (2000), Andrews et al., (1967), and Yardley, (2003).

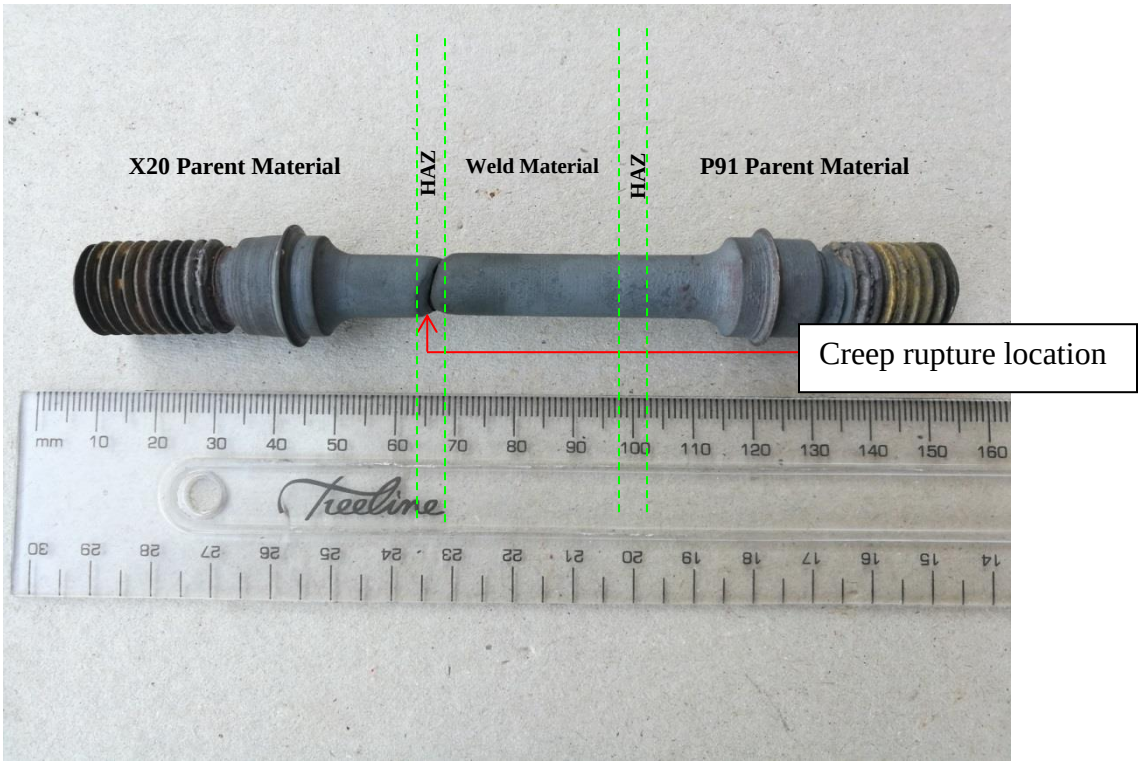


Figure 4.42: Photograph of the uniaxial creep test specimens showing the creep rupture location (X20 HAZ location side)

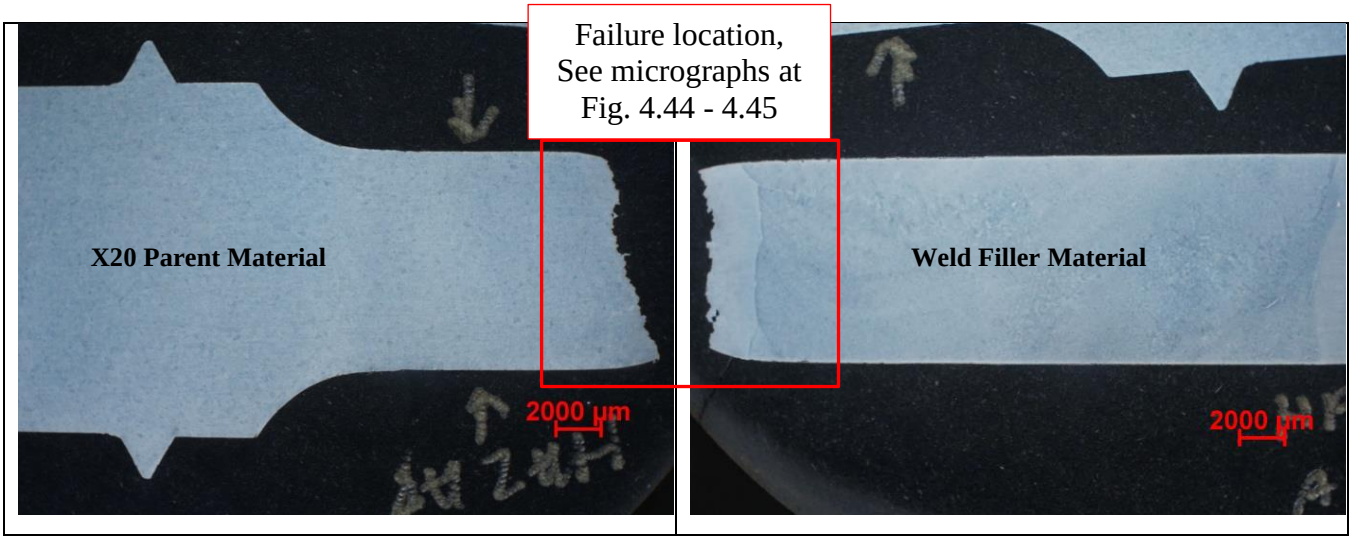


Figure 4.43: Photograph of a ruptured creep test specimen showing the polished and etched longitudinal sectional view at the failure location; on the X20 HAZ side. Necking of the creep test specimen is also observed adjacent to the failure / rupture location.

Figures 4.44 and 4.45 show the micrographs (at 50X and 500X magnification respectively) of the inter-critical heat affected zone (ICHAZ) at a location where the creep rapture / failure occurred. It is worth noting that all failures were experienced on the inter-critical HAZ (ICHAZ) as expected since this region

of the HAZ / inter-critical HAZ is known for being depleted from creep resistance microstructural features. When the weldment is subjected to creep application, it fails as a result of a failure mechanism called Type-IV creep cracking in this ICHAZ (Abe *et al.*, 2008; Masuyama, 2000; Zhang *et al.*, 2020).

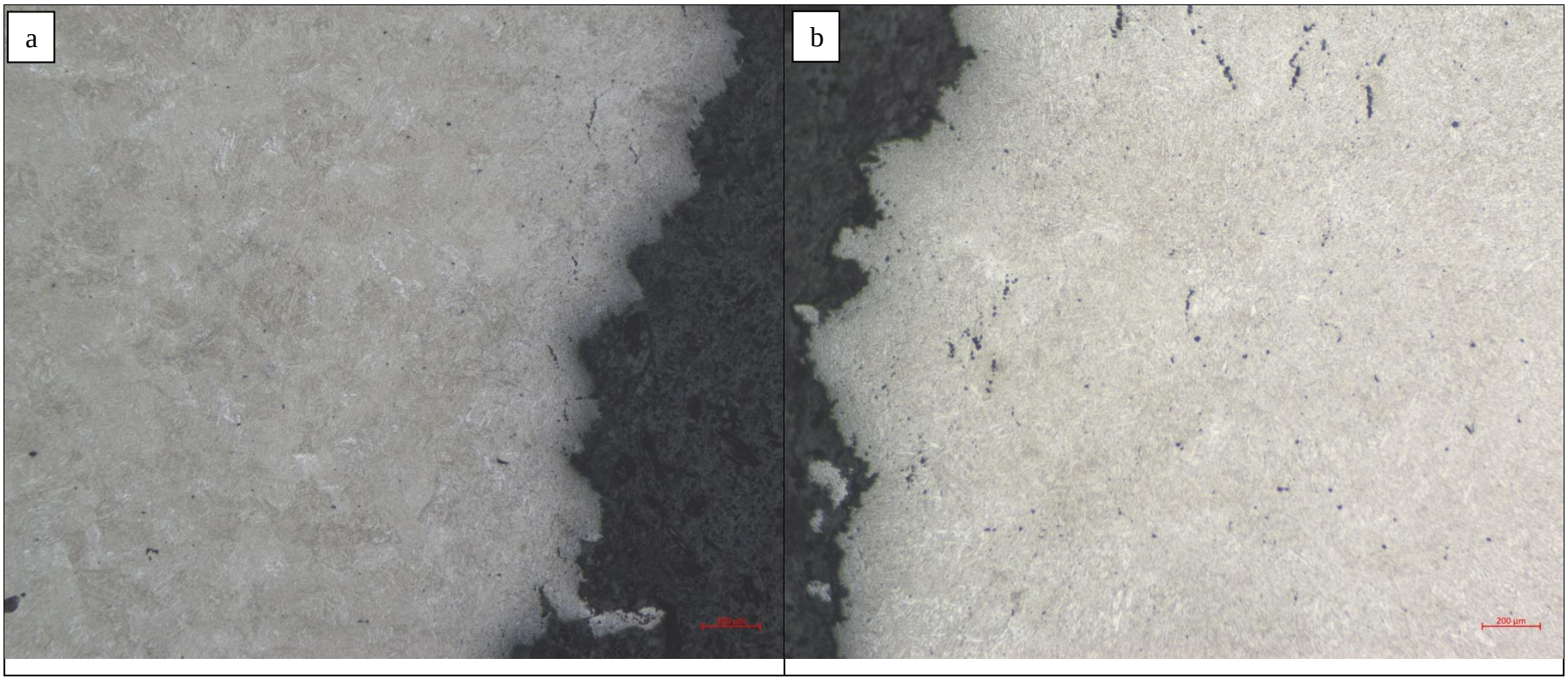


Figure 4.44: Micrograph of the longitudinal section view for the uniaxial creep tested specimen showing micro creep cracks and voids adjacent to the creep rupture location (ICHAZ on X20 material side), (a); X20 parent metal side, (b); P91 weld filler [Etched in Villella's reagent, 50X Magnification].

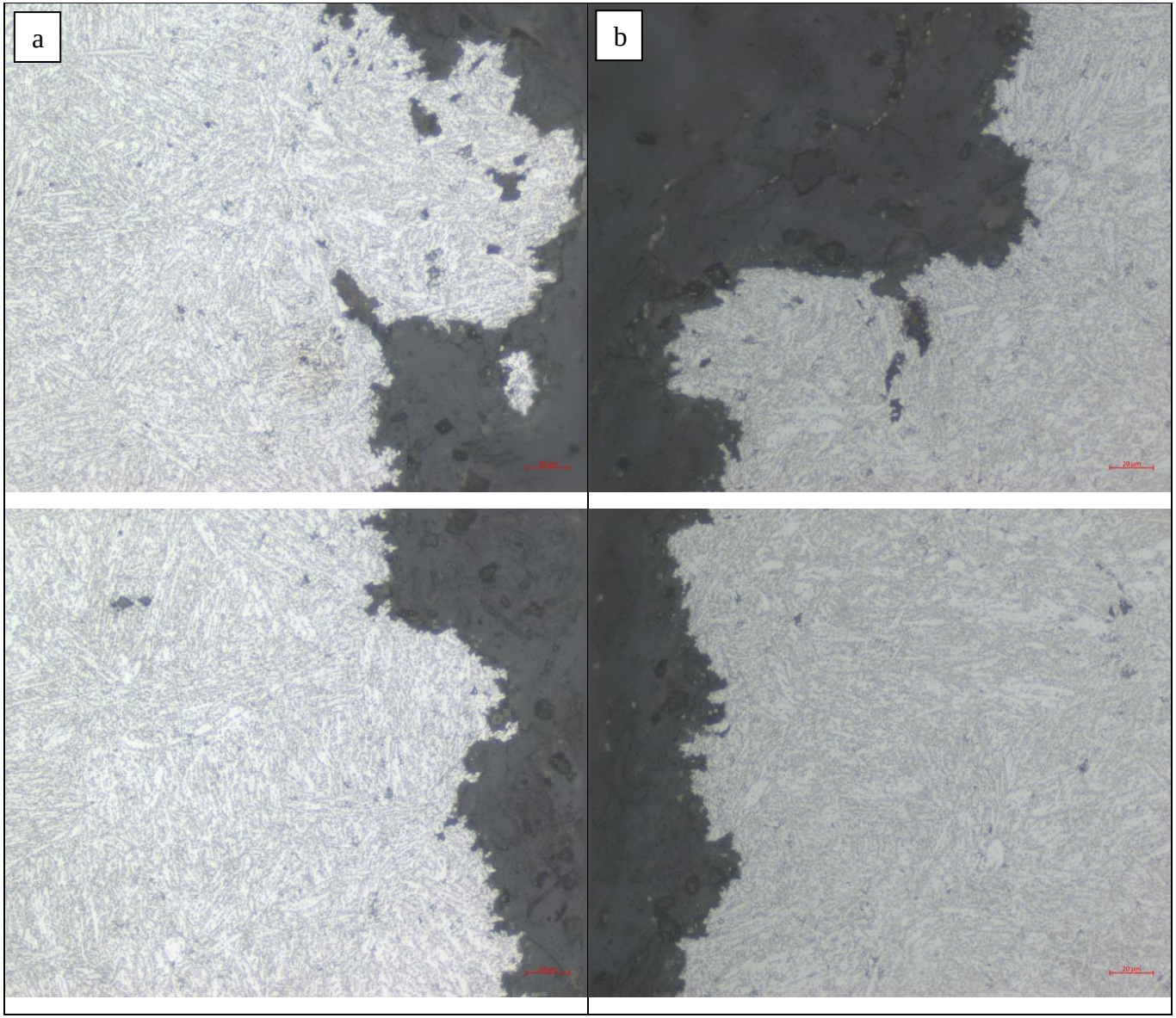


Figure 4.45: Micrograph of the longitudinal section view for the uniaxial creep tested specimen showing micro creep cracks and voids adjacent to the creep rupture location (ICGHAZ on X20 material side (a)) [Etched in Villella's reagent, 500X Magnification].

Stereo microscope images of the fracture surface of all creep ruptured specimen revealed similar features of the cup and cone ductile failure mode, with necking adjacent to the fracture surface, as shown in Figure 4.46. Ductile fracture occurred as a result of micro-void coalescence, due to plastic deformation. When ductile materials are loaded, uniform elongation occurs until the point of plastic instability is reached where necking starts to occur and de-cohesion of particle/matrix interfaces takes place (Milovic´, *et al*., 2013).

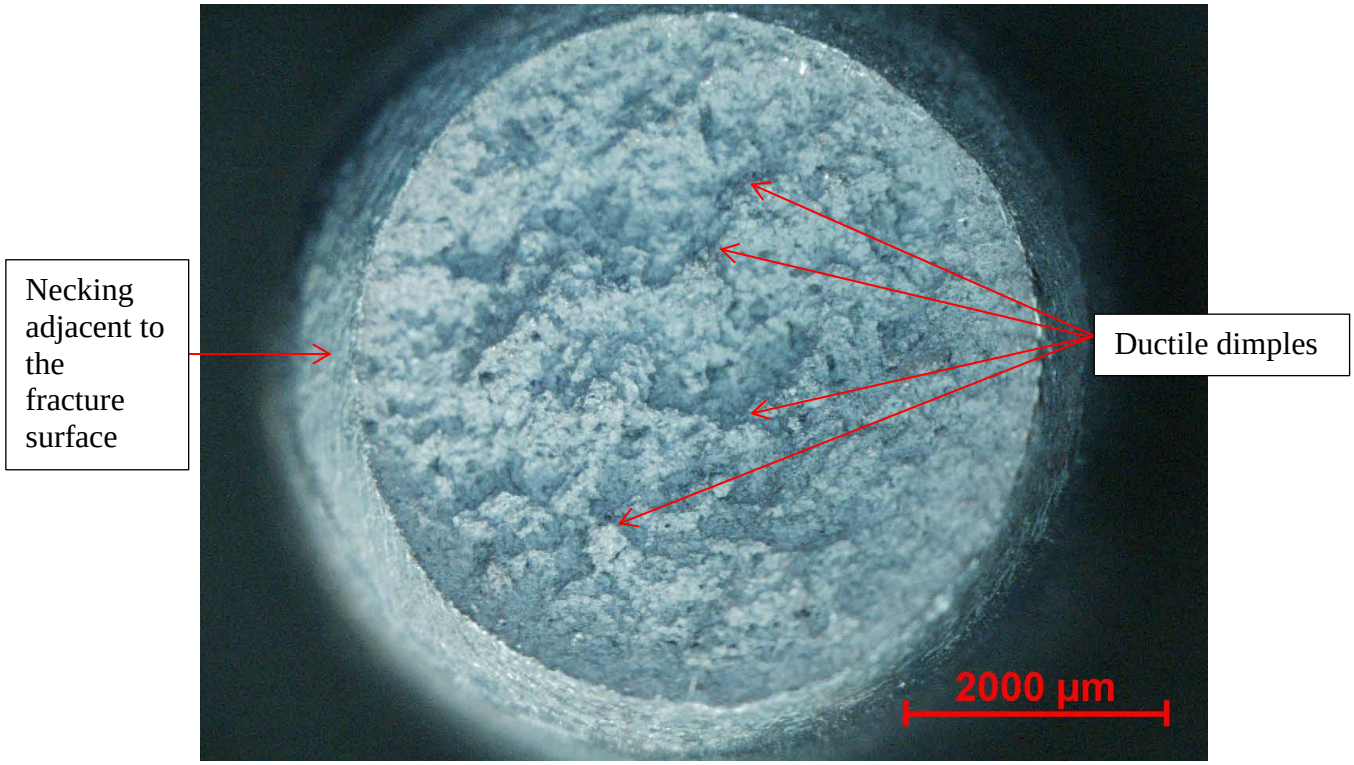


Figure 4.46: Stereo macrograph of the creep fracture surface specimen showing the ductile failure mode features (i.e. ductile dimples, "cup and cone shape", dull grey colour appearance and necking adjacent to fracture surface). [10X Magnification]

4.9 Chapter Summary

In summary, based on the overal characterisation results from this research study, the use of either X20 or P91 weld filler for a dissimilar butt weld of creep aged X20 and virgin P91 pipes material does not have a distinct effect on the creep life and on the weldment failure location/area. Both weld fillers (X20 and P91) are deemed to be suitable because very limited interdiffusion (~20 µm in width) of chromium and carbon at the dissimilar weld-interface was observed by utilising the SEM secondary electron analysis

technique across the fusion line. The presence of a carbon 'denuded' zone was limited to approximately 20 μm in width based on the results from local measurements of the precipitate phase fractions using image analysis and from elemental analysis using EDS. However the nanoindentation hardness measurements across the fusion line could not detect any 'soft' zone at the dissimilar weld interface. The effect of this tiny denuded zone was also not evident on mechanical testing (tensile and Charpy impact energy) and creep (uniaxial and SPCT) property testing.

The applied NDT (i.e. surface crack test and volumetric inspections) also revealed that the use of either X20 or P91 weld filler had no relevant recordable weld defects indications on both butt welds pipe samples. Both welds were acceptable in accordance with the NDT acceptance criteria specification.

Residual stress analysis results confirmed that there are no significant differences in the stresses found in the two cross welds. Both weld fillers had the same residual stress distribution effects across the welded joints. This could be attributed to the fact that X20 and P91 have similar properties and are therefore comparable.

Based on macro and micro hardness tests result, there are no observed differences between X20 and P91 weld filler cross weld joint. Both weld fillers had the same hardness profile across the welded joints. It is therefore conclusive that both weld fillers have similar effect on the hardness trends for the HAZ and PM areas.

Tensile tests results for the 3 tensile test conditions (21°C room temperature, 500°C and 550°C), indicated that the strength performance of both cross welds samples fused by either X20 or P91 weld metals are satisfactory meeting the code requirements (BS EN 10216-2, 2013). As expected and in line with literature, the tensile strength decreased with an increase in test temperature i.e. UTS at room temperature was ranging from 724 – 738 MPa, at 500°C was 452 – 457 MPa, and at 550°C was 404 – 413 MPa. Similar trend was also observed on the yield strength results. Therefore, it is conclusive that based on the mechanical tensile test results, both weld fillers (X20 and P91) are compatible to fuse the virgin P91 to creep aged X20 materials.

Microstructural characterisation observations revealed that there is no noticeable difference on the HAZ microstructure as a result of using either X20 or P91 weld filler. A very limited interdiffusion (~20 μm in

width) of chromium and carbon at the dissimilar weld-interface was observed using the SEM secondary electron analysis technique across the fusion line consitatantly on both weld joint samples. However the nanoindentation hardness measurements across the fusion line could not detect any ‘soft’ zone at the dissimilar weld interface. Therefore, it is conclusive that both weld fillers (X20 and P91) are compatible to fuse the virgin P91 to creep aged X20 materials considering the short-term creep test results that were conducted in this research study.

CHAPTER 5

5. DISCUSSION

From the study, it was observed that the samples X20 and P91 were successfully joined by TIG and MMA process without any reportable indications. Microstructural analysis showed the typical phases observed in ferritic/martensitic steels used in power generation plants. The main zone of importance in the HAZ is the IGHAZ. This region is deemed to be of importance because it is an area where welded components operating in creep regime fail as a result of a failure mechanism called Type-IV creep cracking (Abe *et al.,* 2008; Masuyama, 2000; Zhang *et al.,* 2020).

The contribution to creep strength is determined by the several metallurgical parameters such as precipitate density, sub-grain and dislocation density (Abson and Rothwell, 2013; Maile, 2007; Masuyama, 2000). When X20 and P91 are exposed to high temperature they experience microstructural evolution such as precipitation of secondary phases, growth of precipitates and recovery of tempered martensite (Panait *et al.,* 2010). Therefore it is important to characterise these strengthening parameters. The microstructural characterisation on the ICHAZ which is the most creep susceptible zone (Maridurai *et al.,* 2015) showed higher sub-grain values and $M_{23}C_6$ precipitates coarsening on the X20 compare to P91 ICHAZ. The $M_{23}C_6$ precipitates phase fraction ranged between 5.23 vol.% - 5.65 vol.% in the X20 ICHAZ location. The $M_{23}C_6$ precipitates measured on the P91 ICHAZ ranged between 3.37 vol.% - 2.87 vol.%. The reason for higher phase fraction of $M_{23}C_6$ precipitates on X20 ICHAZ is attributed to high chromium content in the X20 parent material (10 – 12.5 wt.%) compared to that in the P91 parent material (8 – 9.5 wt.%), (Abson and Rothwell, 2013; Maile, 2007; BS EN 10216-2: 2002). It was also observed that the $M_{23}C_6$ precipitates are coarser on the X20 ICHAZ than on the P91 ICHAZ. The coarser precipitates found in the X20 ICHAZ was as a result of previous service history of the X20 parent material that has already operated for 167303 hours on creep regime.

The phenomenon of precipitates coarsening at creep operating conditions has also been reported by Abbaschian (1992), Masuyama (2000), and Yardley (2003). Precipitate coarsening is a common phenomenon in creep exposed 9-12%Cr steels (Abson and Rothwell, 2013), which result in the loss of precipitation hardening and consequently leads to the loss of creep strength in the material (Dawson, 2012; Panait, 2010; Abe, 2008; Holzer and Kozeschnik, 2008; Buchmayr *et al.,* 1989). In this study it is apparent that the micro-grain size was predominantly high on both X20 and P91 HAZ regions. This could be

attributed to the welding thermal cycle that resulted in the coarsening of the microstructure's sub-grain structure in the ICHAZ. Abe *et al.* (2008) reported similar findings, whereby the applied heat input contributed to the coarsening of grains and sub-grains on the 9-12%Cr steels ICHAZ. This microstructural notch contributes to the weak creep zone in the weldment and promotes the formation of Type-IV creep cracking on the ICHAZ during creep loading (Abe *et al.*, 2008; Zhang *et al.*, 2020).

Residual stress measurement on the surface of both the cross-weld joints showed similar residual stress distribution. This could have been due to the fact that X20 and P91 have similar properties and are therefore comparable as per the EN 10216 code (BS EN 10216-2, 2013). The post weld heat treatment that was applied reduced the residual stresses on both samples from compressive stresses of -185 MPa and -148 MPa to -52 MPa and -43 MPa in the X20 and P91 welds respectively. This observation is similar to the work that was conducted by Brikstad et al. (1998) using a finite element analysis to study the residual-stress level on the circumferential weld constructed by multi-pass welding, the study showed that as the number of weld passes increase. The residual stress on the outside surface can go into compression (Brikstad *et al.*, 1998). A study by Paddea *et al.* (2012) is also in agreement with this observation of residual stress reduction after post weld heat treatment on 9-12 %Cr creep resistant steels.

The localised carbon and chromium denuded zone of approximately 20 μm in width was analysed by using the SEM secondary electron analysis technique across the fusion line. The results showed that the denuded zone did not have any effect on the mechanical properties and this was confirmed by the nano-indentation measurements. According to observations by Brozda *et al.*, (1998), the limited denuded zone was due to a small difference in chromium content between the weld and the parent metal. Furthermore, the negligible localised carbon denuded zone was found to be in agreement with theoretical studies of determining the chemical potential gradient of carbon in dissimilar cross weld joints using the Kirkady model (Elder, 2011; Kirkaldy and Young, 1987). The study by Dawson (2012) regarding the up-hill diffusion of carbon during PWHT period and during elevated temperature application on dissimilar weld joint is also in agreement with the observations in this study.

The mechanical properties of X20 and P91 materials used in this study were comparable to findings by Maridurai *et al.* (2015) and Masuyama (2000). These authors reported values of tensile test results that are within the code requirements (BS EN 10216-2, 2013). Tensile tests results for the 3 tensile test

conditions (21°C room temperature, 500°C and 550°C), indicated that the strength performance of both cross welds samples fused by either X20 or P91 filler weld metals satisfactorily met the code requirements (BS EN 10216-2, 2013). As expected and in line with literature, the tensile strength decreased with an increase in test temperature i.e. UTS at room temperature was ranging from 724 – 738 MPa, at 500°C was 452 – 457 MPa, and at 550°C was 404 – 413 MPa. The effect of change in temperature showed similar behaviour on yield strength results, whereby the yield strength was decreasing with increasing temperature.

The Vickers macro and micro hardness traverses that were obtained from the weld joint samples were also aligned to the obtained room temperature tensile strength, this correlation was also observed by Madyira *et al.* (2017) who conducted a comparative study on the effect of TIG and SMAW welding on the mechanical performance of P91 and 10CrMo9-10. From the study it was found that UTS and hardness are aligned. Furthermore, the hardness traverse results in this study revealed clear distinction in 4 distinct weld zones (i.e. parent metal, HAZ, fusion line and weld metal), similar observation was found by Mayr *et al.,* (2018) and Madyira *et al.,* (2017) in which the hardness mapping was used to locate the distinct zones of the weldment for further characterisation on a specific zone.

Creep degradation in the power generation plant components manifests mainly by grain boundary sliding and diffusional creep that degrades the microstructural strengthening features at elevated temperature as reportedly found by Bano *et al.* (2014), Padmanabhan *et al*. (2001) and Bhadeshia *et al.* (1998). The dominant mechanism in which deformation manifests is governed by the temperature and stress magnitude (Frost and Ashby, 1982; Ashby and Jones, 1989). It is reportedly found that under typical power plant operating conditions, creep occurs by dislocation glide and climb, rather than by bulk diffusion (Abbaschian, 1992; Yardley, 2003). Based on the uniaxial creep test results obtained in this study, it is evident that the samples tested at lower stress of 63 MPa had longer creep rupture time (averaging at 1210 hours) while the higher test stress (80 MPa) samples had shorter creep rupture time (averaging at 518 hours). It is beneficial to note that when comparing the observed creep curves of the two filler welded samples there was no distinct performance on sample welded with either X20 or P91 filler concerning the creep rupture life obtained under constant test conditions. Therefore, the use of either X20 weld filler or P91 weld filler did not affect the creep rupture life of dissimilar welds between creep exposed X20 and new P91 as informed by the short-term creep assessments undertaken herein study.

The overall observation drawn from all discussed results in this study indicate that it is inconclusive to determine which weld filler will perform better in service. Therefore, it can be considered that both weld fillers (X20 and P91) are compatible to fuse the virgin P91 to creep aged X20 materials.

CHAPTER 6

6. CONCLUSIONS AND RECOMMENDATIONS

6.1 CONCLUSIONS

In this study, dissimilar welds between X20 and P91 joint using two different filler metals were evaluated. The microstructures and mechanical properties of the two dissimilar welds were compared. From the findings of this research study, the following conclusions were drawn.

- The inter-diffusion of chromium and carbon at the dissimilar weld interface was limited to approximately 20 μm.
- Nano-indentation hardness measurements could not detect any 'soft' zone at the dissimilar weld interface.
- The effect of the denuded zone was also not evident on mechanical tensile, small punch creep test and cross weld uniaxial creep tests.
- Microstructural quantification of the HAZ regions, parent material, and the weld metals revealed results that are consistent with theory of welding of 9-12%Cr steels. The microstructures in the HAZ regions were insensitive to the type of weld filler that was used.
- Overall characterisation results in relation to the objective of this study reveal no distinctive performance of either using X20 or P91 weld filler for a butt weld of creep aged X20 and virgin P91 pipes material. Both weld fillers (X20 and P91) are deemed to be suitable since they gave comparable results from short term uniaxial creept tests (i.e. max. 1302 hours of creep test). Therefore, long-term creep test (≥ 10 000 hours) are to be conducted to study the microstructural evolution in the HAZ due to long term diffusional creep mechanism.

6.2 RECOMMENDATIONS FOR FURTHER WORK

- Long-term (≥ 10 000 hours) creep test must be carried out to study the diffusional creep mechanism as experienced in the power plant operating conditions.
- Determine the effect of material creep strength mismatch due to different weld fillers (that influences the offloading of creep damage) on the resultant creep life.

7. REFERENCES

1. Abe, F., Kern, T., Viswanathan, R., (2008), *Creep-resistant steels.* New York Washington, DC, pp 478-480.
2. Abe, F., (2008), *Precipitate design for creep strengthening of 9% Cr tempered martensitic steel for ultra-supercritical power plants*, Science and Technology of Advanced Materials, Vol. 9(1), pp 1-14.
3. Abso, D.J., Rothwell, J.S., (2013), *Review id type IV cracking of weldments in 9-12%Cr creep strength enhanced ferritic steels*, International Materials Reviews, Vol.58(8), pp437-473.
4. Abstoss, K.G., Schmigalla, S., Schultze, S., Mayr, P., (2019), *Microstructural changes during creep and aging of a heat resistant MARBN steel and their effect on the electrochemical behaviour*, Materials Science and Engineering A., pp 233-242.
5. Ahmed, I.I., Adebisi, J.A., Abdulkareem, S., Sherry, A.H., (2018), *Investigation of surface residual stress profile on martensitic stainless steel weldment with X-ray diffraction*, Journal of King Saud University, Engineering Sciences, Vol. 30, pp 183-187.
6. Anand, A., (2006), *Coal IGCC turbine technology improvements for carbon-free fuels*, 23rd Annual Pittsburgh International Coal Conference, Pittsburgh, pp 1-9.
7. Aghajani, A., (2009), *Evolution of microstructure during mong-term creep of a tempered martensitic ferritic steel*, Bochum University, PhD thesis, pp 1-86.
8. Albert, S.K., Kondo, M., Tabuchi, M., Yin, F. X., Sawada, K., Abe, F., (2005), *Improving the creep properties of 9Cr-3W-3Co-NbV steels and their weld joints by the addition of boron*, Metallurgical and Materials Transactions A, pp 333-343.
9. Andrews, K.W., Dyson, D.J., Keown, S.R., (1967). *Interpretation of electron diffraction patterns*, Hilger and Watts, London, pp 40-59.
10. Armaki, H.G., Chen, R., Maruyama, K., Igarashi, M., (2010), *Premature creep failure in strength enhanced high Cr ferritic steels caused by static recovery of tempered martensite lath structures*, Materials Science and Engineering A., Vol. 527, pp 6581-6585.
11. Arivazhagan, B., Vasudevan, M., (2014), *A comparative study on the effect of GTAW processes on the microstructure and mechanical properties of P91 steel weld joints*, pp 305.
12. Askeland, D.R., Phule, P.P., (2003), *The science and engineering of materials*, Fourth Edition, pp 134.
13. ASTM: A370 – 97a, (1997), *Standard test methods and definitions for mechanical testing of steel products.*
14. ASTM: E23 − 12c, (2016), *Standard test methods for notched bar impact testing of metallic materials.*

15. Auerkari, P., Holmstrom, S., Veivo, J., Salonen, J., (2007), *Creep damage and expected creep life for welded 9–11% Cr steels*, International Journal of Pressure Vessels and Piping, Vol. 84, pp 69-74.
16. Bano, N., Koul, A.K., Nganbe, M., (2014), *A deformation mechanism map for the 1.23Cr-1.2Mo-0.26V rotor steel and its verification using neural networks*, The Minerals, Metals & Materials Society and ASM International, pp 4-12.
17. Beech, S.M., Selway, J.W., Batte, A.D., (1984), *Factors influencing creep crack development in 1% CrMoV steam turbine rotor forging steels*, 2nd International Conference on Creep and fracture of engineering materials and structures, Pineridge Press, Swansea, pp 925-936.
18. Bezuidenhout, M., Bhimma, D., Doubell, P., Downes, A., Havinga, F., Mkhize, M., Newby, N., Scheepers, R. and Smit, W., (2008), *Integrity and lifing of defect free components in Eskom power plant*, HIDA – 5 Conference on plant integrity, defect assessment, fitness-for-service, risk based inspection and maintenance, Guildford, UK, pp 3-12.
19. Bhadeshia, H.K.D.H., Strang, A., Gooch, D. J., (1998), *Ferritic power plant steels: remnant life assessment and approach to equilibrium*, International Materials Review, Vol. 43(2), pp 45-69.
20. Böhler welding, Edition 6, (2009), *Technical handbook of* böhler *welding products*, pp.119-138.
21. Blondeau, R., (2008), *Metallurgy and mechanics of Welding*, ISTE Ltd and John Wiley & Sons Inc, London, United Kindom, pp 102.
22. Blum, R. and Hald, J., (2000), *Materials development for power plants with advanced steam parameters – Utility point of view*, VGB-ESKOM International Materials Conference, Pretoria, South Africa, pp 15-30.
23. Brikstad, B., Josefson, B.L., (1998). *A parametric study of residual stresses in multi-pass butt-welded stainless steel pipes*, International Journal of Pressure Vessels and Piping, Vol. 75, pp 18-19.
24. British Standard, EN 10216-2 (2013), *Seamless steel tube for pressure purposes – Technical delivery conditions, Part 2: Non-alloy and alloy steel tubes with specified elevated temperature properties*, European, pp13-14.
25. British Standard EN ISO 6507-1 (2005), *Metallic materials - Vickers hardness test - Part 1: Test method.*
26. British Standard EN ISO 6892-1 (2009), *Metallic materials, Tensile testing, Method of test at ambient temperature*.
27. British Standard EN ISO 6892-2 (2011), *Metallic materials, Tensile testing, Method of test elevated temperatures.*

28. British Standard PD 6525, (1990), *Elevated temperature properties for steels for pressure purposes*, Part 1, pp 1-90.
29. Brozda, J., Lomozik, M., Zeman, M., (1998), *Welding of P91 steel to other grades of steel for elevated temperature service*, Welding International, Vol.12(7), pp 509-518
30. Bròzda, J., Zeman, M., (2003), *Wrong heat treatment of martensitic steel welded tubes caused major cracking during assembly of resuperheaters in a fossil fuel power plant*, Engineering Failure Analysis, Vol. 10, pp 569-579.
31. Buchmayr, B. Cerjak, H., Fauland, H.P., (1989), *The effect of the precipitation behaviour on the HAZ properties of 1%Cr-Mo-V steel*, in 2nd International Conference Trends in Welding Research, Gattinburg, TN, 14–18 May 1989, ASM International, Materials Park.
32. Cerjak, H., Mayr, P., (2008), *Creep strength of welded joints of ferritic steels.* Graz University of Technology, Australia, pp 476-480.
33. Cerjak, H., Letofsky, E., Feigl, G., Pichler, P., (1998), *The role of welding for components made from advanced 9-12%Cr steels*, Materials for Advanced Power Engineering, Part I, pp 401-406.
34. Cerri, E., Evangelista, E., Spigarelli, S., Bianchi, P., (1998), *Evolution of microstructure in a modified 9Cr-1Mo steel during short term creep*, Materials Science and Engineering A., Vol. 245, pp 285-292.
35. Sawada, K., (2008), *Z-Phase formation in welded joints of high chromium ferritic steels after long-term creep*, pp 1161-1167.
36. David, S.A., Siefert, J.A., Feng, Z., (2013), *Welding and weldability of candidate ferritic alloys for future advanced ultrasupercritical fossil power plants*, Science and Technology of Welding and Joining, pp 631-651.
37. Dawson, K.E., (2012), *Dissimilar Metal Welds*, University of Liverpool, PhD thesis. pp.52.
38. Dong, P., Song, S., Zhang, J. (2014), *Analysis of residual stress relief mechanisms in post-weld heat treatment*, International Journal of Pressure Vessels and Piping, pp 6-14.
39. ECCC Recommendations (2005), *Residual Life Assessment and Microstructure,* Vol. 6 (Issue 1), pp 2-27.
40. Eggeler, G., Ramteke, A., Coleman, M., Chew, B., Peter, G., Burblies, A., Hald, J., Jefferey, C., Rantala, J., Dewitte, M., and Mohrmann, R., (1994), *Analysis of creep in a welded P91 pressure vessel*, International Journal of Pressure Vessels and Piping, Vol. 60, pp.237-257.
41. El-Azim, M.E., Ibrahim, O. H., El-Desoky, O.E. (2012). *Long term creep behaviour of welded joints of P91 steel at 650°C*, Materials Science and Engineering A., pp.680-682.

42. Elder, D.L., (2011), *Carbon migration across dissimilar metal welds related to power plant*, Cambridge University, PhD Thesis, pp. 46-51.
43. Eskner, M., Sandström, R., (2004), *Mechanical property evaluation using the small punch test*, Materials Science, Journal of testing and evaluation, pp.1-6.
44. Evans, R.W., Wilshire, B., (1985), *Creep of Metals and Alloys*, The Institute of Materials, London, pp 31-38.
45. Fleury, E., Ha, J.S., (1998), *Small punch tests to estimate the mechanical properties of steels for steam power plant: I. mechanical strength*, International Journal of Pressure Vessels and Piping, Vol.75. pp 699-706.
46. Foldyna, V., (1996), *Creep Resistant Metallic Materials*, Materials Science and Engineering A., Vol. 67. pp 375-381.
47. Fukuda, Y., (2011), *Development of advanced ultra-supercritical fossil power plants in Japan: Materials and high temperature corrosion properties*, Materials Science Forum, pp 1-7.
48. Hald, J., (1996), *Metallurgy and creep properties of new 9-12%Cr steels*, Materials Science and Engineering A., Vol. 67. pp 369-374.
49. Hagen, I.V., Bendick, W., (2002), *Creep Resistant Ferritic Steels for Power Plants*. International Symposium on Niobium, Orlando, pp 1-23.
50. Holzer, I., (2010), *Modelling and Simulation of Strengthening in Complex Martensitic 9-12% Cr Steel and a Binary Fe-Cu Alloy*, Graz University of Technology, PhD thesis, pp 13-32.
51. Holzer, I., Kozeschnik, E., (2008), *Predicted Precipitate Back-stress and Creep Rupture Strength of the Advanced 9-12%Cr Steels COST E2*, Carl Hanser Verlag, Munich, Germany, pp 417.
52. Igarashi, M., Sawaragi, Y., (1997), *Development of 0.1C-11Cr-3W-3Co-V-Nb-Ta-Nd-N ferritic steel for USC boilers*, Proceedings of International Conference in Power Engineering, Vol. 2, pp. 107.
53. Iseda, A., Sawaragi, Y., Kato, S., Masuyama, F., (1992), *Creep Characterization, Damage and Life Assessment*, Proceeding of the 5th International Conference of Creep of Materials, ASM International, Metal Park, OH, USA, pp 389.
54. Iseda, A., Teranishi, H., Yoshikawa, K., Masuyama, F., Daikoku, T., Haneda, H. (1988), *Development of 9Cr Ferritic Steel Tube and Pipe SAVE12AD for Advanced Power Boilers*, Thermal Nuclear Power, Vol. 39, pp 897.
55. Juffes, L. (2012), *Welding Principles and Applications*, Edition 7, Delmar. pp 267-274.
56. Kalwa, G., Haarmann, K. and Janssen, J.K. (1983), Trends in the development of heat resistant steels for seamless tubes in power station construction, VGB Kraftwerkstech, Vol. 15, pp 356-364.

57. Kirkaldy, J.S. and Young, D.J, (1987), *Diffusion profiles associated with the onsager matrix in non-equilibrium A-A-vacancy and A-B-vacancy solutions*, Acta Metallurgica, Vol. 35, Issue 6, pp 1273-1279.
58. Kostka, A., Tak, K.G., Hellmig, R.J., Eggeler, G., (2007), *On the contribution of carbides and micrograin boundaries to the creep strength of tempered martensite*, Acta Materialia. Vol. 55. pp 539-550.
59. Krauss, G., (1999), *Martensite in steel: strength and structure*, Materials Science and Engineering A., Vol. 273-275, pp 40-57.
60. Madyira, D.M., Liebenberg, J.A., Kaymacki, A., (2017), *Comparative characterization of P91 and 10CroMo9-10 creep resistant steel welds*, Procedia Manufacturing, Vol. 8, pp 345-352.
61. Maile, K., (2007), *Evaluation of microstructural parameters in 9–12% Cr-steels*, International Journal of Pressure Vessels and Piping, Vol. 84 pp 62-67.
62. Maridurai, T., Syed, M.Z., Sandhyarani, B., (2015), *Mechanical properties and fracture characteristics of ASTM A335 P91 steel used in boiler materials*, International Journal of ChemTech Research, Vol. 7(2), pp 654-665.
63. Maruyama, K., Sawada, K., Koike, J., (2001), *Strengthening Mechanisms of Creep Resistant Tempered Martensitic Steel*, ISIJ International, Vol. 41, pp 641-653.
64. Marx, G., (2016), *Quantitative Microstructural Evaluation of 12Cr Creep Aged Steels after Welding*, MSc dissertation, Nelson Mandela Metropolitan University, pp 18-194.
65. Masuyama, F., (2007), *Creep rupture life and design factors for high-strength ferritic steels*, International Journal of Pressure Vessels and Piping, Vol. 84, pp 53-60.
66. Masuyama, F., Haneda, H. and Roberts, B.W., (1988), *EPRI Report CS-5181-SR*, 1st international conference on improved coal-fired power plants, Palo Alto, CA, pp 85-108.
67. Masuyama, F., (2000), *History of power plants and heat resistant steels*, ISIJ International, Vol. 41, No. 6, pp 612-625.
68. Masuyama, F., (1998), *Steam Plant Material Developments in Japan, Materials for Advanced Power Engineering*, Part III, Forschungs-zentrum, pp 2-7.
69. Martin, J. W., (1980), *Micro-mechanisms in Particle-hardened Alloys*, Cambridge University Press, pp 2-9.
70. Mayr, P., Schlacher, C., Siefert, J.A., Parker, J.D., (2019), Microstructural features, mechanical properties and high temperature failures of ferritic to ferritic dissimilar welds, International Materials Reviews, Vol. 64(1), pp 1-26.

71. Milovic´, L.J., Vuherer, T., Blacic´, I., Vrhovac, M., Stankovic´, M. (2013). *Microstructures and mechanical properties of creep resistant steel for application at elevated temperatures*, Materials and Design. Vol. 46: pp 660-667.
72. Molokwane, T.J., (2013), *Microstructural and property assessment of creep aged 12Cr steel after welding*, MSc dissertation, University of Cape Town, pp 7-29.
73. Nabarro, F.R.N., de Villiers H.L., (1995), *The Physics of Creep*, Taylor & Francis Ltd publications, London, pp 15-34.
74. Nutting, J., (1999), Advanced Heat Resistant Steels for Power Generation, eds R. Viswanathan and J. Nutting, Institute of Materials London, pp 12-30.
75. Oates, W.R., Saitta, A.M., (1998), *Welding Handbook*, American Welding Society, Miami, Vol. 4, pp 59-62.
76. Ohgami, M., Hasegawa, Y., Naoi, H., Fujita, T. (1997), *Creep properties of heavy wall components for forged 9Cr-1.8W-0.5Mo-NbVN(NF616) steel*, IMechE Conference Transcript Advanced in Steam Plant, London, pp 115.
77. Paddea, S., Francis, J.A., Paradowska, A.M., Bouchard, P.J., Shibli, I.A., (2011), *Residual stress distributions in a P91 steel-pipe girth weld before and after post weld heat treatment*, Materials Science and Engineering A., Vol.534, pp 663-672.
78. Padmanabhan, K.A., Vasin, R.A., Enikeev, F.U. (2001). *Superplastic Flow, Phenomenology and Mechanics*, Springe, Verlag Berlin Heidelberg, pp 237-247.
79. Panait, C., (2010), *Evolution of dislocation density, size of subgrains and MX-type precipitates in a P91 steel during creep and during thermal ageing at 500°C for more than 100 000 h*, Materials Science and Engineering A., Vol. 527, pp 4062-4069.
80. Pandey, C., Mahapatra, M.M., Kumar, P., Saini, N., (2018), *Some studies on P91 steel and their weldments*, Journal of Alloys and Compounds, Vol. 743, pp 332-364.
81. Paterson, A.N., (1997), *Advanced steam plant*, IMechE Conference Transcript in Advanced Steam Plant, London, UK, pp 33.
82. Pešička, J., Kužel, R., Dronhofer, A., Eggeler, G., (2003), *The evolution of dislocation density during heat treatment and creep of tempered martensite ferritic steels*, Acta Materialia, Vol. 51, pp 4847-4862.
83. Prevéy, P.S., (1986), *X-ray Diffraction Residual Stress Techniques*, American Society for Metals, Metals Handbook, Vol.10, pp380-392.

84. Reed-Hill, R. and Abbaschian, R. (1992), *Physical Metallurgy Principles*, PWS Kent, Boston, pp 144-177.
85. Sikka, V.K., Ward, C.T, Thomas, K.C., (1981), *Modified 9Cr-1Mo steel – An improved alloy for steam generator application*, ASM International Conference on Production, Fabrication, Properties and Applications of Ferritic Steels for High-Temperature Applications, Warren, PA, pp 5-9.
86. Sonderegger, B., (2005), *Characterisation of the Substructure of Modern Power Plant Steels using the EBSD-Method*, Graz University of Technology, PhD thesis, pp 103-162.
87. Sonderegger, B., (2006), *Modifications of stereological correction methods for precipitate parameters using transmission microscopy*, Ultramicroscopy, Vol. 106, pp 941-950.
88. Sonderegger, B., Mitsche, S., Cerjak, H., (2008), *Microstructural analysis on a creep resistant martensitic 9–12% Cr steel using the EBSD method*, Materials Science and Engineering A., Vol. 481-482, pp 466-470.
89. Spigarelli, S., and Quadrini, E., (2002), *Analysis of the creep behaviour of modified P91 (9Cr-1Mo-NbV) welds*, Materials & Design, Vol. 23, pp 547-552.
90. Thomson, R.C. (1992), *Carbide composition changes in power plant steels as a method of remnant creep life prediction*, PhD thesis, Department of Materials Science and Metallurgy, Newnham College, University of Cambridge
91. Tuma, J.V., and Kosec, G., (2007), *Effect of microstructure on the accelerated creep of 20CrMoV12-1 and P 91 steels*, Steel Research International, Vol. 78, pp 643-647.
92. The Welding Institute, What determines the creep strength of an alloy, viewed 31 January 2020, <https://www.twi-global.com/technical-knowledge/faqs/faq-what-determines-the-creep-strength-of-an-alloy>.
93. Ule, B., Sustar, T., Dobes, F., Milicka, K., Bicego, V., Tettamanti, S., Maile, K., Schwarzkopf, C., Whelan, M.P., Kozlowski, R.H., and Klaput, J., (1999), *Small punch test method assessment for the determination of the residual creep life of service exposed components: outcomes from an interlaboratory exercise*, Nuclear Engineering and Design, pp1-11.
94. Vaillant, J.C., Vandenberghe, B., Hahn B., Heuser, H., Jochum, C. (2008), *T/P23, 24, 911 and 92: New grades for advanced coal-fired power plants: Properties and experience*, International Journal of Pressure Vessels and Piping, pp 1-9.
95. Viswanathan, R., Coleman, K., Rao, U., (2006), *Materials for ultra-supercritical coal-fired power plant boilers*, International Journal of Pressure Vessels and Piping, pp778-783.

96. Wang, Y., Li, L., Kannan, R., (2018), *Transition from type IV to type I cracking in heat-treated grade 91 steel weldments*, Materials Science and Engineering A., Vol. 714, pp 1-13.

97. Watanabe, T., (1993), *Grain boundary design and control for high temperature materials*, Materials Science and Engineering A., Vol.166, pp 11-28.

98. Xiong, M., Liew, J.Y.R., (2020), *Experimental study to differentiate mechanical behaviours of TMCP and QT high strength steel at elevated temperatures*, Construction and Building Materials, Vol. 242, pp 1-11.

99. Yardley, V., (2003), *Magnetic Detection of Microstructural Change in Power Plant Steels*, University of Cambridge, PhD thesis. pp 5-19.

100. Yoshioka, Y., (2017), *Current status of Japanese thermal power plants and life assessments of high temperature steam and gas turbine components*, Materials at High Temperatures, Vol. 43, pp 386-396.

101. You, Y., Shiue, R., Shiue, R., Chen, C., (2001), *The study of carbon migration in dissimilar welding of the modified 9Cr-1Mo steel*, Journal of Materials Science Letters, Vol. 20, pp 1429-1432.

102. Yukitoshi, T., Yuzawa, H., Yoshikawa, K., Daikoku, T., Tsuruta, N and Masuyama, F., (1980), *Experience of high chromium ferritic steel tubes in power plant*, Thermal Nuclear Power, Vol. 31, pp 33-35.

103. Zhang, W., Wang, X., Wang, Y., Xinghua, Y., Gao, Y., Feng, Z., (2020), *Type IV failure in weldment of creep resistant ferritic alloys: Micromechanical origin of creep strain localization in the heat affected zone*, Journal of the Mechanics and Physics of Solids, Vol. 134, pp 1-13.

104. Zhang, Z., Farrar, J.C.M., Barnes, A.M. (2000), *Weld metal for Grade P91 - tough enough*, Fourth International EPRI Conference on Welding and Repair Technology for Power Plants, Florida, USA, pp 1-7.

8. RESEARCH PAPERS

8.1 First Paper: Characterisation of Suitable Fillers for Butt Weld of Creep Aged X20 and Virgin P91 Pipes

Joint EPRI – 123HiMAT International Conference on
Advances in High Temperature Materials
October 21–24, 2019, Nagasaki, Japan
J. Shingledecker, M. Takeyama, editors

Copyright © 2019 ASM International®
All rights reserved.
www.asminternational.org

CHARACTERISATION OF SUITABLE FILLERS FOR BUTT WELD OF CREEP AGED X20 AND VIRGIN P91 PIPES

Thendo Mphaphathi[1,2], Nthabiseng Maledi[1]
School of Chemical and Metallurgical Engineering, University of the Witwatersrand, Private Bag 3, Johannesburg, South Africa

Marthinus Bezuidenhout[2], Thobeka Pete[2]
ESKOM, Research Testing and Development (RT&D), Johannesburg, 1401, South Africa

Johan Westraadt[3],
Centre for High Resolution Transmission Electron Microscopy, Nelson Mandela University, Port Elizabeth, South Africa

Bernard Dreyer[4]
Department of Mechanical Engineering, Nelson Mandela University, Port Elizabeth, 6001, South Africa

ABSTRACT

Components such as tubes, pipes and headers used in power generation plants are operated in a creep regime and have a finite life. During partial replacement, creep exhausted materials are often welded to virgin materials with superior properties. The aim of this study was to identify a suitable weld filler material to join creep aged X20CrMoV12-1 to a virgin P91 (X10CrMoVNbV9-1) steel. Two dissimilar joints were welded using the gas tungsten arc welding (GTAW) process for the root passes, and manual metal arc (MMA) welding for filling and capping. The X20 and the P91 fillers were selected for joining the pipes. The samples were further heat treated at 755°C to stress relief the samples. Microstructural evolution and mechanical properties of the weld metals were evaluated. The average hardness of X20 weld metal (264 HV_{10}) was higher than the hardness measurement of P91 weld metal (206 HV_{10}). The difference in hardness was attributed to the high carbon content in X20 material.

The characterisation results revealed that the use of either X20 or P91 weld filler for a butt weld of creep aged X20 and virgin P91 pipes material doest not have a distinct effect on the creep life and creep crack propagation mechanism. Both weld fillers (X20 and P91) are deemed to be suitable because limited interdiffusion (<10 μm) of chromium and carbon at the dissimilar weld interface was observed across the fusion line. The presence of a carbon 'denuded' zone was limited to <10 μm in width, based on the results from local measurements of the precipitate phase fractions using image analysis and from elemental analysis using EDS. However the nanoindentation hardness measurements across the fusion line could not detect any 'soft' zone at the dissimilar weld interface. The effect of the minute denuded zone was also not evident when the samples were subjected to nanoindentation hardness testing, tensile mechanical testing, Small Punch Creep Test (SPCT) and cross weld uniaxial creep testing.

INTRODUCTION

In power generating plants, components (tubes, pipes and headers) that are operating in creep regime (temperature greater than 450°C) are subjected to damage such as creep, stress corrosion, and fatigue [1], which compromises the structural integrity of these components. The growing demand to increase steam temperatures to enhance thermal efficiencies has seen the introduction of high chromium ferritic-martensitic alloy steels in power plants. These materials are preferred because of their improved ductility, high structural stability, and superior resistance to corrosion and oxidation [2].

With material advances, it is expected that most welded components will be made out of dissimilar welds of different grades. Although the practice of having dissimilar metal welds (DMWs) is common in pulverised coal power plants, premature failure due to these welds have been reported [3]. Bettahar et al. [4] attributed the major disadvantages of DMWs to the inhomogeneous microstructure due to weld thermal cycles. Other authors found common failures to be due to the incompatibility of coefficient of thermal expansion (CTE) between base materials, reactive diffusion of carbon at the interface where there is a difference in chromium content, phase precipitation, and residual stresses in welds, among other factors [2, 3, 5, 6]. Therefore, it is imperative that a suitable filler material and appropriate postweld heat treatment (PWHT) cycle [2, 3] are selected when welding DMWs to avoid failures.

Recent studies on joining of DWMs focused on the microstructural evolution under creep loading [3,7], low cycle fatigue behaviour [8], and characterization of DMW using different filler metals [9]. Whilst there is literature on welding DMWs [10, 11], a suitable weld filler metal for joining a creep aged X20CrMoV12-1 steel (installed design material) and a virgin P91 (X10CrMoVNbV9-1) steel (superior material with improved creep resistance properties) has not yet been fully researched. Therefore the aim of this work is to study the effect of using the X20 and P91 welding consumables when making a weld joint between a creep aged X20 steel and virgin P91 steel. The two fillers were selected because of their compatibility with the base metals. These weld fillers have minimal metallurgical notch when welded to their respective parent materials. The weldability and creep life extension on creep aged materials are dependent on factors such as, the microstructure (precipitates and damage / dislocations), the welding processes applied, the post-weld heat treatment, the intended operation time, and the operating conditions. The knowledge gained in this study will be incorporated in the extensive life management and life extension knowledge base that exists to define the appropriate weld filler for welding service exposed X20 material to new P91 material pipework.

Experimental procedure

The base materials used in this research work are seamless pipes of new (virgin) normalized and tempered Grade 91 steel and service exposed X20 steel pipes. The creep cavitation damage level of the service exposed X20 material as expressed in terms of creep void density was 60 voids / mm^2, and this was confirmed by the creep voids counting on the lifted replica micrographs shown in Fig. 1(a). Figure 1(b) shows the microstructure of P91 without any creep damage. The nominal chemical compositions of the base and filler materials are given in Table 1.

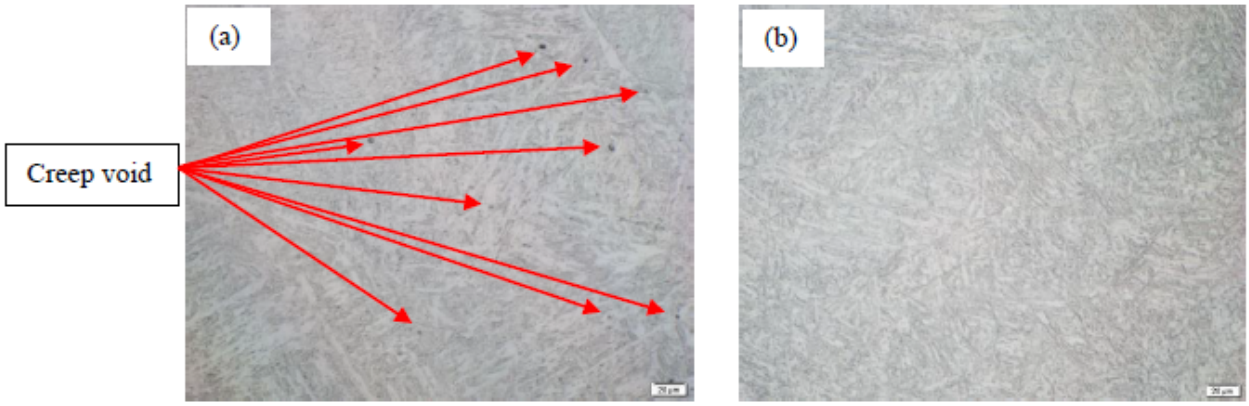


Figure 1: Replication micrograph of the base materials used. (a) X20 with < 100 creep voids / mm^2 as pointed out by red arrows and (b) P91 without creep damage (virgin material) at 500X magnification

Table 1: Nominal chemical composition of the base and filler materials (wt.%)

Steel Grade	C	Si	Mn	P	S	Cr	Mo	Ni	Al	Cu	Nb	V	N	W
X10CrMoVNb9-1 base material	0.09	0.33	0.46	0.007	0.007	8.61	0.97	0.18	0.013	0.13	0.094	0.20	-	
X20CrMoV11-1 base material	0.16	0.22	0.56	0.009	0.007	11.7	0.96	0.69	0.029	0.08	0.021	0.29	-	
X10CrMoVNb9-1 rod filler	0.11	0.35	0.45	-	-	9.0	1.0	0.75		-	0.06	0.2	0.04	1.05
X20CrMoV11-1 rod filler	0.19	0.37	0.55	0.010	0.003	11.1	0.85	0.1		<0.1	<0.01	0.25	-	0.42
X10CrMoVNb9-1 coated filler	0.09	0.26	0.59	0.01	0.013	8.59	1.03	0.49	-	0.05	0.061	0.22	-	-
X20CrMoV11-1 coated filler	0.12	0.28	0.67	0.009	0.012	10.8	0.92	0.49	-	0.04	0.022	0.22	-	-

The welded joints of creep aged X20 and as-received P91 were prepared in accordance with Eskom's qualification welding procedure for new P91 to X20 steel pipework. The pipes were welded using the Gas-Tungsten Arc Welding (GTAW / TIG) process for the root pass, and Manual Metal Arc (MMA) welding process for filling the joint. The weld preheat was set at 250°C, whilst the interpass temperature was kept at temperature ranges between 200°C-300°C. The essential welding parameters that were used for filling passes are listed in Table 2.

Table 2: Welding parameters for the dissimilar joint

Welding process	Filler material	Welding current (A)	Welding voltage (V)	Time per run (s)	Weld length (mm)	Travel speed (mm/s)
MMA	X20 filler/P91 filler	104-127	19.7-22.8	59	120	2.034

Post weld heat treatment (PWHT) of the weld joints was carried out at 755°C at a heating rate of 50°C per hour, the samples were held at the temperature for 4 hours (soaking time) and subsequently air-cooled to room temperature at the cooling rate of 50°C per hour.

Metallographic sections of the cross welds were prepared following standard procedure for ferrous alloys. The samples were ground using silicon carbide paper (80, 120, 240, 500, 800 and 1200 grit size) and polished to 1 µm finish using diamond paste. The samples were then etched using Villela's reagent (1 gram picric acid, 5 ml hydrochloric acid, and 100 ml ethanol) to observe all microstructural details.

Microstructural characterisation

High resolution microstructural characterisation was carried out using the JEOL JSM 7001F scanning electron microscope (SEM) fitted with an X-Max 20 mm^2 energy dispersive spectrometer (EDS) from Oxford Instruments. SEM-EDS was used to determine the composition and phases present in the weldments. SEM imaging was performed using secondary electrons (SE) and backscattered electrons (BSE) mode. The electron backscattered diffraction (EBSD) and transmission Kikuchi diffraction (TKD) data were collected using a Nordlys HKL high-sensitivity detector. Simultaneous EDS measurements were taken from the samples during the EBSD/TKD acquisition using the AZTec software from Oxford Instruments. The results were processed using the Channel 5 HKL software package for the visualisation and exporting of data.

The transmission electron microscope (TEM) was used to analyse the morphology of the carbides precipitates and sub-grains. The evolution of creep voids, carbide precipitates, and dislocation networks during welding operation and creep test was studied on both weld joints made with P91 and X20 weld fillers on the creep aged X20 and new P91 materials. Low angle annular dark-field (ADF) images were collected from the jet-polished samples using a JEOL JEM 2100 LaB6 transmission electron microscope (TEM) in scanning mode (ADF-STEM) using a camera length of 40 cm. MIPAR™ was used for the automatic thresholding and quantification of the different microstructural features from the various images collected on the electron microscopes.

The dislocation densities in the samples were determined using powder X-ray diffraction peak profile analysis. The samples were scanned from 20° to 120° degrees 2θ, to include ferrite iron peaks. A silicon powder reference sample was used to calibrate the instrumental line broadening. TOPAS™ software was used to apply the whole pattern Rietveld refinement to determine the crystallite size (Crys-L) and micro-strain (ε_0) in the samples, from which the dislocation density was determined.

Hardness testing

Macro hardness tests were carried out on the prepared samples using EMCO TEST DURASCAN Vickers hardness testing machine. Hardness profiles were obtained across the weldments using a load of 10 kgF and dwell time of 5 seconds. The Vickers hardness test method was as per the ISO 6507-1 standard of metallic materials, Vickers hardness test method (ISO 6507-1, 2005). The distance between each indentation was 1 mm. Hardness tests were carried out across the base metal (BM), heat affected zone (HAZ) and the weld metal (WM).

Uniaxial creep testing

Uniaxial creep tests were conducted using the Applied Test Systems (ATS) 2330-CCM-230 Series 2330-CCM Lever Arm Tester creep machine. The weld joints (WJ) were used to study the microstructural evolution due to creep aging degradation mechanism. The creep tests were carried out at 610°C under the applied stress of 63 MPa and 80 MPa in argon inert gas environment to

avoid excessive high temperature oxidation. The tests were performed twice for repeatability. Cylindrical test specimens with a 77 mm (length) × 10 mm (diameter) uniform gauge cross section were machined from the pipe samples.

RESULTS AND DISCUSSIONS

Figure 2 shows the micrographs of the weld filler metals. The overall microstructural evaluations made from optical images indicated the characteristic tempered martensite. Tempered martensite is finely distributed in X20 weld filler metal.

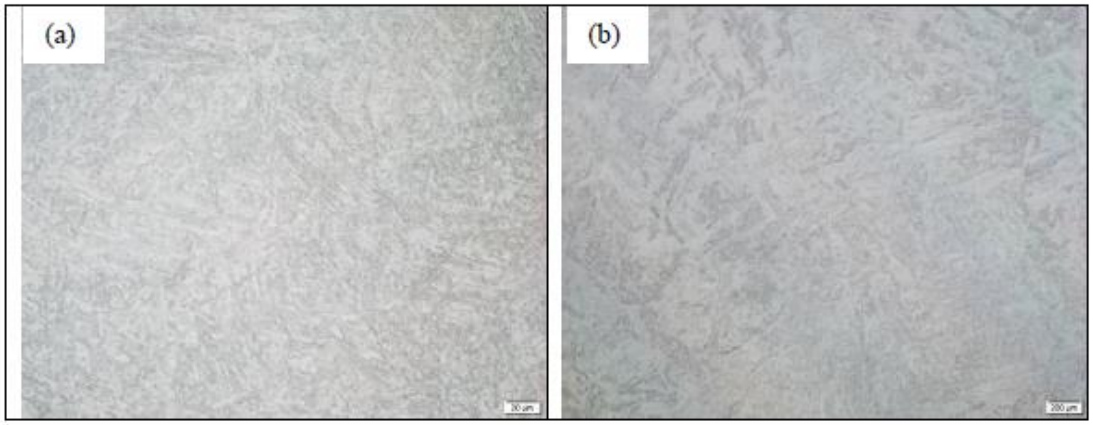
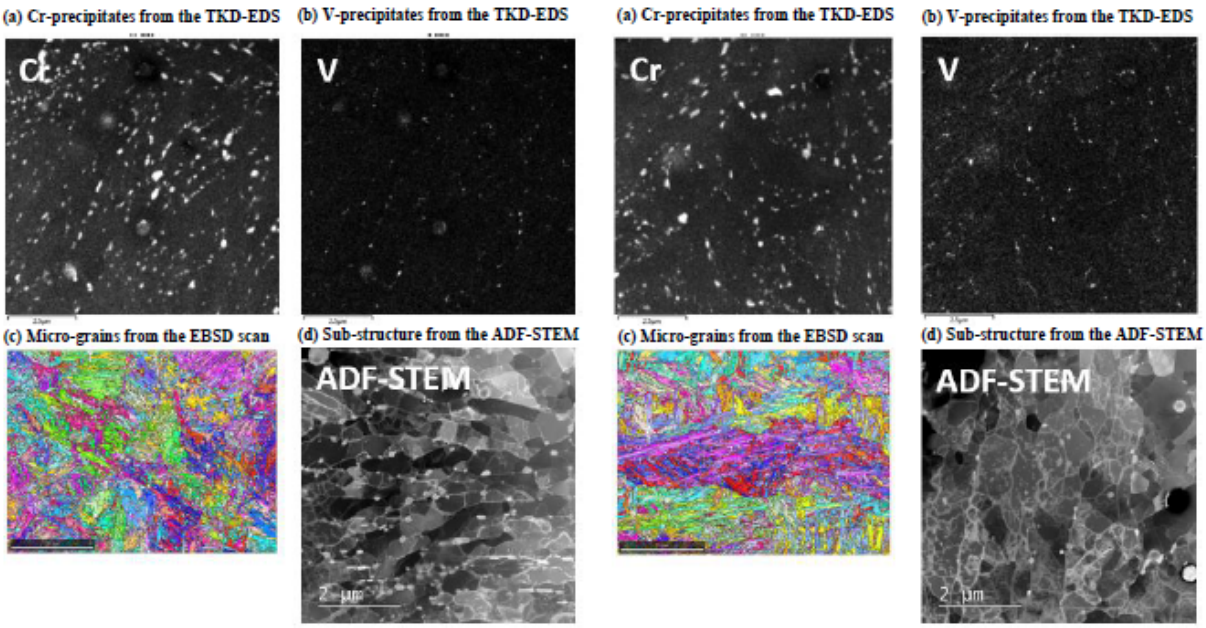


Figure 2: Optical micrograph of (a) X20 weld filler metal showing tempered martensite and (b) P91 weld filler metal showing tempered martensite.

The DMWs failure is associated with microstructural evolution in the HAZ. Microstructural characterization was carried out on the specific locations of the cross weldments, that were carefully identified in order to quantify the microstructural evolution of precipitates (MX-carbonitrides, where M = V, Nb, and X = C, N or $M_{23}X$-carbides, where M= Cr, Fe, Mo) and substructures such as sub-grains and dislocation densities. The evolution of these parameters is often correlated with creep behaviour of creep resistant steels [12, 13].

Figure 3 shows the distribution of the $M_{23}C_6$ (Cr-map), MX (V-map), sub-grains (band contrast) and dislocation network (ADF-STEM) for the WM materials. Based on the uncorrected mean measured parameters in Table 3, the phase fraction of $M_{23}C_6$ is 4.20 vol.% for X20 WM and 3.31 vol.% for P91 WM. The higher phase fraction of $M_{23}C_6$ precipitates in X20 WM is attributed to high chromium content in X20 welding rod filler.



X20 weld filler metal **P91 weld filler metal**

Figure 3: Microstructural constituents maps showing the distribution of: a) Cr-precipitates from the TKD-EDS (Top Left Image), b) V-precipitates from the TKD-EDS (Top Right Image), c) Micro-grains from the EBSD (Bottom Left Image) and d) Sub-structure from the ADF-STEM (Bottom Image) for the both X20 and P91 weld filler metals.

Table 3: Microstructural measurements for WM of X20 and P91

			X20 filler	P91 filler
Precipitates	$M_{23}C_6$	*Mean equivalent circle diameter (ECD) (nm)*	120 ± 6	130 ± 7
		Fraction (vol.%)	4.20	3.31
	MX	*ECD (nm)*	89 ± 4	96 ± 4
		Fraction (vol.%)	0.93	1.50
Elongated micro-grains (µm)			0.999	0.958
Sub-structure (µm)			0.23 ± 0.02	0.18 ± 0.01
Free-dislocations (10^{-14} m^{-2})			3.07	2.35

Precipitates

The equivalent circle diameter (ECD) and the mean inter-particle spacing between precipitates were calculated, and the results are presented in Table 3. The hindrance of dislocation movement is directly related to the mean inter-particle spacing. This parameter is a function of not only the particle size, but also the phase fraction of the particle. In the calculation of the mean inter-particle parameter, the effect of sectioning the precipitates due to the TEM sampling as well as the foil projections are accounted for in order to calculate the true 3D inter-particle spacing. Figure 4 shows the comparison of the mean surface-to-surface particle spacing calculated from the different precipitate ($M_{23}C_6$ and MX) distributions of the different microstructural zones.

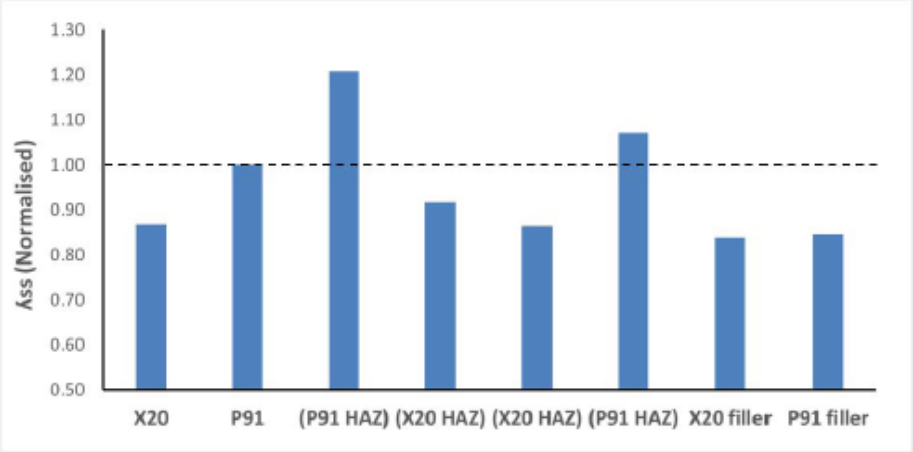


Figure 4: Normalised mean surface-surface measurements of the precipitates ($M_{23}C_6$ and MX)

Higher values indicate lower resistance to dislocation movement, and lower creep-strength. The highest inter-particle ($M_{23}C_6$) spacing were measured for the P91 HAZ regions, due to the precipitate coarsening during welding. The smallest inter-particle ($M_{23}C_6$) spacing were measured in the WM of X20 and P91 filler joints, due to the rapid cooling from a molten metal and subsequent growth of the precipitates during the post-weld heat treatment. The inter-particle spacing measurements for MX precipitates in the different microstructural regions was similar to inter-particle spacing for $M_{23}C_6$ precipitates, and this is partly due to the limitations of the measuring technique.

Grain size

Figure 5 shows the comparison of the mean linear intercept size of the sub-structure measured in the different microstructural zones using the ADF-STEM images. The creep-aged X20 parent plate had a larger sub-grain structure as compared to the virgin P91 parent material.

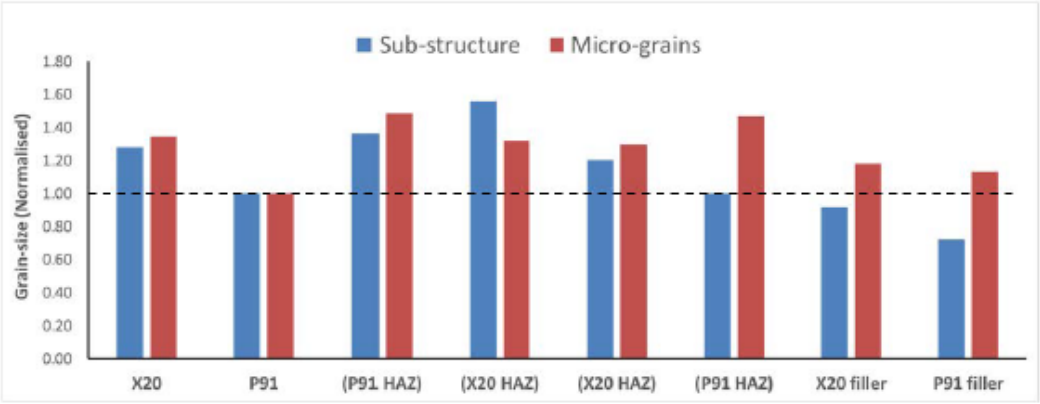


Figure 5: Sub-grain size of the different microstructural areas imaged using ADF-STEM

Dislocation density

Figure 6 shows the typical ADF-STEM images taken from the different microstructural zones in the weldment. The virgin P91 had numerous dislocations within smaller sub-grains compared to

the creep-aged X20 parent material. The fine grained heat affected zone (FGHAZ) in the P91 material (see Fig. 6c) show significant growth of the sub-grains and very low dislocation density. The X20 weld filler material had small sub-grains and contained significant number of free dislocations within the sub-grains. The dislocation density has a strong influence on the dislocation creep strength of the materials.

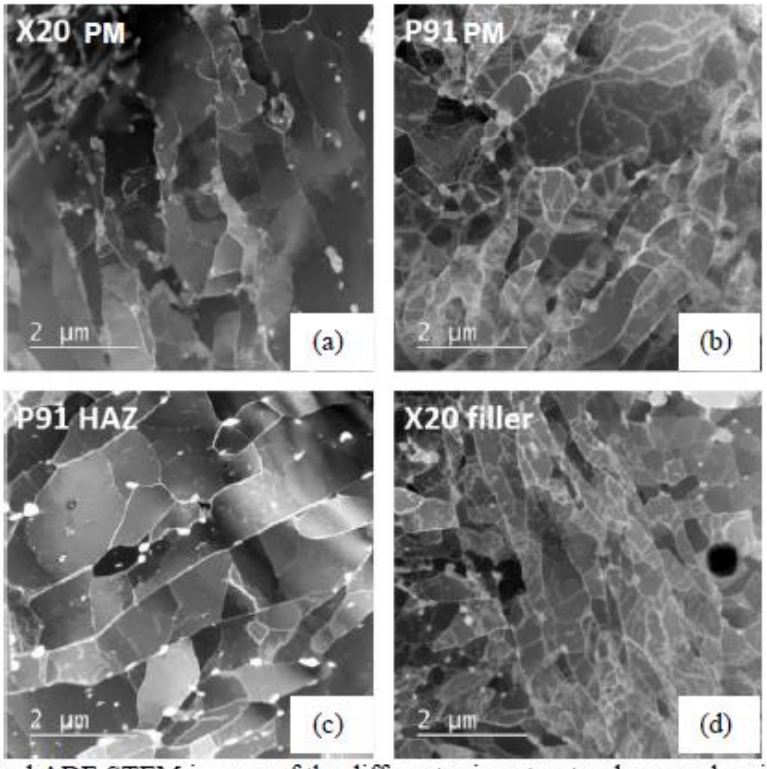


Figure 6: Typical ADF-STEM images of the different microstructural zones showing the relative sub-structure size and dislocation density.

Figure 7 shows the free dislocation density of the different sections in the cross weld. The dislocation density of the virgin P91 (PM) is the highest, while the Orowan strength contribution for the dislocations for the creep-aged X20 steel is only 35% of that value. The precipitate contribution to the Orowan strength is higher for the X20 steels, due to the higher phase fraction of carbides, hence lower the interparticle spacing.

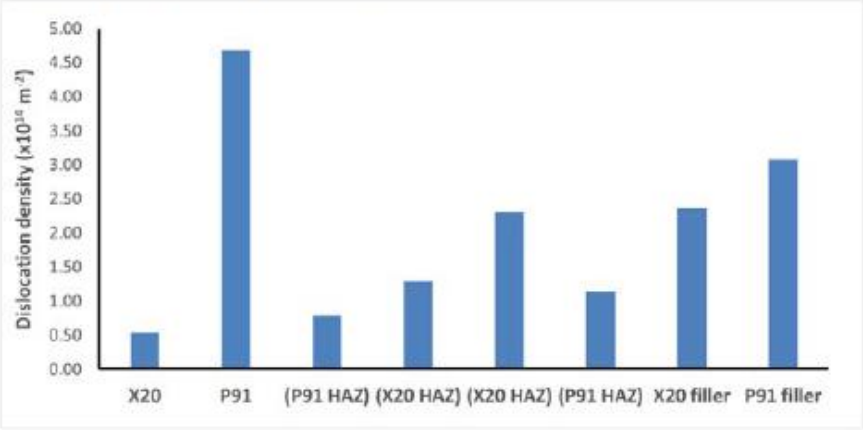


Figure 7: Free dislocation density determined from XRD peak measurements

Diffusion chemical analysis

Welding on dissimilar materials can result in carbon diffusion across the weld fusion line which is detrimental to mechanical and creep properties of the weld joint. The EDS chemical analysis revealed no noticeable Cr diffusion across the dissimilar fusion lines as shown in Fig. 8. The analyses also confirmed that the parent materials (X20 and P91) and weld metal contain the required concentration of Cr as per EN standards (BS EN 10216-2, 2002) specification.

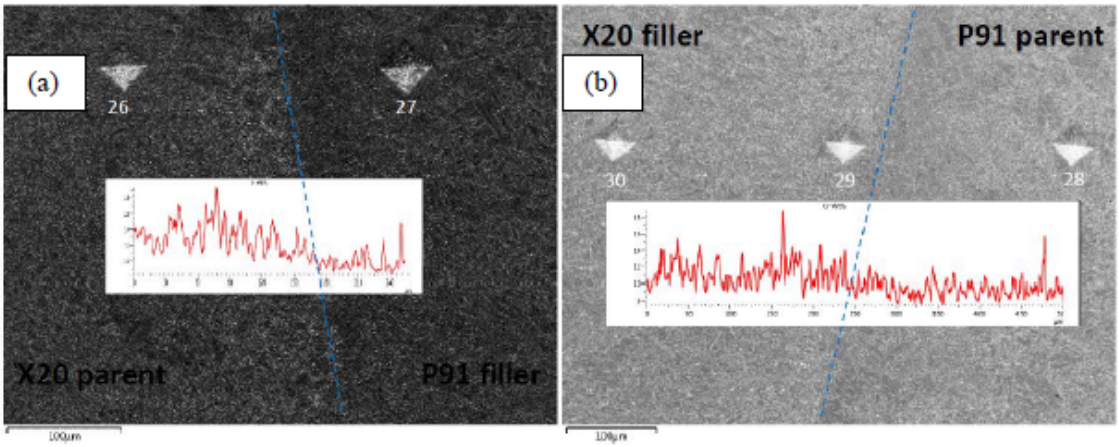


Figure 8: EDS chemical analysis on the micrograph samples showing the chromium concentration across dissimilar X20 Parent Metal - P91 Weld Filler Metal, and P91 Parent Metal - X20 Weld Filler Metal cross welds. Dotted lines indicate the position of the fusion line.

Carbon migration was analysed using SEM Secondary Electron Analysis and nanoindentation hardness test across the fusion line. To investigate the presence of a "*carbon denuded zone*" at the fusion line, the nano-hardness measurements, local measurements of the precipitate phase fractions using image analysis and elemental analysis using EDS were carried out. The position of the fusion-line is seen by the change in contrast of the secondary electron image. The nanoindentation measurements (60 μm spacing) followed the same profile as the Vickers hardness measurements. From these measurements, there is no clear indication of a "*soft-zone*" at either side of the dissimilar fusion lines as shown in Fig. 9(a). High-resolution SEM images were taken and processed to measure the precipitate phase fraction as a function of position over a sliding area of approximately 7×7 μm as shown on the coloured image in Fig. 9(b). The phase fraction increases from the P91 to X20 material as evidenced by the change in colour *[dark blue = 0; yellow: 12 vol.%]*. The EDS-elemental line profile shows an increase in the Cr-content from the P91 side (~9 wt.%) to the X20 side (~12 wt.%). Both the precipitate phase fraction and the EDS measurement indicated a localised "denuded zone" <10 μm in width. The effect of this tiny denuded zone was also not evident on mechanical tensile testing, Small Punch Creep Test (SPCT) and cross weld uniaxial creep test results.

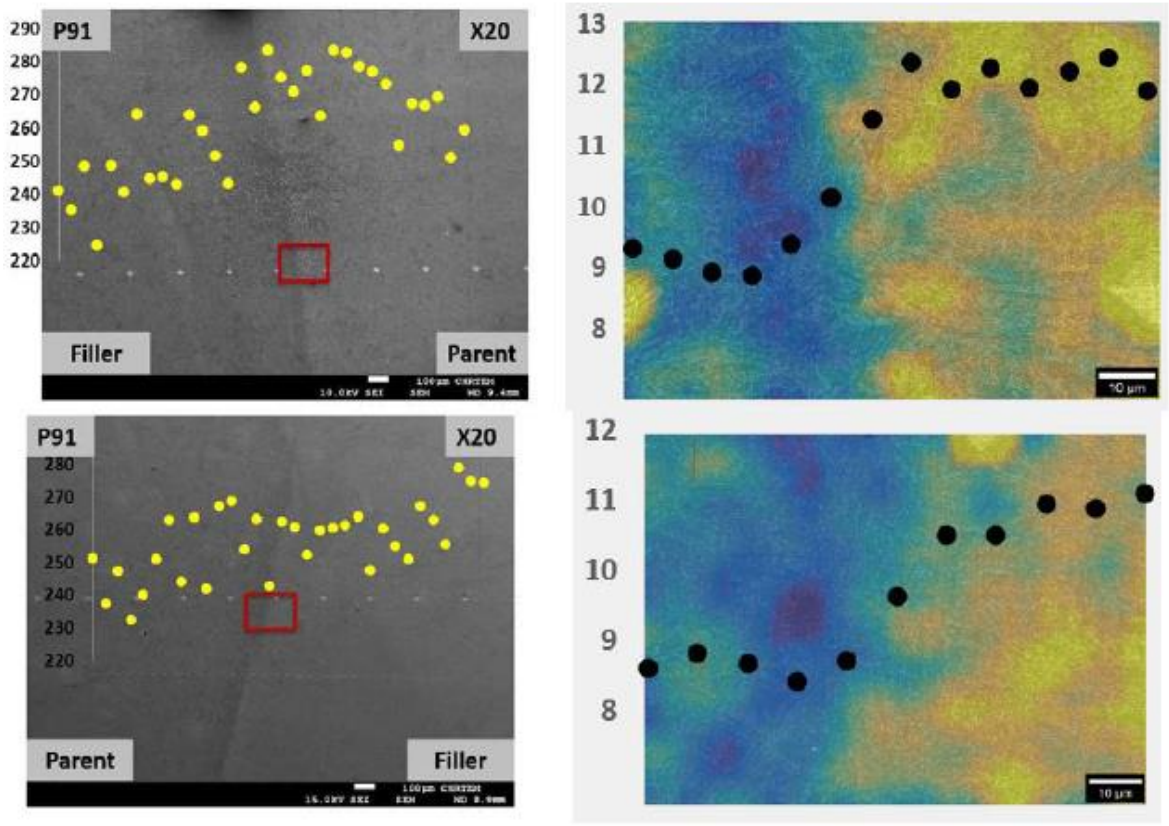


Figure 9: *(a)* Secondary electron images of the fusion-lines for the dissimilar weldments, with the nanoindentation hardness measurement overlay. *(b)* Precipitate phase fraction colour plot (12 vol% max), with EDS-profile analysis (Cr wt.%) overlay for the fusion-line region, indicated with the red rectangle on the left. [dark blue: 0; yellow: 12 vol.%]

This negligible localised carbon denuded zone observed in the 9-12%Cr dissimilar weld is in agreement with the theoretical studies of determining the chemical potential gradient of carbon in the dissimilar cross weld joint using the Kirkady model [14, 15].

Hardness tests

The macro hardness profile related to the different areas across the welded specimen is shown in Fig. 10. The hardness of the weld metal for X20 filler is 262 HV_{10}. The hardness in the HAZ was approximately 255 HV_{10}. In the case where P91 weld filler was used, the weld metal hardness measured was 264 HV_{10} and 240 HV_{10} for the HAZ. The variation in hardness in the different areas is due to compositional and microstructural changes that takes place during welding. It is worth noting that the average hardness values obtained on the X20 PM (238 HV_{10}) is higher than that of P91 (206 HV_{10}). The difference in hardness values between X20 PM and P91 PM was attributed to high carbon content in X20 (C = 0.16 wt.%). High carbon content leads to an increased hardness. The hardness results also correlate with the measured sub-grain structures, where the filler materials had the smallest sub-grain structures.

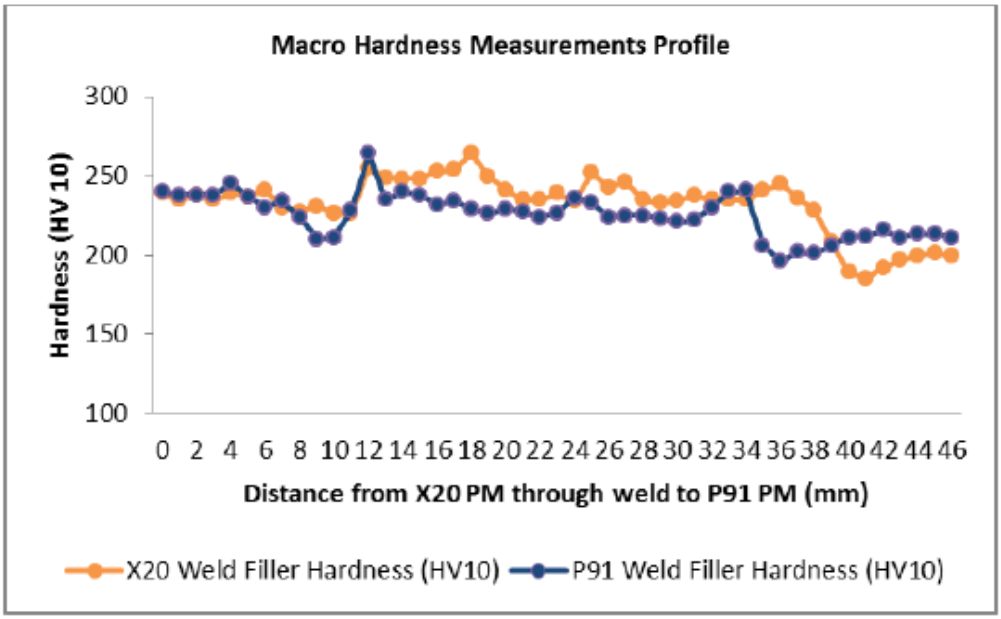


Figure 10: Macro hardness traverse for both X20 and P91 weld filler cross weld joints.

Uniaxial tests

Figure 11 illustrate creep curves (creep strain vs time) for cross weld samples that are consisted of creep aged X20 PM to X20 weld filler to new P91 PM at 60 MPa and 80 MPa as well as their duplicates, creep aged X20 PM, X20 weld filler and P91 PM at 60 and 80 MPa as well as their duplicates. All these creep tests were carried out a constant temperature 610℃. From the figure it can be seen how the creep strain increases with the time in hours. It can be observed that the total strain accumulation at rupture ranges from 1.15 % - 3.02 %. The creep rupture time ranged from 312 hours – 1302 hours. A considerable increase of creep strain at the final stages of the creep curves can be attributed to local deformation known as necking. This phenomena of necking was also observed by Aghajani, 2009, [16] in the study of the "Evolution of Microstructure during Long-term Creep of a Tempered Martensitic Ferritic Steel"

For comparison purposes, additional uniaxial creep test was carried out on the creep aged X20 parent material (PM) from the same material batch that was used for the cross weld samples, to determine the effect of welding on the aged material which is technically known as the weld reduction factor on creep aged material. From the results, it is apparent that the aged X20 parent material has longer creep rupture time (2774 hours) as compared to that of the cross weld samples (ranges from 312 hours – 1302 hours).

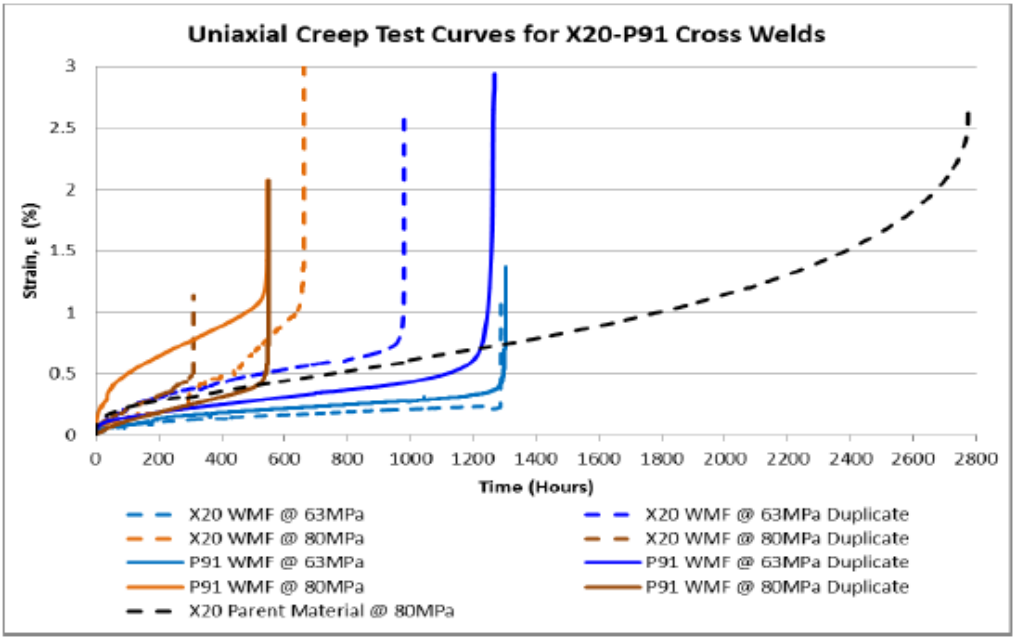


Figure 11: Creep curve (creep strain Vs time) for creep aged X20 PM in comparison with creep aged X20 PM – X20 weld filler – new P91 PM at 60 MPa and its duplicate, creep aged X20 PM – X20 weld filler – new P91 PM at 80 MPa and its duplicate, creep aged X20 PM – P91 weld filler – new P91 PM at 60 MPa and its duplicate, creep aged X20 PM – P91 weld filler – new P91 PM at 80 MPa and its duplicate cross weld samples.

CONCLUSIONS

In this study, dissimilar welds between X20 and P91 using two different filler metals were evaluated. The microstructural evolution and mechanical properties of the welds were compared. From the findings presented, the following conclusions were drawn.

- There were very limited interdiffusion (<10 µm) of chromium and carbon at the dissimilar weld interface. The presence of a 'denuded' zone was limited to <10 µm in width. Nanoindentation could not detect any 'soft' zone at the dissimilar weld interface. The effect of this tiny denuded zone was also not evident on mechanical tensile testing, SPCT and cross weld uniaxial creep testing.
- The microstructural quantification of the HAZ regions, parent material, and the weld metals revealed results that are consistent with theory of welding of 9-12%Cr steels. The microstructures in the HAZ regions were insensitive to the type of weld filler that was used.
- The X20 weld filler exhibited better mechanical properties compared to P91 weld filler. The X20 weld metal filler had an average hardness of 264 HV_{10}, whilst P91 weld metal filler had an average hardness of 206 HV_{10}.
- Overall characterisation results in relation to the objective of this study reveal no distinctive performance of either using X20 or P91 weld filler for a butt weld of creep aged X20 and virgin P91 pipes material. Both weld fillers (X20 and P91) are deemed to be suitable since they have the same characterization results from the applied short term uniaxial creept test (i.e max. 1302 hours of creep test). Therefore long term creep test (≥ 50 000 hours) are to be conducted to study the microstructural evolution in the HAZ due to long term diffusional creep mechanism.

REFERENCES

[1] Zhang, Q., Zhang, J., Zhao, P., Huang, Y., Yu, Z., Fang, X., "Low-cycle fatigue behaviors of a new type of 10% Cr martensitic steel and welded joint with Ni-based weld metal," *International Journal of Fatigue*, Vol. 88 (2016), pp 78-87.

[2] Collini, L., Giglio, M., Garzeira, R., "Thermomechanical stress analysis of dissimilar welded joints in pipe supports: Structural assessment and design optimization," *Engineering Failure Analysis*, Vol. 26, (2012), pp 31-49.

[3] Akram, J., Kalvala, P.R., Misra, M., Charit, I., "Creep behaviour of dissimilar metal weld joints between P91 and AISI 304" *Materials Science and Engineering A*, Vol. 688, (2017), pp 396-406.

[4] Bettahar, K., Bouabdallah, M., Badji, R., Gaceb, M., Kahloun, C., Bacroix, B., "Microstructure and mechanical behavior in dissimilar 13Cr/2205 stainless steel welded pipes" *Materials and Design*, Vol. 85, (2015), pp 221-229.

[5] Mayr, P., Schlacher, C., Siefert, J.A., Parker, J.D., "Microstructural features, mechanical properties and high temperature failures of ferritic to ferritic dissimilar welds" *International Materials Reviews*, Vol. 64, No. 1, (2019), pp 1-26.

[6] Subramaniam, M., Galler, J., DuPont, J., Kombaiah, B., Yu, X., Feng, Z., Babu, S., "Heterogeneous creep deformation in dissimilar metal welds (DMWs)", *Materials Science and Engineering A*, Vol. 749, (2019), pp 1-13.

[7] Vijayanand, V.D., Vanaja, J., Das, C.R., Mariappan, K., Thakur, A., Hussain, S., Prasad Reddy, G.V., Sasikala, G., Albert, S.K., "An investigation of microstructural evolution in electron beam welded RAFM steel and 316LN SS dissimilar joint under creep loading conditions", *Materials Science and Engineering A*, Vol. 742, (2019), pp 432-441.

[8] Zhang, Q., Zhang, J., Zhao, P., Huang, Y., Yu, Z., Fang, X., " Low cycle fatigue behaviour of a new type of 10% Cr martensitic steel and welded joint with Ni-based weld metal" *International Journal of Fatigue*, Vol. 88, (2016), pp 78-87.

[9] Shojaati, M., and Beidokhti, B., "Characterization of ASI 304/AISI 409 stainless steel joints using different filler materials" *Construction and Building Materials*, Vol. 147, (2017), 608-615.

[10] Wang, W., Lu, Y., Ding, X., Shoji, T., "Microstructures and microhardness at fusion boundary of 316 stainless steel/Inconel 182 dissimilar welding," *Materials Characterization*, Vol. 107, (2015), pp 255-261.

[11] Vashishtha, H., Taiwade, R.V., Sharma, S., Patil, A., "Effect of welding processes on microstructural and mechanical properties of dissimilar weldments between conventional autenitic and high nitrogen austenitic stainless steels," *Journal of Manufacturing Processes*, Vol. 25, (2017), pp 49-59.

[12] Kafexhiu, F., Podgornik, B., Vodopivec, F., "Ageing Effect on the Creep Performance of Simulated Weld HAZ for the Steels X20 and P91," *5th International Conference of Engineering Against Failure*, Greece, June. 2018.

[13] Panait, C., Zielinska-Lipiec, A., Koziel, T., Czyrska-Filemonowicz, A., Gourgues-Lorenzon, F., "Evolution of dislocation density, size of sub grains and MX-type precipitates in a P91 steel during creep and during thermal ageing at 600°C for more than 100 000 h", *Materials Science and Engineering A*, Vol. 527, (2010), pp 4062-4069.

[14] Race, J. M., "Carbon Diffusion Across Dissimilar Steel Welds", St. John's Collage, Cambridge, Doctor of Philosophy dissertation, (1992).

[15] Elder, D. L., "Carbon migration across dissimilar metal welds related to power plant", (2011). pp. 46-51.

[16] Aghajani, A. "Evolution of Microstructure during Long-term Creep of a Tempered Martensitic Ferritic Steel", Bochum. Phd. (2009). pp.1-86.

ACKNOWLEDGEMENTS

The authors would like to acknowledge the financial support from ESKOM.

8.2 Second Paper: Microstructural Characterisation and Small Punch Creep Testing of 9-12Cr Steel Weldments

Joint EPRI – 123HiMAT International Conference on
Advances in High Temperature Materials
October 21–24, 2019, Nagasaki, Japan
J. Shingledecker, M. Takeyama, editors

Copyright © 2019 ASM International®
All rights reserved.
www.asminternational.org

MICROSTRUCTURAL CHARACTERIZATION AND SMALL PUNCH CREEP TESTING OF 9-12%Cr STEEL WELDMENTS

JE Westraadt
Centre for HRTEM, Nelson Mandela University, Port Elizabeth, South Africa

D Bernard
eNtsa, Nelson Mandela University, Port Elizabeth, South Africa

T Mphaphathi and M Bezuidenhout
Eskom Sustainability Division, Johannesburg, South Africa

ABSTRACT

Small punch creep testing (SPCT) is a small-scale, accelerated creep test that allows for the determination of creep data using a limited amount of material. The question, however, remains how the data generated by this technique correlate to more established techniques such as uniaxial testing and ultimately to predictions regarding the remaining service life of a plant component. This empirical study investigated the microstructure-to-property relationship of welded 9-12%Cr steels as measured using SPCT. Virgin P91 (X10CrMoVNb9-1) steel was joined to service exposed X20 (X20CrMoV12-1) steel using two different filler materials (X20 and P91) via fusion welding. Site-specific samples were extracted from the parent plates, heat affected zones and weld metals using electro-discharge machining. Small punch creep testing were performed using a 276 N load at a temperature of 625°C. The untested sample microstructures were quantitatively characterized using a range of electron microscopy techniques to determine the precipitate ($M_{23}C_6$, MX) spacing, subgrain sizes and dislocation densities for each region of the weldments. Multiple linear regression analysis found that the subgrain size (λ_{sg}) played the largest contribution to the SPCT rupture life. The heat affected zones had the lowest SPCT rupture times (49-68 hours), which corresponded to the largest subgrain sizes (1.1-1.3 μm). The P91 parent plate material had the longest SPCT rupture time (349 hours), which corresponded to the lowest subgrain size (0.8 μm). The P91 weld metal sample showed lower initial deflection rates during the SPC testing, however the presence of non-metallic SiO_2 inclusions in this zone contributed to accelerated brittle failure.

INTRODUCTION

Conventional mechanical testing as a means of determining the remaining life of a plant component needs a large amount of material, hence the component is destroyed. The development of novel sampling and friction hydro pillar processing (FHPP) repair methods allows for the sub-surface extraction of small samples from plant components [1]. The availability of limited testing material has necessitated the development of small sample designs and associated test methods, particularly for the determination of static and creep behavior of a sample material. Small punch creep testing (SPCT) has attracted much interest due to its potential to characterize the full uniaxial creep curve (specimen is taken to fracture) from a 8 mm diameter and 0.5 mm thickness sample in a test lasting typically 200-1000 hours [2]. Several efforts are currently underway for the standardization of the technique with regards to the experimental setup and creep data interpretation [3].

It is often purported that the same mechanisms responsible for deformation in a uniaxial creep tests are also present in SPCT, due to the similarity in shape (primary, secondary and tertiary regions) observed in creep strain vs time plots (from uniaxial testing) and displacement versus time plots (from SPCT) [2]. Therefore, it is often reported that there exists a relationship between the minimum strain rate observed in uniaxial creep rupture tests and the minimum displacement rate (MDR) found in SPCT. This relationship is then used to correlate the SPCT to uniaxial data by applying either the Monkman-Grant [4] or Larson-Miller parameter [5] approaches.

In reality, however, the three regions in the SPCT have generally different physical meanings than those of the standard creep curves, which are related to the interaction of initial plasticity, geometrical stiffening and creep-damage in the material [2]. Analytical methods, such as those described in the 2006 Code of Practice [6] employ a membrane stretching model to relate the test results between uniaxial creep and SPCT. This model introduces a correlation factor (K_{sp}) that accounts for the changes in the localized necking during specimen deformation due to different levels of creep ductility, which unfortunately has to be determined empirically. The complex nonlinear mechanisms operating in the sample during SPCT can be modelled using finite element methods [7]. Importantly, these methods further allow for more realistic constitutive materials models that includes the effects of initial plasticity and damage development during the test [8]. Inverse-modelling approaches have been employed to determine material properties from the SPCT data [9]. It is therefore clear that the microstructural state of the material plays an important role in the SPCT measurement.

Creep strength enhanced Ferritic (CSEF) steel (9-12% Cr) microstructure consists of hierarchically related internal interfaces [10] (prior austenite grain boundaries, prior block boundaries, prior lath boundaries, after tempering these interfaces constitute high angle ferrite boundaries). The microstructure contains high dislocation densities associated with accommodation processes which occur during tempering. Secondary phases such as precipitates ($M_{23}C_6$, MX) act as obstacles to dislocation movement [11] and stabilize the subgrain structure [12]. Microstructural instabilities such as a decrease in dislocation density, subgrain and precipitate growth, and the formation of new phases (Laves and Z-phase) are considered to be responsible for the loss of creep-strength during long-term in-service operation [13]. Microstructural analysis could thus be used in principle as an additional indicator for the remaining life through the use of suitable physical-based microstructure-to-property models. The "*backstress*" model discussed by Holzer [11] assumes that the microstructural features counteracts the external stress via an internal stress σ_i, which can be expressed as a superposition of individual microstructural contributions:

$$\sigma_{eff} = \sigma_{ext} - \sigma_i \text{ where } \sigma_i = \Sigma M^*(\tau_{precitates} + \tau_{subgrains} + \tau_{dislocations}) \text{ (M is the Taylor factor)}$$

Type IV cracking in the fine-grained heat affected zone (FGHAZ) is the main life-determining mechanism for welded 9-12% Cr CSEF structures [14]. Several authors [15, 16, 17, 18] have investigated the use of SPCT as a means of measuring the creep properties of the heat affected zone of 9-12% Cr steels welds. The technique naturally lends itself due to its localized nature and allows for the determination of the creep properties without the constraint conditions that are normally experienced by the fine-grained heat affected zones in a cross-weld uniaxial creep test. However, the aforementioned SPCT studies mainly focused on the creep properties and very limited microstructural characterization were reported.

The aim of this paper is to present preliminary results on the empirical relationship between the quantitative microstructural analysis of the different microstructural zones of dissimilar (X20/P91) weldments and its associated creep-properties as measured using SPCT.

EXPERIMENTAL DETAILS

The base materials consisted of service exposed X20 (X20CrMoV12-1) and virgin P91 (X10CrMoVNb9-1). Two weldment types were prepared using P91 and X20 welding rod consumables. The chemical composition of the pipe and filler materials are listed in *Table 1*. The welded joints were prepared as a single V-joint using Gas-Tungsten Arc Welding (GTAW / TIG) process for the root pass, and Manual Metal Arc (MMA) welding for the filler passes. Magnetic particle inspection and ultrasonic testing were conducted after welding to ensure that welding defects are detected prior to testing. Post-weld heat treatments were performed at 755°C for 4 hours using a ramp rate of 50°C per hour.

Table 1: Measured chemical composition in wt.% of the parent plate and filler materials.

Steel Grade	C	Cr	Mo	V	Si	Ni	Nb	Al	Cu
P91 (pipe)	0.09	8.61	0.97	0.20	0.33	0.18	0.094	0.013	0.130
X20 (pipe)	0.16	11.7	0.96	0.29	0.22	0.69	0.021	0.029	0.080
P91 (filler)	0.08	8.59	1.03	0.22	0.26	0.49	0.061	-	0.050
X20 (filler)	0.12	10.8	0.92	0.22	0.38	0.49	0.022	-	0.040

The microstructural zones were identified using optical microscopy on the polished and etched surfaces (top and cross-section) of the weldment. The heat affected zones were extracted as thin slithers using electro-discharge machining. *Figure 1* shows the location of extracted HAZ samples. The extracted materials were cut into 8 mm diameter disks and ground to a thickness of 500 ± 5 µm for testing. To ensure that the samples from the HAZ were of the correct structure, the sectioned disks were ground incrementally. Both faces were polished and etched, and the surfaces were inspected using light microscopy to ensure that the microstructures were consistent with that of a fine-grained heat affected zone.

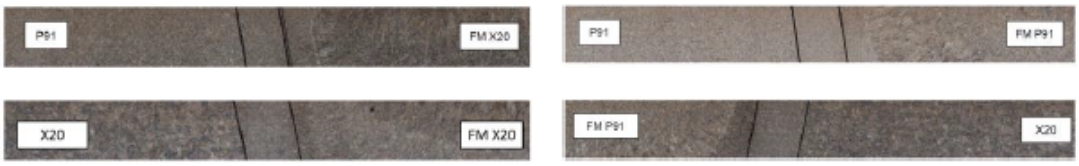


Figure 1: Site specific sampling of the fine-grained heat affected zones in the weldments

Eight samples were tested utilizing the small punch creep testing (SPCT) methodology, at eNtsa (Nelson Mandela University), which is compliant to the 2006 Code of Practice [6]. The test parameters were chosen such that the P91 parent material would reach an estimated rupture time of approximately 500 hours using a load of 276 N at a temperature of 625°C. The creep-tested samples were subsequently cross-sectioned using electro-discharge machining, mounted and polished to a colloidal silica (50 nm) finish and imaged using backscattered electron (BSE) imaging at 10 kV to investigate the grip and fracture regions of the tested samples.

Untested disk samples were thinned down to 80-100 µm and punched into 3 mm disks. The disks were thinned to electron transparency using a Struers Tenupol 5 twin-jet electro-polisher with a 5% Perchloric – Methanol solution cooled to -20°C at 21 V. The electro-polished surfaces were investigated using 3 kV backscattered electron (BSE) imaging to observe the precipitate distribution and grain channeling contrast. A total of 4x (30 x 20 µm) areas were imaged for each weldment zone. Electron backscattered diffraction (EBSD) was performed over an 180 µm x 150

µm area using a step size of 0.2 µm to observe the grain orientations at 15 kV. Transmission Kikuchi diffraction (TKD) in combination with energy dispersive spectroscopy (EDS) was used to investigate the electron transparent areas of the thin foils. By placing the sample at a -20° incident angle the 30 kV electron beam travels through the thin (<100 nm) areas of the sample. This greatly reduces the beam-specimen interaction volume as compared to more traditional bulk SEM analysis. Spatial resolutions down to 10 nm for orientation mapping and 20 nm for EDS analysis can be obtained using this SEM-based technique. A total of 2x (10 µm x 10 µm) areas were analyzed using a step size of 20 nm from each weldment region. Annular dark field scanning transmission electron microscopy (ADF-STEM) (collection angle: 18 – 47 mRad) at 200 kV (LaB_6) allows for the simultaneous observation of dislocations networks, grain boundaries and precipitates. A total of 10x (5 x 5 µm) areas were imaged for each weldment region.

Semi-automated image analysis was performed using MIPAR™ [19] to quantify the different features of interest. Stereological corrections were applied to the precipitate measurements to convert the projected area measurements into a volume fraction and volume number density based on an estimated sample thickness of 100 nm [20]. The precipitate measurements ($M_{23}C_6$ and MX) were then grouped into a single parameter (λ_{ss}) representing the mean inter-particle spacing [20]. The mean subgrain short width (λ_{sb}) was determined by applying a critical misorientation angle of 4° to outline the subgrain boundaries. The subgrains were then fitted with an ellipse and the mean minor axis value taken as the short-width. Free mobile dislocation densities (ρ_m) were determined using whole pattern peak profile analysis of X-ray diffraction patterns collected from the different weldment regions [21].

The microstructural measurements (λ_{ss}, λ_{sb}, ρ_m) were converted into a microstructural strength by considering them as obstacles for dislocation movement according to the backstress model discussed by Holzer [11]. *Table 2* lists the relationships for each microstructural feature.

Table 2: "Backstress" contribution per microstructural feature [11].

Precipitate Hardening (PH)	$\sigma_{0r} = \frac{0.8MGb}{\lambda}$ $\lambda = \sqrt{\frac{\ln 3}{2\pi N_V \bar{r}} + 4\bar{r}^2} - 1.63\bar{r}$	(1)	Where: σ_{0r} ≡ Orowan stress λ ≡ Mean 2D surface-to-surface interparticle spacing M ≡ Taylor factor (3) G ≡ Shear modulus (65 GPa) b ≡ Burgers vector (2.5 x 10^{-10} m) $\bar{r} = \frac{d}{2}$ ≡ Mean particle radius of precipitates
Sub-Boundary Hardening (SBH)	$\sigma_{sg} = \frac{10Gb}{\lambda_{sg}}$	(2)	Where: σ_{sg} ≡ SBH stress λ_{sg} ≡ Elongated subgrain short width
Dislocation Hardening (DH)	$\sigma_\rho = 0.5\, MGb\sqrt{\rho_f}$	(3)	Where: σ_{sg} ≡ DH stress ρ_f ≡ Free dislocation density

There are a number of critical assumptions in this simple microstructure-to-property model, and the development of accurate yet computationally efficient micro-mechanical models for creep is still an active research area. The calculated strengths contributions were then normalized relative to the virgin P91 parent for each microstructural feature. The relationship between the calculated microstructural strength and the SPCT rupture times were investigated with the multiple linear regression function in the *Statsmodels* [22] python package.

RESULTS AND DISCUSSION

Figure 1 shows the Vickers (300 g) hardness traverses of the weldments made with the two filler materials through the centre line of the pipe. The hardness profiles showed a similar trend for the HAZ regions of the two weldments on both the P91 parent and X20 parent material sides. The dash-dotted central line indicates that the hardness measurements were not taken completely through the weld metal region. The scatter in the weld metal regions are due to the tempering effects of the multipass welding method.

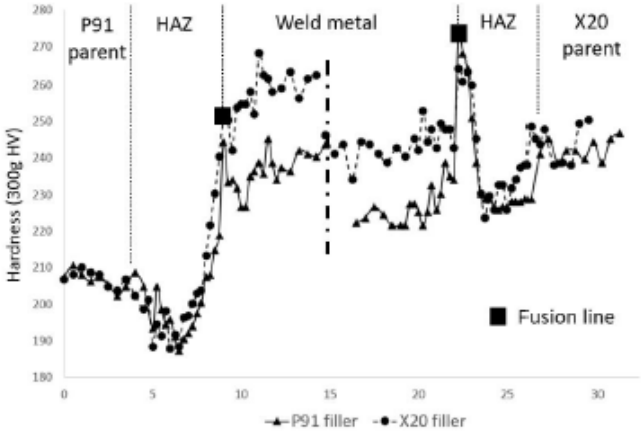


Figure 1: Vickers indentation hardness measurements of the weldments

The small punch creep test deflection and deflection rate versus time curves are shown in *Fig. 2*. The four HAZ samples had the lowest rupture times (49 - 68 h). This result is consistent with the previous works [15, 16, 17, 18] of SPCT of 9-12% Cr steel weldments. The P91 parent had the longest rupture time (349 h) compared to the service exposed X20 parent (276 h). The filler materials showed intermediate rupture times (X20_FM – 176h and P91_FM – 91h). The creep rate curves of the P91 filler material are of interest, since the initial deflection and deflection rates are lower in the early stages of the test. In addition, the P91 filler sample (solid line) creep-rate versus time curve showed atypical behavior, which could be an indication of brittle crack formation in the sample [2].

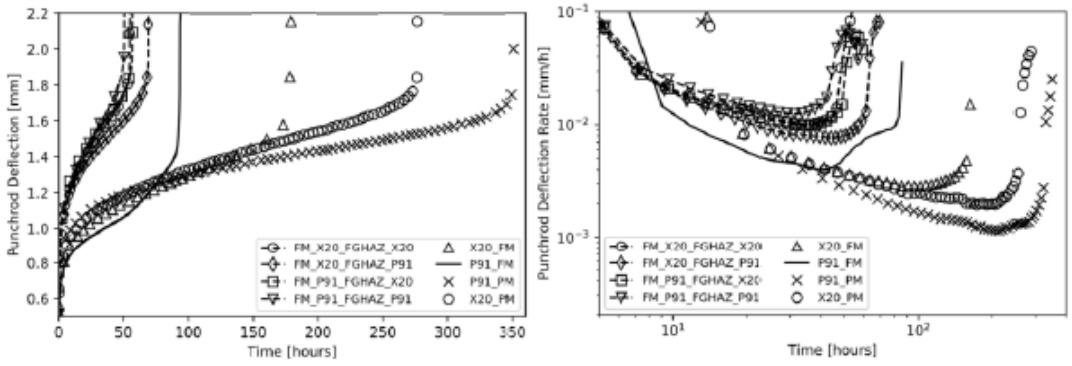


Figure 2: Punch rod deflection (left) and deflection rate (right) as a function of time.

BSE imaging of the electro-polished surfaces show the distribution of the various precipitates ($M_{23}C_6$, MX) due to the atomic number contrast and preferential etching around precipitates. In addition, subgrains can be visualized due to the variations of electron channeling for different ferrite crystal orientations. *Figure 3* shows BSE images taken from the P91 parent, P91 HAZ and P91 weldment regions. The P91 parent microstructure consists of elongated subgrains and $M_{23}C_6$ carbides decorating the subgrain boundaries. The P91 HAZ region shows rounded subgrains and several $M_{23}C_6$ carbides not located on a grain boundary. The P91 weld metal showed a fine microstructure similar to the P91 parent material, but also contained numerous non-metallic inclusions, identified as SiO_2 using EDS.

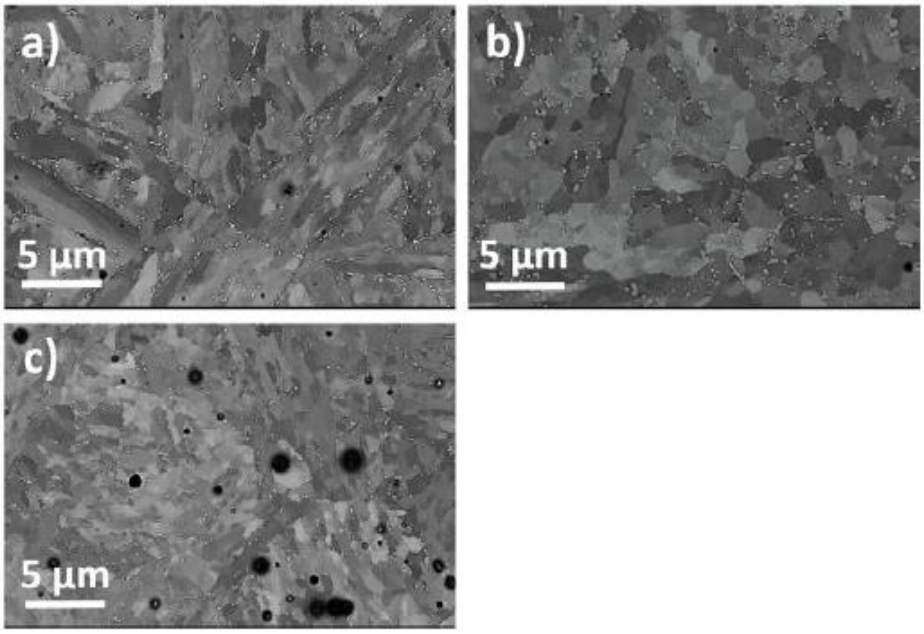


Figure 3: BSE images of (a) P91 parent, (b) P91 HAZ and (c) P91 weld metal

Figure 4 shows the orientation maps taken from the P91 parent, P91 HAZ and P91 weld metal regions. The P91 parent material had elongated subgrains with a mean short-width of 0.8 ± 0.1 µm. The P91 HAZ region had rounded subgrains with a mean short-width of 1.3 ± 0.1 µm. The P91 weld metal subgrains showed a similar structure to the P91 parent material and had a mean short-width of 1.0 ± 0.1 µm.

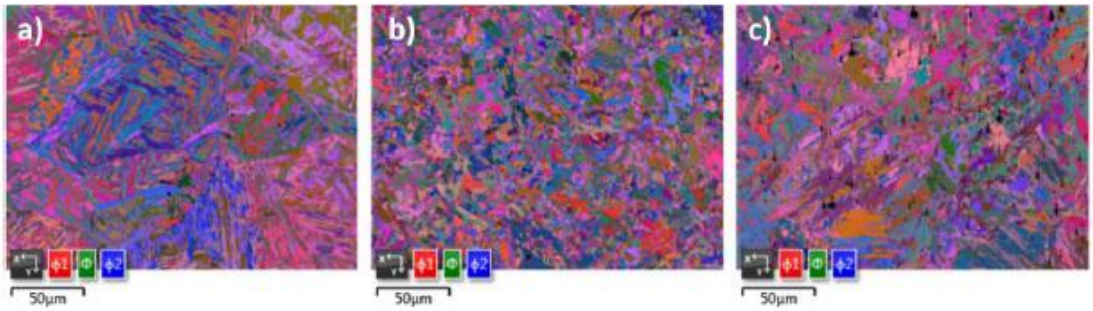


Figure 4: All Euler orientation maps of the (a) P91 parent, (b) P91 HAZ and (c) P91 weld metal

Figure 5 shows the elemental maps for chromium-rich ($M_{23}C_6$), vanadium-rich (MX), and the band contrast (BC) representative of the grain structure within the investigated areas. The elemental maps were segmented using image analysis in order to calculate the projected area measurements. This result was then used to calculate the combined interparticle spacing (λ_{ss}) for each microstructural region.

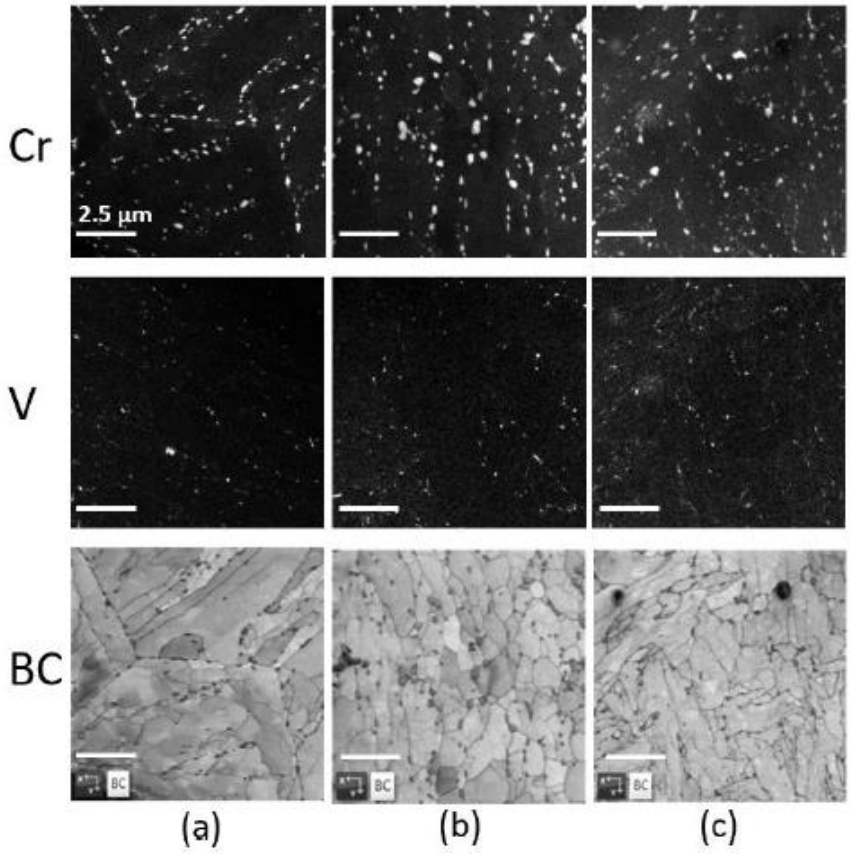


Figure 5: TKD-EDS maps showing the distribution of $M_{23}C_6$ precipitates (Cr-rich), MX precipitates (V-rich) and grain boundaries (BC) in the (a) P91 parent, (b) P91 HAZ and (c) P91 weld metal.

Figure 6 shows ADF-STEM images for the P91 parent, P91 HAZ and P91 weld metal regions respectively. The P91 parent material showed a fined grained microstructure and with numerous free-dislocations inside the subgrains. The P91 HAZ showed a marked decrease in the free dislocation density and an increased subgrain size. The P91 weld metal showed a very high dislocation density and a fine-grained subgrain structure. This result needs to be interpreted with care due to the localized nature of the imaging and the highly inhomogeneous microstructure resulting from tempering during the multipass welding method. Bulk mobile dislocation density measurements were made using X-ray diffraction line profile analysis of each microstructural region of the weldments. *Table 3* gives a summary of the microstructural feature measurements for each of the weldment regions tested with SPCT.

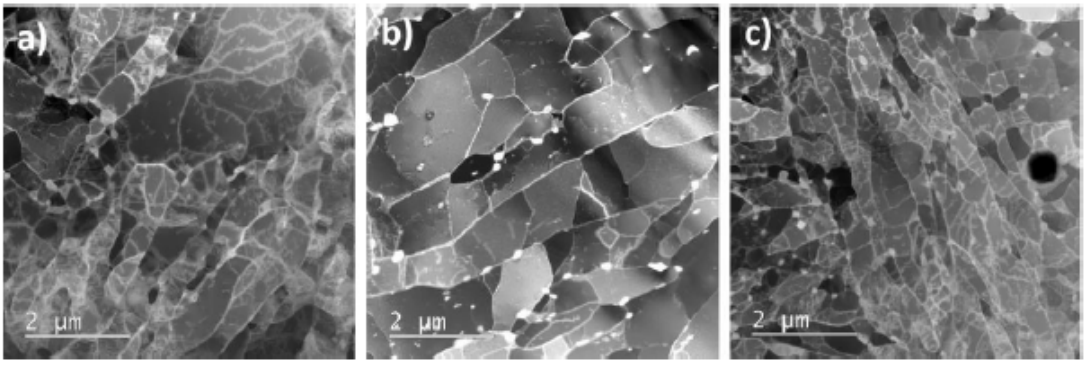


Figure 6: ADF-STEM images the (a) P91 parent, (b) P91 HAZ, and (c) P91 weld metal

Table 3. Summary of the microstructural feature measurements for each of the weldment regions.

Sample	Precipitates (λ_{ss}) (nm)	Subgrains (λ_{sb}) (µm)	Dislocation density (ρ_m) (m^{-2})
X20 PM	322	1.1	5.4E+13
P91 PM	371	0.8	4.7E+14
FM X20_FGHAZ P91	449	1.3	7.8E+13
FM X20_FGHAZ X20	340	1.1	1.3E+14
FM P91_FGHAZ X20	321	1.1	2.3E+14
FM P91_FGHAZ P91	398	1.2	1.1E+14
X20 filler	311	1.0	2.4E+14
P91 filler	314	1.0	3.1E+14

Systematic errors due to sample preparation, specimen-beam interactions, image processing, stereological corrections and statistical processing will have a strong influence on the *accuracy* of the microstructural measurements. The microstructural features were considered separately and normalized relative to the P91 parent material in order to reduce the effect of the aforementioned systematic errors. Random errors due to sampled volumes and microstructural inhomogeneities (short-range and long-range) will impact on the *precision* of the microstructural measurement. Optimization of the characterization techniques, sample preparation, representative sampling volumes, automated image analysis, data processing and reporting are part of ongoing research project with the industrial sponsor.

Figure 7 shows a summary of the normalized strength contributions due to each microstructural feature for each of the weldment regions. *Dislocation density* was the highest (increased strength) in P91 parent material and significantly reduced for the HAZ regions, while the service exposed X20 parent material had the lowest dislocation density. These measurements are consistent with the qualitative ADF-STEM imaging conducted on the microstructural zones. *Interparticle spacing* for X20 microstructural zones had smaller interparticle spacings (increased strength) compared to the respective P91 zones due to the increased phase fraction of $M_{23}C_6$. This is due to the increased chromium and carbon content of this material grade. The P91_HAZ regions had larger interparticle spacings (lowered strength) due to the increase in $M_{23}C_6$ precipitate diameters compared to the P91 parent material. The area investigated in the P91 weld metal had decreased interparticle spacing (increased strength) due to the presence of smaller $M_{23}C_6$ precipitates. This result needs to be interpreted with care due to the localized nature of the imaging and the highly inhomogeneous microstructure resulting from tempering during the multipass welding method.

The HAZ samples showed the largest *subgrain short-width* (lowered strength). The service exposed X20 material and the weld metal regions show larger subgrain short-width (lowered strength) compared to the P91 parent material.

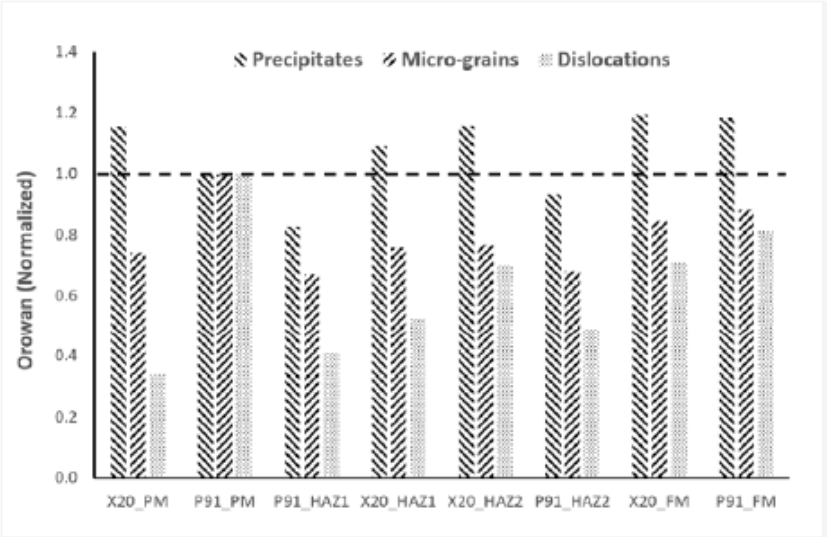


Figure 7: Normalised backstress per microstructural feature for each weldment region (HAZ1 – X20 filler; HAZ2 – P91 filler)

The microstructural strength contributions can be related to the rupture time using multiple linear regression. The normalized backstress for each measured microstructural feature were used as inputs and fitted to the SPCT rupture time, resulting in the following empirical relationship:

$$\text{Rupture time (hours)} = -738 + (-71)*\sigma_{PH} + (1736)*\sigma_{SBH} + (-580)*\sigma_{DH} \quad [R^2_{adj} = 0.79]$$

This result needs careful interpretation since the expectation is that all the fitting coefficients and the intercept should be positive values. It should be noted that this study had a very small sample size of only eight data points. Including more material conditions will improve the confidence in this relationship. This relationship implies that the subgrain size is mainly responsible for the differences in SPCT rupture times.

The empirical relationship suggests that the precipitate interparticle spacing (λ_{ss}) is not important for SPCT rupture life. Assumptions made in the micro-mechanical model influenced this result. The simplistic precipitate strengthening calculations used in this study did not take the location of the precipitates into account. BSE imaging showed that the $M_{23}C_6$ precipitates formed a bi-modal size distribution with numerous smaller precipitates forming during the welding process in the HAZ regions. Furthermore, numerous large precipitates were located on the interior of the subgrains and not on the subgrain boundaries.

The dislocation density measurements from the X-ray diffraction peak profile analysis are very sensitive to sample surface preparation and the Rietveld refinement fitting procedure. Furthermore, the assumption of a linear combination assumes that each microstructural feature operates independently from each other. Non-linear approaches such the Bayesian machine

learning described by Murugananth [23] can be applied if more data are available. This approach would be able to take the interaction between the different microstructural features into account.

Figure 8 shows BSE images of the grip region of the P91 weld metal SPCT sample after testing. The sample contains numerous SiO_2 inclusions that formed during the welding process, probably due to insufficient oxygen shielding. The atypical creep-strain curves and early failure can be attributed to low creep-ductility in the sample due to the presence of the non-metallic inclusions. BSE images of the bend area confirmed that significant cracking occurred in the sample.

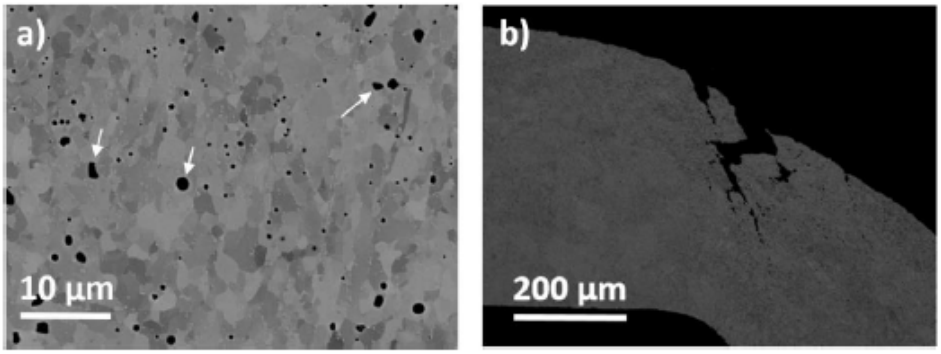


Figure 8: BSE images of the (a) grip region of the P91 weldment SPCT sample, showing the presence of numerous SiO_2 inclusions (indicated with the arrows), and (b) bend region of the P91 weld metal SPCT sample showing extensive crack formation.

CONCLUSIONS

This study showed preliminary results of the empirical relationship between the microstructure and rupture-life measured by SPCT for different 9-12% Cr steel weldment regions. The microstructural features of interest were; interparticle spacing (λ_{ss}), subgrain short-width (λ_{sb}), and mobile dislocation density (ρ_m). The multiple linear regression performed on the microstructural and creep data suggests that the subgrain size is the most important parameter. The short SPCT rupture times (49-68 hours) and increased MDR of the HAZ samples compared to the P91 parent material is due to its increased subgrain size. Furthermore, numerous $M_{23}C_6$ were located in the interior of the subgrains for the HAZ regions, however, location of the precipitates was not taken into account in the micro-mechanical model used for this study.

The P91 weld metal sample showed reduced creep-ductility due the presence of non-metallic SiO_2 inclusions. The small punch deflection curve and ultimate rupture time is a function of the microstructural state and testing conditions. The presence of larger microstructural discontinuities such as voids, cracks and inclusions could influence the damage development during the test, which will impact the reliability of remnant life-predictions based on minimum deflection rates. This could be particularly important for service exposed materials with excessive voids and/or cracks. The combination of small-scale testing with quantitative microstructural analysis on small samples has the potential to reduce the uncertainties in the remnant-life predictions of 9-12% Cr steels by providing data on the mechanical properties as well as the microstructural state. In order to realize the potential of microstructural-based life assessments significant developments on automated characterization, automated image processing and computationally efficient micro-mechanical models are needed.

ACKNOWLEDGMENTS

We want to acknowledge the Material and Mechanics Specialization Group (University of Cape Town) of the Eskom Power Plant Engineering Institute (EPPEI) for funding this research project.

REFERENCES

[1] Hattingh, D. G., James, M. N., Newby, M. N., Scheepers, R. and Doubell, P., "Damage Assessment and Refurbishment of Steam Turbine Blade/Rotor Attachment Holes", *Theoretical and Applied Fracture Mechanics* (2015) doi:https://doi.org/10.1016/j.tafmec.2015.11.001.

[2] Rouse, J. P., Cortellino, F., Sun, W., Hyde, T. H. and Shingledecker, J., "Small Punch Creep Testing: Review on Modelling and Data Interpretation", *Materials Science and Technology*, Vol. 29, No. 11 (2013), pp. 1328-1345.

[3] Bruchhausen, M. Altstadt, E., Austin, T., Dymacek, P., Holmström, S., Jeffs, S., Lacalle, R., Lancaster, R., Matocha, K., Petzova, J., "European Standard on Small Punch Testing of Metallic Materials", Ubiquity Proceedings, 1(S1): 11 doi:https://doi.org/10.5334/uproc.11.

[4] Dobes, F. and Milicka, K., "On the Monkman-Grant Relation for Small Punch Test Data", *Materials Science and Engineering,* Vol. A336 (2002), pp. 245-248.

[5] Komazaki, S., Kato, T., Kohno, Y. and Tanigawa, H., "Creep Property Measurements of Welded Joint of Reduced-activation Ferritic Steel by Small-Punch Creep Test", *Materials Science and Engineering,* Vol. A510, No. 11 (2018), pp. 229-233.

[6] CEN Worskshop Agreement, "Small Punch Test Method for Metallic Materials" CWA15627:2006 E, December 2006.

[7] Wang, J. P., Chen, G., Zhai, P. C. and Zhang, Q. J., "Investigation on the Effect of Test Parameters on Small Punch Creep Tests by Finite Element Method", *Multiscale Multifunct. Funct. Graded Mater.,* Vol. 6313-632 (2010), pp. 393-398.

[8] Murakami, S., Lui, Y. and Mizuno, M., "Computation Methods for Creep Fracture Analysis by Damage Mechanics', *Comp. Meth. Appl. Mech. Eng.,* Vol. 183, No. 1-2 (2000), pp. 15-33.

[9] Li, Y., Stevens, P., Geng, J., Ma, D. and Xu, L., "Determination of Creep Properties from Small Punch Test with Reverse Algorithm", *Key Engineering Materials,* Vol. 734 (2017), pp. 212-236. https://doi.org/10.4028/www.scientific.net/KEM.734.212.

[10] Payton, E. J., Aghajani, A., Otto, F., Eggeler, G. and Yardley, V.A., "On the Nature of Internal Interfaces in Tempered Martensite Ferritic Steel and their Evolution During Long-Term Creep", *Scr. Mater.,* Vol. 66 (2012), pp. 1045-1048.

[11] Holzer, I., "Modelling and Simulation of Strengthening in Complex Martensitic 9-12% Cr steel and a binary Fe-Cu alloy", *PhD Thesis*, Graz University of Technology (2010).

[12] Kostka, A., Tak, K. G., Hellmig, R. J., Estrin, Y. and Eggeler, G., "On the Contribution of Carbides and Micrograin Boundaries to the Creep Strength of Tempered Martensite Ferritic Steels", *Acta Materialia*, Vol. 55, No. 2 (2007), pp. 539-550.

[13] Aghajani, A., Somsen, C., Eggeler, G., "On the Effect of Long-Term Creep on the Microstructure of a 12% chromium Tempered Martensitic Ferritic Steel", *Acta Mater.*, Vol. 57 (2009), pp. 5093-5106.

[14] Abson, D. J. and Rothwell, J. S., "Review of Type IV Cracking of Weldments in 9-12%Cr Creep Strength Enhanced Ferritic Steels", *International Materials Reviews,* Vol. 58, No. 8 (2013), pp. 437-473.

[15] Komazaki, S., Nogawa, S., Yamashita, H. and Hasegawa, Y., "Local Creep Property Measurement of High Cr Ferritic Steel Welded Joint by Small Punch Test", *Journal of the Society of Material Science Japan*, Vol. 66, No. 2 (2017), pp. 101-107

[16] Zhao, L., Jing, H., Xu, L, Han, Y., Xiu, J. and Qiao, Y., "Evaluating of Creep Property of Distinct Zones in P92 Steel Welded Joint by Small Punch Creep Test", *Materials and Design,* Vol. 47 (2013), pp. 677-686.

[17] Komazaki, S., Kato, T., Nakata, T., Gatsenko, A. and Kohno, Y., "Small Punch Creep Properties of Welded Joint of High Cr Ferritic Steel", *Proc. ECCC Creep Conf*, Zurich, April. 2009, pp. 1102-1112.

[18] Gulcimen, B. and Hahner, P., "Determination of Creep Properties of a P91 Weldment by Small Punch Testing and a New Evaluation Approach", *Materials Science and Engineering,* A588 (2013), pp. 125-131.

[19] Sosa, J. M., Huber, D. E., Welk, B. and Fraser, H. L., "Development and application of MIPAR™: a novel software package for two- and three-dimensional microstructural characterization", *Integrating Materials and Manufacturing Innovation,* Vol. 3:10. https://doi.org/10.1186/2193-9772-3-10.

[20] Sonderegger, B., "Modifications of Stereological Correction Methods for Precipitate Parameters using Transmission Electron Microscopy", *Ultramicroscopy*, Vol. 106 (2006), pp. 941-950.

[21] Soleimanian, V. and Mojtahedi, M., "A Comparison between different X-ray Diffraction Line broadening Analysis Methods for Nanocrystalline Ball-milled FCC Powders", *Applied Physics A,* Vol. 119, No. 3 (2015), pp. 977-987.

[22] Seabold, S. and Perktold, J. "Statsmodels: Econometric and Statistical Modeling with Python." *Proceedings of the 9th Python in Science Conference*, Austin, TX, June. 2010.

[23] Murugananth, M and Bhadeshia, H. K. D. H. "Components of the Creep Strength of Welds," in Mathematical Modelling of Weld Phenomena—VI, (H. Cerjak and H. K. D. H. Bhadeshia, Eds.), (Institute of Materials, 2002), pp. 243–260.